BINARY AND TERNARY PYROTECHNIC SYSTEMS CONTAINING MANGANESE, MOLYBDENUM, BARIUM PEROXIDE AND STRONTIUM PEROXIDE

THESIS

Submitted in fulfilment of the

requirements for the Degree of

DOCTOR OF PHILOSOPHY

of Rhodes University

by

ROBIN LENNOX DRENNAN

JANUARY 1991

FOR GAIL

ABSTRACT

Barium peroxide was selected as oxidant in a fundamental physico-chemical study of binary pyrotechnic systems on account of its apparently simple decomposition stoichiometry. With this selection, the choice of fuel was governed by the requirements of a self-sustaining reaction at combustion temperatures below the melting point of the platinum/rhodium thermocouples (~ 1760 °C) used for recording temperature-time profiles during burning, and at burning rates not exceeding the response of the sensors used to monitor combustion. Both manganese and molybdenum metal powders satisfied the above requirements. Strontium peroxide was also available as an oxidant and so the combustion of binary metal/oxidant systems using both fuels and both BaO_2 and SrO_2 oxidants was investigated.

The Mn/BaO_2, Mo/BaO_2 and Mn/SrO_2 systems burnt over a wide range of compositions, but the range of ignitable compositions for the Mo/SrO_2 system was very limited. The linear burning rates, for all these systems, ranged from 2 to 12 mm s^{-1} and burning rates were increased by the use of smaller particle-sizes of fuel and greater loading pressures. Inert additives generally decreased the burning rate.

Temperature-time profiles were recorded for all the compositions which sustained combustion. Kinetic parameters were estimated from the shapes of these profiles using procedures developed by Hill *et al* and Boddington and Laye. Activation energies derived from the profiles were low (3 to 40 kJ mol^{-1}) and support suggestions that reactions at high temperatures are controlled by diffusion processes.

Thermal analysis was used to identify the processes occurring in the four systems. The main exothermic events were observed to correspond approximately with the onset of oxidant decomposition. A pre-ignition reaction was tentatively identified in the Mn/BaO_2 system. Oxidation of the metal fuels was generally incomplete, probably because of the formation of protective layers of product. Activation energies, derived from thermal analysis results, were in the range of from 70 to 720 kJ mol^{-1}.

Ternary systems containing either mixed fuels or mixed oxidants were also examined. No interactions between the fuels or between the oxidants were observed.

Other techniques used included bomb calorimetry, measurement of thermal conductivity, X-ray powder diffraction, infrared spectroscopy and scanning electron microscopy.

ACKNOWLEDGEMENTS

I would like to express my most sincere appreciation and gratitude to Professor Michael E. Brown for his outstanding generosity of his time and effort. His unending patience and guidance were an important ingredient of this thesis.

I would also like to thank:

- Mr R. A. Rugunanan for his friendship and helpfulness,
- Mr F. Ranftelshöfer for his technical assistance,
- Mr J. Lucas and the late Mr B. K. Guthrie for their help with computer software and electronic equipment,
- Professor P. Terry and Mr D. Williams for further invaluable assistance with computer software,
- Dr M. Taylor of AECI, for his assistance,
- the Foundation for Research Development for its financial assistance and
- AECI Ltd. for the use of scientific equipment.

Further, I gratefully acknowledge the loving support of my wife, my parents and my family without whom I would never have been able to complete this indulgent task.

I wish also to share with any aspirant thesis writers who read this work, that the key to my completion of this thesis, with my sanity intact, included a sound Christian faith, ample support from friends and a good sense of humour.

CONTENTS

LIST OF FIGURES

LIST OF TABLES

Chapter 7

Chapter 9

LIST OF SYMBOLS

A pre-exponential factor in Arrhenius equation
B diffusion coefficient
C intercept of Y axis by a straight line
D thermal diffusivity (s^{-1})
E_a activation energy (J mol^{-1})
G power function
H height (mm)
I special integral in Section 6.1
M mass (g)
N percentage composition
P loading pressure (MPa)
Q rate of heat supply (J)
R gas constant or radius (mm)
T temperature (°C)
U excess temperature (°C)
V millivolt values (mV)
X percentage diluent
Y digital data

A point of ignition
O reaction zone
R reacted zone
U unreacted zone
V volume fraction

Phys physical factors

a effective radius (mm)
c specific heat capacity
d thermocouple diameter (mm)
f a special function
g a function for the rate equation
h lateral heat loss coefficient or height (mm)
k rate coefficient
m slope of a straight line
n "order" of reaction
q heat of reaction (J g^{-1})

r radius (mm)

t time

u radial distance

v linear burning rate (mm s^{-1})

w $d\alpha/dt$

z distance (mm)

α fraction of reaction

β special variable used in Section 6.1

Φ past heat evolution (J)

γ special variable used in Section 6.1

φ heating rate (°C min^{-1})

λ thermal conductivity (W m^{-1} K^{-1})

ρ density (g cm^{-3})

Subscripts:

calc calculated value

exp experimental value

ign ignition value

obs observed value

maj major component value

max maximum value

min minor component value

th thermal relaxation value

a ambient value

d decay value

e effective value

f final value

g of the gas

p of the probe

r rise value

s of the bulk solid

Superscript:

* value ignoring lateral heat losses

CHAPTER 1: INTRODUCTION AND PREVIOUS WORK

The use by man of chemical substances to produce heat, light, smoke, noise and motion has been known for several thousand years, originating most probably in China or India (ref 1). Early use of this chemical energy was concentrated in the military sphere, although it later spread into the cultural heritage of many countries in the form of fireworks (ref 1). In modern times a large commercial demand has developed for high energy reactions (ref 2), for use in mining, excavation and demolition.

"High energy" chemical compositions (ref 1) consist of a mixture of at least one reducing agent (or fuel) and at least one oxidizing agent which are able to sustain combustion in isolation from any source of heat or oxygen. Sometimes the oxidizing and reducing groups may form part of a single molecule. The rate at which this combustion moves through the unreacted mixture is used to classify this family into three categories:

- explosives, with propagation rates of the order of km s^{-1}, which is referred to as detonation,
- propellants, with propagation rates of the order of m s^{-1}, which is referred to as deflagration and
- pyrotechnics, with propagation rates of the order of mm s^{-1}, which is referred to as burning.

In pyrotechnic systems, the initially solid starting materials sometimes include a binder, often an organic compound, which is primarily used to increase the intimacy of mixing. During the exothermic reaction, under approximately adiabatic conditions, in such a system the combustion can be self-sustaining despite the possible endothermic contributions due to melting or decomposition.

Pyrotechnic systems have a wide range of applications (ref 3) from coloured flares used by the rescue services to the many military uses such as the thunderflash used to simulate battle noises. These applications have changed little over the last century, but totally new applications are continually being found for pyrotechnic reactions. One of the latest developments is in the field of "self-propagating, high temperature systems" (SHS) used to produce bulk chemicals by pyrotechnic reaction (ref 4).

A major application of pyrotechnic systems is their use as "delay fuses" used to control the time between an initial electrical pulse, which initiates the combustion, and a subsequent action, usually detonation, produced on completion of combustion or "burn through". The first pyrotechnic delays were the fuses of the fireworks used by Chinese artisans (ref 5). In the early 1800's, W. Bickford of Cornwall made "safety fuse" by wrapping black powder in paper (ref 5). The earliest delay detonators were made in Britain in 1910 and simply consisted of a safety fuse and a detonating explosive jointly contained in a metal and paper cylinder (ref 2).

The two World Wars provided the impetus for the rapid development of modern precision delay detonators. Ambient air pressure severely affected the delays in high-altitude projectiles. Consequently black powder was replaced by pyrotechnic mixtures whose products remained in the condensed phase. The lack of gaseous discharge ensured constant delay times at any pressure.

The mixtures used in delay elements contain an easily-oxidized element or alloy (fuel) and an easily-reduced metal oxide or oxy-salt (oxidant). The first such mixture to be widely used consisted of antimony and potassium permanganate (ref 2). However it is clear that many different mixtures are possible and that the choice will depend on the circumstances of use.

Pyrotechnic systems for use in delay fuses should meet at least the requirements of:

(i) safety and health standards;

(ii) stability on storage; and

(iii) reliability of ignition and propagation.

For a fundamental study, the system chosen should also, ideally (refs 6, 7):

(iv) be binary;

(v) be gasless;

(vi) be chemically simple - so that there is a chance of determining the stoichiometry and, possibly, the mechanism of reaction;

(vii) burn at temperatures below 1760°C - so that noble-metal thermocouples can be used to monitor combustion;

(viii) burn sufficiently slowly so as not to pose problems of response times of sensors; and

(ix) be capable of "simple" chemical variation by substitution of the fuel or (and) the oxidant by closely-related compounds.

In the search for a chemically-simple system (refs 6, 7), attention was focussed on the oxidant (ref 8), since many traditional oxidants, such as permanganates, dichromates, chlorates, etc, yield extremely complex solid products of decomposition. Barium peroxide is reported (refs 8, 9) to decompose to BaO(s) and O_2(g). In spite of this apparent chemical simplicity, BaO_2 is known to be variable in its properties, but a factor in its favour was the possibility of extending the study by substituting SrO_2 for BaO_2.

With barium peroxide chosen as oxidant, the choice of a fuel that satisfied the above criteria formed part of a preliminary study and included non-metals such as Si and C and the following transition metals: Mn, Mo, Cr, Nb and W. Mn and Mo powders were eventually chosen as the main fuels (see below).

Factors which determine the burning characteristics of any particular pyrotechnic composition include:

(i) the actual chemicals chosen;

(ii) the physical form, particle size and history of preparation of these chemicals;

(iii) the container in which the combustion takes place;

(iv) the compression with which the composition is loaded in the container, and

(v) the presence of additives included in the mixture by intent, or the presence of impurities in the original chemicals.

1.1 PYROTECHNIC MIXTURES WITH PEROXIDES AS OXIDANTS

The use of BaO_2 and SrO_2 as oxidants in pyrotechnic mixtures is widespread, but little has been published in the open chemical literature. Many of the references cited are in the form of patents. BaO_2 has been used mainly in delay systems (refs 10, 11) and SrO_2 in tracer compositions (refs 12, 13, 14). SrO_2 has also been used (ref 15) with fuels such as Zr, CaB_6, B and Mg, in essentially non-gaseous high altitude flare systems, where luminosity of the burning mixture must not diminish as the ambient pressure drops.

The most significant early work on the theory of pyrotechnic propagation was that by Spice and Staveley. Their two papers (refs 6, 7) are now regarded as the foundation of fundamental research in this field (ref 16). In the first paper, they showed by using a magnetic technique that many systems containing Fe as fuel underwent a pre-ignition reaction (PIR) and that solid-solid reactions occurred in at least the Fe/BaO_2 and $Fe/K_2Cr_2O_7$ systems. In their second paper, they noted that the linear burning rates of different compositions of the same system varied over a far wider range of values than either the specific heat or the thermal conductivity of the different compositions. They suggested that the burning rate is determined mainly by the kinetics of the PIR, and that the burning characteristics of a binary pyrotechnic mixture are more dependent on the properties of the oxidant than of the fuel. They proposed the following stoichiometry for the Fe/BaO_2 system:

$$2Fe(s) + 3BaO_2(s) \rightarrow 3BaO(s) + Fe_2O_3(s)$$

They also reported some results for the Mn/BaO_2, the Mo/BaO_2 and S/BaO_2 systems.

The next advance was the development, by Klein (ref 17) and Hill (refs 18, 19) and their respective co-workers, of a thermocouple technique, which was used by Hill *et al* to measure the temperature-time history at a point in a pyrotechnic mixture as a combustion wave passes by. Booth (ref 20), Boys and Corner (ref 21) and Nakahara (ref 22) also made significant contributions in this area (see below). The thermocouple technique was later refined by Boddington *et al* (refs 23, 24). More details of these developments are described in Section 1.3.

Amongst the systems studied by Hill *et al* (ref 18) were the Mo/BaO_2, Fe/BaO_2 and S/BaO_2 systems. They found good agreement between the observed and calculated linear burning rates for the Fe/BaO_2 system and fair agreement for the Mo/BaO_2 system. The equation used to calculate these linear burning rates is based on the energy balance equation for the propagation of a flame through a gas, ignoring lateral heat losses. It relates the propagation velocity of the combustion wave to the scaled final temperature, the thermal diffusivity and the mean reaction time (see Section 1.3 A). In a later publication (ref 19), improved correlation between observed and calculated burning rates was achieved for the 80% $Fe/KMnO_4$ system by greater control over materials and experimental conditions. The thermal constants of this system were assumed to remain unchanged during the course of reaction.

Kinetic analysis of the temperature profiles gave low values for the activation energy (13 to 33 kJ mol^{-1}) and a thermal conduction mechanism was proposed to account for the burning rate.

Hill and Wallace (ref 25) discussed a possible two-stage reaction mechanism for the very rapid reaction between Mo and $KMnO_4$. They suggested that the first stage of the reaction, at temperatures below 120°C, took place when Mo ions diffused along the grain boundaries of the $KMnO_4$ crystal lattice. This stage ended when the internal surfaces of the $KMnO_4$ were completely covered with a product layer. Then the second stage, a bulk reaction with $KMnO_4$ at temperatures below 850°C, took place. They suggested that the Fe/BaO_2 system reacted in a similar fashion.

Hogan and Gordon (ref 26) used thermogravimetry (TG) and differential thermal analysis (DTA) to investigate the ternary system of Mg/BaO_2/calcium resinate (see Section 1.2). In their study they also considered the binary system of Mg/BaO_2 and proposed the following stoichiometry:

$$Mg(s) + BaO_2(s) \rightarrow BaO(s) + MgO(s)$$

with an ignition temperature of 540°C and an activation energy of ignition of 155 kJ mol^{-1}. The value for the activation energy, E_a, was obtained from an Arrhenius plot using the times to ignition at various isothermal temperatures as measures of 1/k (where k is the rate coefficient).

In their study of factors affecting the ignition temperature of pyrotechnic mixtures, Barton *et al* (ref 27) investigated the Mg/BaO_2/acaroid ternary system using DTA. They showed that a binder/oxidant reaction was responsible for lowering the ignition temperature of the Mg/BaO_2 binary system from above 500°C to about 350°C on the addition of the binder.

Nakahara and Hikita (ref 28) studied both temperature and pressure data as a function of time for several pyrotechnic systems including the Mo/BaO_2 system. Combustion gas pressures and temperatures along the length of the pyrotechnic mixture, packed in a closed steel container, were measured by inserting open-pipe type manometers and thermocouples along the length of the container at regular intervals. These measurements revealed that the combustion gas pressure increased with distance travelled by the combustion front and that the combustion pressure wave preceded the temperature rise. They also quoted linear burning rates for a range of compositions (20 to 70% by mass of Mo) of from 9 to 22 mm s^{-1}.

The Se/BaO_2 system is a commonly used delay mixture in the U.S.A. (ref 2) and has been investigated by Johnson (ref 11). He distinguished three processes occurring at different temperatures, of which two were below the ignition temperature. The first process led to an increase in contact area between the Se and the BaO_2 by the migration of the Se atoms which form a surface coating on the BaO_2 at temperatures below the ignition point. It was not established whether this migration of Se atoms occurred in the solid-state or in the vapour phase. The second process is an exothermic, product-

forming reaction between Se and BaO_2 which is not self-sustaining. The third process was the self-propagating concurrent reaction described by the equations:

$$Se(s) + 3BaO_2(s) \rightarrow BaSeO_4(s) + 2BaO(s) \qquad \Delta H = -400 \text{ kJ mol}^{-1}$$

$$2Se(s) + 2BaO_2(s) \rightarrow BaSeO_4(s) + BaSe(s) \qquad \Delta H = -508 \text{ kJ mol}^{-1}$$

Johnson's findings were in agreement with the conclusions of Hill and Wallace (ref 25) for $Mo/KMnO_4$; Spice and Staveley (refs 6, 7) for $Fe/K_2Cr_2O_7$ and Fe/BaO_2; and Hill *et al* (refs 18, 19) for various compositions. All proposed at least a two-stage reaction. The first stage is the diffusion of the mobile species (whether this is the fuel or oxidant is not agreed upon) so that it surrounds the stationary species with a layer of product. This layer prevents further reaction until the temperature is sufficiently high to allow penetration of the stationary species by the mobile species. This initiates the second stage which is a bulk reaction at temperatures above the ignition temperature.

Recently, Yoshinaga *et al* (ref 29) investigated the reactions between Mo and BaO_2 using thermogravimetry, differential thermal analysis, X-ray powder diffraction and chemical analysis. They observed the thermal decomposition of BaO_2 at a temperature of ~400°C and identified small amounts of $BaCO_3$ and $Ba(OH)_2$ in the BaO_2 as a result of exposure to the air or due to grinding. The reaction between BaO_2 and Mo occurred at 385°C and was retarded by the presence of $BaCO_3$. The heat of the combustion reaction increased as the amount of Mo was increased. They quoted values for the ignition temperature ranging from 425° to 500°C and for the ignition energy of from 11 to 12 kJ mol^{-1}. They also recorded linear burning rates for some compositions of Mo/BaO_2 at different densities (Table 1.1).

TABLE 1.1 LINEAR BURNING RATES OF Mo/BaO_2 (REF 29)

DENSITY / g cm^{-3}	2.3	2.6	2.9
COMPOSITION / %	BURNING RATE / mm s^{-1}		
30	1.00	1.67	0.76
50	1.20	2.35	1.55
70	1.54	-	1.88

Beyens and Dubois (ref 10) noted the variations in the linear burning rates of Mg/BaO_2 compositions which had been made from different batches of BaO_2. Although no chemical differences between the batches could be detected, they did notice a link between different shapes of BaO_2 particles and the linear burning rates. They also identified the presence of $BaCO_3$ in the oxidant formed by exposure to the air.

1.2 THE OXIDANTS

A. Structure. The crystal structures of the two peroxides (BaO_2 and SrO_2) have been determined (refs 30, 31, 32, 33). X-ray studies have shown that the structures are analogous to the structure of CaC_2, the only difference being that the elongated shape of the O_2^{2-} ion results in a tetragonal unit cell instead of a cubic unit cell. The dimensions of the unit cells for both peroxides are listed in Table 1.2.

TABLE 1.2 DIMENSIONS OF UNIT CELL & O-O BOND LENGTH

PEROXIDE	DIMENSION / Å a	c	O - O	REFERENCE
BaO_2	5.34	6.77	1.29	30
BaO_2	3.77	6.77		33
SrO_2	5.02	6.55	1.35	30

B. Decomposition. Many studies of the decompositions of peroxides have been reported in the literature (refs 8, 9, 33, 34, 35, 36, 37, 38, 39). Decomposition is generally agreed to be endothermic and reversible, and the products include the solid oxide and gaseous oxygen. The values reported for the decomposition temperature of BaO_2 vary with the partial pressure of oxygen and with the sample mass as shown in Table 1.3.

TABLE 1.3 LITERATURE VALUES FOR DISSOCIATION OF BaO_2

TEMP / °C	CONDITIONS	REF
843	In TG $p(O_2)$=1.000 atm Mass: 1-2 g	8
840	$p(O_2)$=1 atm	40
800	$p(O_2)$=1 atm	41
790	$p(O_2)$=1 atm	42
740	$p(O_2)$=1 atm	43
738	In TG $p(O_2)$=0.21 atm Mass: 30-50 mg	9
670	In TG $p(O_2)$=0.208 atm Mass: 1-2 g	8
670	In TG in air Mass: 30-50 mg	9
600	In TG heated at 15°C Mass: < 200 mg	26

Values reported for the enthalpy of dissociation of BaO_2 are 80.0 kJ mol^{-1} (ref 8), 80.8 kJ mol^{-1} (ref 9) and 74.5 kJ mol^{-1} (ref 33).

Hogan and Gordon's investigation (ref 26) of the decomposition of BaO_2, using TG and DTA, revealed that a mass loss, equivalent to the loss of one atom of oxygen per BaO_2 unit, began at about 600°C, but this mass loss was not accompanied by any endotherm or exotherm in their DTA trace. The only thermal event which they reported was a low temperature ($\sim$100°C) loss of adsorbed water.

DTA traces of Mg/BaO_2 reported by Barton *et al* (ref 27) showed no exothermic event at temperatures around 300°C.

In Beck's (ref 44) investigation of the decomposition of BaO_2, using simultaneous TG/DTA, he reported a mass loss beginning at ~650°C which accelerated to a maximum at 800°C. His DTA trace showed an endothermic event beginning at ~800°C.

The decomposition of SrO_2 has been proposed (refs 34, 35) to be a two-step process:

$$SrO_2(s) \rightarrow SrO(s) + O(ads)$$

$$O(ads) + SrO_2(s) \rightarrow SrO(s) + O_2(g)$$

This mechanism was proposed after careful observation of the quantity of oxygen evolved during isothermal decomposition. Only at temperatures above the equilibrium temperature, does a period of re-association separate the initial rapid dissociation step from the later, slow dissociation period. A possible explanation for this behaviour was the formation of a layer of a solid solution of oxygen in SrO_2. As this layer begins to form it temporarily stops the dissociation, and dissociation in this hindering layer only becomes measurable at higher temperatures.

In later work (ref 39), Azuma *et al* did not support a two-step mechanism. They also reported that the decomposition of most peroxides accelerates under atmospheres of H_2O or CO_2, where the peroxides form hydroxides and carbonates, respectively.

The reported temperatures of decomposition of SrO_2, under different experimental conditions, are listed in Table 1.4.

TABLE 1.4 TEMPERATURES OF DECOMPOSITION OF SrO_2

TEMP / °C	EXPERIMENTAL CONDITIONS	REFERENCE
212	1 atm O_2	35
>350	TG-DTA	39
215	1 atm O_2	36
410	thermograph	38

The enthalpy of dissociation of SrO_2 has been reported as 56.5 kJ mol^{-1} (ref 37), 41.8 kJ mol^{-1} (ref 35) and 48.0 kJ mol^{-1} (ref 9).

Thus both the temperature and the energy requirements for dissociation are lower for SrO_2 than for BaO_2. This agrees with the sequence of decreasing stability of the alkali earth peroxides shown by Vannerberg (ref 45) to be Ba:Sr:Ca, with dissociation pressures at 100°C of 10^{-13} atm:0.1 atm:50 atm. The variation in the stability of these peroxides is probably due to the different ionic radii of the three alkali earth metals (Ba^{2+} 0.135 nm, Sr^{2+} 0.113 nm and Ca^{2+} 0.099 nm). These different sizes place different amounts of strain on their respective crystal lattice structures which are all of the same type (CaC_2). The lattice energies reported (ref 45) for SrO_2 and BaO_2 are 4179 and 2711 kJ mol^{-1}, respectively.

C. Impurities. There is little mention in the literature of the storage requirements of either BaO_2 or SrO_2 for use in pyrotechnic compositions. There are, however, reports of reactions of BaO_2 with humid air. Hedvall is quoted (ref 8) as proposing the existence of a solid solution of $Ba(OH)_2$ in BaO_2 arising from exposure to small amounts of water. Tzentnershver and Blumenthal (ref 36) have also reported the tendency of peroxides to form solid solutions with their respective hydroxides. This behaviour may affect the burning of pyrotechnic compositions containing peroxides. Furthermore, Beyens and Dubois (ref 10) have reported a rapid initial reaction of BaO_2 with CO_2, catalysed by water vapour. The $BaCO_3$ forms a surface layer over the BaO_2 which slows down further reaction. The proportion of $BaCO_3$ found varied from one preparation of BaO_2 to another and could reach as much as 20% by mass. As mentioned above, Yoshinaga *et al* (ref 29) reported the presence of $BaCO_3$ and $Ba(OH)_2$ in BaO_2 formed during the preparation of the Mo/BaO_2 system.

1.3 ANALYSIS OF TEMPERATURE PROFILES

As a way of determining the kinetics of pyrotechnic reactions, Hill *et al* (refs 18, 19) and Klein (ref 17) used a noble metal thermocouple to measure the temperature in a burning pyrotechnic mixture. The changes in temperature of the reaction mixture were recorded as a function of time as a pyrotechnic reaction front passed the embedded thermocouple junction. The resulting temperature-time data are referred to as a temperature profile.

The theory for temperature profile analysis (TPA) is based on the analogous layer-to-layer propagation of a flame through a gas. This mechanism, described by Mallard and Le Chatelier (ref 46), is dependent on the forward conduction of heat produced by the combustion reaction. The overall energy balance equation for the model is:

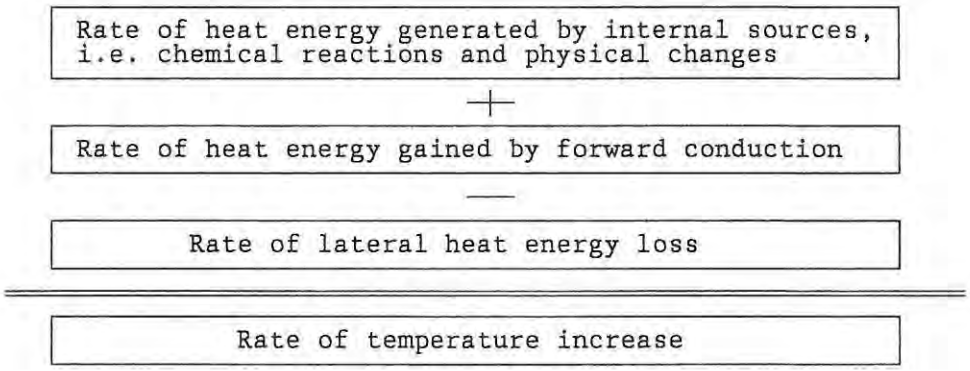

Hill and Cottrell (ref 19) developed the theory assuming that lateral loss of heat through the walls of the container could be neglected. Booth (ref 20) also contributed to this theory by assuming that the kinetics of the pyrotechnic reaction will take the form:

$$d\alpha/dt = f(Phys, \alpha, T)$$

where α is the fraction of the reducing agent oxidized at time t at a fixed point in the burning mixture, Phys is a parameter denoting the relevant physical factors which influence the function f (e.g. the

particle size, the compression etc.), and T is the temperature at the point. The velocity, v, with which the combustion wave moves through the mixture under steady-state conditions is then:

$$vdT/du = f(Phys, \alpha, T)$$

where u is a function of time and velocity. Booth used an approximate method, developed by Boys and Corner (ref 21), to solve this relationship for the velocity of the combustion wave. Boddington, Laye and co-workers (refs 23, 24, 47), at the University of Leeds, later extended the analysis (see below) and included allowance for lateral heat losses. The theory is based on the assumption that heat is not transported by the movement of matter and therefore, only applies strictly to gasless pyrotechnic mixtures.

A. The "Hill" approach. The model (Figure 1.1) used by Hill *et al* to describe the layer-to-layer combustion of pyrotechnic mixtures has a reaction zone, *O*, moving with a uniform velocity, v, along a cylindrical rod of powder of uniform composition. Ignition of the pyrotechnic mixture took place at *A*. At some time t, the reaction zone *O*, at a distance z from *A*, divides the material into a reacted zone, *R*, and an unreacted zone, *U*.

The following basic assumptions were made (ref 20).

(i) The driving influence maintaining the propagation of the reaction is the conduction of heat from *R* to *U* through *O* and radiation of heat and mass transport are neglected.

(ii) The model is one dimensional and therefore all quantities are functions only of distance, z (Figure 1.1), and time.

(iii) Lateral heat loss is ignored.

(iv) The thermal conductivity, λ, specific heat capacity, c, and density, ρ, are constant over the temperature range T_a to the maximum recorded temperature.

The Mallard and Le Chatelier model, with the above restrictions, leads (ref 18) to the equation:

$$vq\rho(d\alpha/dz) + \lambda(d^2T/dz^2) - v\rho c(dT/dz) = 0 \quad \text{——— H.1}$$

where q is the heat of reaction per gram, α is the fraction reacted of the component not in excess, v is the linear burning rate equal to dz/dt, and T is the temperature at point, z.

Integration of equation H.1 between the limits of T_a and T in segment *O* with the knowledge that $\alpha = 0$ and $d^2T/dz^2 = 0$ at $T = T_a$ gives:

$$vq\rho\alpha + \lambda(dT/dz) - v\rho c(T - T_a) = 0 \quad \text{——— H.2}$$

Fig 1.1 Model of combustion wave in a pyrotechnic mixture

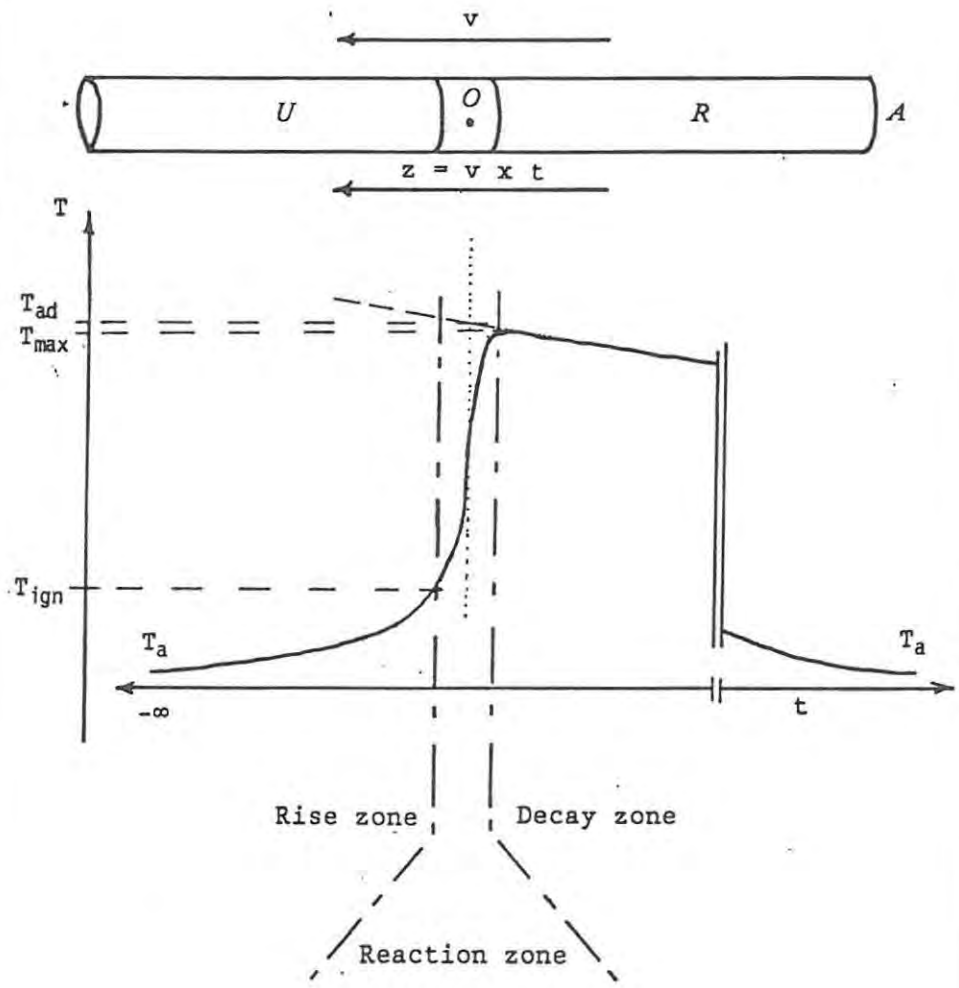

By rearranging equation H.2 and using $q = c(T_f - T_a)$, it can be shown (ref 19) that:

$$\alpha = \frac{(T - T_a) - \{\lambda / (\rho c v^2)\}\, dT/dt}{(T_f - T_a)} \qquad \text{——— H.3}$$

where T_f = final temperature i.e. the maximum temperature on the profile. Then, by using $\theta = (T - T_a)/(T_f - T_a)$

$$d\theta/dt = \{1/(T_f - T_a)\}\{dT/dt\}$$

and by substituting this result in equation H.3:

$$\alpha = \theta - (\lambda / \rho c v^2)\,(d\theta/dt) = \theta - (1/S)\,(d\theta/dt) \qquad \text{——— H.4}$$

where $S = (\rho c v^2)/\lambda$. A value for S may be obtained from extrapolation of a plot of $d\theta/dt$ vs θ to $\theta = 0$, since from equation H.4:

$$S = \lim_{\theta \longrightarrow 0} (d\theta/dt)/\theta$$

Linear burning rates. The linear burning rate can be calculated from the value of S if values of λ, ρ and c are available or can be measured, since $v_{calc} = (S \lambda / \rho c)^{1/2}$ i.e. $v_{calc} = (SD)^{1/2}$ where thermal diffusivity, $D = \lambda / \rho c$. Such calculated burning rates can be compared with independently measured burning rates.

Kinetic information. Values of α obtained from equation H.4 may be differentiated with respect to time to give values for $d\alpha/dt$. A rate equation of the form:

$$\text{rate} = d\alpha/dt = g(\alpha)\, A \exp(-E_a/RT)$$

where $g(\alpha) = (1 - \alpha)^n$ (for n^{th} order kinetics) was assumed by Hill. Hence:

$$\ln(d\alpha/dt) = \ln A - E_a/RT + n \ln(1 - \alpha) \qquad \text{——— H.5}$$

To derive the values of the kinetic parameters E_a and A, plots of $\{\ln(d\alpha/dt) - n \ln(1 - \alpha)\}$ against 1/T are constructed and n is adjusted to optimize linearity. This method is fairly insensitive (ref 19) to the value of n, but generally $0 < n < 2$.

B. The "Leeds" approach. The Leeds approach for TPA is also based on the Mallard and Le Chatelier model of propagation of a flame through a gas. Boddington *et al* (refs 23, 24), however, make provision for lateral heat loss.

The fundamental equation is:

$$(\lambda/v^2)(d^2T/dt^2) - \rho c(dT/dt) + \rho q(d\alpha/dt) - h(T - T_a) = 0 \quad \text{— L.1}$$

HEAT LOSS BY CONDUCTION	-	OVERALL HEAT PRODUCTION	+	HEAT PRODUCED BY REACTION	-	LATERAL HEAT LOSS	= 0

where h is the lateral heat transfer coefficient. Hill and others ignored the lateral heat loss term. T is the average temperature, over any particular cross-section normal to the direction of propagation, at time t.

The Leeds group then defined the temperature excess above ambient to be $U = (T - T_a)$, and division of equation L.1 by ρc gives:

$$(\lambda/v^2 \rho c)(d^2U/dt^2) - dU/dt + w/c - hU/\rho c = 0$$

where $w = d\alpha/dt$. By grouping the following terms, the thermal diffusivity, $D = \lambda/(\rho c)$, and the thermal relaxation time of the system due to lateral heat loss, $t_{th} = (\rho c)/h$, equation L.1 can be simplified to give:

$$(D/v^2)(d^2U/dt^2) - dU/dt + w/c - U/t_{th} = 0 \quad \text{——— L.2}$$

The term, $G = w/c = dq/dt$, which is the rate of temperature rise that would occur in an adiabatic system due to the local internal power is introduced so that:

$$t^*(d^2U/dt^2) - dU/dt + G - U/t_{th} = 0 \quad \text{——— L.3}$$

where t^* is the time Dv^{-2} and each of these terms has units of energy per time, i.e. power.

Zones of zero internal power. Zones may exist in the temperature profile which are free of heat sinks or sources, i.e. times during which there are no phase changes and all chemical reactions take place at negligible rates. In these inert zones, G, the local internal power due to both phase changes and chemical reactions, will equal zero. Thus, in these inert zones, equation L.2 becomes:

$$t^*(d^2U/dt^2) - dU/dt - U/t_{th} = 0 \quad \text{——— L.4}$$

If lateral heat loss is negligible in these zones, then in the resulting one-dimensional forewave, t_{th} will be very large and the last term will be small. Thus equation L.4 becomes:

$$t^*(d^2U/dt^2) - dU/dt = 0 \qquad \text{——— L.5}$$

and integration gives:

$$t^*(dU/dt) - U + \text{constant} = 0$$

Before any appreciable reaction begins, $dU/dt \rightarrow 0$ as $U \rightarrow 0$ and therefore the constant must equal zero. So:

$$t^*(dU/dt) = U$$

Integrating this equation again gives:

$$t/t^* = \ln U + \text{constant}$$

Since $U \rightarrow 0$ as $t \rightarrow -\infty$, this constant is arbitrary which agrees with the lack of a unique time zero in the profile (see Section 5.1.2 C). Thus:

$$1/t^* = d(\ln U)/dt$$

in the early part of the profile, or:

$$t^* = t_r$$

for a large t_{th}, i.e. negligible lateral heat loss, where t_r is the rise time and is equal to $\{d(\ln U)/dt\}^{-1}$.

During the cooling part of the same profile, the conduction term $t^*(d^2U/dt^2)$ is negligible and so equation L.4 becomes:

$$dU/dt + U/t_{th} = 0$$

Hence:

$$-\{d(\ln U)/dt\} = 1/t_{th}$$

in the latter portion of the profile. Thus:

$$t_{th} = t_d$$

for negligible axial conduction, where t_d is the decay time and is equal to $-\{d(\ln U)/dt\}^{-1}$.

Thus the slopes of plots of lnU against t over these remote zones will be $1/t_r$ and $1/t_d$, respectively. In practice, t_d is usually much greater than t_r and so $t^* \approx t_r$ and $t_{th} \approx t_d$.

The time, t^*, can be used as an independent estimate of the linear burning rate, since $v_{calc} = (D/t^*)^{1/2}$ (see equation L.3). By comparing this equation with the Hill approach (Section 1.3, A), it can be seen that $t^* = 1/S$. Calculated values of v (ref 23) are usually significantly lower than experimental values, especially as v_{exp} increases. Values of t^* need to be corrected for the finite size of the thermocouple junction. Plots of t_r vs d^2 (d is the thermocouple junction diameter) were found to be approximately linear and, by extrapolation to d equal to 0, gave corrected t_r values which could be used to recalculate t^* and v_{calc}. Comparisons of these corrected values with v_{exp} gave much better correlation.

The thermocouple diameter also affects the amplitude of the recorded (ref 24) temperature profile and so corrections have to be made to the excess temperature, U. Boddington *et al* (ref 24) used the relationship: $U = (1 + a)U_{exp} + b(dU_{exp}/dt)$ where U_{exp} is the experimentally determined value for the excess temperature and, a and b are functions of temperature which also depend on thermocouple diameter and, to a lesser extent, on the composition of the pyrotechnic mixture.

Thermochemical Information. Between the remote inert zones, the total amount of heat (per unit mass of reactant mixture) evolved by internal changes is given by the integral of w over some time period, t_1 to t_2. So, $\Delta\phi$, a measure of past heat evolution is given by:

$$\Delta\phi = 1/c \int_{t_1}^{t_2} w\, dt = \int_{t_1}^{t_2} G\, dt \qquad \text{——— L.6}$$

and from equation L.6:

$$\Delta\phi = 1/t_{th} \int_{t_1}^{t_2} U\, dt + U\Big|_{U(t_1)}^{U(t_2)} + t^*(dU/dt)\Big|_{U(t_1)}^{U(t_2)} \qquad \text{——— L.7}$$

The total heat evolved (ref 23) is then:

$$Q = cU_{ad} = \Delta\phi(-\infty,\infty) = 1/t_{th} \int_{-\infty}^{\infty} U\, dt + U\Big|_{-\infty}^{\infty} \qquad \text{——— L.8}$$

U_{ad} can thus be calculated by integrating the excess temperature function between arbitrary times t_1 and t_2 in the remote rise and decay zones respectively. Values calculated from $Q = cU_{ad}$ can be compared

with values determined by thermal analysis and bomb calorimetry (see Sections 4.4 and 7.2). Reference 23 reports acceptable correlation for the $W/K_2Cr_2O_7$ system.

Kinetic Information. If it is assumed that the power function, G, in equation L.4 arises only from the chemical reaction and is not complicated by contributions from phase changes, then kinetic information can be extracted from the profiles as follows. The reaction rate is assumed to be given by:

$$d\alpha/dt = g(\alpha)\ A\ \exp(-E_a/RT) \qquad \text{——— L.9}$$

where $g(\alpha) = (1 - \alpha)^n$ for n^{th} order kinetics. G can then be calculated in two ways:
(i) from the power terms derived from the profile:

$$G_{exp} = dU/dt + U/t_{th} - t^* d^2U/dt^2$$

and
(ii) by use of the plot of G against t from which the G value at t is proportional to $d\alpha/dt$, and the partial area under the curve up to time t is proportional to α. (Both proportionality constants are equal to U_{ad}). Then:

$$G_{calc} = U_{ad}\ A\ (1 - \alpha)^n\ \exp(-E_a/RT)$$

The problem then is to minimize the sum of residuals $(G_{exp} - G_{calc})^2$ and thus obtain the optimal kinetic parameters, E_a, A and n.

The low values obtained by Boddington *et al* (ref 24) for the activation energies of the reactions in different compositions of the $W/K_2Cr_2O_7$ system (8 to 15 kJ mol^{-1}) are consistent with the low values reported by Hill *et al* for similar but not identical systems (ref 23). Boddington *et al* (ref 24) propose that these low values indicate that the rate controlling step is probably a diffusion process. They also warn that activation energies in excess of 150 kJ mol^{-1} are found for reaction under the non-ignition conditions of thermal analysis and thus the mechanisms of the lower temperature processes may be significantly different to the mechanisms controlling combustion.

The above treatments both assumed that the temperature dependence of the kinetics of reaction follows the simple Arrhenius equation: $k = A \exp(-E_a/RT)$. In a study of combustion transfer in gasless pyrotechnics, Boddington *et al* (ref 48) introduced a more complex dependence of the rate coefficient of reaction:

$$k^{-1} = k_{AR}^{-1} + (BT^n)^{-1}$$

$$\text{where } k_{AR} = A_{AR} \exp(-E_{AR}/RT)$$

and B is a diffusion coefficient.

In the early stages of reaction, at low temperatures, k, and hence the reaction rate is determined by the Arrhenius term. At higher temperatures the rate is determined by the diffusion term. The kinetic parameters for the higher temperature region are those derived from the temperature profiles. At low temperatures, below an effective ignition temperature, T_{ign}, the reaction rate is negligible. T_{ign} may be estimated from thermal analysis experiments. So, at high temperature:

$$k_{TPA} = A_{TPA} \exp(-E_{TPA}/RT) \qquad \text{——— L.10}$$

and

$$k_{TPA}^{-1} = k_{AR}^{-1} + (BT^n)^{-1} \qquad \text{——— L.11}$$

hence

$$B^{-1} = T^n(k_{TPA}^{-1} - k_{AR}^{-1}) \qquad \text{——— L.12}$$

1.4 THERMAL ANALYSIS

Thermal analysis, in general, and differential scanning calorimetry (DSC) and differential thermal analysis (DTA), in particular (ref 16), may be used to contribute significantly to the understanding of mechanisms of pyrotechnic reactions (ref 49). Care has to be taken in the extrapolation of results from thermal analysis to reaction under self-propagation conditions. The development of specialized thermal analysis techniques and their application to the study of pyrotechnic reactions have been recently reviewed (refs 16, 48, 49, 50). Little previous thermal analysis work specifically on pyrotechnic mixtures containing either BaO_2 or SrO_2 has been published (see Section 1.2).

CHAPTER 2: AIMS OF PRESENT STUDY

Much of the work on the combustion of pyrotechnic systems has been empirical and systems most extensively studied have been those long in commercial use. The general aim of this investigation was to improve the understanding of the factors which affect the combustion of several chemically related pyrotechnic systems. The ultimate aim of all such research is to be able to make predictions with confidence about the burning characteristics of any given pyrotechnic system from the properties of its constituents.

The binary and ternary systems selected for investigation contained Mn and/or Mo and BaO_2 and/or SrO_2 (Figure 2.1). Reasons were sought for the different burning characteristics observed for these systems. A question (refs 6, 7, 18) of chemical interest in the reactions involving $BaO_2(s)$ and $SrO_2(s)$ as oxidants, is whether oxidation of the fuel occurs through a condensed-phase reaction (solid-solid or solid-liquid) or through a solid-gas reaction between the metal and oxygen gas produced by decomposition of the oxidant.

Fig 2.1 Scheme of work

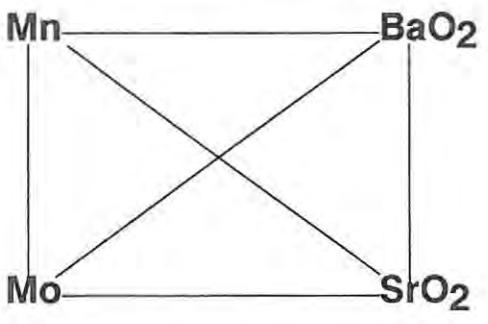

CHAPTER 3: EXPERIMENTAL

3.1 MATERIALS

The materials used throughout this thesis are listed in Table 3.1. Samples from different sources sometimes behaved differently under the same experimental conditions so details of any treatment and a brief description of the preparation of each sample, where necessary, are given. The reported and measured purities, as checked by chemical analysis (see below); the particle sizes (see below); and the bulk densities are listed (ref 52, 53).

TABLE 3.1 MATERIALS USED

SAMPLE	SOURCE	TREATMENT	PURITY / % REPORTED	PURITY / % MEASURED	PARTICLE SIZE / μm	DENSITY / g cm^{-3}
A. OXIDANTS					MEDIAN VALUES	
BaO_2	Merck	Ground & sieved	85	86.0 ± 0.1	36.6	4.96
BaO_2	BDH	Ground & sieved	85-90	78.1 ± 0.1	10.2	4.96
SrO_2	Bernardy France	Ground & sieved	85	88.0 ± 0.1	3.5	4.56
B. FUELS					MEDIAN VALUES	
Mn	Cerac		99.95		16.6	7.20
Mo	Cerac		99.9		34.4	10.20
Cr	Cerac		99.6		< 40	7.20
Nb	Cerac		99.8		< 40	8.57
W	Cerac		99.9		< 40	19.35
C. ADDITIVES						
Al_2O_3	Baird & Tatlock	Ground & sieved	GPR		< 120	3.97
BaO	BDH		Technic-		< 120	5.72
$Ba(OH)_2$	Merck	Ground, sieved & heated	98 al		< 120	2.18
$BaCO_3$	Merck	Ground & sieved	98		< 120	4.43
SrO	Unknown	Ground, sieved & heated	-		< 120	4.7
$Sr(OH)_2$	BDH	Ground, sieved & heated	97		< 120	3.62
$SrCO_3$	Coleman & Bell	Ground & sieved	GPR		< 120	3.70
MnO_2	BDH	Sieved	70 ical		< 120	5.03
MoO_3	AnalaR	Sieved	Analyt-		< 120	4.69

A. Oxidants. Two barium peroxide samples, from different sources, and a single strontium peroxide sample were used as oxidants in the pyrotechnic mixtures. The reported purities of these samples were checked by chemical analysis. A known mass of sample was dissolved in a solution of 0.3 mol l^{-1} boric acid and 1 mol l^{-1} hydrochloric acid. The boric acid prevented the loss of active oxygen by the formation of stable "perboric acid" (ref 54). 50 cm^3 aliquots of this solution were titrated against a standard (0.02 mol l^{-1}) potassium permanganate solution. The analyses confirmed the reported purities of the samples, except for the BDH sample of BaO_2. Samples of oxidant were hand ground, brushed through the appropriate sieve, and stored in a desiccator containing silica gel.

The particle-sizes of the oxidants used throughout this work are those listed in Table 3.1, unless otherwise stated. These sizes are listed as either less than a certain sieve size, or as the median values of the particle-size range determined by a Malvern Mastersizer. In this instrument (ref 55) a monochromatic and coherent light beam is passed through an agitated suspension of the particles in a suitable medium and the particle-size is determined by analysing the resulting diffraction pattern. The technique is based on the Mei-Rayleigh theory (ref 56, 57) of light scattering and is therefore subject to the restrictions that the size of the measured particles must be at least one-twentieth of the incident wavelength, and that the particles are assumed to be spherical.

B. Fuels. Five different fuels (manganese, molybdenum, chromium, niobium and tungsten) were used in the pyrotechnic mixtures, with particular attention being paid to Mn and Mo. Since all these metals were commercially available in a very pure and finely divided state, they were not subjected to any further treatment. The particle-size ranges (listed in Table 3.1) of Mn and Mo were also confirmed using the Malvern Mastersizer.

C. Additives. Some of the additives were chosen for their inert properties with respect to the expected pyrotechnic reactions, e.g. Al_2O_3; others were chosen because they were probable products of the pyrotechnic reactions (ref 6 and Chapter 8), e.g. BaO, SrO, MnO_2 and MoO_3; still others were chosen because they are common contaminants of the oxidants (refs 8, 10, 29, 53), e.g. $Ba(OH)_2$, $BaCO_3$, $Sr(OH)_2$ and $SrCO_3$. The quantity of additive is quoted as a percentage of the total mass of the pyrotechnic mixture, e.g. 5% $Ba(OH)_2$ in 20% Mn/BaO_2 gives a ratio of:

```
4.8:19.0:76.2
additive:fuel:oxidant
```

The particle-sizes of the additives quoted in Table 3.1, refer to the size of sieve through which they were passed during their preparation. The heat treatment consisted of exposing the sample to air in a convection oven at $\sim 100\,^{\circ}C$ for at least 24 hours.

D. Pyrotechnic mixtures. Four different binary pyrotechnic systems were studied in detail: the Mn/BaO_2 system, the Mo/BaO_2 system, the Mn/SrO_2 system and the Mo/SrO_2 system. The BaO_2 used was the Merck sample unless otherwise stated. The composition of these systems is always stated as a percentage by mass, of the fuel. Binary pyrotechnic mixtures using the other metal fuels listed in Table 3.1 (Cr, Nb and W) were also investigated. Ternary pyrotechnic systems, consisting of either two metal fuels and one oxidant, or a single fuel with both the oxidants, were also studied. The compositions of the ternary systems are quoted as percentages by mass of each constituent. The constituents of all the pyrotechnic mixtures were mixed by end-over-end tumbling in a mixing vessel, containing rubber balls, for at least 15 minutes, or, where specifically stated, by being brushed together three times through an appropriately-sized sieve.

Some of the materials listed in Table 3.1 were especially prepared so that the effects on combustion due to the aging of pyrotechnic oxidants could be investigated. These materials are listed in Table 3.2.

TABLE 3.2 SPECIALLY PREPARED MATERIALS

SAMPLE	SOURCE	TREATMENT	PURITY / % REPORTED	PURITY / % MEASURED	PARTICLE SIZE/ μm
BaO_2	Merck	Ground, sieved & exposed to humid atm. for 36 hrs	85	76.5 ± 0.7	< 120
BaO_2	BDH	Ground & sieved & heated at 100°C for 24 hours	85-90	77.7 ± 0.1	< 120
SrO_2	Bernardy (France)	Ground, sieved & exposed to humid atm. for 36 hrs	85	86.1 ± 0.1	< 120
SrO_2	Bernardy (France)	Ground & sieved & heated at 100°C for 24 hours	85	87.8 ± 0.1	< 120

Both thermal analysis (Chapter 4) and the burning experiments (Chapter 5) indicated different behaviour for the BaO_2 samples from the two sources (Merck and BDH). The BDH BaO_2 sample was old and had been inadequately stored and therefore was suspected of being contaminated with $Ba(OH)_2$ and $BaCO_3$ (Chapter 8). The retarding effects on combustion of pyrotechnic mixtures containing contaminated BaO_2 have been previously reported (refs 10, 29). This behaviour was investigated by artificially aging samples of Merck BaO_2 and SrO_2 by exposing them to a humid atmosphere for at least 36 hours. Furthermore, samples of BDH BaO_2 and SrO_2 were dried in a pre-heated convection oven at a temperature of ~100°C for at least 24 hours. Hereafter, the two artificially aged samples will be referred to as moist BaO_2 (Merck) and moist SrO_2 while the two dried samples will be called dried BaO_2 (BDH) and dried SrO_2. The particle sizes of these moist and dried samples were checked by sieving (120 μm) and their peroxide content was chemically analysed (see above). The results are listed in Table 3.2.

3.2 APPARATUS

Pyrotechnic reactions may be studied under the controlled conditions of thermal analysis and under the less-controlled conditions of ignition. In thermal analysis, changes of a physical property, e.g. mass, of a sample are measured as a function of temperature during a controlled heating programme (ref 58). In this way the main thermal events of a pyrotechnic mixture or its separate constituents in the presence of either an inert or reactive atmosphere may be identified and characterized. Depending on the conditions of the thermal analysis experiment (i.e. sample mass, heating rate etc.), ignition of a pyrotechnic sample may or may not occur during the heating programme.

In ignition studies (also called burning experiments) a sample of the pyrotechnic composition is pressed into a rectangular channel and an intense but local source of heat is applied to one end. If this initiates combustion, the resulting temperature changes are recorded as a function of time as the combustion front passes a fixed point in the mixture. The resulting temperature-time data is analysed to determine

the kinetic parameters of the pyrotechnic reaction. The time taken for the combustion front to travel a fixed distance is also used to calculate the burning rate of the pyrotechnic mixture.

The unreacted starting materials and the products of reaction during thermal analysis and ignition studies were characterized using X-ray powder diffraction (XRD) and infrared (IR) spectroscopy. Scanning electron microscopy (SEM) was also used to detect the changes in external appearance during ignition and controlled heating experiments.

The rate of propagation of combustion depends, among other things, on the thermal conductivity of the pyrotechnic system. A technique for measuring the thermal conductivities of powders was available (Chapter 6). The quantity of heat released during reaction was determined using bomb calorimetry.

The details of each experimental technique are given in the relevant chapters.

Note: Unless stated otherwise the errors given in this thesis are standard deviations of a minimum of three results.

CHAPTER 4: THERMAL ANALYSIS

Thermal analysis of the individual reactants and of binary and ternary pyrotechnic mixtures was conducted and results are given in this chapter. Preliminary discussion of the results is presented here but further discussion is given in Chapters 9 and 10.

4.1 EXPERIMENTAL

4.1.1 Apparatus:

Two thermal analysis techniques were available, namely differential scanning calorimetry (DSC) and thermogravimetry (TG), to examine the thermal behaviour of pyrotechnic mixtures and their separate constituents.

A Perkin-Elmer DSC-7 differential scanning calorimeter and an IBM compatible (CW Sprint) microcomputer were used (unless otherwise stated) to record and analyse DSC responses during a programmed heating routine. A Perkin-Elmer DSC-2 differential scanning calorimeter, linked either to an Apple II Plus microcomputer or a Perkin-Elmer 56 chart recorder (equipped with an event marker) to record the temperature, was also used on specified occasions. The carrier gas in both instruments was either N_2 or O_2, as specified. In the DSC-7 the carrier gas had a flow rate of 40 cm^3 min^{-1}, while in the DSC-2 it was passed through a drying tube containing silica gel at an inlet pressure of ~207 kPa. Samples were heated in both instruments in either aluminum or platinum pans, depending on the temperature range of the experiment, with lids that were not crimped. The temperature and calorimetric ranges of both instruments were calibrated using the melting of pure indium (melting point = 156.4°C and ΔH_{fusion} = 28.5 J g^{-1}) and various heating rates were used over the maximum temperature range of 50° to 725°C.

A Perkin-Elmer Delta Series TGA-7 thermogravimetric analyser and IBM compatible (CW Sprint) microcomputer were used to record mass changes during an increasing temperature programme. Samples were analysed in platinum pans without lids and the carrier gas was either N_2 or O_2 with a flow rate of 40 cm^3 min^{-1}. The TG furnace was calibrated using the Curie points of nickel (354°C) and iron (780°C). Various heating rates were used, as specified, over the maximum temperature range of 50° to 950°C.

On average the N_2 was allowed to flush the system for 10 minutes after loading the sample. A limited number of samples containing metals were examined after flushing the TG with N_2 for at least five hours. Even these traces showed some mass gains, indicating reaction with oxygen or water vapour retained in the thermobalance housing.

4.1.2 Materials:

Thermal analysis was conducted on the materials listed in Tables 3.1 and 3.2. Pyrotechnic mixtures were mixed by end-over-end tumbling as described in Section 3.1 D and those which contained BaO_2 were prepared with the Merck sample of BaO_2, unless otherwise stated.

4.2 THERMAL ANALYSIS OF THE OXIDANTS

4.2.1 Barium peroxide:

DSC in N_2. DSC traces were recorded for four different samples of BaO_2, i.e. BaO_2 (Merck), moist BaO_2 (Merck), BaO_2 (BDH) and dried BaO_2 (BDH), in N_2 with a heating rate of 10°C min^{-1} and with sample masses of less than 10 mg. The samples of BaO_2 (Merck) and its artificially aged equivalent (moist BaO_2 (Merck)) gave similar DSC responses in the temperature range 50° to 725°C (Figure 4.1). Under the same experimental conditions, the DSC traces for the other two BaO_2 samples (i.e. BaO_2 (BDH) and dried BaO_2 (BDH)) lacked the three low temperature (< 370°C) endotherms and the single endotherm observed corresponded approximately to the onset temperature of the high temperature (~600°C) endotherm of the two Merck samples (Figure 4.1). The measured enthalpy changes, ΔH, and onset temperatures are recorded in Table 4.1.

TABLE 4.1 DSC RESULTS FOR BaO_2 SAMPLES HEATED AT 10°C min^{-1} IN N_2 (FIG 4.1)

SAMPLE	ONSET TEMP / °C	ΔH/J g^{-1}
BaO_2 (MERCK)	55 ± 7 100 ± 5 360 ± 5 600 ± 6	18 ± 6 16 ± 2 5 ± 1 382 ± 35*
MOIST BaO_2 (MERCK)	52 ± 5 100 ± 1 365 ± 4 600 ± 11	- # - - -
BaO_2 (BDH)	620 ± 32	11 ± 8*
DRIED BaO_2 (BDH)	600 ± 10	18 ± 10*

*These exotherms were incomplete at the limit of the temperature range (725°C).
#No ΔH values are given for the moist sample since there was uncertainty about the amount of water in a gram of sample.

The two low temperature endotherms (< 110°C) were probably caused by the loss of loosely adsorbed water and showed great variability from sample to sample. At increased heating rates (for example 20 °C min^{-1}) these two endotherms were often not resolved. These endotherms appeared unchanged in the DSC traces of pyrotechnic mixtures containing BaO_2 (see below).

There are some conflicting reports of the thermal behaviour of BaO_2. Mention is made (refs 1, 6, 10) of melting (ref 52) at about 450°C, but Hogan and Gordon (ref 26) reported that BaO_2 (A. R.

Mallinckrodt, 88%) showed no thermal event, other than the low temperature (< 100°C) desorption of water, in the range of 25° to 900°C. Their DTA traces also did not show an endotherm corresponding to the mass loss (decomposition) on their TG traces above 600°C. Beck's (ref 44) TG/DTA traces in air show a mass loss starting at about 650°C with the accompanying DTA endotherm only at about 800°C. The DSC traces in this work did not indicate any melting. The literature values for the decomposition temperature of BaO_2 vary widely and are strongly dependent on the partial pressure of oxygen and on sample mass as shown in Table 1.3.

A reproducible endotherm with onset temperature of about 360°C, not reported in other thermal analyses of BaO_2 (refs 8, 26, 27, 44), was observed in the DSC traces for Merck BaO_2 recorded in N_2 and in O_2 (Figures 4.1 and 4.2). This endotherm was absent in the DSC traces of the BDH BaO_2. The endotherm was not accompanied by a mass change in the corresponding TG trace. The onset temperature of the endotherm did correspond closely to the onset temperature (~370°C) of a sharp endotherm in the DSC trace for $Ba(OH)_2$. The presence of $Ba(OH)_2$ in samples of BaO_2 has been reported (refs 10, 29, 45, 53) and was shown by XRD and IR studies (Chapter 8) to be present in the Merck sample. By comparison of DSC traces of pure $Ba(OH)_2$ (see Section 4.2.2) with traces for BaO_2, the endotherm at about 360°C in the two samples of Merck BaO_2 was attributed to the presence of $Ba(OH)_2$. This endotherm was assigned to a complex process in the dehydroxylation of $Ba(OH)_2$ which preceded a mass loss (without enthalpy change) at a higher temperature in the corresponding TG trace of $Ba(OH)_2$. Hedvall (ref 8) has reported the possibility of a solid solution forming between $Ba(OH)_2$ in BaO_2 arising from the exposure to small amounts of water. Vannerberg (ref 45) has described the reaction of solid peroxides with gaseous CO_2 giving solid carbonate and $O_2(g)$ (as used in submarines) and Beyens and Dubois (ref 10) have reported the formation of a surface layer of $BaCO_3$ formed during the exposure of BaO_2 to a moist atmosphere. Furthermore, the effects on the reactions of BaO_2 of these impurities have been reported (refs 10, 29).

The high temperature (≥ 600°C) endotherm in the DSC traces of all the BaO_2 samples was attributed to the decomposition of the BaO_2. The expected enthalpy change for the decomposition of BaO_2 to solid BaO and gaseous O_2, calculated from standard enthalpies of formation (ref 59), is 334 J g^{-1}. The measured value of 382 ± 35 J g^{-1} is for 85% pure BaO_2 and this converts to ~450 J g^{-1} for pure BaO_2 which is in good agreement with the value of 473 ± 12 J g^{-1} reported by Till (ref 8). Samples of BaO_2 heated to temperatures between that for the proposed thermal decomposition of $Ba(OH)_2$ and the proposed decomposition temperature of the peroxide were analysed using XRD (Chapter 8). The results showed little change in the BaO_2 content and no evidence for $Ba(OH)_2$.

DSC in O_2. Similar masses of the four samples of BaO_2 were heated at 10°C min^{-1} in the DSC in O_2. The traces for the two Merck BaO_2 samples (Figure 4.2) were similar to the traces recorded in N_2 for temperatures below ~400°C. The high temperature (≥ ~600°C) decomposition endotherm was, however, absent from the DSC traces of all four types of BaO_2 up to the instrument limit of 725°C.

Fig 4.1 DSC traces for BaO_2 samples heated in N_2 at 10°C min^{-1}

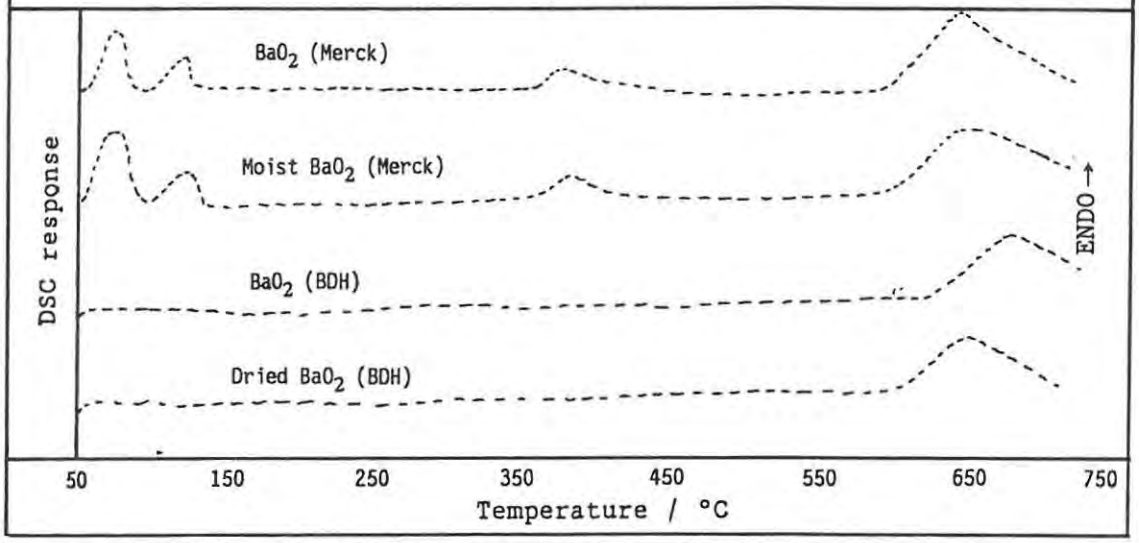

Fig 4.2 DSC traces for BaO_2 samples heated in O_2 at 10°C min^{-1}

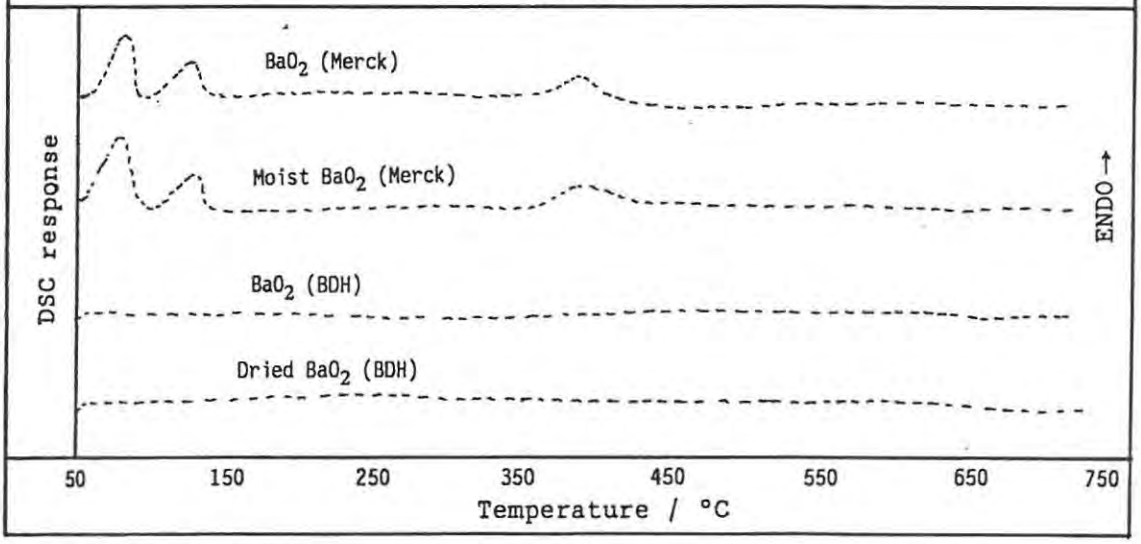

Fig 4.3 TG trace for BaO_2 (Merck) heated in N_2 at 20°C min^{-1}

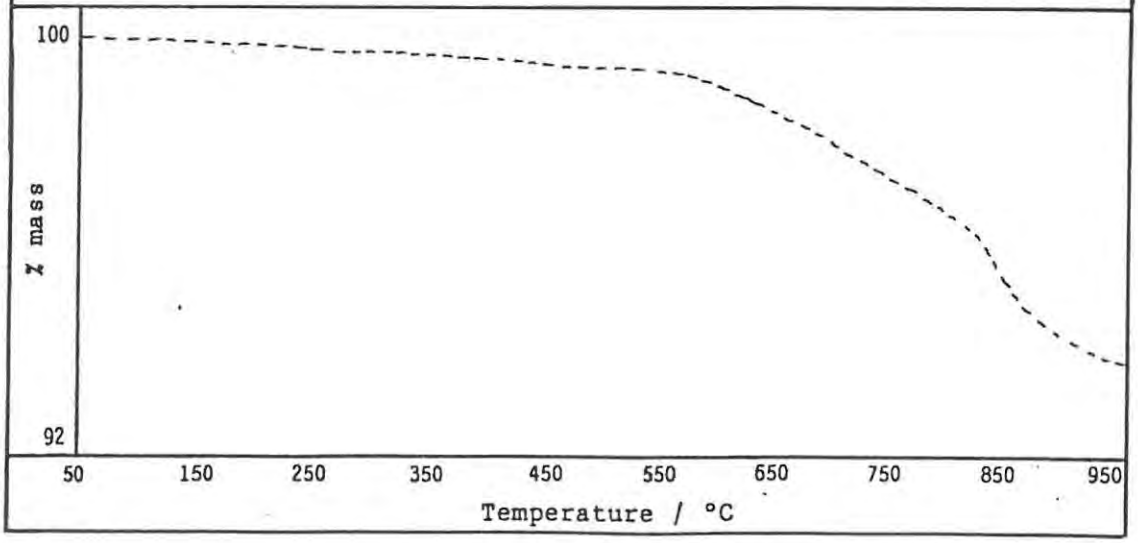

TG in N_2. The four samples of BaO_2 gave similar TG traces in N_2 with a heating rate of 20°C min^{-1} to a maximum temperature of 950°C (Figure 4.3). The TG trace for Merck BaO_2 showed a gradual mass loss of 0.71 ± 0.02% of the original mass extending from ~50° up to ~570°C corresponding to the loss of adsorbed water. Decomposition began at ~570°C where the mass loss accelerated up to a temperature of ~820°C and then accelerated further. The average mass loss between ~570° and ~820°C was 3.9 ± 0.2% and from ~820°C onwards it was 2.5 ± 0.2%. The over all mass loss was 7.7 ± 0.2% of the original sample mass. In the TG trace for moist BaO_2 (Merck) the rapid mass loss began at a slightly higher temperature (~580°C) and the mass loss, which was not complete below 950°C, was only 3.5 ± 0.1% of the original sample mass. The rapid mass loss in the TG trace of BaO_2 (BDH) started at an even higher temperature (~585°C) resulting in a loss of 7.0 ± 0.1% of the original mass with no significant signs of a second mass loss acceleration. The TG trace for the dried sample of BaO_2 (BDH) showed no low temperature mass loss while the accelerated mass loss, attributed to decomposition, started only above ~600°C, resulting in 6.9 ± 0.4% of the original mass being lost.

The expected mass loss for the decomposition of pure BaO_2 to solid BaO and gaseous O_2 is 9.5%, which converts to 8.2% for 86% pure BaO_2 (i.e. the Merck sample), 7.3% for 77% pure BaO_2 (i.e. the moist BaO_2 (Merck)) and 7.4% for 78% pure BaO_2 (i.e. the BDH BaO_2 and dried BaO_2 (BDH)).

The TG traces for moist BaO_2 (Merck) and for dried BaO_2 (BDH) had indications of onset of a further incomplete stage at high temperature (~900°C), which could be due to the decomposition of the $BaCO_3$ impurity.

TG in O_2. On changing the carrier gas to O_2, the TG trace for BaO_2 (Merck, Figure 4.4) again showed a well-defined mass loss starting at ~110°C of 0.3 ± 0.1% assigned to the loss of adsorbed water. Despite the fact that the decomposition of BaO_2 was suppressed in O_2 in the DSC, the TG traces for Merck BaO_2 showed an incomplete mass loss of 8.7 ± 0.1% starting at ~625°C. The TG trace of BaO_2 (BDH) under the same conditions showed no low temperature (~100°C) loss of water but at ~700°C an incomplete mass loss of 6.9 ± 0.2% indicated the decomposition of BaO_2.

Reversibility of the endothermic processes. After the initial heating cycle, the samples were cooled to 50°C and allowed to stand for at least 30 minutes in the DSC sample holder with the N_2 gas flowing continuously. The solid residues from the initial DSC scans on each of the four types of BaO_2 were then *rescanned* at 40°C min^{-1} from 50° to 725°C. The DSC trace for *rescanned* BaO_2 (Merck) displayed two endotherms, one with onset temperature of ~380°C and the other, which was incomplete under these conditions, had an onset temperature of ~560°C. It is possible that the presence of water in the N_2 might have been responsible for the reversibility of these two endothermic events. To check these results samples of BaO_2 (Merck) were *rescanned* in the DSC-2, whose gas line was fitted with a freshly regenerated silica gel drying tube, at a heating rate of 20°C min^{-1}. All other experimental conditions were replicated as closely as possible. The two endotherms were observed at onset temperatures of

~360° and ~550°C with enthalpy changes, measured using a planimeter, of 5 ± 1 J g^{-1} and > 144 ± 7 J g^{-1}, respectively.

The source of oxygen which was responsible for the regeneration of BaO_2 is not clear. The lack of adequate flushing of the DSC does not seem possible since besides the original 10 minutes of flushing before the experiment, the initial heating cycle (during which the N_2 flowed) lasted for 17 minutes. One possible explanation is the presence of small amounts of O_2 in the nitrogen cylinder, the reported contamination was ≤ 2 vpm. If this was the only source of oxygen it would indicate that BaO_2 is readily regenerated.

The BaO_2 (BDH) and dried BaO_2 (BDH) showed only one reversible and incomplete endotherm in each case, with onset temperatures and enthalpy changes of: ~630°C and > 360 ± 23 J g^{-1}; ~600°C and > 370 ± 29 J g^{-1}, respectively.

As expected (ref 9), the decomposition of BaO_2 was also reversible when the solid residues from the initial DSC scans of each of the four types of BaO_2 were exposed to air for 15 minutes.

4.2.2 Other barium containing compounds:

Barium carbonate. $BaCO_3$ showed no DSC response in N_2 at various heating rates in the temperature range 50° to 725°C. The TG trace recorded in N_2 at a heating rate of 20°C min^{-1} showed an incomplete mass loss of 2.3 ± 0.3% on heating to 950°C. $BaCO_3$ is reported (ref 53) as being the most stable of the group IIA carbonates, decomposing only above 1300°C and the expected mass loss on complete decomposition to BaO(s) is 22.3%.

Barium hydroxide. Pure anhydrous $Ba(OH)_2$ was heated at 10°C min^{-1} from 50° to 725°C in the DSC in N_2 (Figure 4.5). Under these conditions four endotherms were observed. Their onset temperatures and the enthalpy changes associated with them are listed in Table 4.2.

TABLE 4.2 DSC RESULTS FOR $Ba(OH)_2$ HEATED AT 10°C min^{-1} IN N_2 (FIG 4.5)

ONSET TEMPERATURE / °C	ΔH/J g^{-1}
90 ± 1	66 ± 22
250 ± 1	7 ± 1
370 ± 1	62 ± 3
500 ± 10	6 ± 1*

*This endotherm was incomplete at the limit of the temperature range (725°C).

Fig 4.4 TG trace for BaO_2 (Merck) heated in O_2 at 20°C min^{-1}

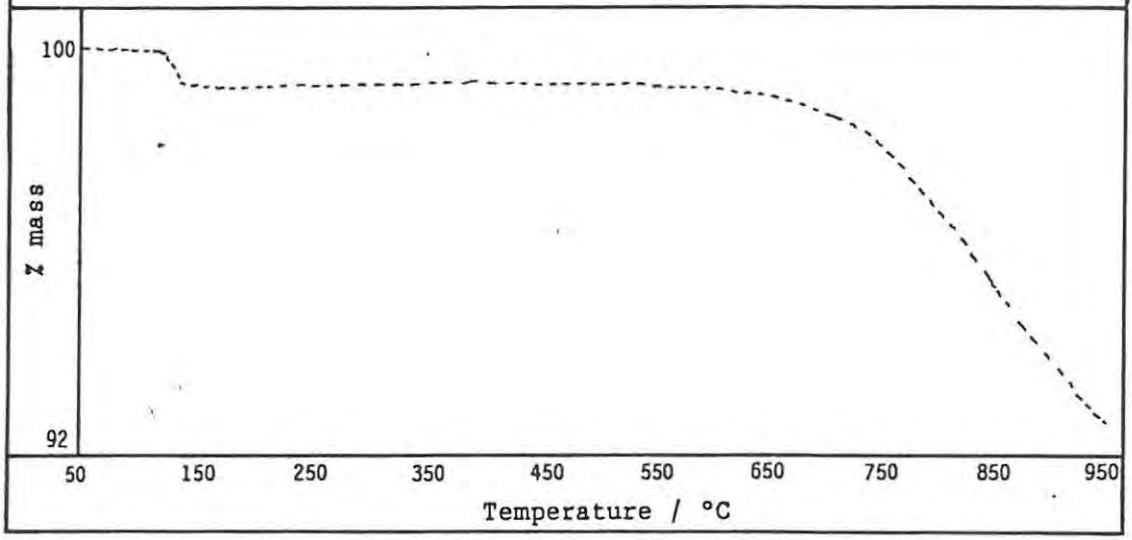

Fig 4.5 DSC trace for $Ba(OH)_2$ heated in N_2 at 10°C min^{-1}

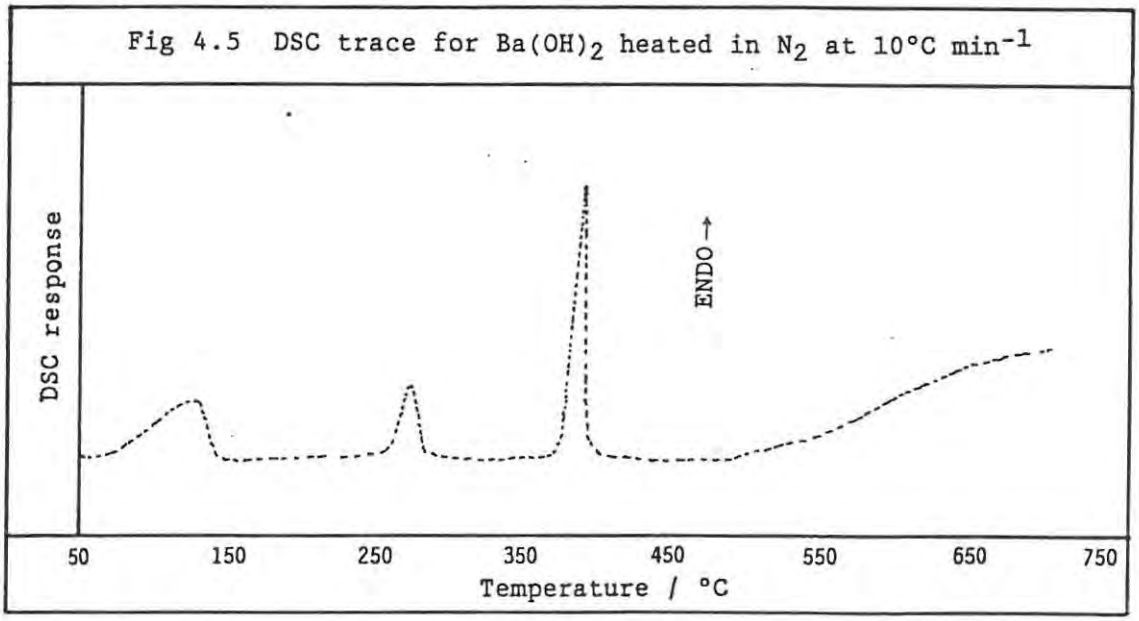

The low temperature (~90°C) endotherm was probably due to the loss of adsorbed water. This is supported by the TG trace for $Ba(OH)_2$ recorded in N_2 at a heating rate of 20°C min^{-1}, which showed a gradual mass loss of 1.6 ± 0.1% of the original mass starting at ~50°C. The next two endotherms at ~250° and 370°C were not accompanied by mass changes and thus probably correspond to structural rearrangements preceding thermal decomposition. Konings *et al* (ref 60) reported a crystalline phase change in $Ba(OH)_2$ at temperatures above 250°C with no equivalent event for $Sr(OH)_2$. The endotherm with onset at ~500°C corresponded approximately to a mass loss of 3.5 ± 0.3% in the TG trace of $Ba(OH)_2$ starting at ~550°C and ending at ~640°C. At higher temperatures there was virtually no mass loss until at ~885°C there was a small and incomplete mass loss of 0.7 ± 0.1%. It is suggested that the decomposition of $Ba(OH)_2$ begins at temperatures above 500°C but is only complete at temperatures beyond the range of the TG furnace. The total mass loss was about 6% of the original sample mass while the expected mass loss for the loss of a water molecule is 11%.

Reheating of the other barium compounds. $BaCO_3$ and $Ba(OH)_2$ were tested for reversible thermal events in the DSC-2 with dry N_2 under the same conditions as for BaO_2 (Section 4.2.1). $BaCO_3$ showed no thermal response on reheating, but the DSC traces for $Ba(OH)_2$ samples showed one endotherm with onset temperature of ~390°C.

4.2.3 Strontium peroxide:

DSC in N_2. The original sample of SrO_2 was treated in two different ways (see Section 3.1) giving a total of three different samples of SrO_2 which were examined: i.e. dried SrO_2, moist SrO_2 and untreated SrO_2. Heated in N_2 at 10°C min^{-1} from 50° to 725°C, the DSC trace for SrO_2 (untreated) showed three endotherms (Figure 4.6). The low temperature endotherm with onset at ~80°C was probably due to the loss of adsorbed water since the corresponding endotherm (onset ~55°C) in the DSC trace for the moist sample of SrO_2 (Figure 4.6) was much larger. In the DSC trace for the dried sample of SrO_2 (Figure 4.6) the low temperature endotherm was absent. The enthalpy changes and onset temperatures for these endotherms are given in Table 4.3.

There are conflicting reports regarding the mechanism for the decomposition of SrO_2. By observing the partial pressure of oxygen above SrO_2 undergoing decomposition, Blumenthal (refs 35, 37) suggested a two-stage mechanism involving an adsorbed oxygen atom (see Section 1.2). More recent studies by Azuma *et al* (ref 39) have favoured a concerted decomposition mechanism. The temperatures of decomposition reported by various workers (refs 35, 36, 38, 39, 52) vary between 212° and 488°C depending on the experimental conditions and specifically on the partial pressure of oxygen.

The next two endotherms in the DSC trace for SrO_2 (Figure 4.6), with onset temperatures of ~390°C and ~535°C would correspond to the decomposition stages. Similar twin endotherms were observed in the DSC traces for dried SrO_2 and moist SrO_2, their onset temperatures and measured enthalpy changes are compared with those for SrO_2 in Table 4.3.

TABLE 4.3 DSC RESULTS FOR SrO_2 HEATED AT 10°C min^{-1} IN N_2 (FIG 4.6)

SAMPLE	ONSET TEMP/ °C	ΔH/J g^{-1}
SrO_2	80 ± 6 390 ± 10 535 ± 8	18 ± 2 185 ± 20 182 ± 29
DRIED SrO_2	390 ± 2 525 ± 28	193 ± 56 133 ± 33
MOIST SrO_2	52 ± 1 410 ± 11 525 ± 3	- # - -

#No ΔH values given for the moist sample since there was uncertainty about the amount of water in a gram of sample.

The expected enthalpy change for the decomposition of SrO_2 to solid SrO and gaseous O_2 is 427 J g^{-1} (ref 59). The total ΔH value for the two endotherms of SrO_2 was 367 J g^{-1} and the value recorded by Fahim and Ford (ref 9) is 402 J g^{-1}.

The intermediate compound was not positively identified, but XRD analysis (Chapter 8) showed that samples heated to ~520°C and cooled for 30 minutes in N_2 contained little peroxide and consisted mainly of SrO.

DSC in O_2. On changing the carrier gas to O_2, but maintaining the other conditions, little change was observed in the general appearance of the DSC traces for the three samples of SrO_2. The details are listed in Table 4.4. In O_2 the onset temperatures of both stages of the thermal decomposition of SrO_2 were increased but were still within the limits of the DSC.

TABLE 4.4 DSC RESULTS FOR SrO_2 HEATED AT 10°C min^{-1} IN O_2

SAMPLE	ONSET TEMP/ °C	ΔH/J g^{-1}
SrO_2	80 ± 5 395 ± 3 550 ± 12	18 ± 2 98 ± 30 128 ± 10
DRIED SrO_2	400 ± 10 505 ± 7	70 ± 18 136 ± 24
MOIST SrO_2	80 ± 2 410 ± 8 555 ± 13	- # - -

#No ΔH values are given for the moist sample since there was uncertainty about the amount of water in a gram of sample.

TG in N_2. The TG trace for SrO_2 (Figure 4.7) heated at 20°C min^{-1} in N_2, confirmed the low temperature loss of adsorbed water with a mass loss of 0.5 ± 0.1% starting at ~100°C, while the TG trace for the moist sample of SrO_2 (under the same conditions) showed a much larger mass loss (34.3 ± 0.2%). The TG trace for the dried sample of SrO_2 showed no mass loss at this temperature.

Fig 4.6 DSC traces for SrO_2 samples heated in N_2 at 10°C min^{-1}

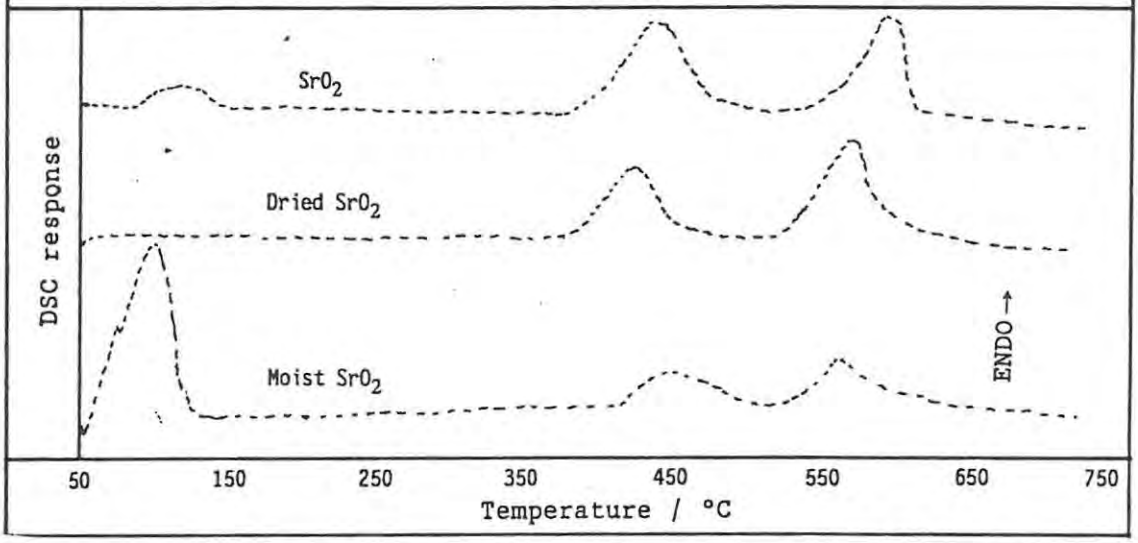

Fig 4.7 TG trace for SrO_2 heated in N_2 at 20°C min^{-1} and its 1st derivative

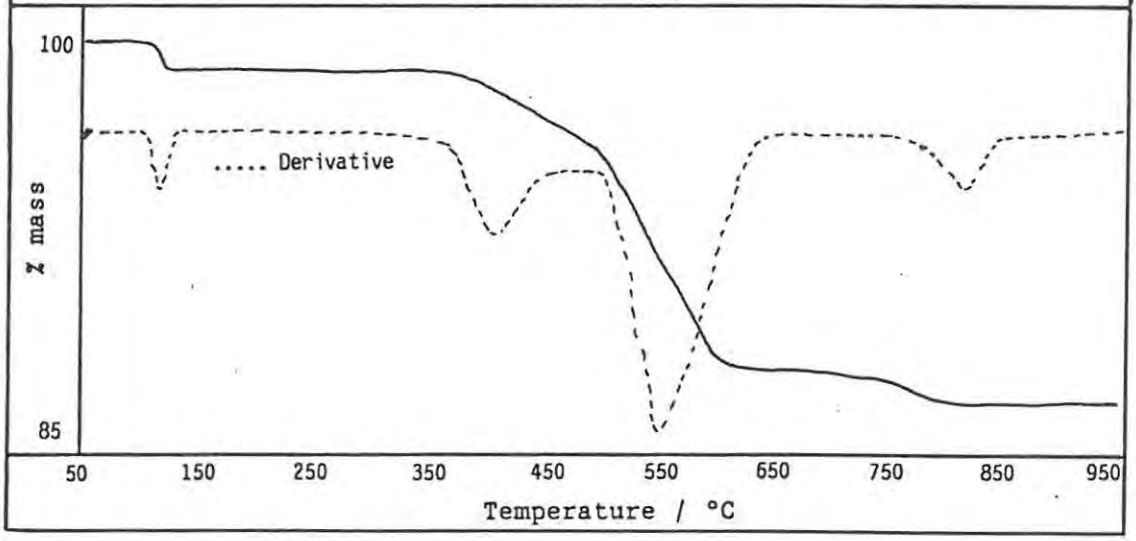

The next mass loss of 13.9 ± 0.1% of the original mass, in the TG trace for SrO_2 (Figure 4.7) began at ~385°C with a sharp acceleration at ~500°C. The curve representing the first derivative of the TG trace supports the two-step decomposition suggested by the DSC traces. The dried and moist samples of SrO_2 showed similar acceleration steps in their TG traces but at slightly different temperatures. Dried SrO_2 had an onset temperature of ~380°C with accelerated mass loss at ~530°C giving a total mass loss of 12.8 ± 0.2% of the original mass, while the decomposition of the moist SrO_2 sample had an onset temperature of ~395°C with acceleration at ~540°C giving a combined mass loss of 12.3 ± 0.2% of the sample mass after the initial loss of water. The calculated mass loss for the decomposition of pure SrO_2 to SrO(s) and $\frac{1}{2}O_2$(g) is 13.4% which decreases to 11.8% for 88% pure SrO_2.

The TG traces for all three SrO_2 samples show a further mass loss at high temperature probably caused by the decomposition of $SrCO_3$. The percentage mass loss and the onset temperatures are recorded in Table 4.5. This event was not recorded in the DSC traces as it occurs beyond the maximum temperature of the DSC.

TABLE 4.5 HIGH TEMPERATURE MASS LOSSES OF SrO_2 SAMPLES, HEATED AT 10°C min^{-1} IN N_2

SAMPLE	MASS LOSS / %	ONSET TEMP. / °C
SrO_2	1.6 ± 0.1	835 ± 8
DRIED SrO_2	2.0 ± 0.2	755 ± 2
MOIST SrO_2	5.2 ± 0.1	740 ± 2

TG in O_2. Changing the carrier gas to oxygen, but maintaining the other experimental conditions, did not alter the general appearance of the TG traces for the three samples of SrO_2. However, the temperatures at which the various thermal events began were slightly increased and the resulting mass losses were slightly decreased, the details of these changes are given in Table 4.6.

TABLE 4.6 TG RESULTS FOR SrO_2 SAMPLES HEATED AT 20°C min^{-1} IN O_2

SAMPLE	MASS LOSS / %	ONSET TEMP. / °C
SrO_2	0.7 ± 0.1	100 ± 1
	12.8 ± 0.2	410 ± 6
		530 ± 2
	1.5 ± 0.1	760 ± 5
DRIED SrO_2	15.1 ± 0.1	410 ± 6
		540 ± 4
	2.4 ± 0.2	750 ± 12
MOIST SrO_2	34.1 ± 0.1	52 ± 2
	6.9 ± 0.1	410 ± 4
		480 ± 15
	4.5 ± 0.1	810 ± 5

Reversibility of the endothermic processes. After the initial heating cycle, the samples were cooled to 50°C and allowed to stand for at least 30 minutes in the DSC sample holder with the N_2 gas flowing continuously. The solid residues from the initial DSC scans on each of the three types of SrO_2 were then *rescanned* at 40°C min^{-1} from 50° to 725°C. The *rescanned* DSC traces for all three samples of SrO_2 displayed no thermal activity under the experimental conditions with either N_2 or O_2 as the carrier gas. In the time scale (30 min) allowed, little or no regeneration took place. However, if the SrO_2 residues were exposed to the air for about 12 hours then some regeneration of peroxide took place which was demonstrated by the presence of an endotherm at ~400°C in a repeat scan. SrO_2 is far less susceptible to regeneration than BaO_2, under the conditions of thermal analysis.

Summary of thermal analysis of BaO_2 and SrO_2. Figure 4.8 compares the TG and DSC traces for BaO_2 (Merck) and SrO_2 heated at 10°C min^{-1} in N_2. Both oxidants showed low temperature (< 110°C) endotherms, sometimes two for BaO_2 but only one for SrO_2, attributed to the loss of adsorbed water. The corresponding loss of mass by both BaO_2 and SrO_2 supported these assignments. The endotherm at about 360°C in the DSC trace for BaO_2, which was not accompanied by a mass loss, was assigned to the thermal rearrangement of the $Ba(OH)_2$ impurity preceding its decomposition. No corresponding DSC response was observed in the trace for SrO_2. The two endotherms assigned to the decomposition of SrO_2 had onset temperatures of ~390° and ~535°C and the corresponding mass losses started at about ~385° and ~500°C. The single decomposition endotherm for BaO_2 started at ~600°C with its corresponding mass loss starting at ~570°C.

The DSC traces for SrO_2 and BaO_2 (Merck) heated 10°C min^{-1} in O_2 showed increases (i.e. 25° and 30°C) in onset temperature of the two endotherms assigned to the decomposition of SrO_2 and the absence of the decomposition endotherm in the trace for BaO_2. Increases of onset temperatures for the mass losses assigned to decomposition of BaO_2 (Merck) and SrO_2 were also observed in the TG traces recorded in O_2 (55°C for BaO_2; 25° and 30°C for SrO_2).

Further discussion of these results is given in Chapter 9.

Fig 4.8 TG & DSC traces for BaO_2 (Merck) & SrO_2 heated in N_2 at 10°C min^{-1}

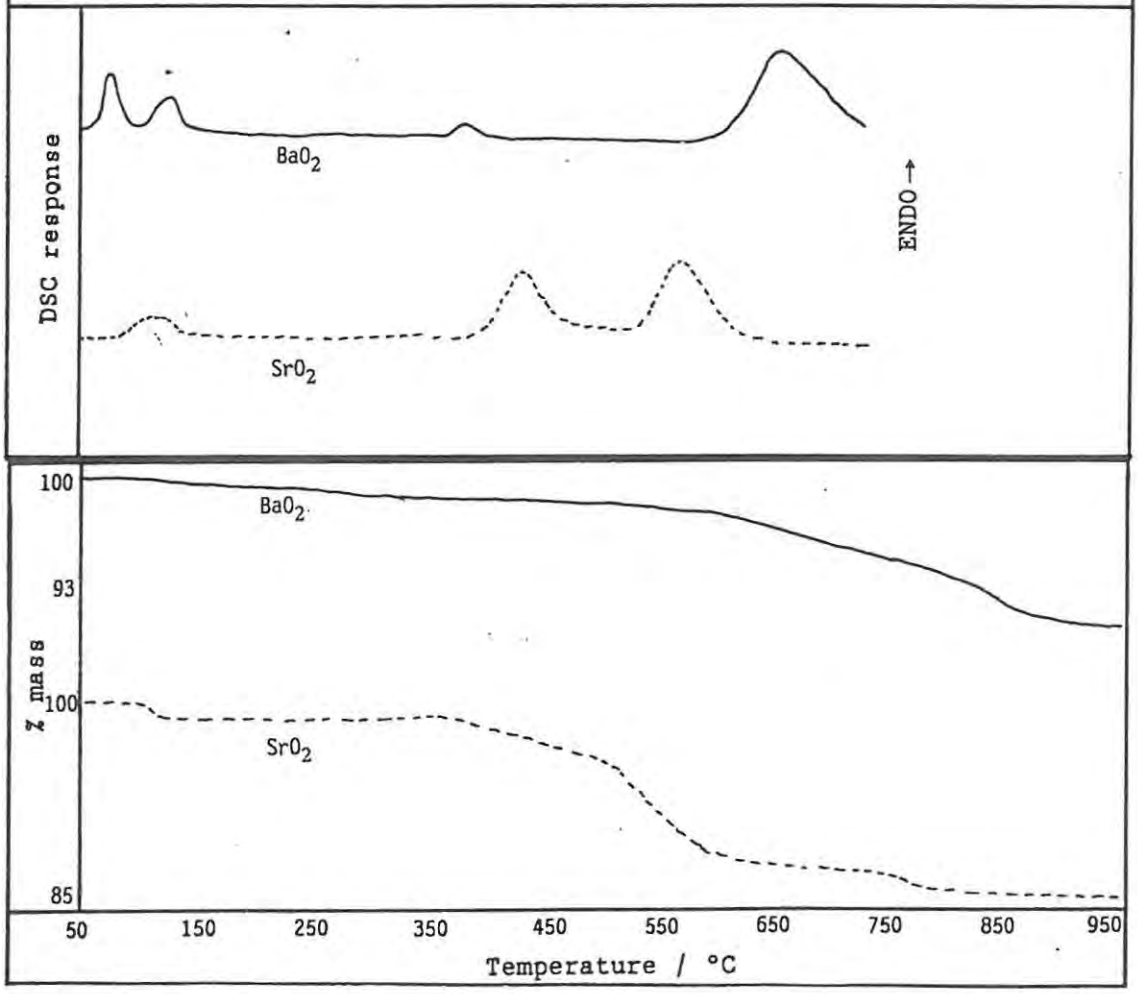

4.3 THERMAL ANALYSIS OF THE FUELS:

DSC and TG in N_2. DSC traces of Mn powder heated in N_2 at 20°C min^{-1} showed a reproducible endotherm at ~675°C with an enthalpy change of 14 ± 1 J g^{-1}. This endotherm was assigned to the α/β allotropic phase change which is reported (ref 53) to occur at 700 ± 3°C (ΔH = 41 J g^{-1}). Conformation for this assignment comes from the corresponding TG trace which showed no accompanying mass change and from the fact that this DSC endotherm was reversible even without exposing the sample to the air. Other small (< 3 J g^{-1}) and variable exotherms at ~330° and ~450°C were attributed to the oxidation of the Mn powder by small amounts of oxygen and/or water vapour in the instrument.

TG traces for Mn powder, heated at 20°C min^{-1}, were recorded after 10 minutes flushing with N_2 and also after at least 5 hours of flushing with N_2. Both TG traces showed small mass losses (~0.1%) starting at ~350°C followed closely by mass gains of variable magnitude above 390°C. In the traces recorded after flushing for only 10 minutes, the mass gains ranged between 11 and 34% of the original sample mass. The complete conversion of Mn into MnO(s) would produce a mass gain of 30%. The traces recorded after extensive flushing (≥ 5 hours), showed smaller but still significant mass gains of about 8% of the original sample mass.

Mo powder showed no DSC response when heated in N_2 at 20°C min^{-1} in the temperature range of the DSC.

The TG trace for Mo powder, recorded after the apparatus was flushed for 10 minutes, showed an incomplete mass increase of 3.5 ± 0.3% with onset at ~500°C due to partial oxidation by small amounts of oxygen and/or water vapour in the TG. After extended flushing (≥ 5 hours), the TG trace for a similar sample showed a small mass gain of 0.23 ± 0.01% above ~550°C. This relatively small mass gain suggests that Mo powder is less sensitive to oxidation by impurities in the TG than Mn powder.

DSC and TG in O_2. On changing the carrier gas to O_2, the DSC trace for Mn powder (Figure 4.9) showed that the exothermic oxidation started above 560°C but was incomplete in the temperature range of the DSC. The mass gain that begins above 360°C in the TG (Figure 4.10) was irreproducible, varying from low values (incomplete oxidation) to 30% (corresponding approximately to formation of MnO(s)). The measured enthalpy for this incomplete exotherm was -0.2 kJ g^{-1} compared to the expected (ref 59) value of -7 kJ g^{-1}.

The oxidation of Mo powder (Figure 4.9) started at ~600°C in the DSC and had a enthalpy change of -4 ± 1 kJ g^{-1}. The expected (ref 59) enthalpy change for formation of MoO_3 is -7.9 kJ g^{-1}. The mass gain (Figure 4.10), above 440°C, was about 44% of the original mass which is close to the mass gain

Fig 4.9 DSC traces for Mn & Mo heated in O_2 at 20°C min^{-1}

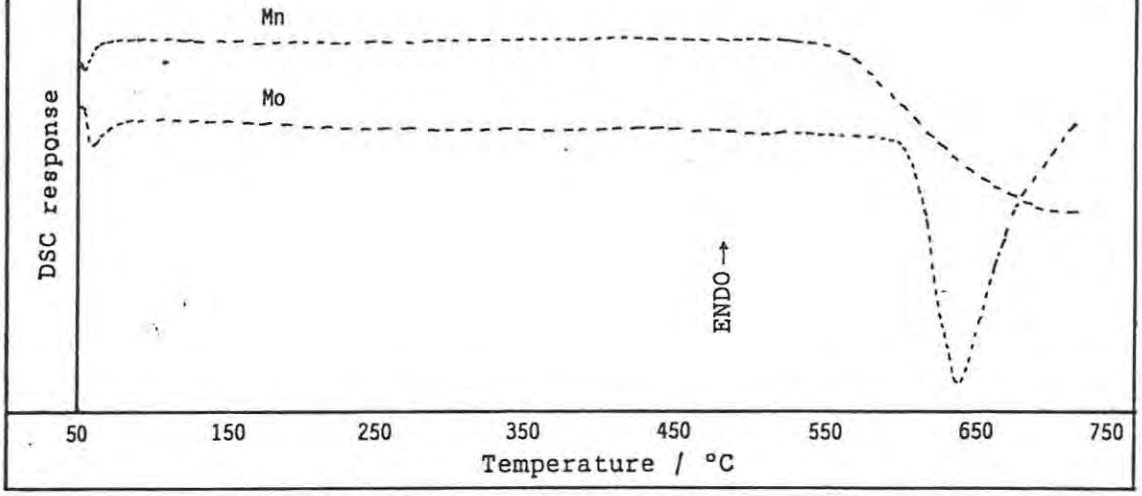

Fig 4.10 TG traces for Mn & Mo heated in O_2 at 20°C min^{-1}

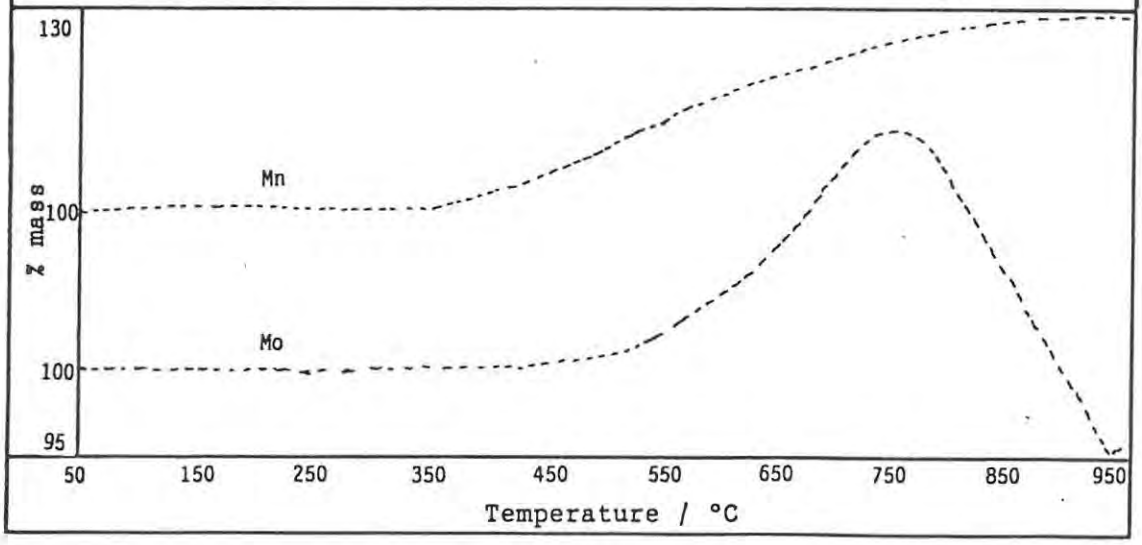

expected for the formation of MoO_3. The mass loss at ~750°C was probably caused by the sublimation of the newly formed MoO_3(s). The reported (ref 52) sublimation temperature is 1155°C at 760 mmHg.

4.4 THERMAL ANALYSIS OF THE BINARY PYROTECHNIC SYSTEMS

4.4.1 The Mn/BaO_2 system:

Compositions containing from 15 to 65% Mn sustained combustion (Section 5.4.1).

DSC in N_2. DSC traces for 40% compositions of Mn/BaO_2 (Merck) heated in N_2 at 20°C min^{-1} in the DSC were recorded using relatively large sample masses ~20 mg (Figure 4.11 a). Four thermal events were observed in these traces: two low temperature (< 200°C) endotherms due to the loss of adsorbed water from BaO_2 (see above), followed by two exotherms with onset at ~365°C and ~605°C, respectively.

The two exotherms in this DSC trace had onset temperatures which corresponded closely to the onset temperatures of endotherms in the DSC trace for BaO_2 heated alone in N_2 (Figure 4.1). The lower temperature exotherm (~365°C) corresponds closely to the endotherm assigned to the thermal rearrangement of $Ba(OH)_2$ (~360°C), while the other exotherm (~605°C) occurs at similar temperatures to the decomposition temperature of BaO_2. The onset temperatures and associated enthalpy changes are listed in Table 4.7.

TABLE 4.7 DSC RESULTS FOR 40% Mn/BaO_2 HEATED AT 20°C min^{-1} IN N_2 (FIG 4.11a)

ONSET TEMP. / °C	ΔH/J g^{-1}
120 ± 7	6 ± 1
175 ± 2	5 ± 1
365 ± 4	-76 ± 12
605 ± 15	-142 ± 40*

*This exotherm was incomplete at the limit of the temperature range (725°C).

Samples of 40% Mn/BaO_2 (BDH) were also heated under the same conditions in the DSC. There was no low temperature (< 110°C) DSC response, but the two exotherms were observed. The enthalpies and onset temperatures are listed in Table 4.8.

TABLE 4.8 DSC RESULTS FOR 40% Mn/BaO_2 (BDH) HEATED AT 40°C min^{-1} IN N_2

ONSET TEMP. / °C	ΔH/J g^{-1}
320 ± 10	-61 ± 8
650 ± 10	-367 ± 89*

*These exotherms were incomplete at the limit of the temperature range (727°C).

The composition (20, 30 and 50% Mn) of the Mn/BaO_2 system had a noticeable effect on the DSC traces with all other experimental conditions being kept as constant as possible. DSC traces measured in N_2 with a heating rate of 20°C min^{-1} and with a sample mass of about 25 mg (Figure 4.12) indicate that the onset temperature of the large exotherm assigned to the oxidation of Mn, decreased from ~620°C for the 20% composition to ~550°C for the 50% composition.

DSC in O_2. On changing the carrier gas to O_2, the DSC trace of 40% Mn/BaO_2 (Figure 4.11 b and Table 4.9) showed the two low temperature endotherms due to the loss of adsorbed water from BaO_2 and the two exotherms which had lower onset temperatures than in N_2 (Table 4.7). The low temperature exotherm (~350°C) had an onset temperature well below the temperature at which the Mn was oxidized by the O_2 (~560°C, Figure 4.9) and its enthalpy change was similar to that of the corresponding exotherm (~365°C, Figure 4.11 a) measured when the sample was heated in N_2. Thus it appears that similar reactions take place between Mn and BaO_2 under both inert and oxidizing conditions, except that under O_2 the reactions occur at lower temperatures.

The high temperature exotherm (onset ~500°C) occurred at temperatures below the onset temperature (~560°C) of the oxidation of Mn powder by the O_2 carrier gas. The exotherm was incomplete in the temperature range of the DSC and the enthalpy change was smaller than that measured in N_2. If this exotherm was due to the complete oxidation of the Mn by the oxygen gas then, based on the ΔH value for Mn heated alone in O_2, the ΔH value would be expected to be ~-80 J g^{-1} of pyrotechnic mixture which is larger than the mean recorded value of ~-54 J g^{-1}. This exotherm could thus be due to further oxidation of the products formed at ~350°C.

TABLE 4.9 DSC RESULTS FOR 40% Mn/BaO_2 HEATED AT 40°C min^{-1} IN O_2 (FIG 11b)

ONSET TEMP. / °C	ΔH / J g^{-1}
54 ± 2	18 ± 2
105 ± 5	22 ± 7
350 ± 3	-70 ± 16
500 ± 4	-54 ± 14*

*This exotherm was incomplete at the limit of the temperature range (725°C).

TG in N_2. After flushing the TG apparatus with N_2 for approximately 10 minutes, the trace for 40% Mn/BaO_2 (Figure 4.13 a), heated at 20°C min^{-1}, showed a low temperature mass loss (0.4 ± 0.1% of the original mass), indicating the loss of adsorbed water from the BaO_2, which was complete by ~110°C. The sample mass then increased by 5.5 ± 0.8% starting at ~340°C with acceleration at ~630°C. The initial mass gain (~340°C) was probably due to the oxidation of the Mn by the oxygen/water vapour remaining in the TG, reported for Mn alone to start above 360°C (Figure 4.10). The gradient change at about 630°C might have been caused by the decomposition of unreacted BaO_2

Fig 4.11 DSC trace for 40% Mn/BaO_2 heated at 20°C min^{-1}

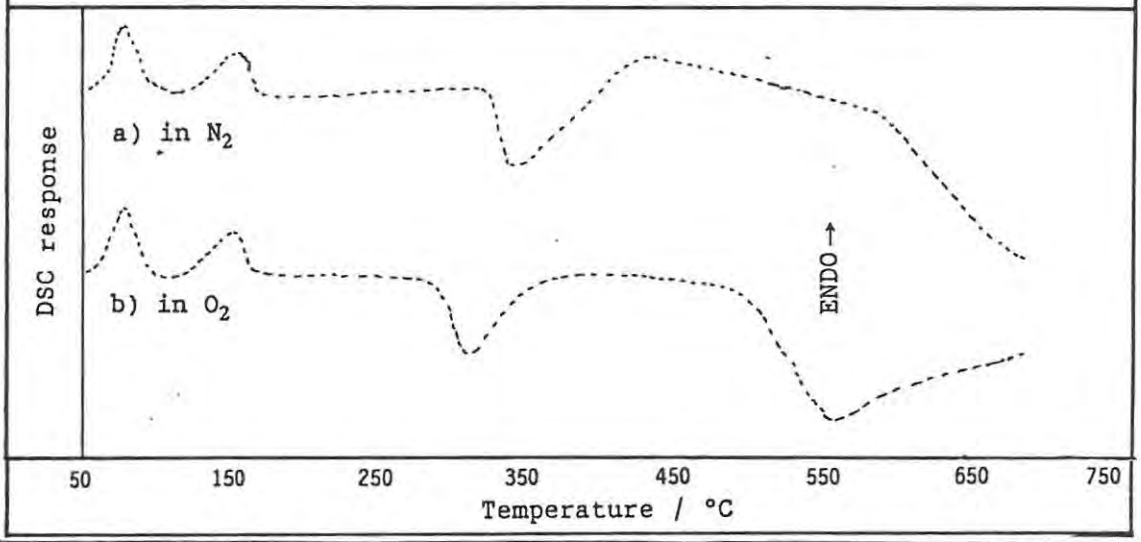

Fig 4.12 DSC traces for different compositions of the Mn/BaO_2 system heated in N_2 at 20°C min^{-1}

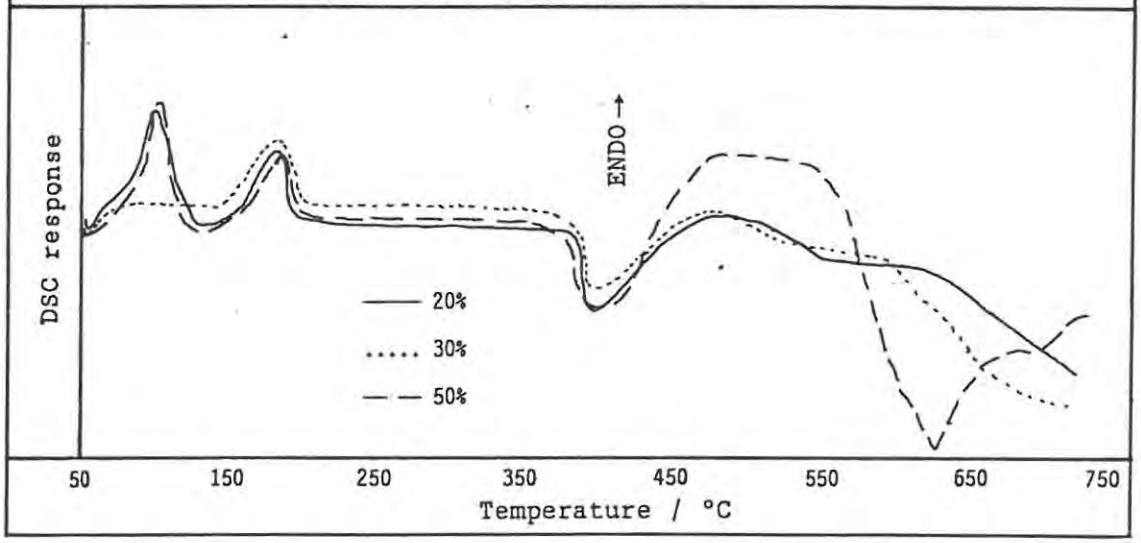

Fig 4.13 TG trace for 40% Mn/BaO_2 heated at 20°C min^{-1}

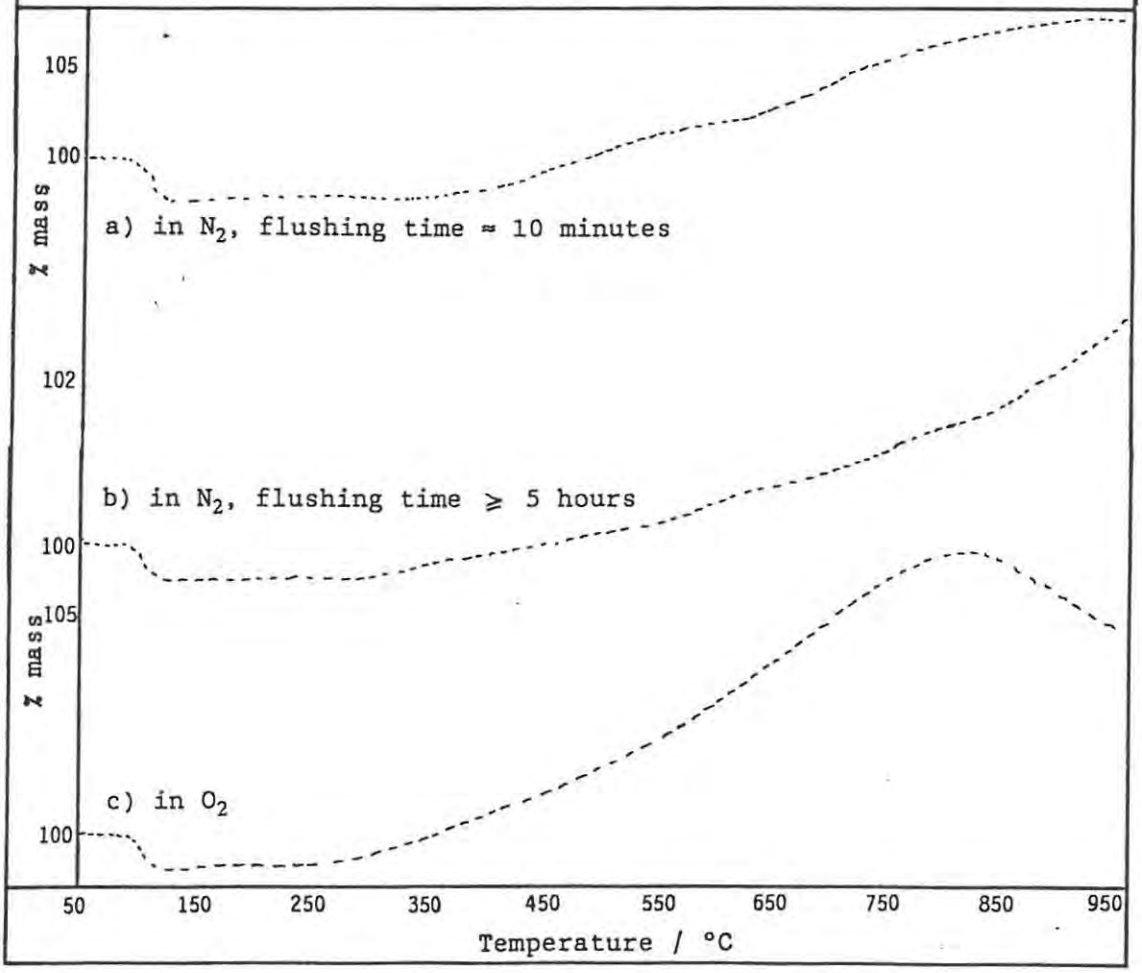

which was reported to occur at ~570°C (Figure 4.3). The temperatures of the initial mass gain and the later acceleration also correspond closely to the onset temperatures of the two exotherms observed using the DSC (Table 4.7).

The TG trace for 40% Mn/BaO_2 heated under the same conditions but after flushing the TG apparatus for at least 5 hours is shown in Figure 4.13 b. The only difference between these traces is the percentage mass gained, i.e. ~6% mass gain after flushing for 10 minutes and ~2% after flushing for more than 5 hours. Despite the extensive time spent flushing with N_2, sufficient oxidizing impurities remained in the system to cause the mass gain above ~300°C. The accelerated mass gain above ~650°C (Figure 13 b) might be due to the increased rate of oxidation of Mn by the gaseous oxygen released during the decomposition of the BaO_2 (~600°C, Figure 4.3).

The TG trace of 40% Mn/BaO_2 (BDH), heated at 20°C min^{-1} in N_2, showed only a high temperature (~390°C) mass gain of 7.5 ± 1.6% with acceleration at ~610°C.

TG in O_2. The TG trace of 40% Mn/BaO_2 in O_2 (Figure 4.13 c) with a heating rate of 20°C min^{-1} showed the low temperature mass loss due to desorption of water from BaO_2 (equal to 0.41 ± 0.01% of the original sample mass) followed by a slow but continually accelerating mass gain of 6.8 ± 0.1% starting at ~290°C and ending at ~830°C, due to the oxidation of the Mn. Mn heated alone in O_2 (Figure 4.9) showed a mass gain above ~360°C which slowed at the upper limit of the TG furnace (950°C). The TG trace for the 40% Mn/BaO_2 (BDH) mixture was similar, except that it showed no low temperature (< 110°C) mass loss.

4.4.2 The Mo/BaO_2 system:

Compositions containing from 20 to 70% Mo sustained combustion (Section 5.4.1).

DSC in N_2. The DSC trace for 40% Mo/BaO_2 (Figure 4.14) recorded in N_2 with a heating rate of 20°C min^{-1} and sample masses of ~20 mg, showed the two low temperature (< 110°C) endotherms due to the loss of adsorbed water from the BaO_2. There was also a small endotherm, with an onset temperature of ~350°C, which corresponds approximately to the onset temperature (~360°C) of the endotherm in the DSC trace of BaO_2 (Figure 4.1) that was assigned to a structural rearrangement in $Ba(OH)_2$ prior to decomposition. This endotherm was followed by a large exotherm with variable onset temperature (~490°C), probably caused by the main pyrotechnic reaction. In all the DSC runs this exotherm appeared to be superimposed on the decomposition endotherm of BaO_2. The enthalpy changes measured for the thermal events are listed together with the corresponding onset temperatures in Table 4.10.

Fig 4.14 DSC trace for 40% Mo/BaO_2 heated in N_2 at 20°C min^{-1}

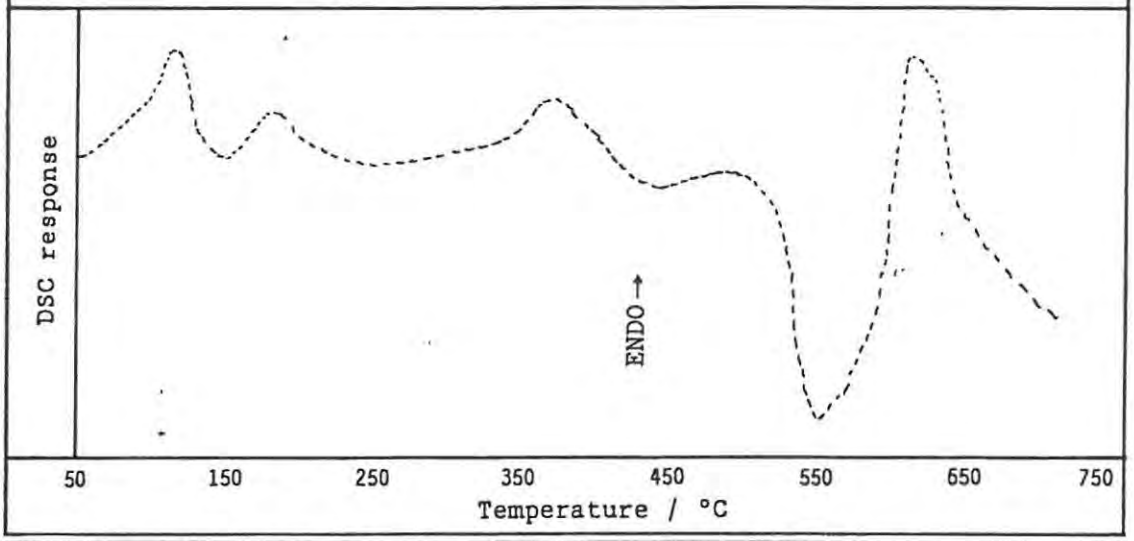

Fig 4.15 DSC traces for different compositions of the Mo/BaO_2 system heated in N_2 at 20°C min^{-1}

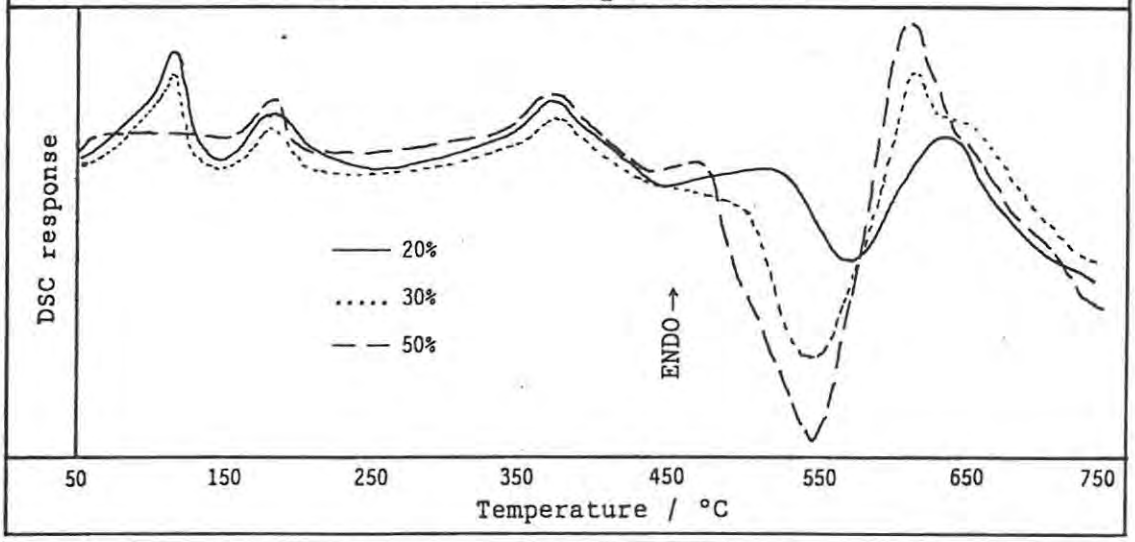

Fig 4.16 DSC traces for 40% Mo/BaO_2 heated in N_2 at 5°, 40° & 80°C min^{-1}

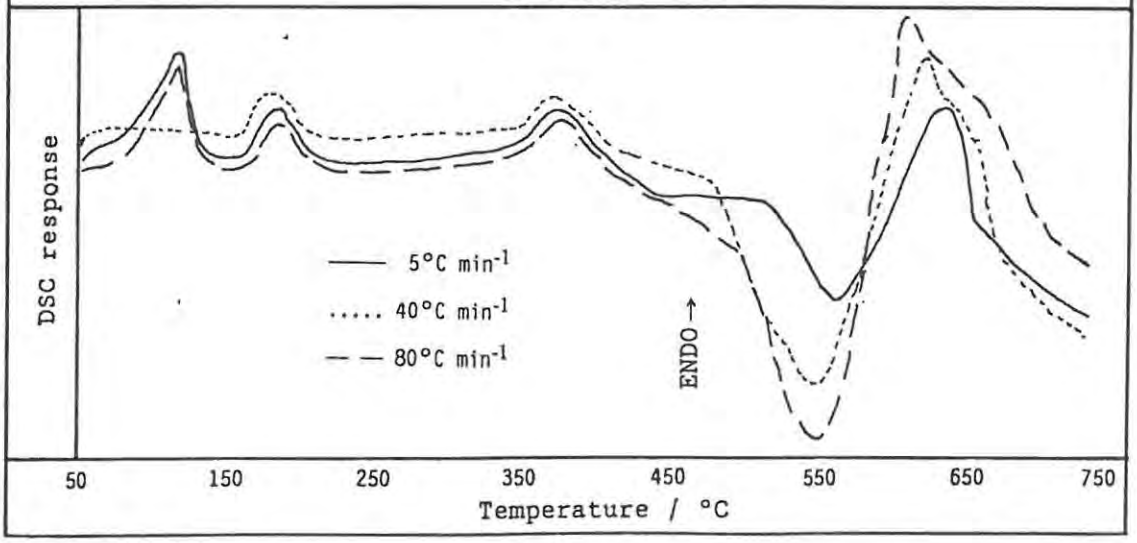

TABLE 4.10 DSC RESULTS FOR 40% Mo/BaO_2 HEATED AT 40°C min^{-1} IN N_2 (FIG 4.14)	
ONSET TEMP. / °C	ΔH / J g^{-1}
65 ± 10	31 ± 7
110 ± 2	14 ± 1
350 ± 1	5 ± 1
490 ± 23	-830 ± 28

The 20, 30 and 50% compositions of Mo/BaO_2 gave similar DSC traces on heating in N_2 at 20°C min^{-1} (Figure 4.15). The onset temperatures of the main exotherm were ~510°C for the 20% composition, ~500°C for the 30% composition, and ~470°C for the 50% composition. The size of the endothermic peak, due to the decomposition of unreacted BaO_2, was variable.

Similar masses of 40% Mo/BaO_2 were heated at different rates between 5° and 160°C min^{-1} (with increments of 2x) in the DSC. The resulting traces are shown in Figure 4.16 (only heating rates of 5°, 40° and 80°C min^{-1} are illustrated), with the onset temperatures and enthalpies listed in Table 4.11. The onset temperature of the main exothermic reaction was lowered as the heating rate was increased: ~500°C for 5°C min^{-1} and ~480°C for 40°C min^{-1}, while for 80 and 160°C min^{-1} the exotherm overlapped with the endotherm making the determination of the precise onset temperature difficult.

TABLE 4.11 DSC RESULTS FOR 40% Mo/BaO_2 HEATED AT DIFFERENT RATES IN N_2 (FIG 4.16)	
ONSET TEMP. / °C	ΔH / J g^{-1}
ϕ = 5°C min^{-1}	
60 ± 1	42 ± 3
130 ± 5	12 ± 1
340 ± 8	9 ± 1
500 ± 13	-489 ± 27
ϕ = 40°C min^{-1}	
75 ± 3	67 ± 4
125 ± 4	13 ± 1
355 ± 7	7 ± 1
480 ± 3	-394 ± 13
ϕ = 80°C min^{-1}	
60 ± 1	39 ± 1
130 ± 8	12 ± 1
355 ± 12	7 ± 1
~470	-377 ± 41

DSC in O_2. On changing the carrier gas to O_2, the DSC trace for 40% Mo/BaO_2 confirmed the low temperature (< 110°C) loss of water from BaO_2. The DSC trace also showed an endotherm with onset of ~350°C and ΔH = 6 ± 1 J g^{-1} which has been previously attributed to a structural rearrangement of $Ba(OH)_2$ (~360°C, Figure 4.1). At temperatures beyond ~500°C there was a general exothermic drift making the determination of the onset of the large and incomplete exotherm (ΔH = ~70 J g^{-1}) difficult to determine. The oxidation of Mo alone by O_2 (Figure 4.9) started at ~600°C

TG in N_2. The TG trace of 40% Mo/BaO_2 (Figure 4.17 a), heated at 20°C min^{-1} in N_2 after 10 minutes of flushing, showed the low temperature (< 110°C) mass loss of 0.22 ± 0.01% due to the loss of adsorbed water. A mass gain of 0.51 ± 0.02% starting at ~380°C was probably due to the oxidation of Mo by the impurities in the TG. However, it was possible that the BaO_2 had some effect on this oxidation since the oxidation of Mo heated alone in N_2 only started above 500°C (Section 4.3). This was followed by a small mass loss starting at ~560°C before, at even higher temperatures (~690°C), there was another mass gain of 1.5 ± 0.1%. The small mass loss corresponded closely to the decomposition temperature of the unreacted BaO_2 (Figure 4.3). The subsequent release of $O_2(g)$ could cause further oxidation of unreacted Mo and/or the initial product thus accounting for the high temperature (~690°C) mass increase. This event was not observed in the corresponding DSC trace because it occurs at a temperature close to the upper limit of the DSC (725°C).

The TG trace for 40% Mo/BaO_2 (Figure 4.17 b), recorded after flushing the apparatus with N_2 for at least 5 hours, was similar, but the mass gains were smaller. At ~400°C there was mass gain of less than 0.1% and at ~620°C there was a mass gain of 0.7 ± 0.1%.

TG in O_2. The TG trace for 40% Mo/BaO_2 heated in O_2 (Figure 4.17 c) showed, in addition to the low temperature loss of mass due to desorption of water, a mass gain of 8.0 ± 0.1% starting at ~470°C. This onset temperature corresponds approximately (~440°C) to the mass gain attributed to the oxidation of the Mo powder by O_2 (Figure 4.10). The mass gain accelerates sharply above ~620°C and slows at ~730°C.

4.4.3 Other binary compositions containing barium salts:

A DSC trace for 40% $Mn/BaCO_3$ heated in N_2 at 40°C min^{-1} was recorded using a relatively large sample mass (> 10 mg). In the temperature range from 50° to 725°C there was only one endotherm with onset at ~620°C (ΔH = 15 ± 2 J g^{-1}). The corresponding endotherm for Mn alone in N_2 (675°C, Section 4.3) was assigned to an allotropic change in the Mn.

The TG trace for 40% $Mn/BaCO_3$ heated in N_2 at 20°C min^{-1} from 50° to 950°C, showed a mass gain of variable magnitude (5.0 ± 2.0%) above ~400°C which could have been due to reaction between the metal and small amounts of oxygen and/or water vapour in the TG. The TG trace for Mn alone (Figure 4.10) showed a mass gain at about 360°C which was also attributed to oxidation by these impurities.

Fig 4.17 TG trace for 40% Mo/BaO_2 heated at 20°C min^{-1}

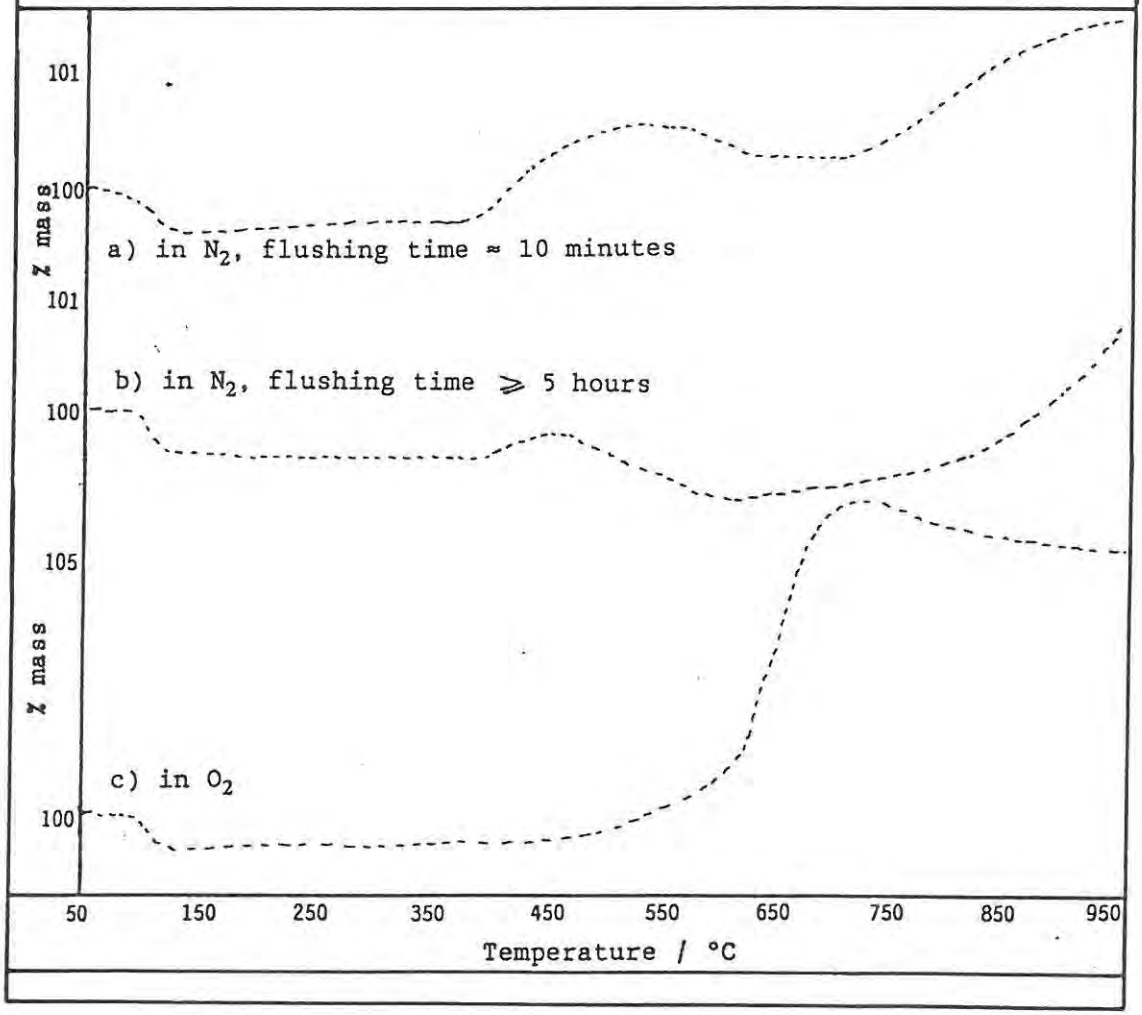

The DSC trace for 40% Mn/$Ba(OH)_2$ heated at 20°C min^{-1} in N_2 (Figure 4.18) showed endotherms with onset temperatures of ~110°C for the loss of adsorbed water from $Ba(OH)_2$, and ~265°C and ~380°C for the proposed structural rearrangements in $Ba(OH)_2$, noted in the DSC trace for $Ba(OH)_2$ alone (see comparison in Figure 4.18). The endotherm at ~380°C was followed by complex, but reproducible, overlapping exothermic and endothermic processes and a shift in the base line. The products of this complex interaction underwent a further exothermic reaction at higher temperatures (~560°C) giving an enthalpy change of -69 ± 5 J g^{-1}.

The TG trace for 40% Mn/$Ba(OH)_2$, heated at 20°C min^{-1} in N_2, showed an initial mass loss of 2.2 ± 0.2% beginning at ~80°C for the loss of water from $Ba(OH)_2$ followed by a slight mass increase at ~385°C which corresponds closely to the temperature of the proposed exothermic activity in the DSC trace. This mass gain was probably due to the oxidation of the Mn powder by small amounts of oxygen/water vapour in the TG (previously noted at about 390°C for Mn alone, Figure 4.10). There was then a small mass loss of 0.4 ± 0.1% above ~540°C probably due to the decomposition of unreacted $Ba(OH)_2$. Similar behaviour was observed at about 550°C in the TG trace of $Ba(OH)_2$ alone (Section 4.2.2). At temperatures above ~640°C there was another mass gain due to oxidation of the remaining Mn metal by the oxygen and/or water vapour remaining in the system.

4.4.4 The Mn/SrO_2 system:

Compositions containing from 20 to 80% Mn sustained combustion (Section 5.4.1).

DSC in N_2. Samples of 40% Mn/SrO_2 were heated at 20°C min^{-1} in N_2. The resulting DSC trace (Figure 4.19) shows the expected low temperature (~80°C) endothermic loss of adsorbed water from SrO_2 (Figure 4.6). This assignment was again confirmed by the DSC trace of the 40% Mn/SrO_2 made with dried SrO_2 in which this low temperature event was absent and the trace for 40% Mn/SrO_2, made from the moist SrO_2, which had a large (ΔH = ~685 J g^{-1}) low temperature endotherm.

A large exotherm probably due to the reaction between Mn and SrO_2 followed at temperatures beyond ~380°C. This exotherm appeared to be superimposed on the two endotherms at ~440° and at ~500°C resulting from the two-stage thermal decomposition of the unreacted SrO_2. The onset temperatures and associated enthalpy changes are listed in Table 4.12. Pyrotechnic mixtures made with the moist and dry samples of SrO_2 also had an exotherm superimposed on the twin decomposition endotherms.

TABLE 4.12 DSC RESULTS FOR 40% Mn/SrO_2 HEATED AT 40°C min^{-1} IN N_2 (FIG 4.19)

ONSET TEMP / °C	ΔH/J g^{-1}
80 ± 2	7 ± 2
380 ± 2	-106 ± 8
440 ± 10	176 ± 19
500 ± 2	121 ± 27

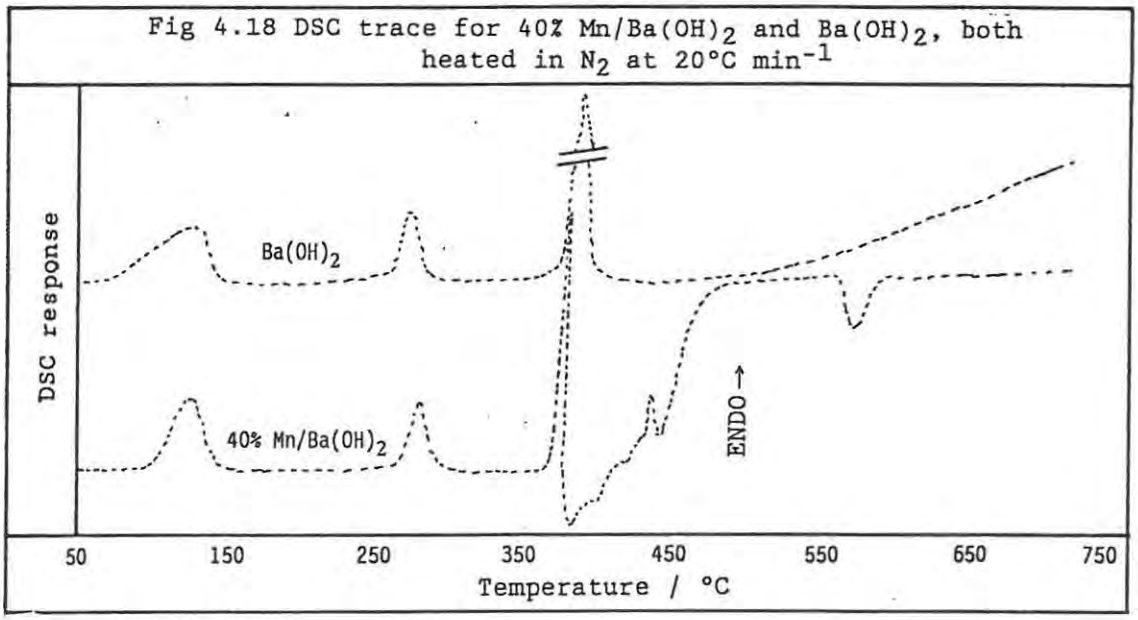

Fig 4.18 DSC trace for 40% $Mn/Ba(OH)_2$ and $Ba(OH)_2$, both heated in N_2 at 20°C min^{-1}

As the composition of the Mn/SrO_2 system was changed from 20 to 50% Mn, the size of the endotherms at about 440° and 500°C (Figure 4.20) decreased in size. There was also a slight decrease in onset temperature of the exotherm assigned to the reaction as the proportion of fuel increased.

TG in N_2. The TG trace of 40% Mn/SrO_2 recorded in N_2 with a heating rate of 20°C min^{-1} (Figure 4.21) confirmed the initial loss of water at a temperature of ~100°C. This was followed by a gradual mass gain above 300°C which was probably due to the oxidation of Mn by oxygen and/or water vapour impurities. In the TG trace of Mn alone this oxidation was noted above 390°C (Section 4.3). The proposed thermal decomposition of unreacted SrO_2 (see above) was confirmed by the 5.4 ± 0.5% mass loss starting at ~420°C (Figure 4.21). The TG trace for SrO_2 alone in N_2 (Figure 4.7) showed a mass loss which was attributed to the first-stage of decomposition at about 385°C with accelerated mass loss at about 500°C attributed to the second-stage of decomposition. The mass gains above ~600°C were possibly due to oxidation of unreacted Mn by either oxygen/water vapour impurities or by oxygen gas produced by the decomposition of SrO_2. It is also possible that this mass gain could have resulted from further oxidation of products of an earlier reaction.

DSC in O_2. The DSC trace of 40% Mn/SrO_2 (Figure 4.22) heated in O_2 showed, in addition to the low temperature endotherm due to the loss of adsorbed water from SrO_2 at ~80°C, the onset of an exotherm at ~350°C due to the reaction between Mn and SrO_2, superimposed on the pair of endotherms produced by the thermal decomposition of unreacted SrO_2, with onset temperatures of ~450° and ~480°C. The onset temperature of the first endotherm of this pair was 10° higher than when the sample was heated in N_2 due to the increased partial pressure of O_2. Up to ~550°C the trace is very similar to the DSC trace in N_2 (Figure 4.19).

Above 550°C there was a large, incomplete exotherm in the trace for Mn/SrO_2 recorded in O_2, due to the oxidation of unreacted Mn. The DSC trace of Mn alone heated in O_2 (Figure 4.9) showed that oxidation started at about 560°C.

TG in O_2. The TG trace of 40% Mn/SrO_2 in O_2 (Figure 4.23) was very similar to the trace in N_2 (Figure 4.21). There was the initial loss of water at ~100°C and the mass gain due to the oxidation of unreacted Mn at ~315°C (Mn heated alone in O_2 was oxidized at about 360°C, Figure 4.10). The 5.9 ± 0.1% mass loss starting at ~420°C was assigned to the decomposition of unreacted SrO_2. SrO_2, when heated alone in O_2 (Figure 4.8) decomposed at about 410°C with accelerated mass loss at 530°C. The mass gain of 8.9 ± 0.8% which started at ~545°C was either due to further oxidation of previously formed products or oxidation of unreacted Mn.

Fig 4.19 DSC trace for 40% Mn/SrO_2 heated in N_2 at 20°C min^{-1}

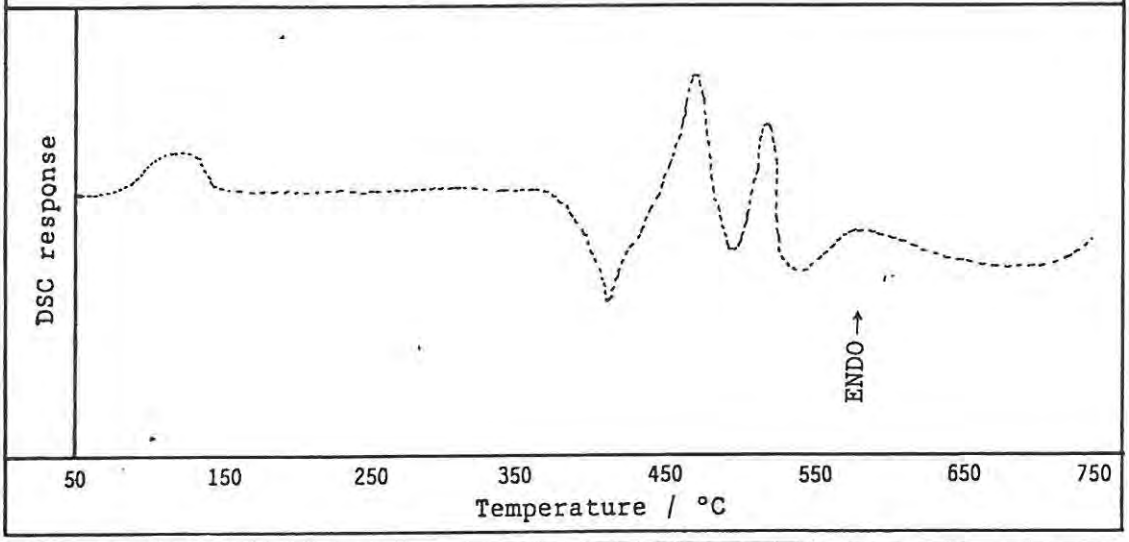

Fig 4.20 DSC traces for different compositions of the Mn/SrO_2 system heated in N_2 at 20°C min^{-1}

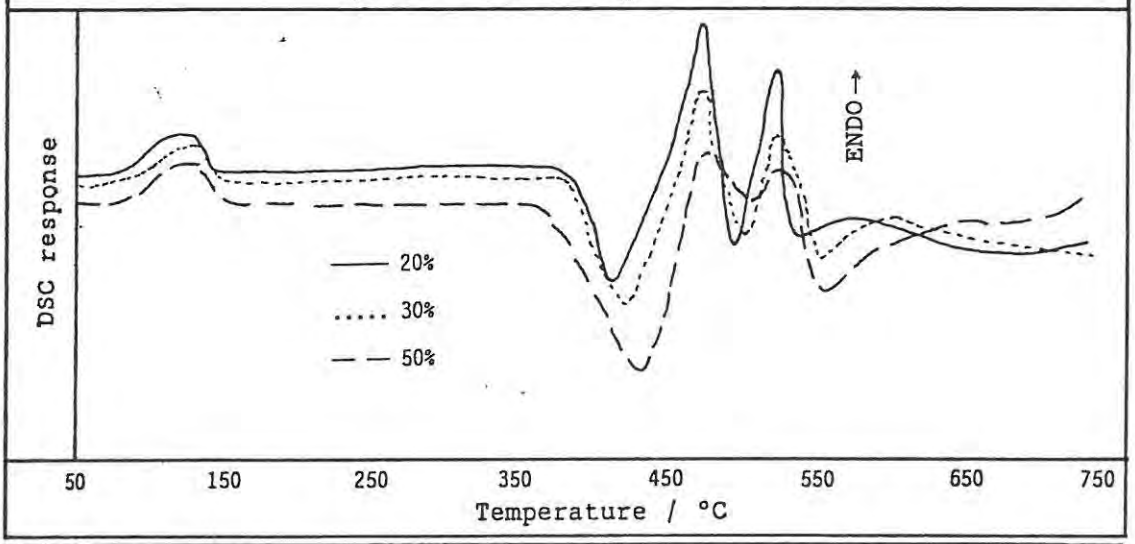

Fig 4.21 TG trace for 40% Mn/SrO_2 heated in N_2 at 20°C min^{-1}

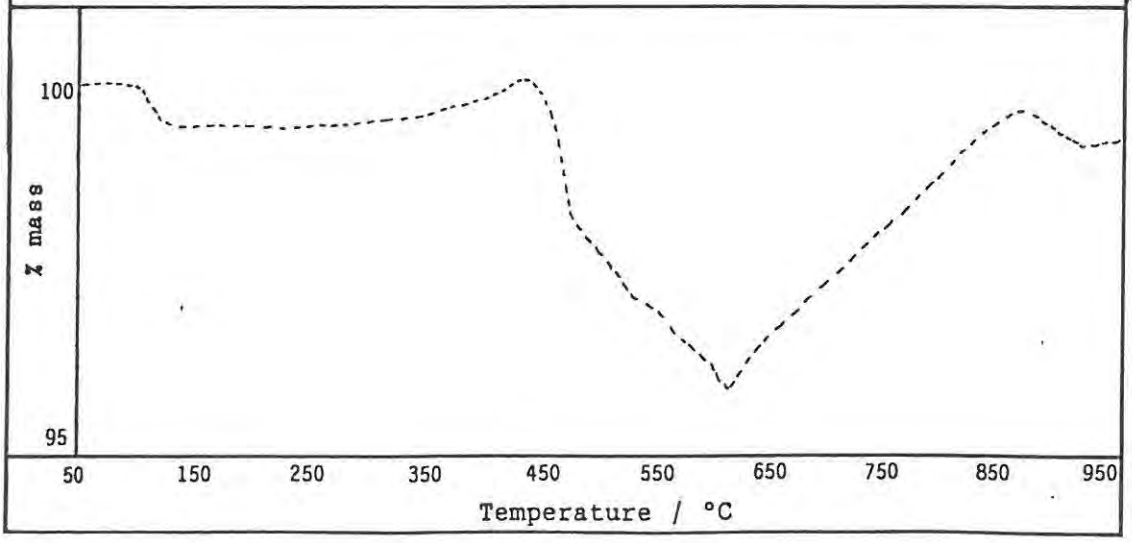

Fig 4.22 DSC trace for 40% Mn/SrO_2 heated in O_2 at 20°C min^{-1}

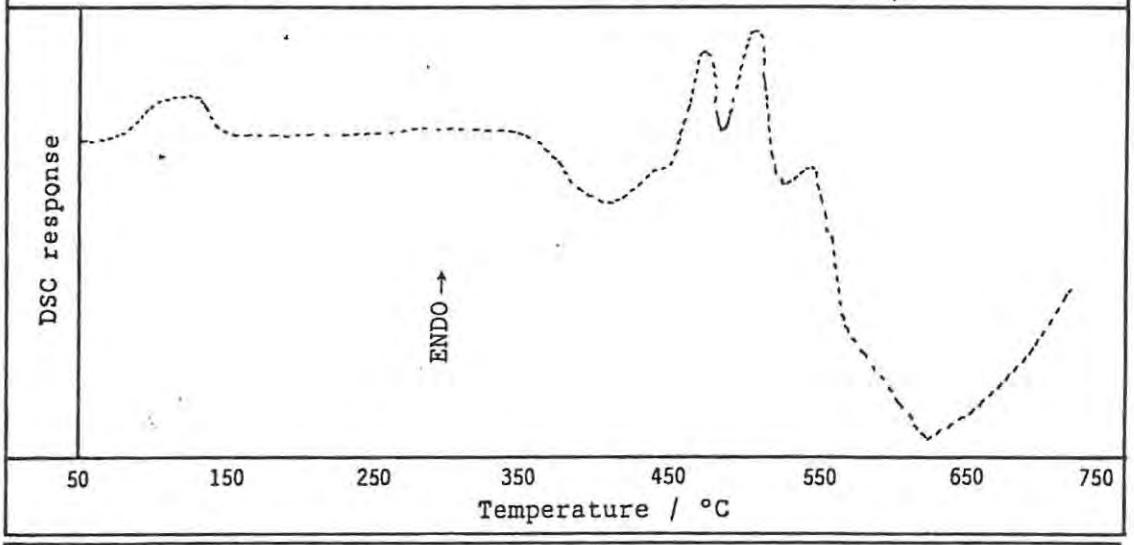

Fig 4.23 TG trace for 40% Mn/SrO_2 heated in O_2 at 20°C min^{-1}

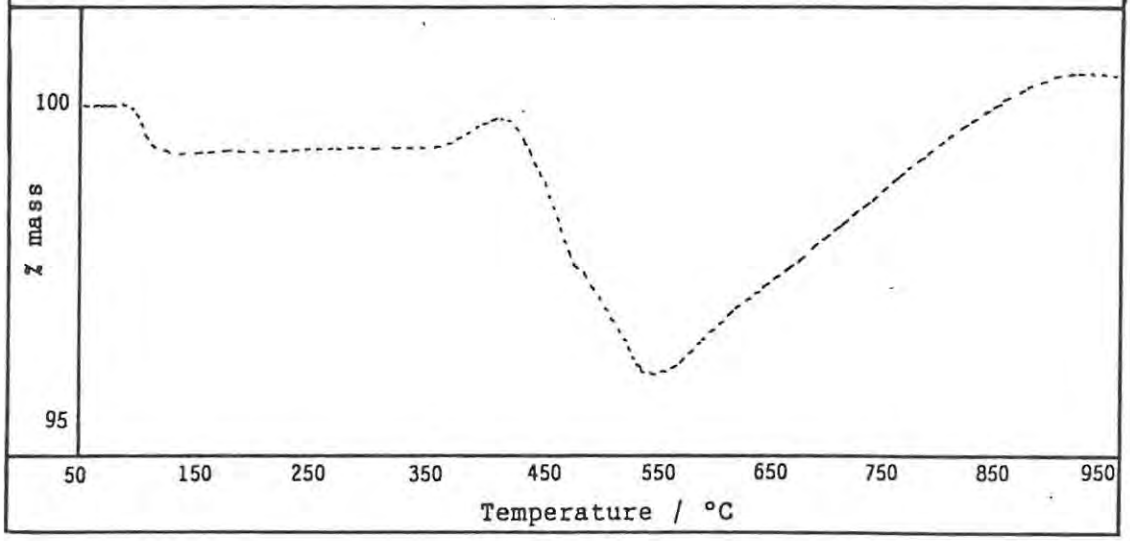

4.4.5 The Mo/SrO_2 system:

Only two compositions, 40 and 45% Mo, sustained combustion (Section 5.4.1).

DSC in N_2. Samples of various compositions (20 to 50% Mo) of the Mo/SrO_2 system were heated in N_2 in the DSC and even with large sample masses (up to 35 mg) and fast heating rates (up to 160°C min^{-1}) no reproducible exothermic events were observed in the resulting DSC traces (Figure 4.24). The usual low temperature (~52°C) endotherm signalled the loss of adsorbed water from the SrO_2 (ΔH = 118 J g^{-1}), followed by two endotherms with onset at ~400°C and ~560°C that were due to the two-stage decomposition of SrO_2 (ΔH = 126 ± 2 and 23 ± 1 J g^{-1}, respectively). These two endotherms were not always clearly resolved but DSC traces of samples of different masses showed that the larger the sample mass the better the resolution. One experiment, (Figure 4.25) using a covered pan containing only ~18 mg of 40% Mo/SrO_2 heated at 40°C min^{-1}, gave a small exotherm with onset temperature of ~580°C corresponding to an enthalpy change of -4 J g^{-1}. The second decomposition endotherm for SrO_2 was absent from this trace.

TG in N_2. The TG trace of 40% Mo/SrO_2 (Figure 4.26), heated at 20°C min^{-1} in N_2, showed in addition to the loss of adsorbed water from SrO_2 at ~115°C, a rapid mass loss of 7.1 ± 0.8% at ~420°C at the start of the thermal decomposition of SrO_2. The expected mass loss for complete decomposition of SrO_2 is 13%. There was no mass gain at temperatures preceding the decomposition of the oxidant as in the TG traces for Mn/BaO_2 (Figure 4.13 a and 4.13 b) and for the Mn/SrO_2 system (Figure 4.21) since the oxygen/water vapour impurity in the TG only caused oxidation of Mo above 440°C (Section 4.3). The next mass change was an 12.2 ± 0.7% gain starting at ~590°C which was attributed to the further oxidation of products or the oxidation of unreacted Mo by either the oxygen/water vapour impurity or by the gaseous oxygen formed during the decomposition of SrO_2. Mo alone, when heated in N_2 in the TG, was oxidized by the impurity at temperatures above 440°C (Figure 4.10).

DSC in O_2. With O_2 as carrier gas, the DSC trace for the 40% Mo/SrO_2 (Figure 4.27) showed the usual low temperature endotherm for the loss of water (~60°C, ΔH = 64 ± 1 J g^{-1}). The lower temperature endotherm of the pair of endotherms caused by the decomposition of SrO_2 appeared at a slightly higher onset temperature due to the increased partial pressure of oxygen (~410°, ΔH = 73 ± 7 J g^{-1} and ~560°C, ΔH = 94 ± 4 J g^{-1}, respectively). The next large exotherm with onset at ~660°C and enthalpy change of -635 ± 141 J g^{-1} was the incomplete oxidation of Mo by the carrier gas, which occurred above ~600°C when Mo was heated alone in O_2 (Figure 4.9).

Fig 4.24 DSC trace for 40% Mo/SrO_2 heated in N_2 at 20°C min^{-1}

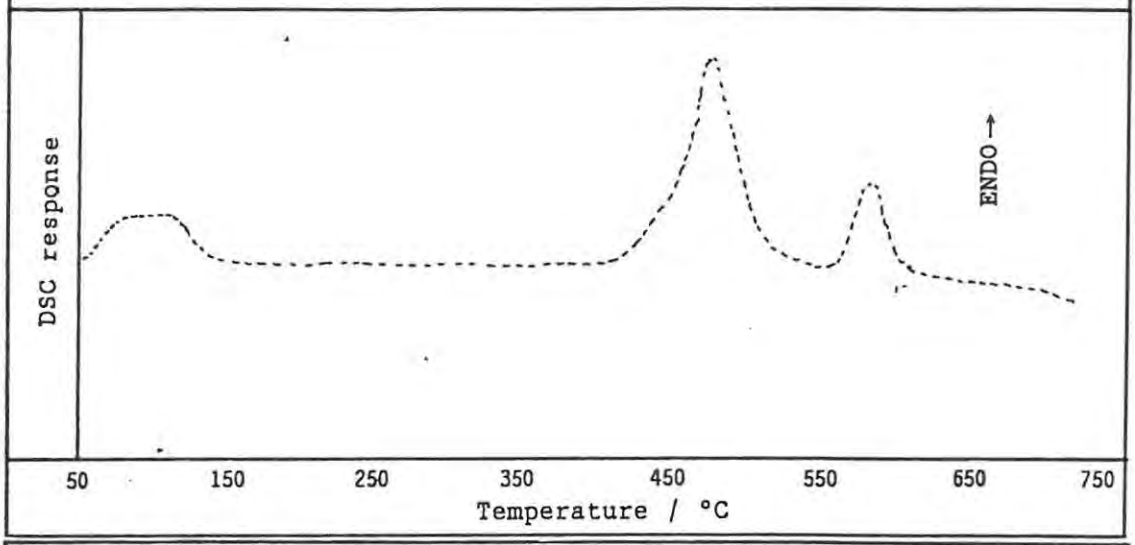

Fig 4.25 DSC trace for 40% Mo/SrO_2 heated in N_2 at 40°C min^{-1} showing a small exotherm

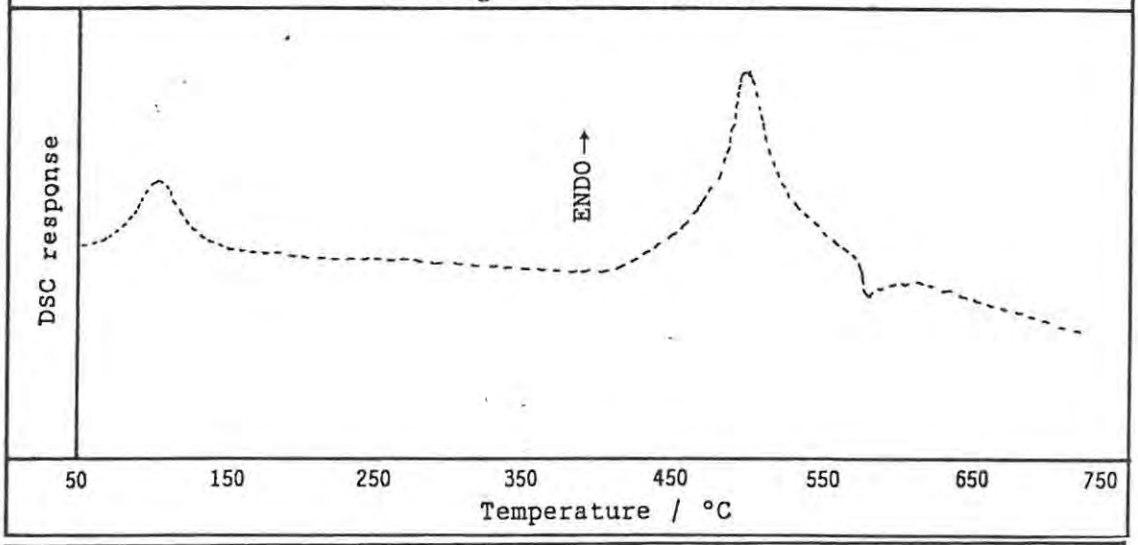

Fig 4.26 TG trace for 40% Mo/SrO_2 heated in N_2 at 20°C min^{-1}

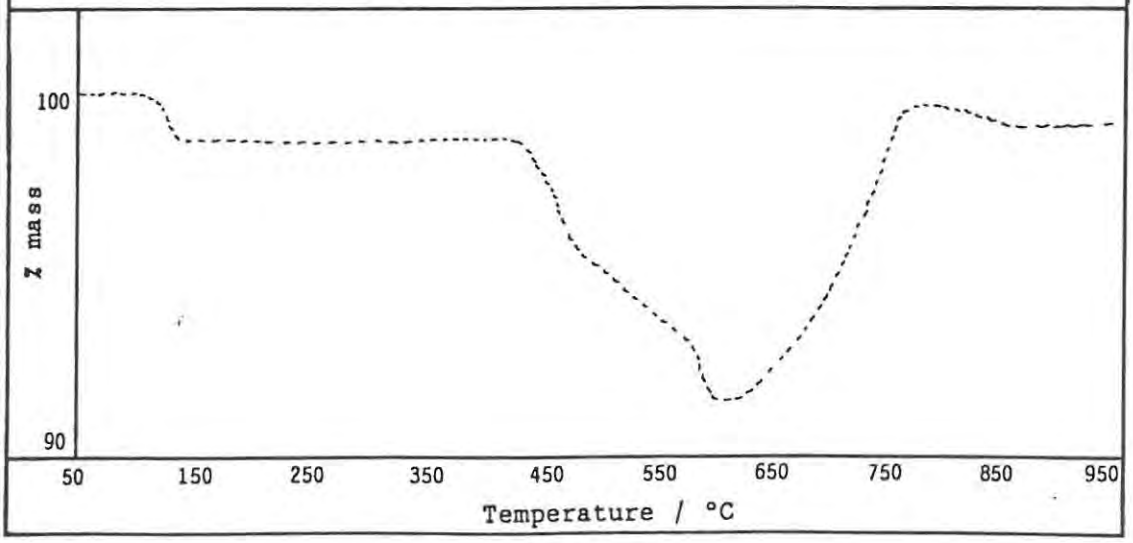

Fig 4.27 DSC trace for 40% Mo/SrO_2 heated in O_2 at 20°C min^{-1}

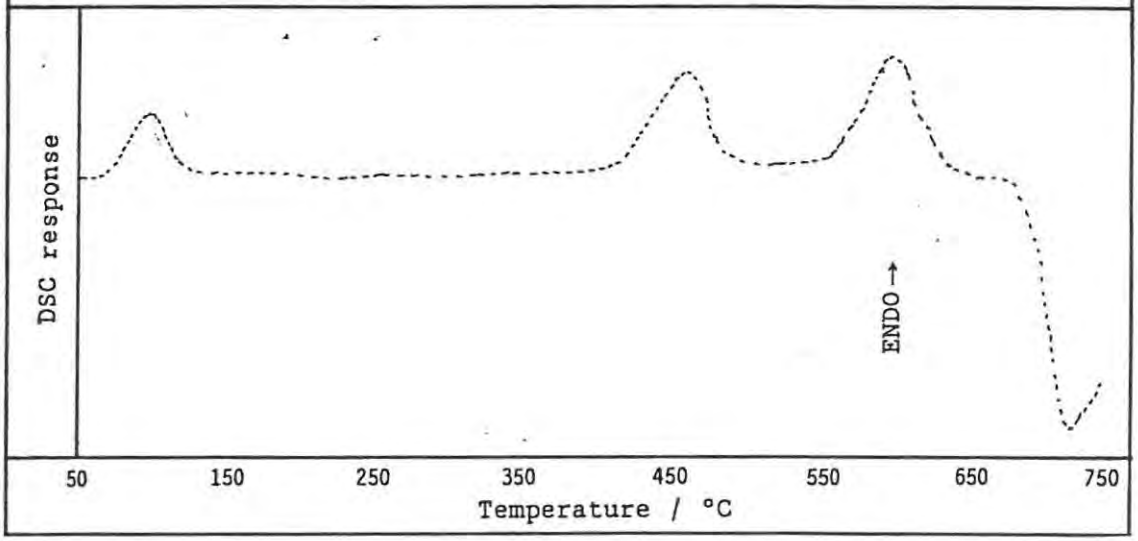

TG in O_2. The TG trace of 40% Mo/SrO_2 heated in O_2 at 20°C min^{-1} showed the initial loss of water at ~100°C and no further mass changes were observed until ~400°C where a total of 6.4 ± 0.1% of the original mass was lost due to the decomposition of SrO_2. Immediately after this at ~600°C there was a rapid mass gain of 11.3 ± 0.3% due to the oxidation of the Mo. Mo, when heated alone in the TG in O_2, was oxidized at temperatures above 440°C (Figure 4.10).

Further discussion of the thermal analysis results for the binary systems is given in Chapter 9.

4.5 THERMAL ANALYSIS OF THE TERNARY PYROTECHNIC SYSTEMS

4.5.1 Barium peroxide/strontium peroxide mixtures:

DSC in N_2. DSC traces were recorded for a 1:1 (by mass) mixture of the Merck sample of BaO_2 and SrO_2 in N_2 with a heating rate of 20°C min^{-1} and with sample masses of ~10 mg (Figure 4.28). Of the six endotherms observed, all corresponded approximately to the endotherms in the DSC traces for the individual oxidants (see Figures 4.1 and 4.6), the details of the endotherms are compared to those of the individual oxidants in Table 4.13.

TABLE 4.13 DSC RESULTS FOR 50% BaO_2/SrO_2 HEATED AT 20°C min^{-1} IN N_2 (FIG 4.28), COMPARED WITH THE RESULTS FOR BaO_2 AND SrO_2

BaO_2/SrO_2		BaO_2		SrO_2	
ONSET TEMP / °C	ΔH / J g^{-1} OF BaO_2 OR SrO_2	ONSET TEMP / °C	ΔH / J g^{-1}	ONSET TEMP / °C	ΔH / J g^{-1}
52 ± 2	65 ± 1	55 ± 7	18 ± 6		
115 ± 5	24 ± 13	100 ± 5	16 ± 2	80 ± 6	18 ± 2
340 ± 1	2 ± 1	360 ± 5	5 ± 1		
400 ± 2	59 ± 1			390 ± 10	185 ± 20
520 ± 3	136 ± 17			535 ± 8	182 ± 29
585 ± 1	144 ± 17	600 ± 6	382 ± 35*		

*This exotherm was incomplete at the limit of the temperature range (725°C).

The processes associated with the lower temperature endotherms were repeated unchanged in this mixture (and in the later ternary mixtures) and therefore will not be discussed again. The three main high temperature endotherms showed that the decompositions of the two peroxides, starting at ~400°C with the first-stage of the SrO_2 decomposition followed by the second-stage at ~520°C and finally the decomposition of BaO_2 starting at ~585°C, occur without significant interference.

TG in N_2. The TG trace for the 50% BaO_2/SrO_2 mixture, recorded in N_2 with a heating rate of 20°C min^{-1}, showed a mass loss, which started at ~385°C and accelerated at ~590°C, giving a total mass loss of 21.1 ± 1.8% of the original sample mass. The expected mass loss for the decomposition of both peroxides is 23%.

Fig 4.28 DSC trace for 50% BaO_2/SrO_2 heated in N_2 at 20°C min^{-1}

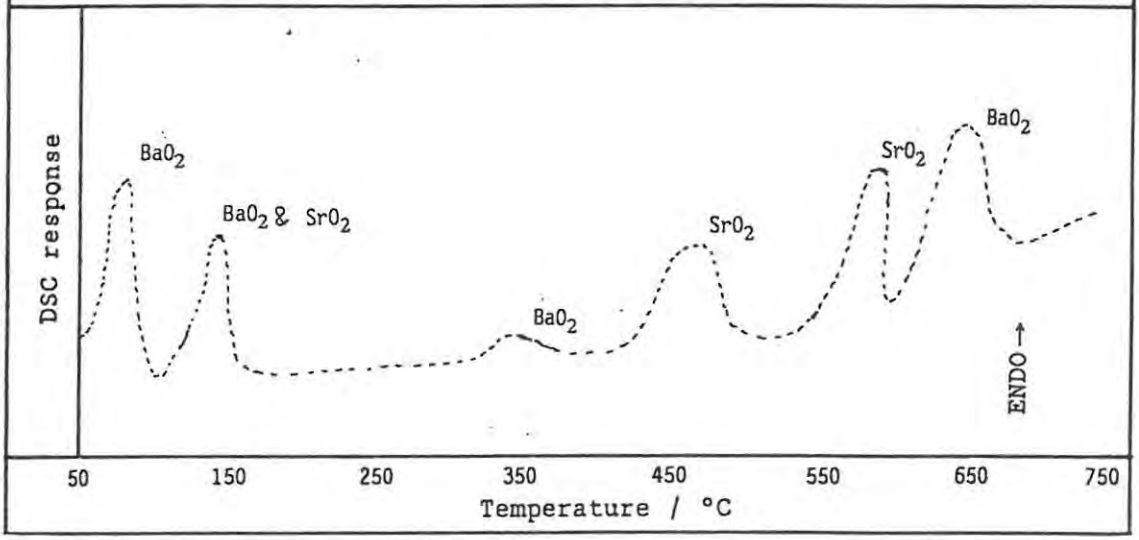

4.5.2 Manganese/molybdenum mixtures:

Within the temperature range of the TG and with sufficient flushing ($\geq$ 5 hours) of the system only small mass gains ($\sim$2%) above $\sim$390°C were observed for a mixture of equal masses of Mn and Mo heated to 950°C in N_2. The DSC trace of the same mixture, also heated in N_2, showed only one endotherm at $\sim$650°C (ΔH = 7 J g^{-1}) which was assigned to the allotropic phase change in Mn (for Mn heated alone in N_2, this phase change occurred at $\sim$675°C, see Section 4.3).

4.5.3 Mixed oxidant systems:

Various compositions of the two mixed oxidant ternary mixtures sustained combustion (Section 5.6.1).

The $Mn/BaO_2/SrO_2$ system. The DSC trace for a relatively large sample mass $\sim$20 mg for the 30:35:35 composition of $Mn/BaO_2/SrO_2$ heated in N_2 at 20°C min^{-1} (Figure 4.29 a) showed the low temperature endotherms associated with the loss of adsorbed water from BaO_2 and SrO_2. The next thermal event was a small exotherm (ΔH = -5 ± 1 J g^{-1}) with onset at $\sim$360°C which was observed in the traces for the Mn/BaO_2 system (Figure 4.11) and which corresponds very closely to the onset temperature of the endotherm assigned to the rearrangement in $Ba(OH)_2$ seen in the DSC trace for BaO_2 (Figure 4.1). The onset temperatures of the next two exotherms correspond approximately to the temperatures of the two endothermic stages for the decomposition of SrO_2. The small exotherm (ΔH = -1.4 ± 0.2 J g^{-1}) with onset at $\sim$400°C was probably due to some reaction initiated by the first-stage of decomposition of the SrO_2 ($\sim$390°C for SrO_2 and $\sim$400°C in the BaO_2/SrO_2 mixture) while the large exotherm (ΔH = -86 ± 10 J g^{-1}) with onset of $\sim$500°C was initiated by the second-stage ($\sim$535°C for SrO_2 and $\sim$520°C in the BaO_2/SrO_2 mixture). The endotherm starting at $\sim$580°C, probably due to the decomposition of unreacted BaO_2 which occurs at 600°C in BaO_2 and at 585°C in the BaO_2/SrO_2 mixture, was superimposed on the large exotherm (onset $\sim$500°C).

On changing the carrier gas to O_2, the higher temperature region of the DSC trace (Figure 4.29 b) showed one broad exotherm at temperatures above 560°C due to the oxidation of Mn by the carrier gas superimposed on the process observed in N_2. The oxidation of Mn by $O_2(g)$ has been noted at about 560°C in the DSC (Figure 4.9).

The TG trace (Figure 4.30) for 30:35:35 $Mn/BaO_2/SrO_2$, heated in N_2 at 20°C min^{-1}, showed a mass loss of 13.1 ± 0.3% above 350°C probably due initially to the decomposition of SrO_2 ($\sim$385°C for SrO_2 heated alone in N_2, Figure 4.7) while at higher temperatures the mass loss was probably caused by the decomposition of BaO_2 (onset at $\sim$570°C for BaO_2 heated alone in N_2, Figure 4.30). The expected mass loss for the decomposition of both these oxidants to their respective solid oxides and gaseous oxygen is 23%. Above 600°C there was a small mass gain ($\sim$2%) due to the oxidation of the unreacted Mn or previously formed products.

Fig 4.29 DSC trace for 30:35:35 $Mn/BaO_2/SrO_2$ heated at 20°C min^{-1}

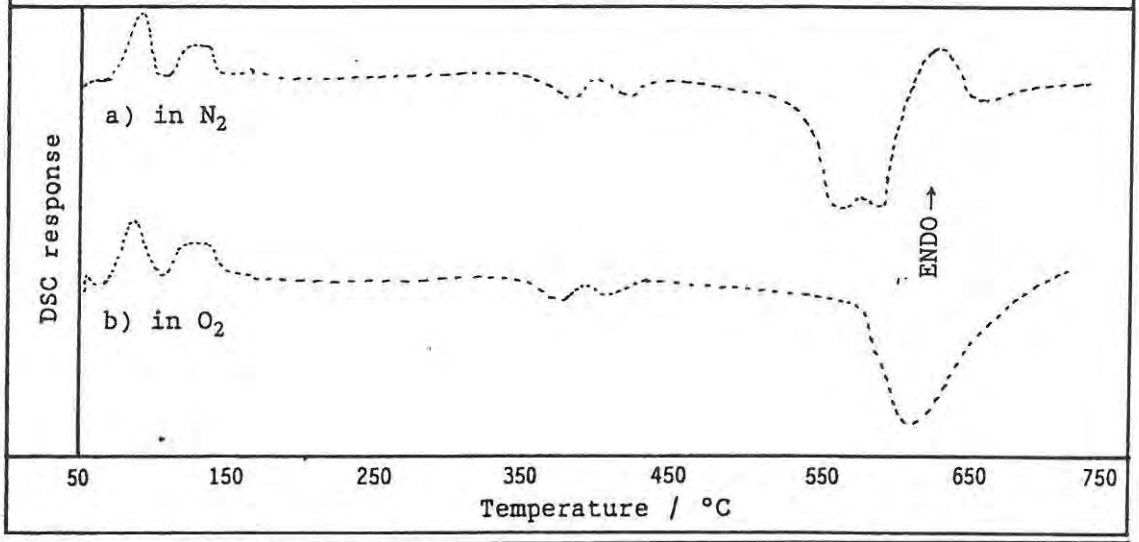

Fig 4.30 TG trace for 30:35:35 $Mn/BaO_2/SrO_2$ heated in N_2 at 20°C min^{-1}

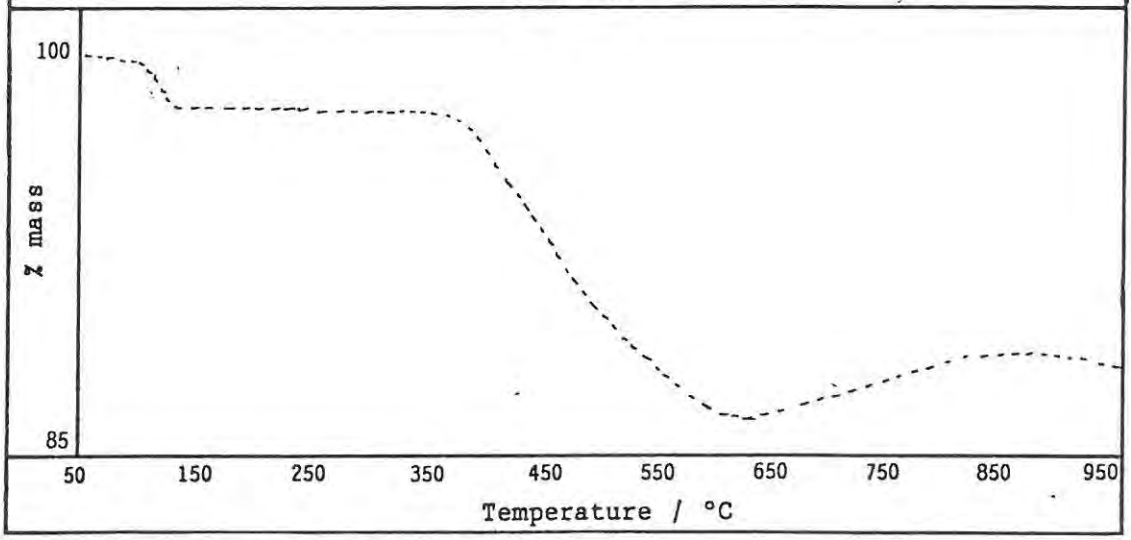

Fig 4.31 TG trace for 30:35:35 $Mn/BaO_2/SrO_2$ heated in O_2 at 20°C min^{-1}

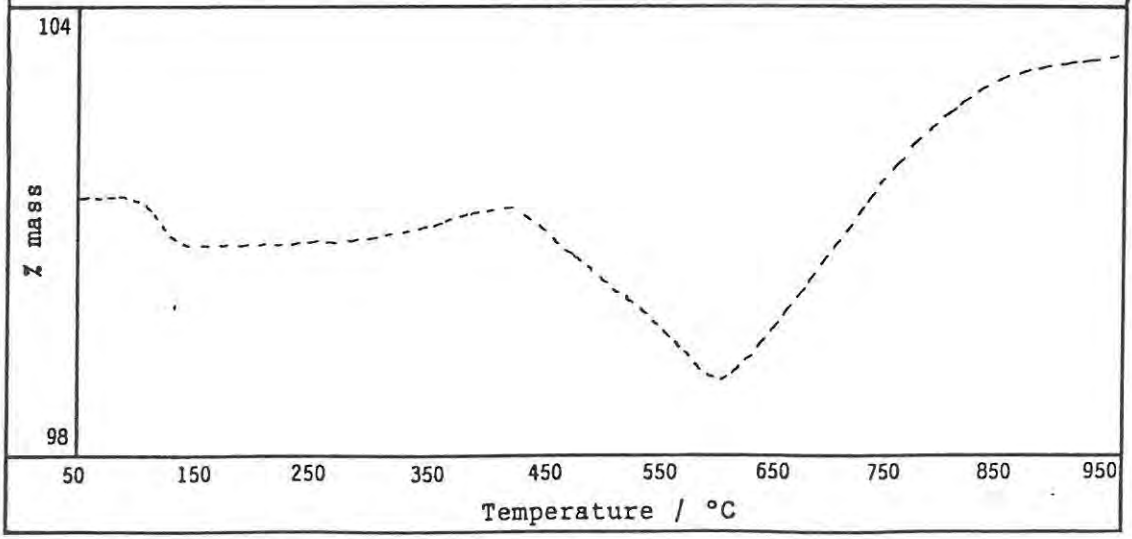

The TG trace, recorded in O_2, for this composition (Figure 4.31) confirmed the oxidation of unreacted Mn at ~250°C causing a mass gain of 0.7 ± 0.1%, while the 1.7 ± 0.1% mass loss starting at ~425°C confirmed the decomposition of the unreacted SrO_2 and the mass gain of 5.5 ± 1.0% starting at ~600°C was probably due either to the oxidation of the unreacted metal or to further oxidation of previously formed products.

The $Mo/BaO_2/SrO_2$ system. The DSC trace for 30:35:35 $Mo/BaO_2/SrO_2$ heated in N_2 at 20°C min^{-1} (with sample mass of ~20 mg) is shown in Figure 4.32 a. As in the DSC trace for the Mo/BaO_2 binary system (Figure 4.14) the endotherm assigned to the rearrangement in $Ba(OH)_2$ with onset at~365°C (ΔH = 0.8 ± 0.1 J g^{-1}) was followed closely by a large exotherm (with onset at ~430°C and with ΔH = -81 ± 6 J g^{-1}) due to reaction between Mo and BaO_2. This exotherm masks the region in which decomposition of SrO_2 occurs, but there is some endothermic contribution (~580°C) towards the end of the exotherm which could be due to the second-stage of SrO_2 decomposition (onset ~535°C, Figure 4.7) or decomposition of BaO_2 (onset ~600°C, Figure 4.3).

In O_2, the DSC trace (Figure 4.32 b) for this composition showed the usual endotherms which have been previously assigned to the loss of water from the oxidants and the rearrangement in the $Ba(OH)_2$ impurity. There was a small exotherm (ΔH = -72 ± 3 J g^{-1}) with onset at ~450°C which was assigned again to the reaction between Mo and BaO_2 (see above). This was followed by some endothermic activity probably due to the second-stage of SrO_2 decomposition (onset ~535°C, Figure 4.7). As in the DSC trace for BaO_2 (Figure 4.2), the decomposition of BaO_2 was not observed in the temperature range of the DSC due to the high partial pressure of O_2. The oxidation of Mo by the carrier gas was indicated by a large exotherm (ΔH = -1304 ± 91 J g^{-1}) with onset of ~620°C. Mo alone was oxidized by the O_2 carrier gas at ~600°C in the DSC (Figure 4.9).

The TG trace (Figure 4.33) in N_2, for the same composition of the $Mo/BaO_2/SrO_2$ ternary system, heated at 20°C min^{-1}, showed a mass loss of 5.1 ± 0.1% which started at ~400°C (this temperature corresponded approximately to the proposed reaction between Mo and BaO_2) and accelerated above 540°C. Since there was a mass loss, any reaction must be preceded, accompanied, or followed by the decomposition of unreacted SrO_2. Since the observed mass loss (5.1 ± 0.1%) was less than the expected mass loss (23%) for complete decomposition of the oxidants, some peroxide was consumed in the reaction. The mass gain at ~740°C was due to the interaction of unreacted metal and/or the newly formed products with the oxygen/water vapour impurity or with the gaseous oxygen formed during oxidant decomposition.

The TG trace, recorded in O_2, for this composition (Figure 4.34) showed a mass loss (onset ~450°C) followed by a mass gain (onset ~600°C). Mo heated alone in O_2 (Figure 4.10) was oxidized above 440°C. Decomposition of at least SrO_2 occurs before oxidation of Mo. The mass gain of 9.8 ± 1.0% starting at ~600°C corresponds approximately with the exotherm assigned to the oxidation of the

Fig 4.32 DSC trace for 30:35:35 $Mo/BaO_2/SrO_2$ heated at 20°C min^{-1}

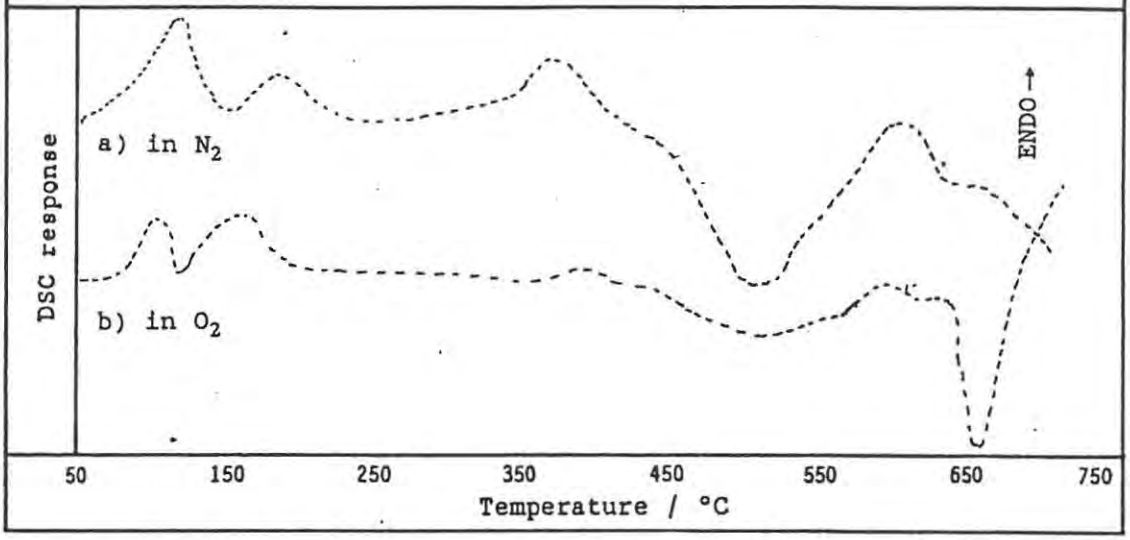

Fig 4.33 TG trace for 30:35:35 $Mo/BaO_2/SrO_2$ heated in N_2 at 20°C min^{-1}

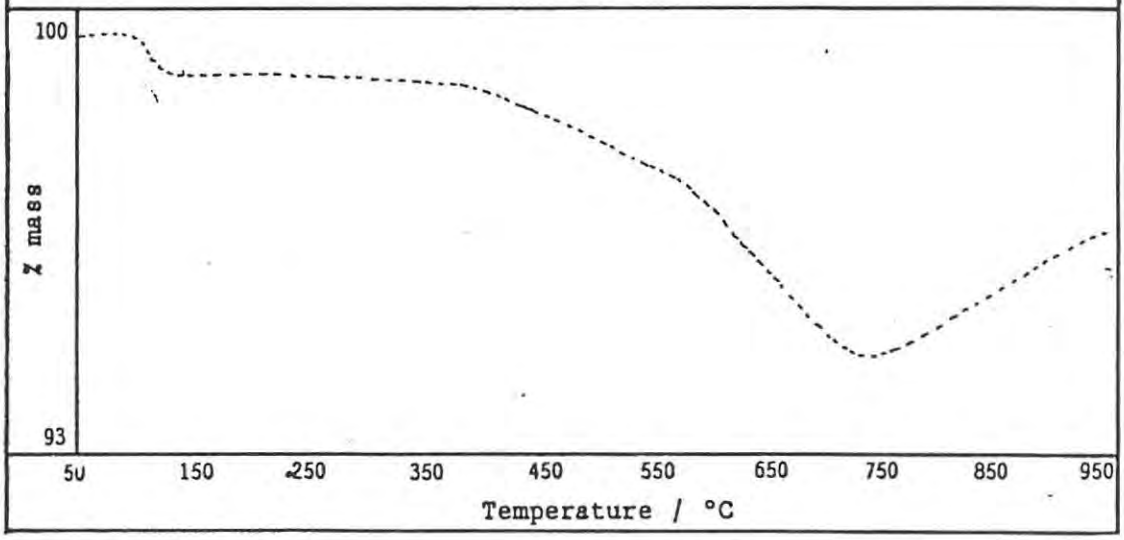

Fig 4.34 TG trace for 30:35:35 $Mo/BaO_2/SrO_2$ heated in O_2 at 20°C min^{-1}

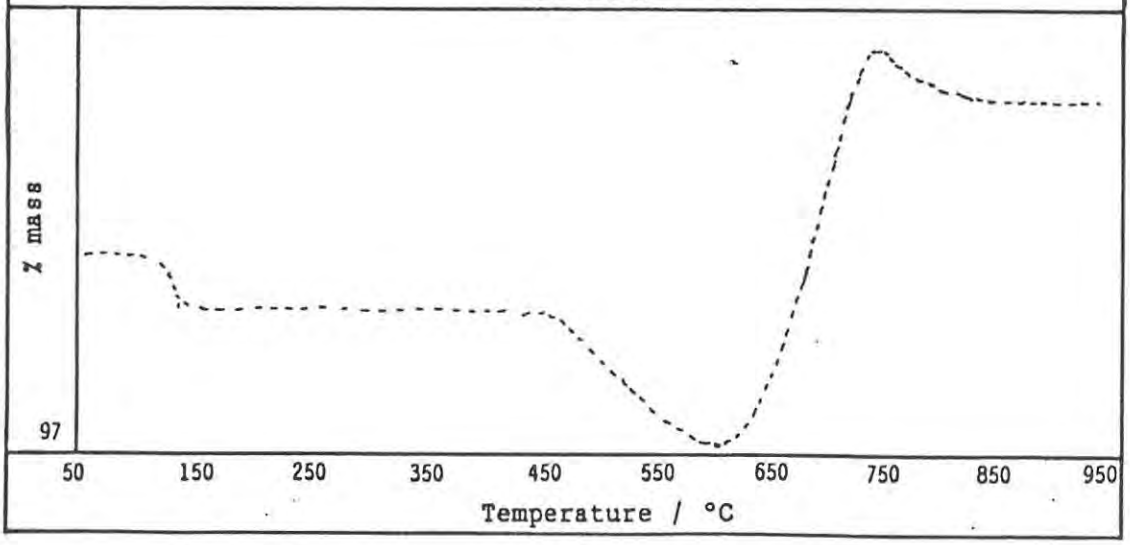

unreacted Mo (Figure 4.32), it could also be due to further oxidation of products formed in lower temperature interactions.

4.5.4 Mixed fuel systems:

Various compositions of the two mixed fuel ternary mixtures sustained combustion (Section 5.6.2).

The $Mn/Mo/BaO_2$ system. The DSC trace for 15:15:70 $Mn/Mo/BaO_2$ heated in N_2 at 20°C min^{-1} was recorded using a relatively large sample mass of ~20 mg (Figure 4.35 a). The small exotherm (ΔH = -4 ± 1 J g^{-1}) with onset at ~390°C, observed in the traces for the Mn/BaO_2 system (onset ~365°C, Figure 4.11), was present. The reaction which caused the next exotherm, with onset at ~425°C, was probably not initiated by the endothermic decomposition of BaO_2, which was expected at higher temperatures (~600°C). This behaviour was similar to that shown in the DSC trace (Figure 4.14) for the Mo/BaO_2 system (exotherm onset at ~490°C). The next large exotherm (onset ~500°C) overlaps the temperature range (~600°C), of the decomposition of the unreacted BaO_2 and hence there may be some endothermic contribution to the complex exotherm, which had a enthalpy change of -123 ± 6 J g^{-1} and was due to the oxidation of both fuels.

In O_2, the DSC trace for $Mn/Mo/BaO_2$ (Figure 4.35 b) showed a complex exotherm with onset ~340°C (ΔH = -23 ± 5 J g^{-1}). This exotherm was assigned to interaction related to the endothermic rearrangement in $Ba(OH)_2$ (onset ~360°C in BaO_2 alone, Figure 4.3) and to the exotherm assigned above (~425°C) to a reaction between Mo(s) and BaO_2(s). The onset of the next exotherm was difficult to determine but had probably started at least by ~500°C. This exotherm was due to the oxidation of both metals by the carrier gas.

The TG trace (Figure 4.36 a) for this composition, heated in N_2 at 20°C min^{-1}, showed a mass gain of 1.7 ± 0.2% starting at ~350°C which was due to the interaction between the sample and the oxygen/water vapour still present in the TG. The small mass loss (0.3 ± 0.1%) starting at ~580°C was probably due to the decomposition of the unreacted BaO_2 in the sample. Decomposition of BaO_2 heated alone in N_2 occurs above 570°C (Figure 4.3). The incomplete mass gain starting at ~640°C was probably due to further oxidation of newly formed products and/or unreacted metals by oxygen/water vapour in the TG, or by the oxygen gas released during the proposed decomposition of BaO_2.

The TG trace, recorded in O_2, for $Mn/Mo/BaO_2$ (Figure 4.36 b) showed an 8.7 ± 1.0% mass gain starting at ~400°C which was attributed to the oxidation of Mn (360°C when heated alone, Figure 4.10) with later mass contributions coming from the oxidation of Mo (440°C when heated alone). The high temperature mass loss above ~820°C was probably due the decomposition of any remaining oxidant, or possibly to the decomposition of products formed at lower temperatures.

Fig 4.35 DSC trace for 15:15:70 Mn/Mo/BaO_2 heated at 20°C min^{-1}

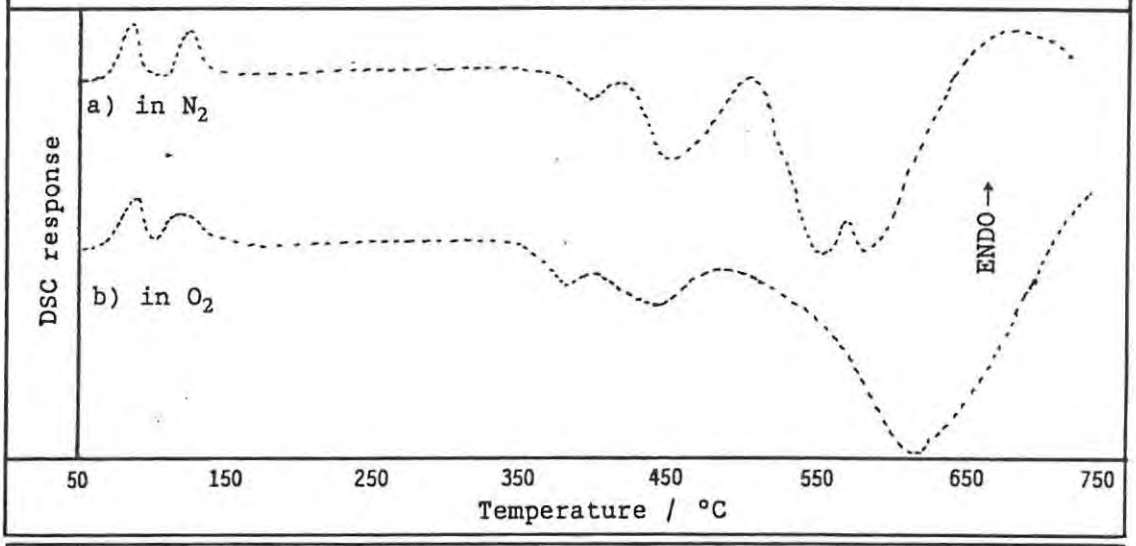

Fig 4.36 TG trace for 15:15:70 Mn/Mo/BaO_2 heated at 20°C min^{-1}

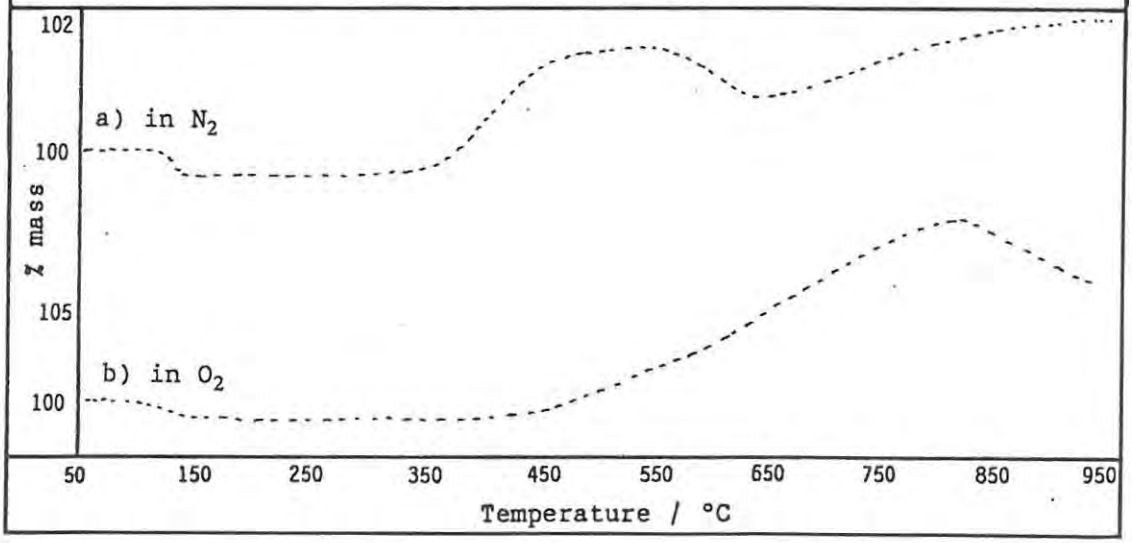

The $Mn/Mo/SrO_2$ system. The DSC trace for 15:15:70 $Mn/Mo/SrO_2$ heated in N_2 at 20°C min^{-1} (with a sample mass of ~20 mg) is shown in Figure 4.37 a. The exotherm at ~375°C corresponded approximately to the exotherm at ~380°C, observed in the DSC trace for the Mn/SrO_2 system (Figure 4.19) which was assigned to the bulk reaction between Mn and SrO_2. The large endotherm at ~430°C (ΔH = 186 ± 48 J g^{-1}) was probably due to the decomposition of the unreacted SrO_2, previously reported in both the Mn/SrO_2 (onset ~440°C, Figure 4.19) and Mo/SrO_2 (~400°C, Figure 4.24) systems. There was an exotherm at temperatures beyond the decomposition of SrO_2, i.e. with an onset temperature of ~575°C and with an enthalpy change of -28 ± 8 J g^{-1}. The onset temperature of this exotherm corresponded approximately to the onset temperature of the exotherm at about 580°C in the DSC trace for the Mo/SrO_2 binary system (Figure 4.25) and was thus probably due a reaction between Mo and SrO_2.

On changing the carrier gas to O_2, the DSC trace for this composition (Figure 4.37 b) showed an exotherm (onset ~370°C) which, as above, was attributed to reaction between Mn and SrO_2. This exotherm had an enthalpy change of -90 ± 10 J g^{-1} and was followed by some endothermic activity due to the decomposition of unreacted SrO_2 (onset ~395° and ~550°C for the two-stages for SrO_2 decomposition heated alone in O_2). The oxidation of both the metals by the carrier gas started at ~550°C and had an enthalpy change of -120 ± 20 J g^{-1}.

The TG trace (Figure 4.38 a) for $Mn/Mo/SrO_2$, heated in N_2 at 20°C min^{-1}, showed a slight mass gain (< 1% of the original mass) at ~320°C due to the oxidation of the sample by the oxygen/water vapour impurities in the TG. At ~410°C the mass loss of 7.1 ± 0.1% due to the decomposition of SrO_2 was observed with the characteristic step at ~465°C. This was followed by the mass gain of 2.5 ± 0.4% at ~610°C previously assigned, in the TG traces for the Mn/SrO_2 (Figure 4.21) and Mo/SrO_2 (Figure 4.26) systems, to the interaction between the newly formed products and either the residual O_2 from the earlier decomposition of SrO_2 or the contaminating gases in the TG.

In O_2, a similar TG trace (Figure 4.38 b) was recorded except the mass gain at ~620°C was much larger (8.0 ± 0.8%) due to the high partial pressure of O_2. The interaction between the sample and oxygen was observed at ~300°C and the decomposition of SrO_2 started above ~410°C and caused a mass loss of 5.4 ± 0.2%.

Further discussion of the thermal analysis results for the ternary systems is given in Chapter 10. .

Fig 4.37 DSC trace for 15:15:70 Mn/Mo/SrO_2 heated at 20°C min^{-1}

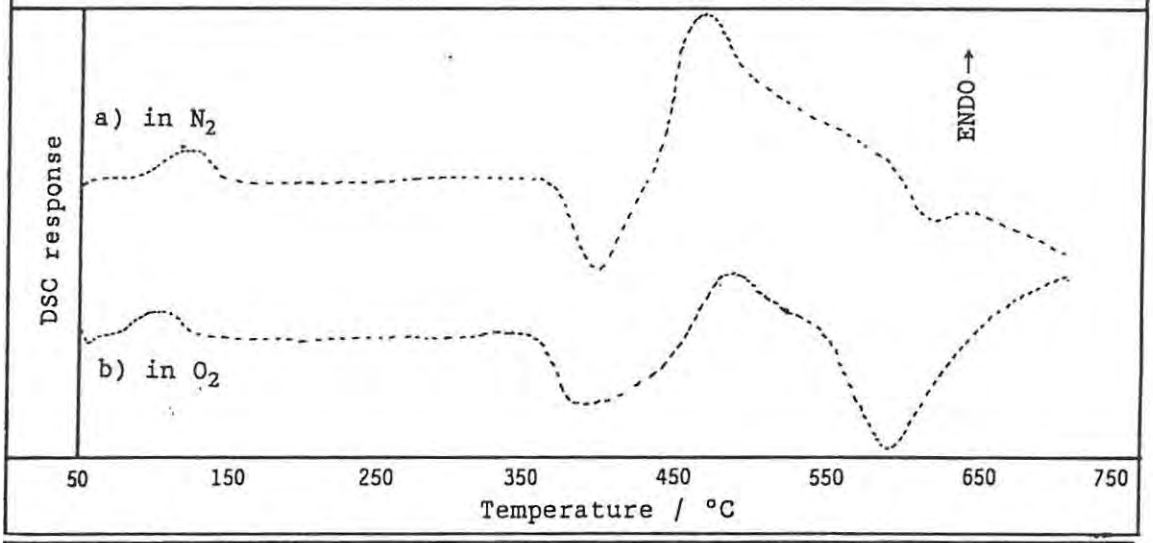

Fig 4.38 TG trace for 15:15:70 Mn/Mo/SrO_2 heated at 20°C min^{-1}

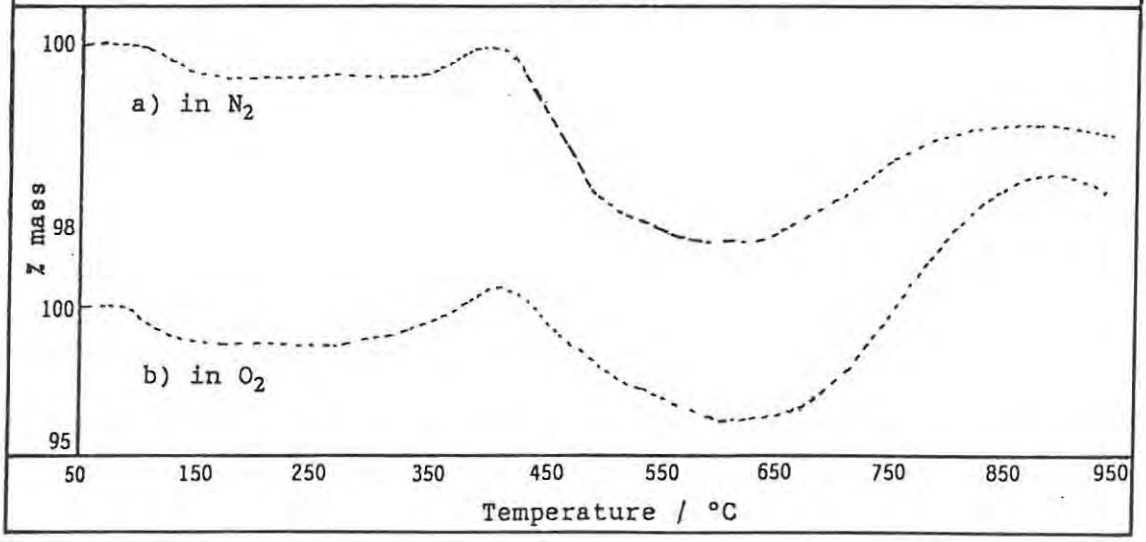

4.6 KINETICS FROM THERMAL ANALYSIS:

Extraction of kinetic information from thermal analysis results is an active, although controversial, field. There are many methods, of varying degrees of complexity, for analysing experimental data. One of these methods, suggested by Borchardt and Daniels (ref 79) is closely related to the Hill method used in the analysis of temperature profiles (Section 1.3). The Borchardt and Daniels method assumes:

(i) the usual form of the rate equation:

$$(d\alpha/dt) = k(1 - \alpha)^n$$

(ii) Arrhenius behaviour:

$$k = A \exp(-E_a/RT)$$

and

(iii) $(d\alpha/dt) = (d\alpha/dT)(dT/dt) = (d\alpha/dT)\phi$

where ϕ is the (constant) heating rate used in the thermal analysis experiment.

The procedure for deriving the values of E_a and A is then calculated:

$$k = (d\alpha/dt)/(1 - \alpha)^n$$

from the thermal analysis curve. For example, in a DSC trace, the DSC response is proportional to $d\alpha/dt$ and the partial area under an exotherm or endotherm is a measure of α. As in the Hill method, a value for n has to be selected by trial-and-error.

The k values obtained in this way are used in a conventional Arrhenius plot of lnk against the corresponding temperature.

Nonisothermal kinetic analysis is not appropriate unless the thermal analysis curve, e.g. DSC or TG, is relatively simple.

The thermal analysis traces (DSC and TG) obtained in this study were examined for suitability for kinetic analysis and the Borchardt and Daniels method was applied to the following representative experiments:

(i) oxidation of Mn - TG trace shown in Figure 4.10

(ii) oxidation of Mo - DSC trace shown in Figure 4.9

(iii) reaction of 40% Mn/BaO_2 - DSC trace shown in Figure 4.11 a

(iv) reaction of 40% Mn/SrO_2 - DSC trace shown in Figure 4.19

(v) reaction of 50% Mo/BaO_2 - DSC trace shown in Figure 4.14

Note: (i) No suitable exothermic response was obtained during thermal analysis during Mo/SrO_2 compositions. (ii) Where several exothermic responses were observed in a DSC trace, only the first exotherm was analysed.

The results of application of the Borchardt and Daniels method are summarized in Table 4.14. Figures 4.39 and 4.40 show the Arrhenius plots, with regression lines, for the oxidation of Mn and Mo. The fact that the E_a values for Mn are significantly lower than those for Mo is consistent with the observation that Mn is more readily oxidized by O_2 in the TG than Mo. Further discussion of these results is given in Section 9.3.6

TABLE 4.14 NONISOTHERMAL KINETIC ANALYSIS (BORCHARDT AND DANIELS METHOD) OF THERMAL ANALYSIS TRACES

SYSTEM	T_{ign} / K	n	E_a / kJ mol^{-1}	$\ln(A/min^{-1})$	r
Mn	525*	0.5	33.4 ± 0.2	-2.73 ± 0.08	0.99
		1.0	37.1 ± 0.2	-2.06 ± 0.11	0.99
		2.0	44.3 ± 0.3	-0.72 ± 0.18	0.98
Mo	815*	0.5	299 ± 4	34.72 ± 0.05	0.99
		1.0	241 ± 4	26.64 ± 0.26	0.98
		2.0	333 ± 2	39.54 ± 0.12	1.00
40% Mn/BaO_2	550	0.5	422 ± 3	82.89 ± 0.07	1.00
		1.0	236 ± 7	43.84 ± 0.35	0.97
		2.0	426 ± 4	83.71 ± 0.23	1.00
40% Mn/SrO_2	500	0.5	459 ± 2	105.07 ± 0.02	1.00
		1.0	434 ± 9	99.20 ± 0.19	0.99
		2.0	716 ± 10	166.76 ± 0.21	0.99
40% Mo/BaO_2	550	0.5	67.8 ± 1.6	4.49 ± 0.28	0.93
		1.0	84.2 ± 2.1	7.34 ± 0.36	0.92
		2.0	117.0 ± 3.1	13.04 ± 0.55	0.91

*Onset of oxidation

Fig 4.39 Arrhenius plot for the oxidation of Mn (n = 1)

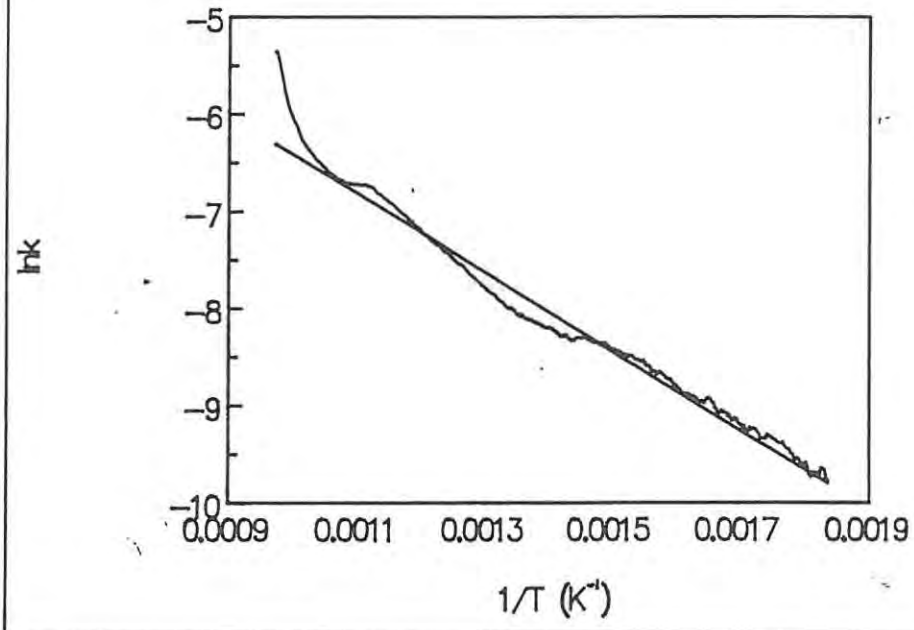

Fig 4.40 Arrhenius plot for the oxidation of Mo (n = 1)

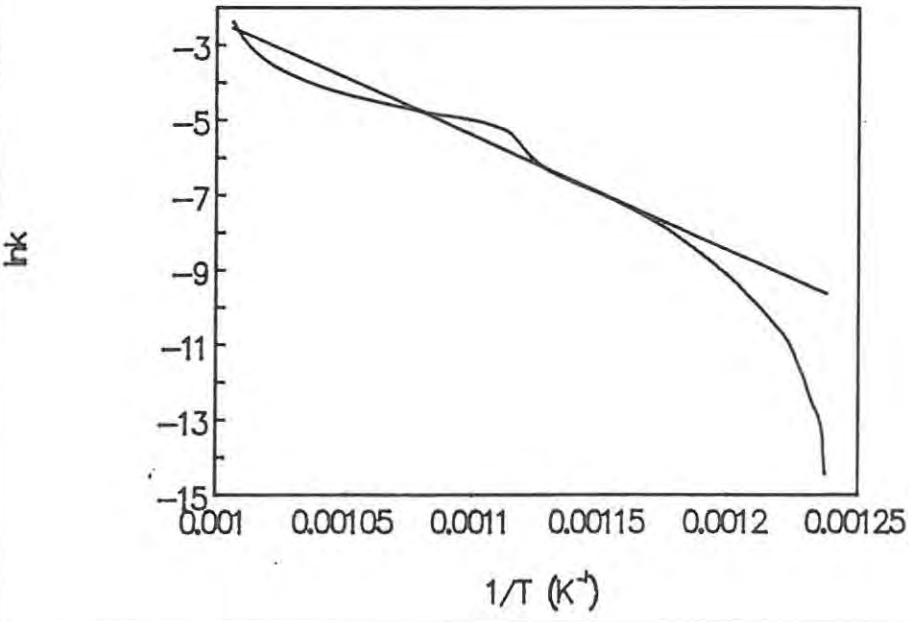

CHAPTER 5: TEMPERATURE PROFILES

The principal technique used in this study of pyrotechnic reactions involved the measurement of the temperature at a fixed point in a block of burning composition as a function of time. The rate of propagation of combustion through the unreacted mixture was also measured and combustion residues were analysed using X-ray powder diffraction (XRD) and infrared spectroscopy (IR). Further discussion of the results presented here is given in Chapters 9 and 10.

5.1 EXPERIMENTAL

5.1.1 Materials:

Pyrotechnic mixtures were prepared as described in Section 3.1 and consisted of materials listed in Table 3.1. Unless otherwise stated, the oxidants used in the burning experiments were Merck BaO_2 and untreated SrO_2.

5.1.2 Apparatus:

A. The channel. The apparatus in which pyrotechnic mixtures were burnt consisted of a stainless-steel channel (Figure 5.1 a) with internal dimensions of 30 mm x 6 mm x 5 mm, into which samples of pyrotechnic compositions were loaded and gently tamped. This filled channel was covered with a lid and hydraulically compacted for 1 minute under loads ranging from approximately 50 to 250 MPa. The height of the pressed sample was measured and used in the calculation of sample density.

A platinum/10% rhodium-platinum thermocouple (Type S), joined by gas-welding of wires of various diameters (0.05 mm, 0.1 mm, 0.2 mm and 0.3 mm) supplied by Johnson-Matthey, was inserted during the loading process into slits cut in the sides of the channel. Only thermocouples with small and regularly shaped junctions were used. The thermocouple wire was electrically insulated from the metal channel by inserting an asbestos paper envelope into each slit. Two additional slits in the channel sides (Figure 5.1 a and 5.1 b) enabled burning times to be measured through the triggering and stopping of a timing circuit by infrared detectors. A starting increment, about 1 mm thick, of a 50% composition of $Mn/KMnO_4$ and a safety match were used to ignite the pyrotechnic mixtures. Unless otherwise specified, "burning rate" implies "linear burning rate". Linear burning rates may be converted to mass burning rates by multiplying by the density and the cross-sectional area.

Fig 5.1a Channel

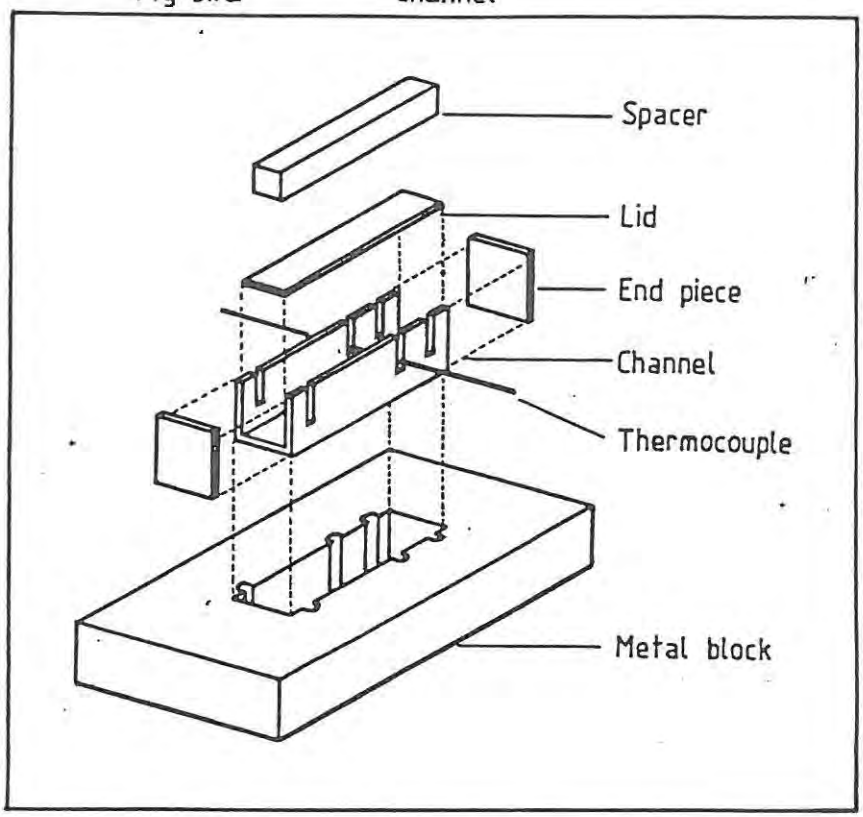

Fig 5.1b Data capture system

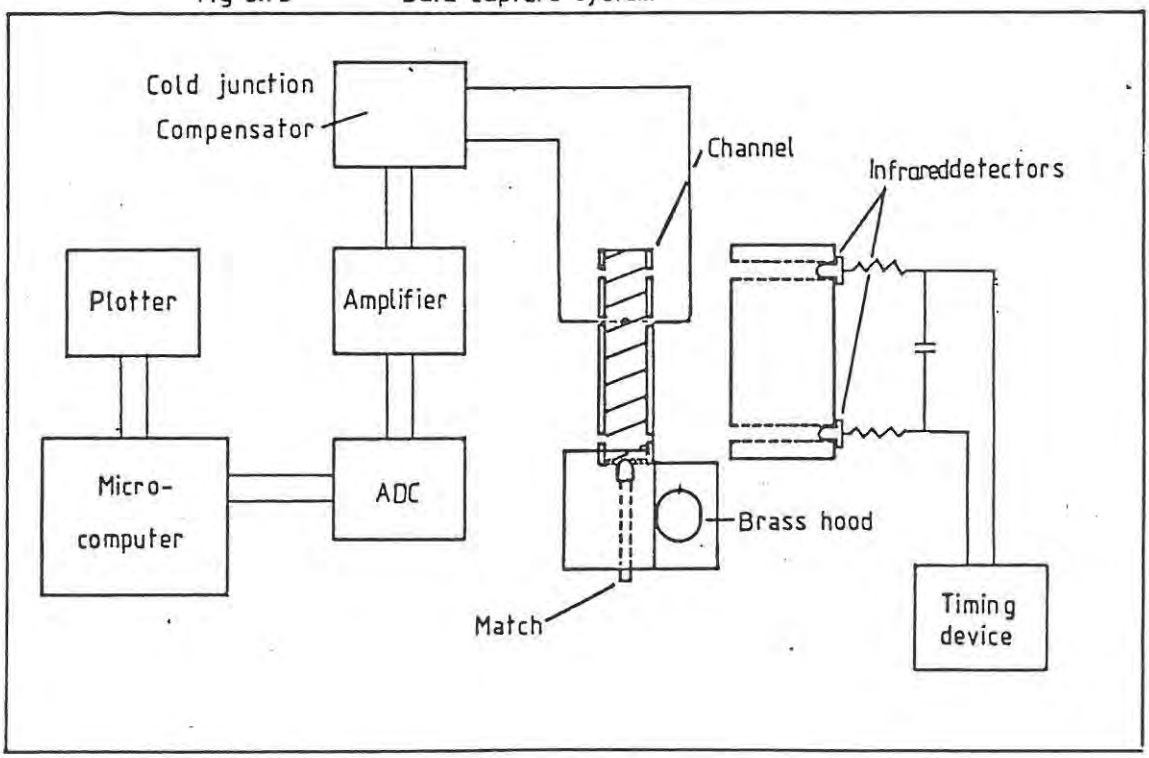

B. Data capture system. The output of the thermocouple was electronically referenced to a temperature of 20°C by a cold junction compensator (Figure 5.1 b). The signal was then amplified (about 253x) and recorded (minimum sampling interval 0.1 ms) using an IBM-compatible microcomputer (12-bit ADC, < 25 μs conversion time). The PASCAL software used to monitor the thermocouple output (PROFILE.PAS) is listed in the Appendix. This program was designed to capture 250 data points preceding a set trigger temperature (~70°C), and then to record up to 30 000 further data points. The buffer system allowed for the capture of essential pre-trigger information.

C. Numerical processing. The digital data, Y, were then converted to millivolt values, V, using the equation:

```
V = Y(resolution)/amplification
```

where the resolution was 2.441 mV for a 12-bit ADC for a monopolar 0 to 10 V range and the amplification was 253.3x. Temperature values were then assigned by using a polynomial of the 4th power based on the 1948 international temperature code (ref 52). The system was calibrated using the melting points of Pb (327.4°C) and Zn (419.6°C) and in all cases gave discrepancies between derived temperatures and fixed values of less than ~3%.

The original temperature profiles (a typical example for the 20% Mn/SrO_2 composition is shown in Figure 5.2) were smoothed using a BASIC program called MSPLINE.BAS (listed in the Appendix) which uses 12-point smoothing and is based on a program published by Ebert *et al* (ref 61). This smoothing produces negligible distortion of the profile (Figure 5.3), but was essential before differentiation (see below). The temperature profiles presented in this work are unsmoothed. After smoothing, the temperature-time data were imported into a spreadsheet (QUATRO) for further analysis.

Analyses have been carried out on individual temperature profiles and the results have been averaged. Attempts to obtain an "average" profile are difficult since there is no unique time-zero (see discussion in Section 1.3 B). For qualitative comparison of temperature profiles, adjustments in the time scales of the various profiles have been made.

5.2 ANALYSIS OF TEMPERATURE PROFILES

The theory for the analysis of temperature profiles has been described in Section 1.3. Figure 5.8 summarizes the procedures.

Fig 5.2 Raw profile

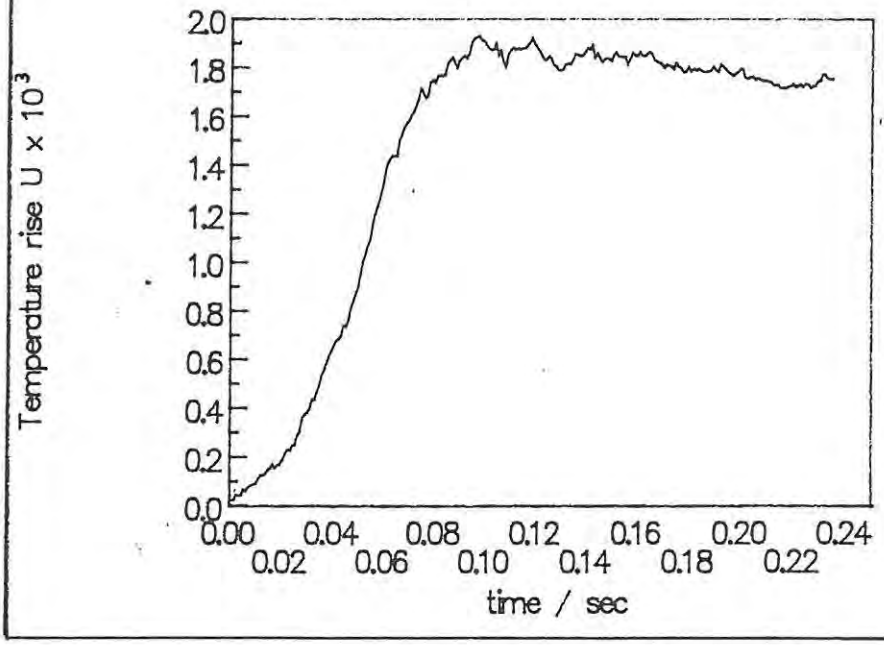

Fig 5.3 Profile (raw and smoothed)

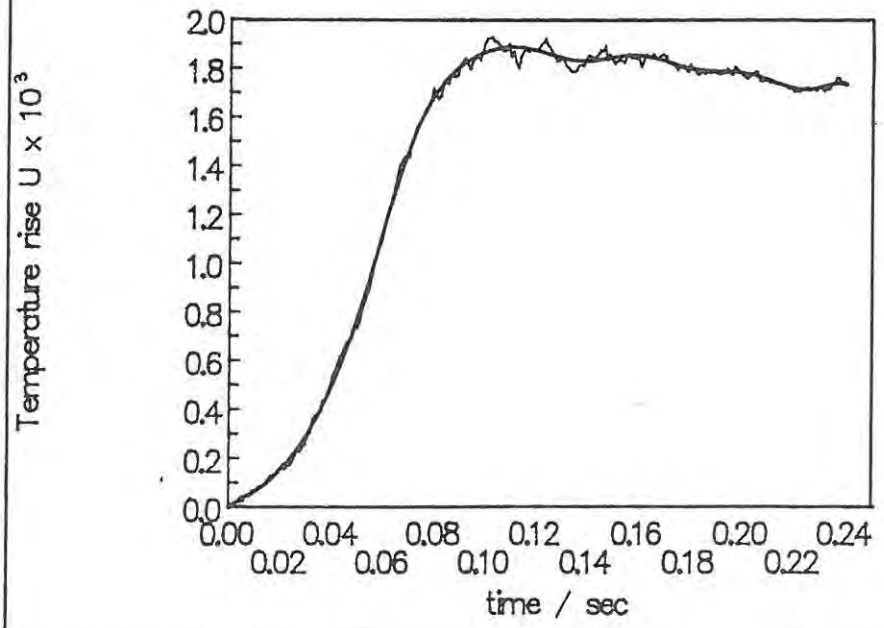

5.2.1 The rise time:

The rise time, t_r, or the corresponding S factor from the Hill analysis, where $t_r = 1/S$, was obtained from either:

(i) a plot of lnU against t (Figure 5.4) the slope of which is equal to $1/t_r$, or

(ii) extrapolation of a plot dU/U (dlnU or $d\theta/\theta$) against U (or θ) (Figure 5.5) to U (or θ) equal to zero.

Neither of these plots defines t_r very clearly, although in combination they suggest, for the profile chosen (Figure 5.3), a value of about 12 ± 1 ms.

Two further possibilities for finding a value for the rise time are to use non-linear regression to fit the data to an equation of the form:

(iii) `U = K(1) exp(K(2)t)`, or

(iv) `U = K(1) exp(K(2)t) + K(3)`

The optimization program NL.BAS, also based on a program published by Ebert *et al* (ref 61), was used and gave the following results:

(iii) $K(1) = 56.0 \pm 2.7$ K

$K(2) = 54.6 \pm 1.2$ s^{-1}

Assuming that $K(2) = 1/t_r$, then $t_r = 18.3$ ms (Figures 5.6 a and 5.6 b).

(iv) $K(1) = 150.8 \pm 3.6$ K

$K(2) = 37.0 \pm 0.4$ s^{-1}

$K(3) = -148.7 \pm 4.8$ K

and $t_r = 1/K(2) = 27.0$ ms (Figures 5.7 a and 5.7 b). Note that the fit was greatly improved, but the significance of K(1) and K(3) would have to be considered. Also the tendency was for the calculated curve to rise above the experimental curve while reaction superimposed on conduction would be expected to cause the opposite effect. The influence of the choice of t_r on the kinetic parameters derived from the analysis is discussed below.

5.2.2 Derivatives:

Values for the first derivatives are required for the Hill analysis, and for the first and second derivatives for the Leeds analysis (see flow diagram, Figure 5.8). These derivatives were obtained using the Savitsky-Golay method (with 9 points). The spreadsheet algorithm is given in Appendix B. The curves of dU/dt and d^2U/d^2t against t are shown in Figures 5.9 a and 5.9 b, respectively.

5.2.3 The decay time:

The decay time, t_d, from the Leeds approach, may be determined from the slope of lnU against t over the cooling section of the temperature profile. This decay time is generally much greater than the rise time and hence has only a small influence on the analysis.

Fig 5.4 Determination of the rise time (lnU vs time)

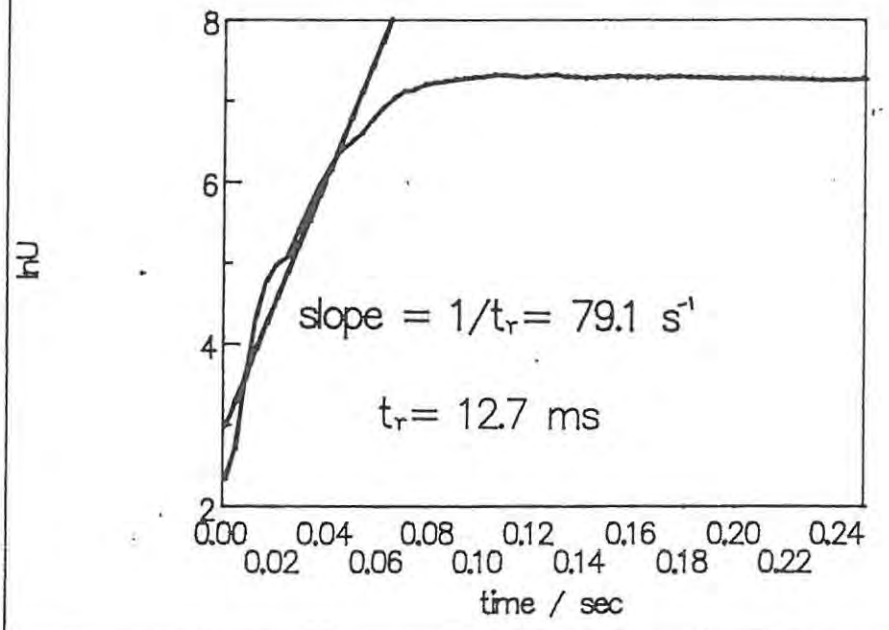

Fig 5.5 Determination of the S factor ({derivative of theta}/theta vs theta)

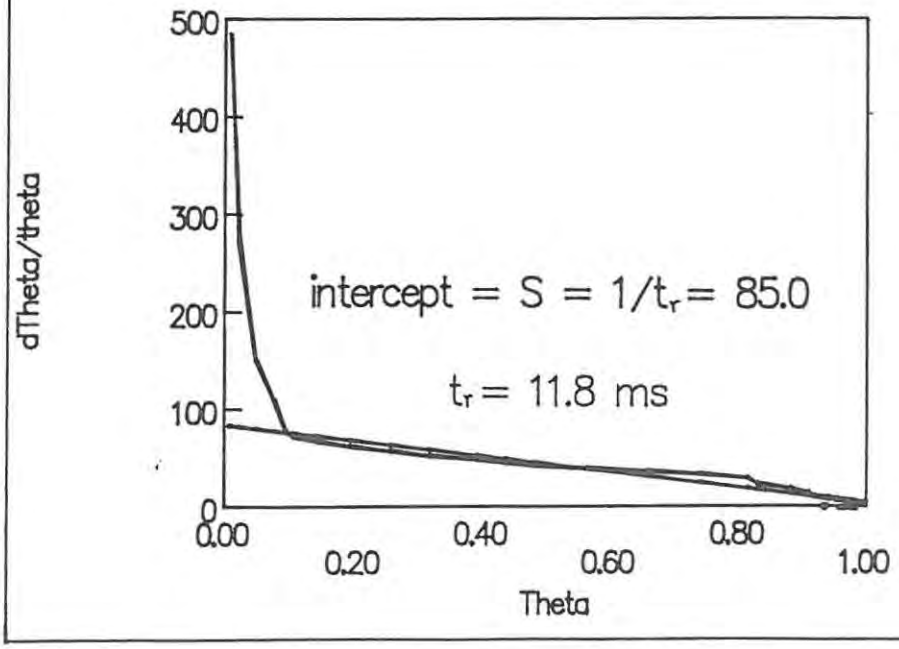

Fig 5.6a Profile, rise–time

t_r=0.01833 s, K(1)=56.02 K, K(2)=54.57 s^{-1}

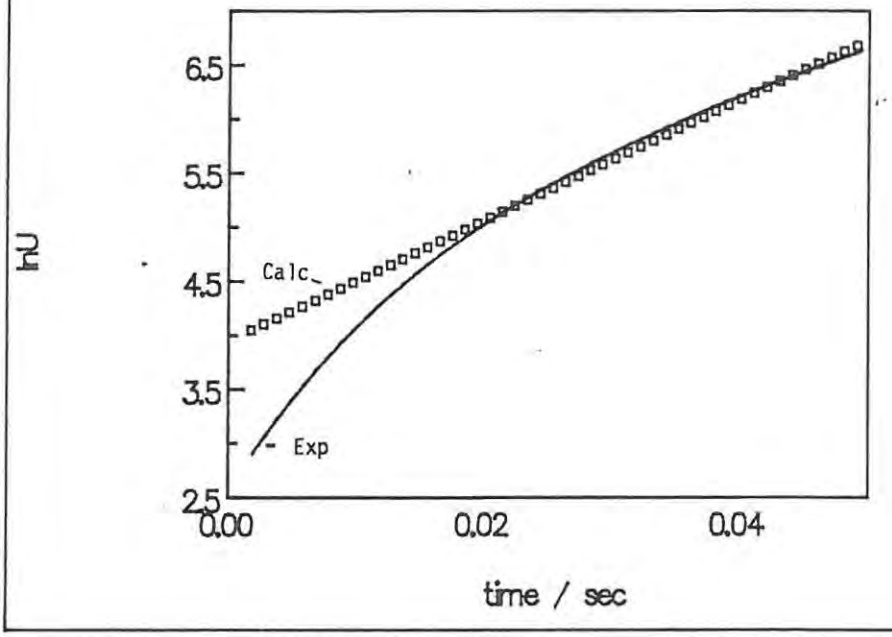

Fig 5.6b Profile, rise–time

t_r=0.01833 s, K(1)=56.02 K, K(2)=54.57 s^{-1}

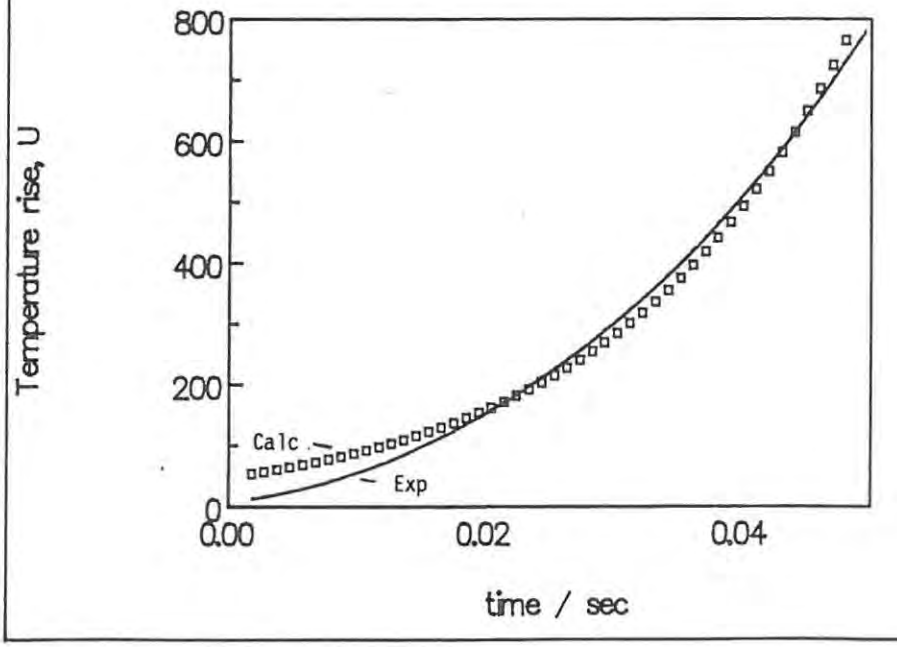

Fig 5.7a Profile, rise–time

t_r=0.02703 s, K(1)=150.4 K, K(3)=–148.2 K

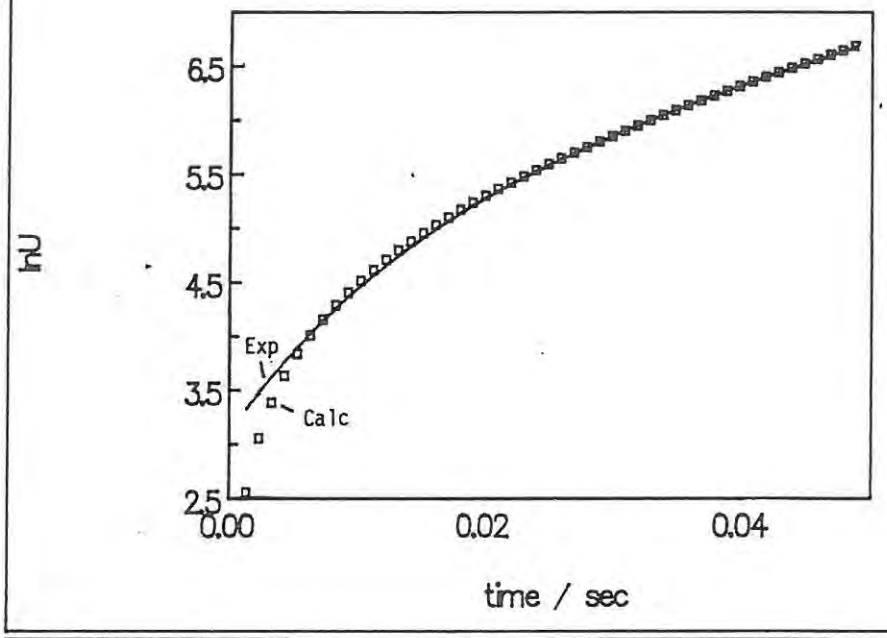

Fig 5.7b Profile, rise–time

t_r=0.02703 s, K(1)=150.4 K, K(3)=–148.2 K

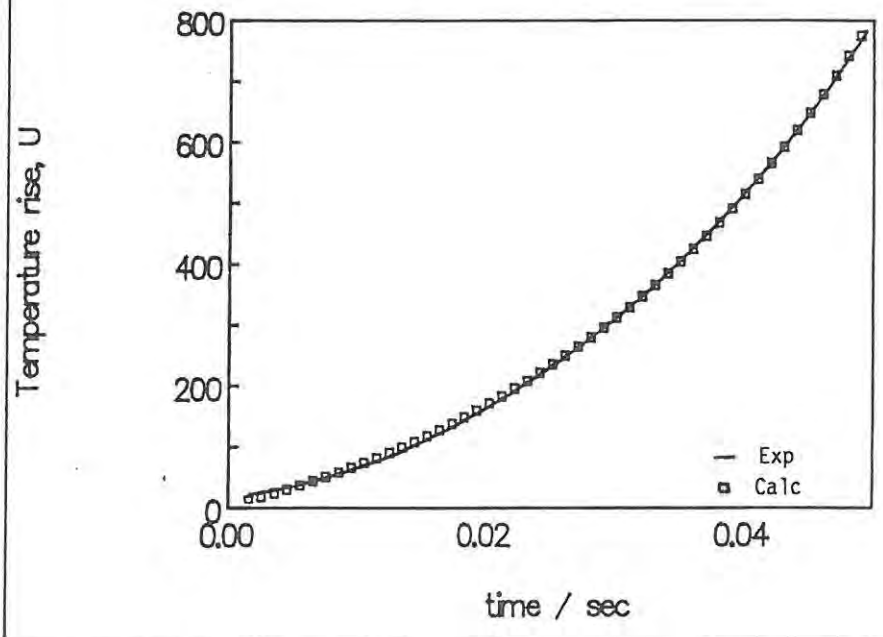

Fig 5. 8 Analysis of temperature profiles

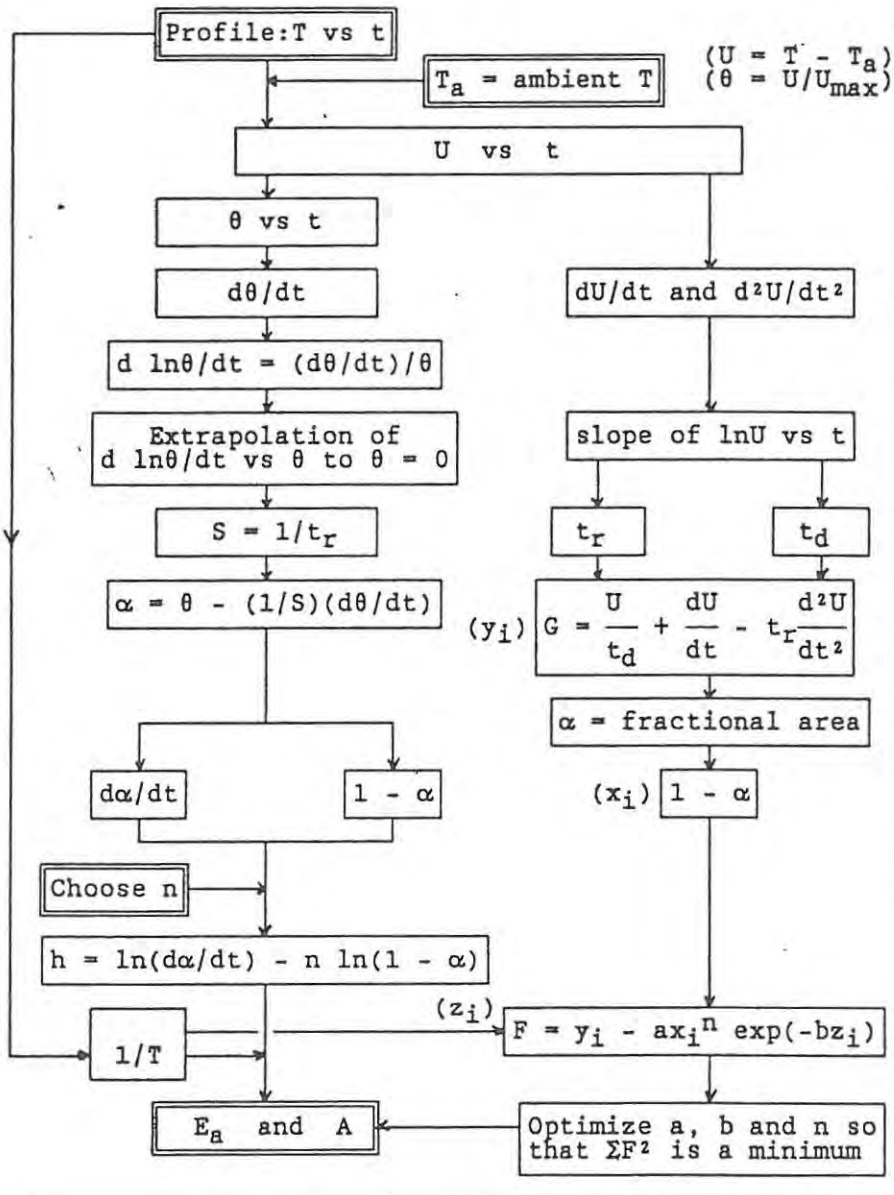

Fig 5.9a First derivative of profile shown in Figure 5.3

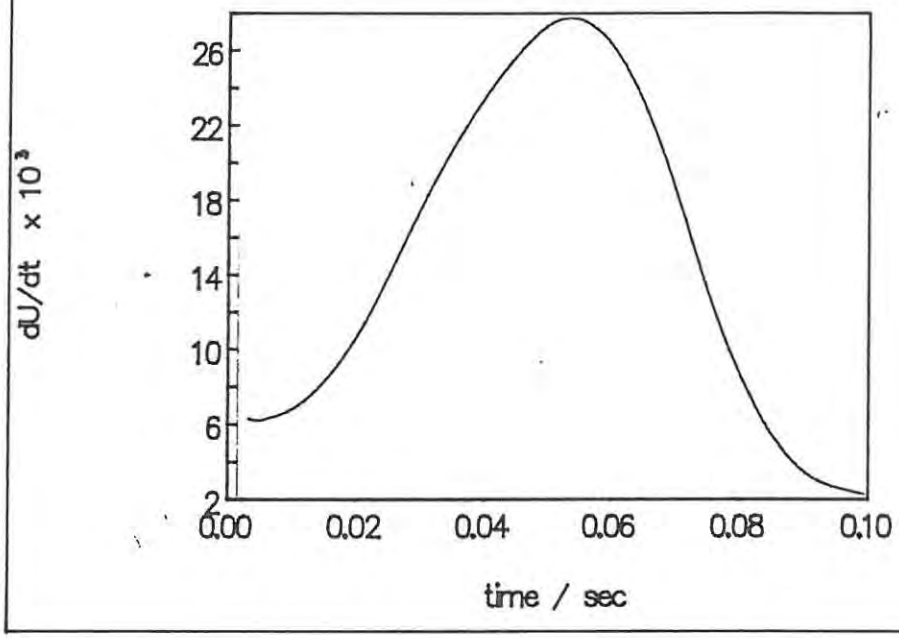

Fig 5.9b Second derivative of profile shown in Figure 5.3

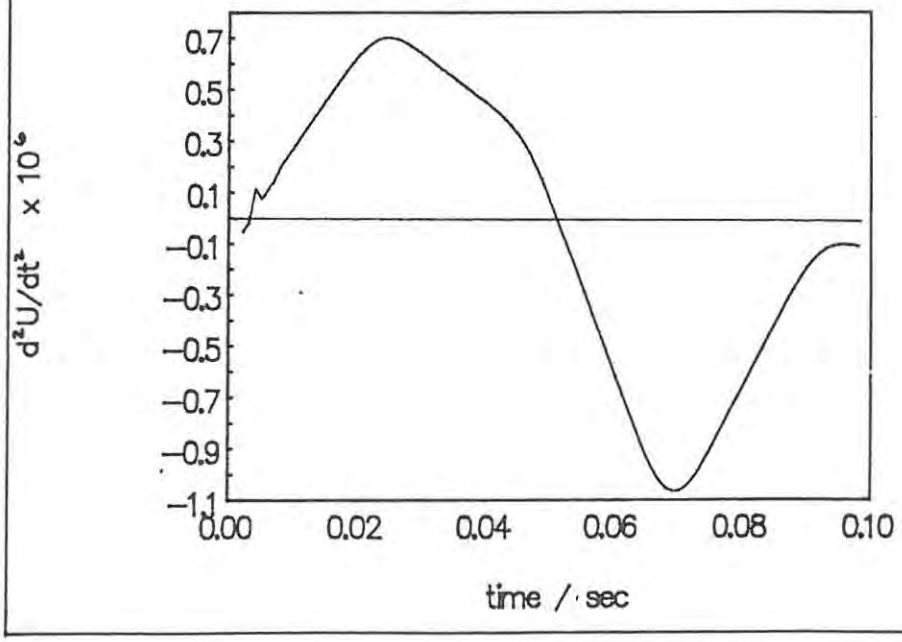

5.2.4 The power function:

The Leeds power function, G, where G is given by:

$$G = (U/t_d) + (dU/dt) - t_r(d^2U/dt^2)$$

lateral heat loss | overall rise | conduction

was calculated from the original profile and the derivative curves using the estimated values of t_r and t_d. The contributing terms are plotted on composite graphs for various values of t_r (Figures 5.10, 5.11 and 5.12).

5.2.5 The extent of reaction:

The value for the extent of reaction, α, is given in the Hill treatment by:

$$\alpha = \theta - t_r(d\theta/dt)$$

where $\theta = U/U_{max}$ and $t_r = 1/S$ and, in the Leeds treatment, from the partial areas under the curve of G against t. α,t and α,T curves for the same profile (T against t) obtained by the two treatments are shown in Figures 5.13 a and 5.13 b and 5.14 a and 5.14 b.

5.2.6 Arrhenius parameters:

The rate equation was assumed to be of the form:

$$d\alpha/dt = k(1 - \alpha)^n = A \exp(-E_a/RT) (1 - \alpha)^n$$

where n is the "order" of the reaction and A and E_a are the conventional Arrhenius parameters. In the Hill treatment the rate equation is rewritten as:

$$h(\alpha) = \ln(d\alpha/dt) - n \ln(1 - \alpha) = -(E_a/RT) + \ln A$$

Various values of n were selected and the linearity of the plots of $h(\alpha)$ against 1/T was examined. (The α,t curve has to be differentiated again to obtain $d\alpha/dt$ values). E_a and lnA values were then determined from the slope and intercept, respectively, of an acceptably linear plot, e.g. Figures 5.15, 5.16 and 5.17. The results for the chosen profile are given in Table 5.1.

TABLE 5.1 KINETIC PARAMETERS USING THE HILL TREATMENT*

n	E_a / kJ mol^{-1}	A
0.5	9.9 ± 0.2	67.6 ± 1.1
1	11.7 ± 0.1	94.1 ± 1.0
2	13.1 ± 0.2	141.6 ± 1.1

*For t_r = 12.7 ms

Fig 5.10 Power functions from profile shown in Figure 5.3, t_r=0.0056 s

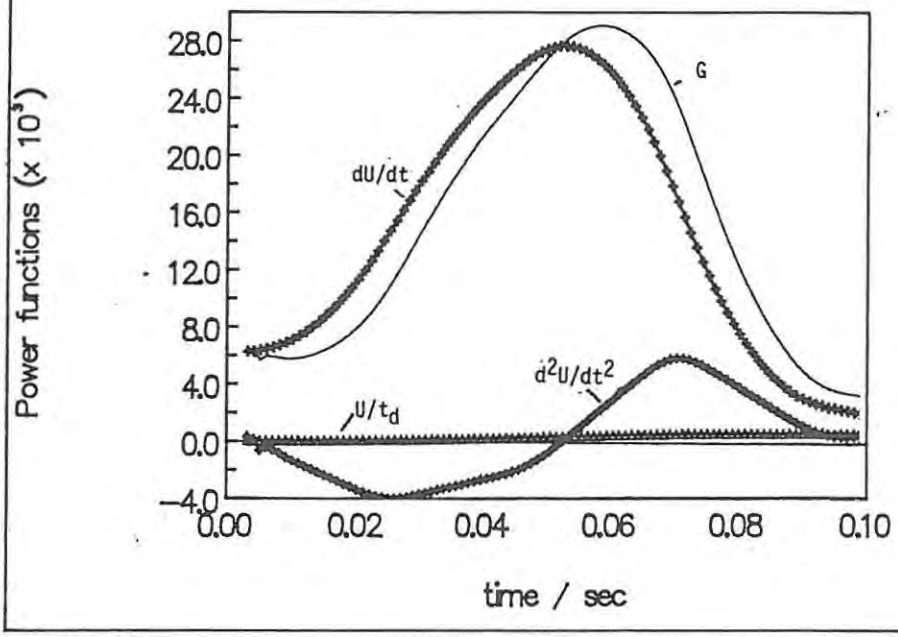

Fig 5.11 Power functions from profile shown in Figure 5.3, t_r=0.0133 s

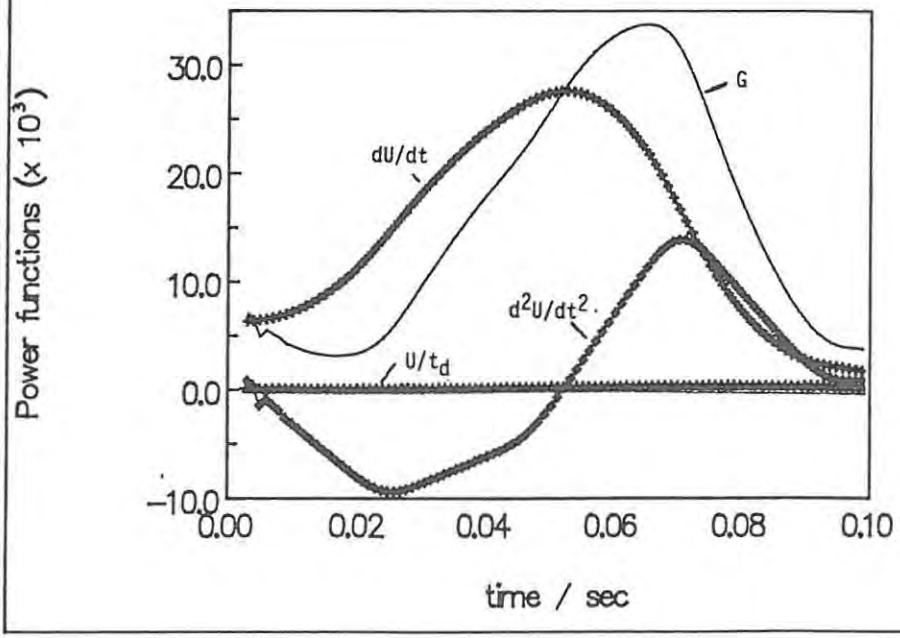

Fig 5.12 Power functions from profile shown in Figure 5.3, t_r= 0.025 s

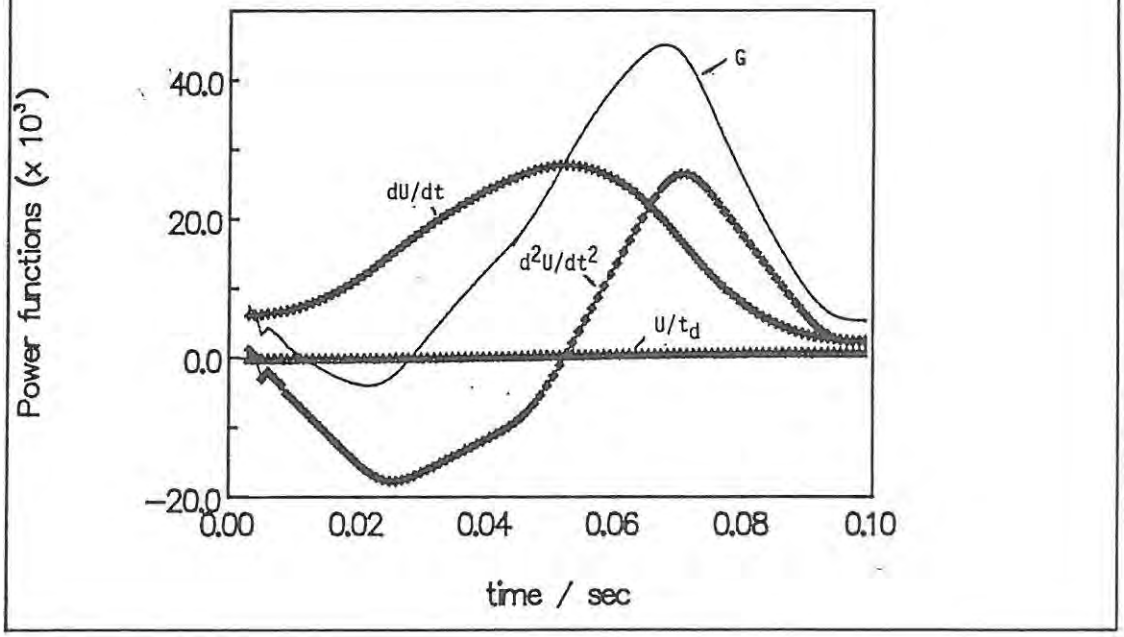

Fig 5.13a Comparison of alpha values

Rise time = 0.025 s

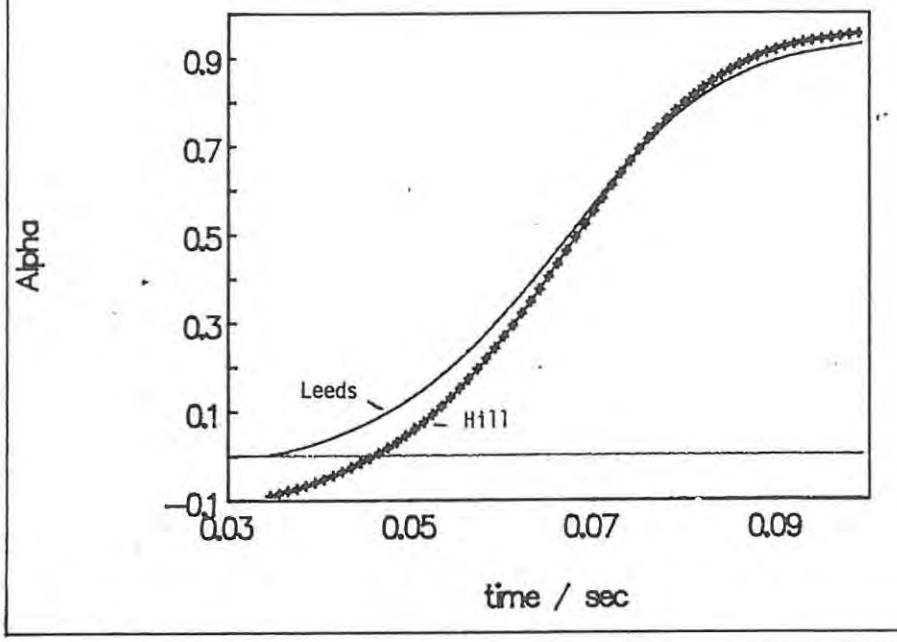

Fig 5.13b Comparison of alpha values

Rise time = 0.0133 s

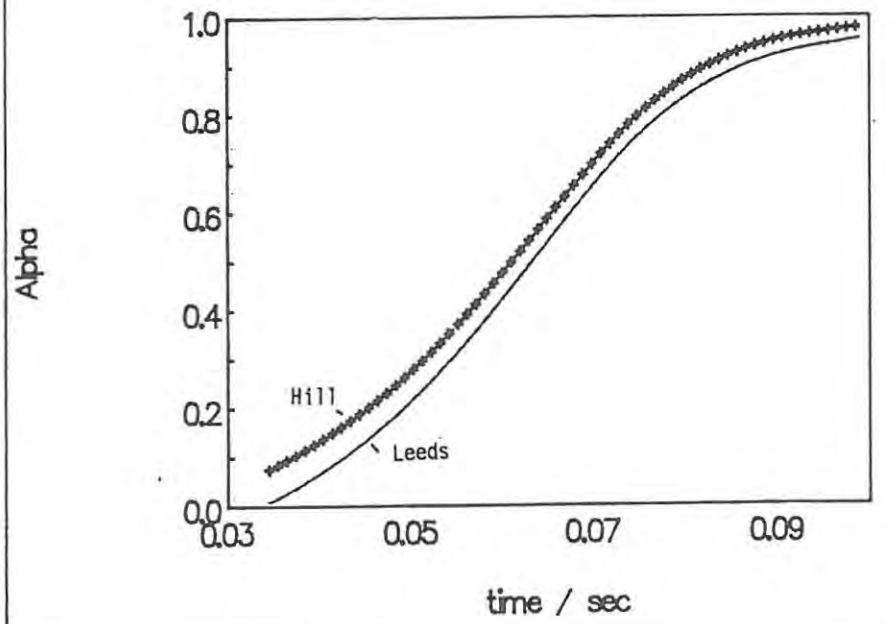

Fig 5.14a Comparison of alpha values

Rise time = 0.025 s

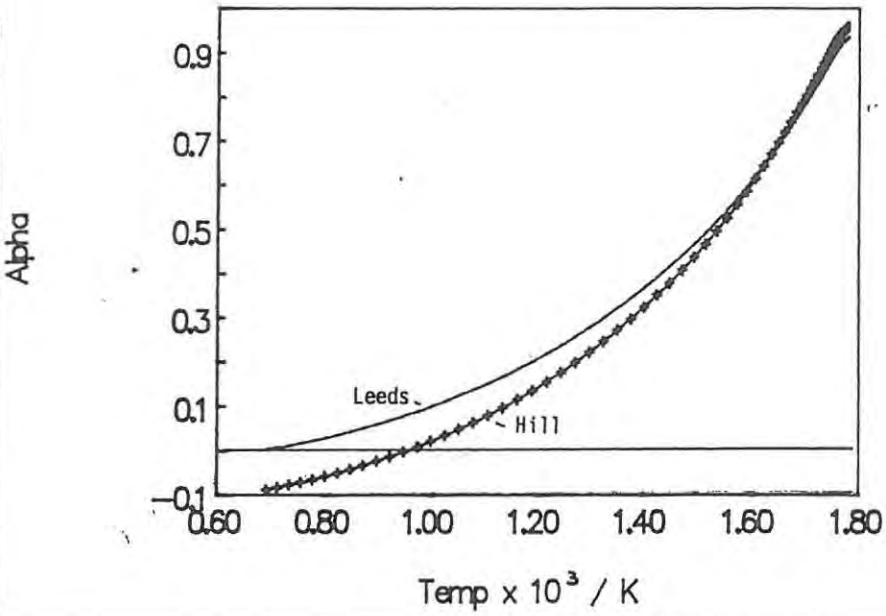

Fig 5.14b Comparison of alpha values

Rise time = 0.0133 s

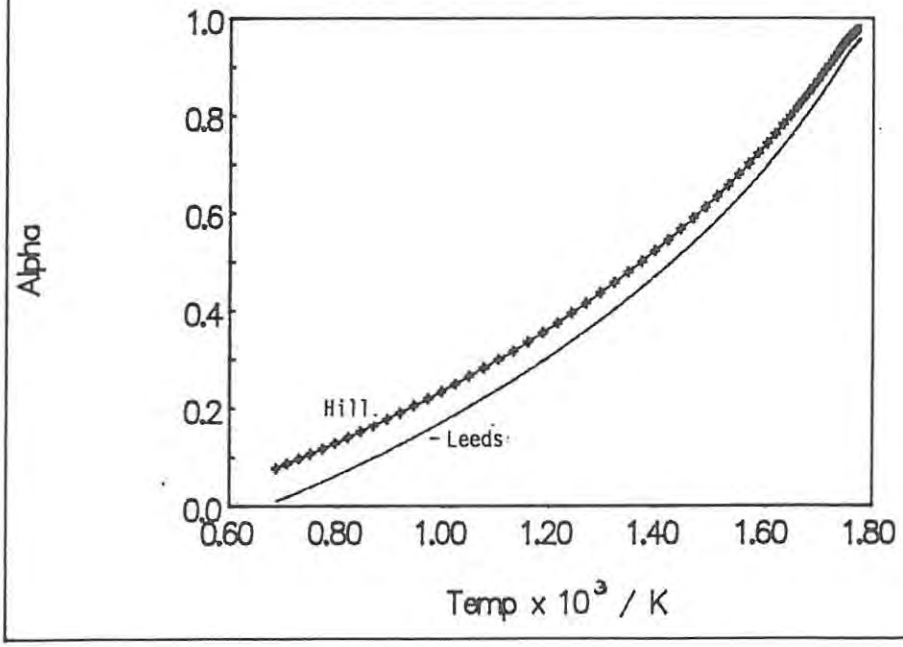

Fig 5.15 Kinetic parameters
Hill treatment (n = 0.5)

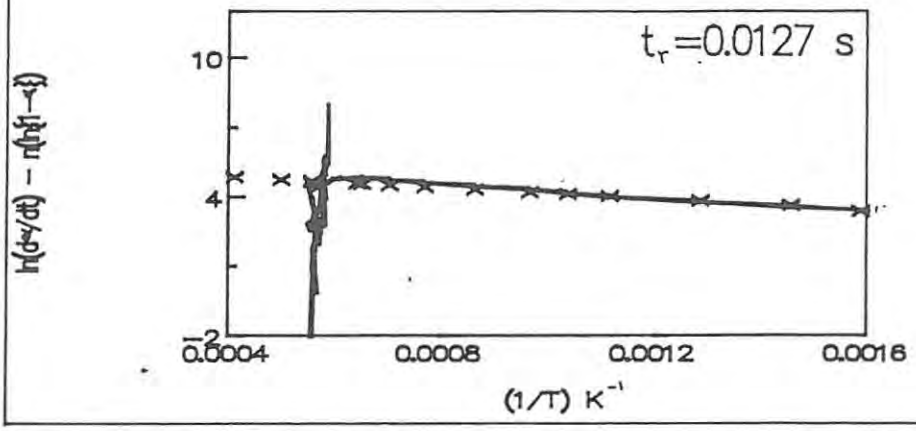

Fig 5.16 Kinetic parameters
Hill treatment (n = 1)

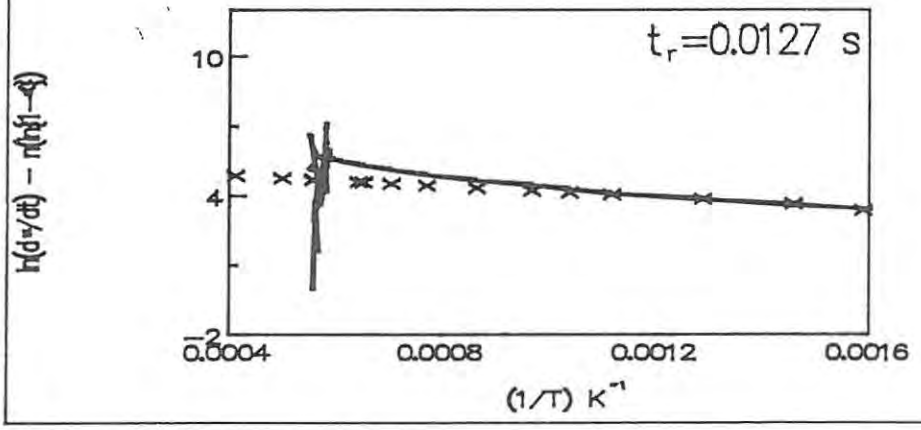

Fig 5.17 Kinetic parameters
Hill treatment (n = 2)

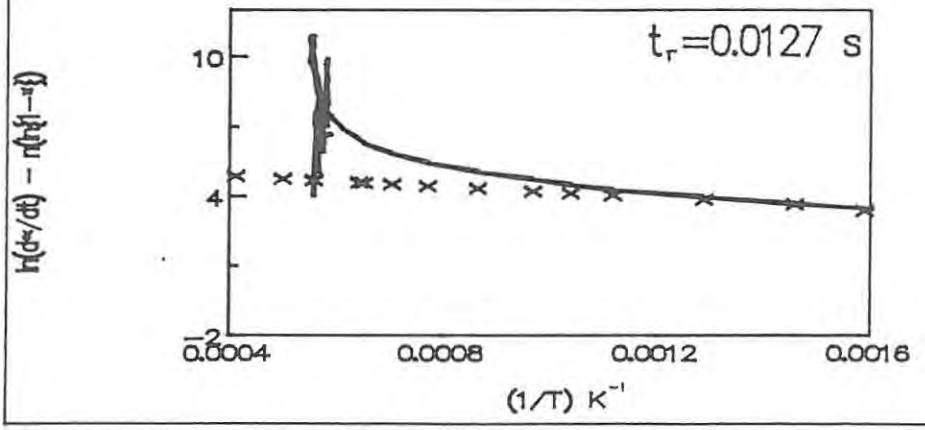

In the Leeds treatment, the values of G are proportional to $d\alpha/dt$:

$$G = U_{ad}(d\alpha/dt)$$

So the rate equation may be written as:

$$G = U_{ad}\, A(1-\alpha)^n \exp(-E_a/RT)$$

The measured quantities were values of G_i and α_i at temperatures T_i. U_{ad} was also obtainable independently from the profiles. The unknowns were thus n, A and E_a. The problem then was to adjust the values of n, A and E_a so that the sum of the squares of the differences:

$$\Sigma \{(G_{exp})_i - (G_{calc})_i\}^2$$

was a minimum. Boddington *et al* (refs 23, 24) used the NAG (Numerical Algorithms Group) routine EO4 FCF for this optimization.

To simplify the problem, the substitutions:

$$y_i = (G_{exp})_i;\ x_i = 1 - \alpha_i;\ z_i = 1/T_i;\ a = U_{ad}A \text{ and } b = E_a/R$$

were made and

$$f = y_i - a(x_i)^n \exp(-bz_i) \qquad \text{——— } 5.1$$

a, n and b were then adjusted so that ΣF^2 was a minimum. Two BMDP (ref 62) routines were used:

(i) BMDP1R based on the linear regression of the natural logarithm form of equation 5.1 above, and

(ii) BMDP3R based on non-linear regression.

The procedures for running these routines on a CYBER mainframe computer are given in the Appendix.

The output from BMDP1R was used as the initial guess for BMDP3R. Plots of G_{exp}, G_{calc} and the residual (G_{calc} - G_{exp}) are given in Figures 5.18 and 5.19. The kinetic parameters obtained from these optimizations, using different values of t_r are given in Table 5.2.

TABLE 5.2 KINETIC PARAMETERS USING THE LEEDS TREATMENT

t_r / s	BMDP	a x 10^3	b	n	E_a / kJ mol^{-1}	A
0.01	L	106.1	1342 ± 20	0.35 ± 0.01	11.2 ± 0.2	65.5
	NL					
0.0133	L	150.7	1698 ± 29	0.45 ± 0.01	14.1 ± 0.2	93.0
	NL	175.9 ± 6.7	1841 ± 39	0.47 ± 0.01	15.3 ± 0.3	105.6 ± 7.1
0.02	L	545.4	3104 ± 144	0.66 ± 0.04	25.8 ± 1.2	336.7
	NL	415.0 ± 27.3	2829 ± 74	0.61 ± 0.02	23.5 ± 0.6	256.2 ± 16.8
0.025	L	611.3	3301 ± 101	0.67 ± 0.02	27.4 ± 0.8	377.3
	NL	795.5 ± 74.3	3617 ± 112	0.70 ± 0.02	30.1 ± 0.9	491.0 ± 45.9
0.02703	L	801.9	3634 ± 122	0.70 ± 0.03	30.2 ± 1.0	495.0
	NL	1027.0 ±112.0	3931 ± 133	0.73 ± 0.08	32.7 ± 1.1	634.0 ± 69.1

Fig 5.18 G test, linear form t_r=0.0133 s

a=150655.3, b=1698.243, n=0.4506

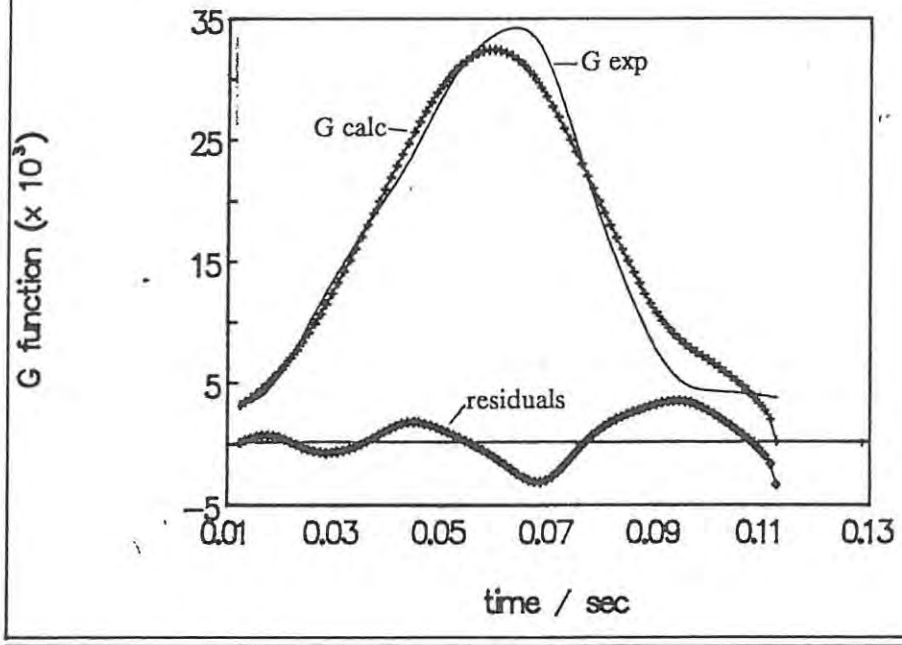

Fig 5.19 G test, non linear form t_r=0.0133 s

a=175906.9, b=1641.26, n=0.4724

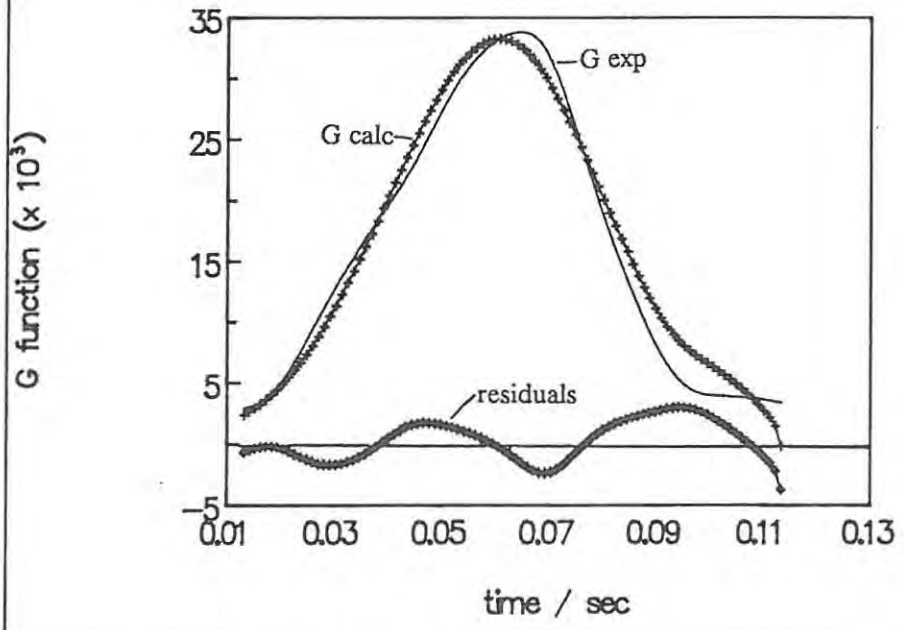

The value of E_a derived increased approximately linearly as the value of t_r used increased, although the value of n was also changing. There was also a "compensation"-type relationship between lnA and E_a.

5.3 ADDITIONAL EXPERIMENTS

A series of experiments was conducted, in which the two oxidants, BaO_2 and SrO_2, were placed individually in air in a pre-heated convection oven before being mixed with the appropriate fuel. The temperature of the oven was 425 ± 20°C for the heating of BaO_2, and 520 ± 10°C for SrO_2 samples. After heating for about one hour, the oxidants were treated in two different ways. The one treatment allowed the oxidants to cool in air over silica gel followed by normal preparation and mixing (see Sections 3.1 and 3.2), also in air. The other treatment involved cooling of the oxidants and complete preparation, except compression, in an atmosphere of nitrogen, over silica gel.

Another series of experiments was conducted to establish the temperature at which each of the four binary systems would ignite and burn completely, within a time period of 10 minutes. The loaded channel, containing 40% compositions, was placed in air in a pre-heated convection oven for a period of 10 ± 1 minutes. If this heat treatment did not ignite the mixture, it was then cooled to room temperature (for about 20 minutes) in air over silica gel. Normal experimental conditions were then used to record a temperature profile and linear burning rate of the combustion of the mixture in the channel. The procedure was repeated three times, for each of the four systems, at the following pre-combustion temperatures; 140 ± 10°C, 220 ± 10°C, 300 ± 10°C, 360 ± 10°C and 420 ± 10°C.

5.4 RESULTS FOR BINARY SYSTEMS

5.4.1 Reaction products:

For all four binary pyrotechnic systems, compositions could be prepared which burnt under the experimental conditions described in Section 3.2. The solid residues of these reactions were examined using X-ray powder diffraction (XRD) and infrared (IR) spectroscopy. The full details of these analyses are given in Chapter 8, but the more important results are discussed below.

In addition to unreacted starting materials, the solid residues contained a complex mixture of metal oxides. The metal:oxygen ratio of these oxides was determined by the amount of fuel present in the unreacted composition. The residues from the combustion of the Mn/BaO_2 system in particular, were in the form of a manganese spinel with the formula $MnO.Mn_2O_3$. The residues from the mixtures containing Mo, especially from the Mo/BaO_2 system, tended to absorb water on cooling to form hydroxides. The presence of molybdates was observed in the XRD patterns of the two Mo containing

systems. Molybdates could be formed directly or, more probably, in secondary reactions (refs 63, 64, ref 1220 in 65):

$$AO(s) + Mo\ oxide(s) \rightarrow AMoO_4(s)$$

where A = Ba or Sr. Table 5.3 lists the compounds that were positively identified by the XRD and IR analyses.

TABLE 5.3 PRODUCTS OF PYROTECHNIC REACTIONS

SYSTEM	PRODUCTS IDENTIFIED
Mn/BaO_2	$MnO.Mn_2O_3$ (i.e. Mn_3O_4), MnO_2, BaO
Mo/BaO_2	MoO_2, MoO_3, $BaMoO_4$, $Mo_5O_7(OH)_8$, BaO
Mn/SrO_2	MnO, Mn_2O_3, SrO
Mo/SrO_2	MoO_2, Mo_9O_{26}, $SrMoO_4$, SrO

To determine whether significant quantities of gas were produced by the pyrotechnic reactions of the four binary systems, the mass-losses during combustion were recorded (cooling was done in air over silica gel) and the results are recorded in Table 5.4. The mass losses may include some small loss of solid material ejected from the channel by the vigorous reactions.

TABLE 5.4 PERCENTAGE MASS LOSS DURING COMBUSTION OF 40% COMPOSITIONS OF ALL FOUR SYSTEMS

SYSTEM	MASS LOSS / %
Mn/BaO_2	10.4 ± 3.7
Mo/BaO_2	6.1 ± 1.7
Mn/SrO_2	16.0 ± 0.1
Mo/SrO_2	1.8 ± 0.9

5.4.2 Linear burning rates:

A. Effects of composition. The range of compositions which sustained combustion in the standard stainless-steel channel varied from system to system, as shown Table 5.5. The ranges of measured burning rates, v_{obs}, and maximum excess temperature rises, U_{max} (where $U = T - T_a$ and T_a is the ambient temperature), for these compositions are also given in Table 5.5.

TABLE 5.5 RANGE OF COMPOSITIONS WHICH SUSTAINED COMBUSTION *

SYSTEM	COMPOSITION / %	v_{obs} / mm s^{-1}	U_{max} / °C
Mn/BaO_2	15 ... 65	1.7 ... 11.7	700 ...> 1760
Mo/BaO_2	20 ... 70	2.7 ... 10.1	857 ... 1708
Mn/SrO_2	20 ... 80	4.5 ... 12.3	620 ... 1733
Mo/SrO_2	40 ... 45	2.2 ... 2.3	1410 ... 1601

* Under the same set of experimental conditions, i.e. mixing by end-over-end tumbling and 50 MPa compaction.

The fairly large standard deviations of the measured burning rates were caused by the usual problems of reproducibility of mixing and preparation. In addition, errors may have been caused by the expulsion of the last portion of the unreacted composition by small amounts of expanding gas. This expulsion can

cause premature triggering of the "stop" circuit (Figure 5.1 b). This error is particularly noticeable in the faster burning compositions of Mn/BaO_2 and Mo/BaO_2.

Mixtures containing the BDH samples of BaO_2 either would not burn or burnt erratically, despite the fact that the particle-size range (Table 5.8) and particle-shape (see Chapter 8) of this sample were similar to that of the Merck sample. Scanning electron microscopy (Chapter 8), however, did reveal the presence of small needle-like crystal structures on the BDH sample which were not present on the Merck sample. These crystals are thought to be formed by the exposure of the aged BDH sample of BaO_2 to a moist atmosphere which promotes (refs 8, 10, 29, 53) the production of a surface layer of $BaCO_3$. Chemical analysis (Table 3.1) confirmed this suggestion by showing that the BDH sample contained about 10% less peroxide than the Merck sample, while XRD and IR analyses (Chapter 8) indicated the presence of $BaCO_3$ and $Ba(OH)_2$ in both samples of BaO_2.

The composition of all four binary pyrotechnic systems had an effect on the burning rates of the mixtures. These effects are shown in the plots of the burning rate, v_{obs}, against composition (i.e. percentage fuel) in Figure 5.20 a for the two BaO_2 systems and in Figure 5.20 b for the two SrO_2 systems. Where available, literature values are included for comparison. Figures 5.21 a and 5.21 b compare the burning rates as a function of composition for the two systems containing Mn and Mo, respectively. These figures show that the burning rates pass through a maximum at a different composition for each system (Table 5.6).

TABLE 5.6 COMPOSITIONS WHICH GAVE MAXIMUM BURNING RATE*

SYSTEM	COMPOSITION / %	v_{max} / mm s^{-1}
Mn/BaO_2	20	11.7
Mo/BaO_2	45	10.1
Mn/SrO_2	75	12.3
Mo/SrO_2	40	2.3

* Under the same set of experimental conditions.

Values of burning rates calculated from temperature profiles (see Section 1.3) are compared with these experimental values in Sections 9.1.2 and 9.2.2.

B. Effect of compaction. Compaction of the sample affected the burning of all four pyrotechnic systems. The density and the void fraction of each of the four systems changed as the pressure used during

compaction was increased from 0 to 250 MPa in 50 MPa steps (Table 5.7). These physical alterations caused a change in the burning rate of all four systems.

TABLE 5.7 DENSITY AND VOID FRACTIONS

PRESSURE /MPa	DENSITY / g cm^3	VOID FRACTION	PRESSURE /MPa	DENSITY / g cm^3	VOID FRACTION
25% Mn/BaO_2			30% Mo/BaO_2		
0	3.53 ± 0.18	0.42	0	3.87 ± 0.07	0.45
50	4.18 ± 0.11	0.32	50	4.60 ± 0.31	0.41
100	4.57 ± 0.24	0.25	100	5.13 ± 0.26	0.27
150	5.13 ± 0.12	0.16	150	5.36 ± 0.10	0.24
250	5.23 ± 0.27	0.14			
20% Mn/SrO_2			40% Mo/SrO_2		
0	1.24 ± 0.27	0.76	0	1.56 ± 0.02	0.78
50	2.51 ± 0.08	0.52	50	3.34 ± 0.10	0.52
100	2.78 ± 0.31	0.47	100	3.45 ± 0.37	0.50
250	3.49 ± 0.16	0.34	250	4.10 ± 0.20	0.41

The relationship between the mass burning rate, with units of g s^{-1}, and the loading compression (Figure 5.22) has been used as an indication of the nature of the pyrotechnic reaction (ref 5). Figure 5.22 shows that the mass burning rate increases with compaction for all four binary systems. Such behaviour has been used as evidence of occurrence of solid-solid reactions, but other interpretations are discussed in Section 9.2. The increase of the mass burning rate in the two BaO_2 systems is proportionally much greater than the corresponding increase for the two SrO_2 systems, which might indicate that different reaction mechanisms are active. The plot of mass burning rate against compaction for the Mo/BaO_2 system clearly indicates that there exists a compaction beyond which the mass burning rate does not increase.

C. Effect of particle-size. The effect of the particle-size of both constituents on the burning of the binary pyrotechnic mixtures was examined. Particle-size (diameter) ranges and surface areas were determined as described in Section 3.1 A and the results are summarized in Table 5.8.

TABLE 5.8 PARTICLE SIZES OF CONSTITUENTS OF ALL FOUR SYSTEMS

MATERIAL	SURFACE AREA / m^2 kg^{-1}	NUMBER OF MODES	90^{th} QUARTILE / μm	10^{th} QUARTILE / μm	MEDIAN / μm
Mn large	8.0	1	167.1	80.7	112.6
Mn small*	85	1	40.5	4.9	16.6
Mo large	9.3	1	83.6	50.4	64.0
Mo medium*	19	1	57.1	19.9	34.4
Mo small	64	1	30.5	5.4	13.8
BaO_2 large*	62	1	80.2	11.9	36.6
BaO_2 small	800	2	24.1	0.4	10.2
BaO_2 (BDH)	490	2	58.2	1.5	24.1
SrO_2 large*	1370	3	15.3	0.3	3.5
SrO_2 small	1300	3	31.7	0.3	3.0

* These are the standard particle-sizes which are used throughout this work, unless stated otherwise.

Fig 5.20a Burning rate vs composition for the two BaO_2 systems

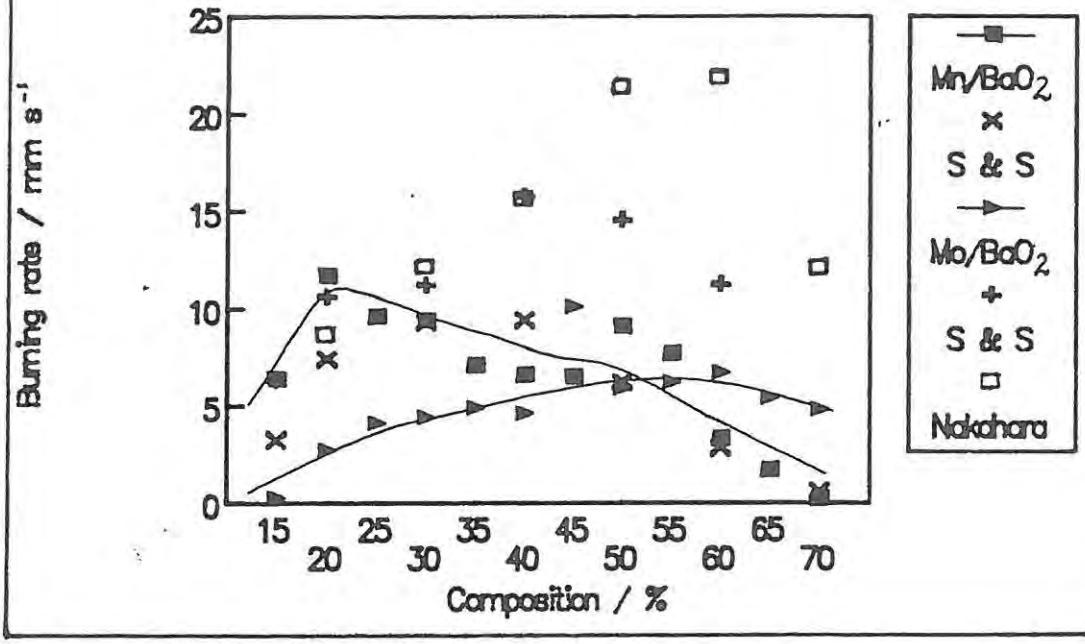

Fig 5.20b Burning rate vs composition for the two SrO_2 systems

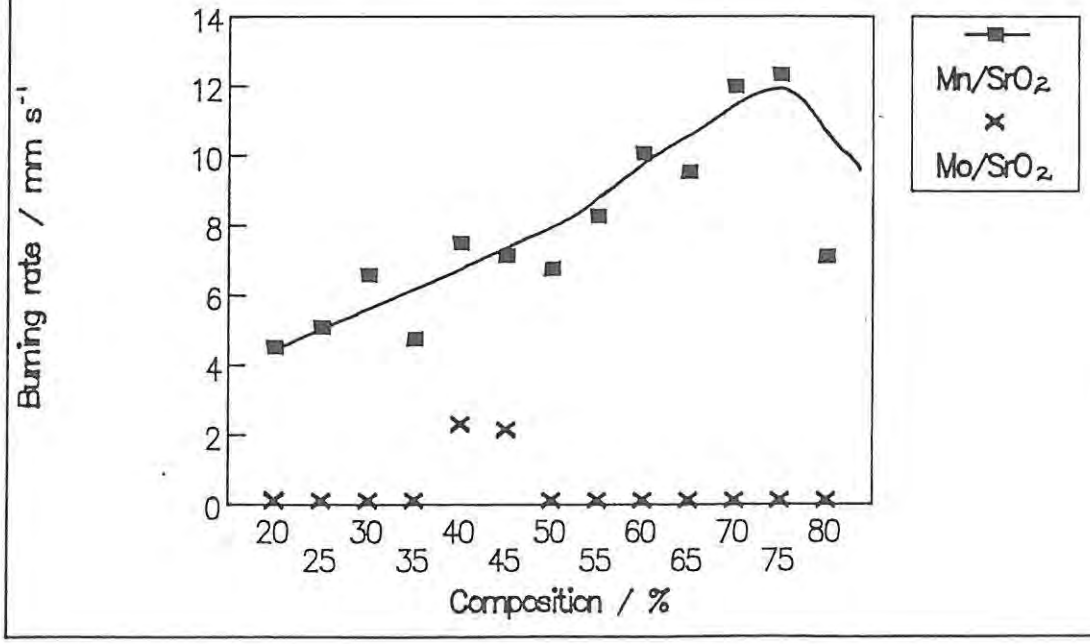

Fig 5.21a Burning rate vs composition for the two Mn systems

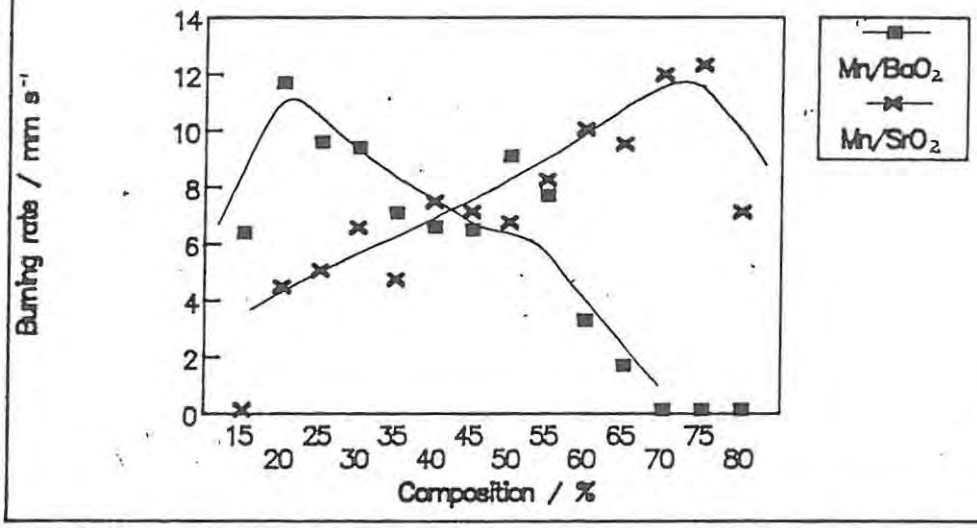

Fig 5.21b Burning rate vs composition for the two Mo systems

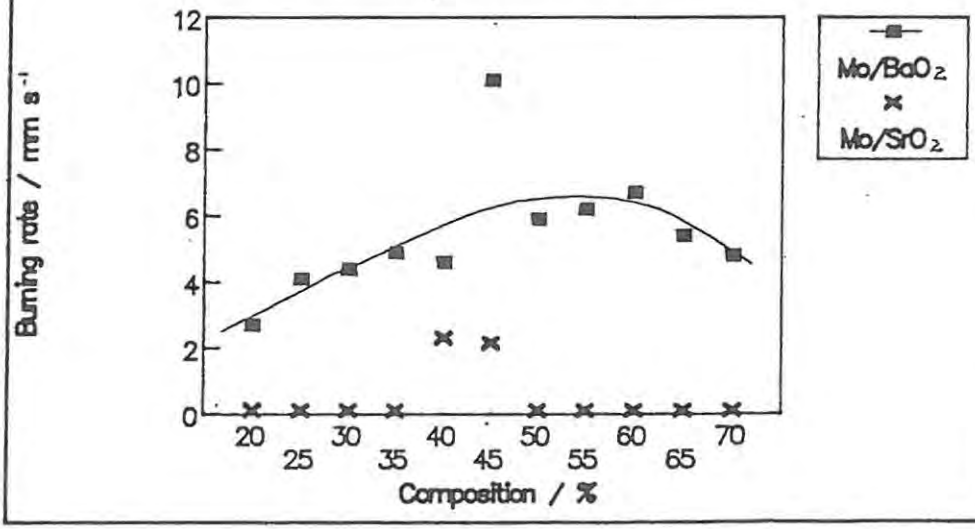

Fig 5.22 Effect of compression on the mass burning rate

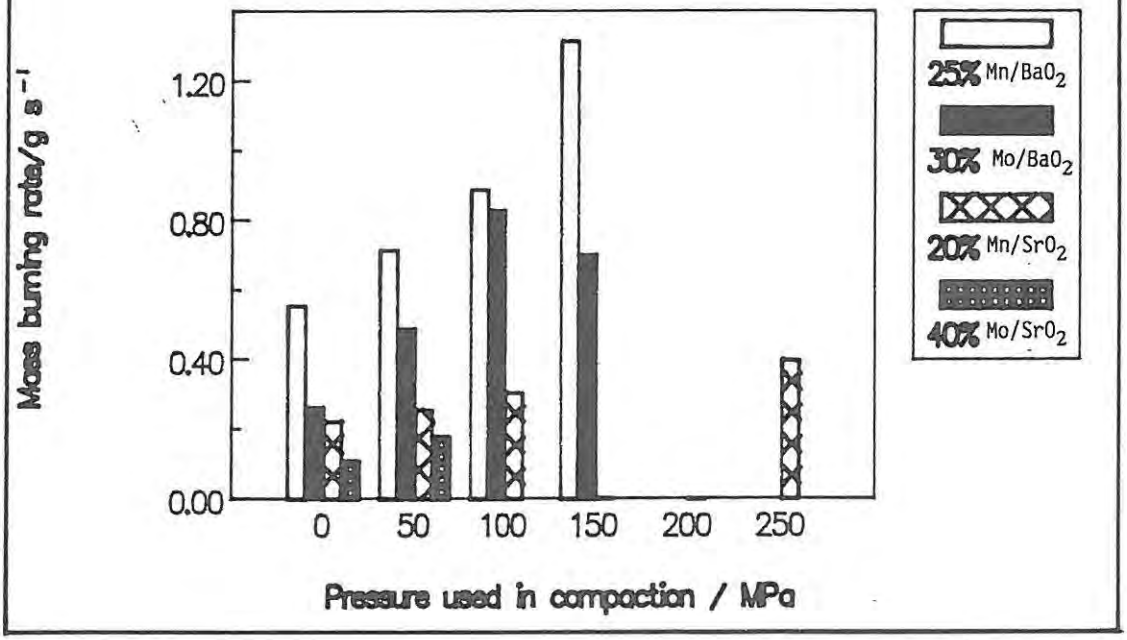

Fuels. Two particle-size ranges of Mn metal (Table 5.8) were commercially available and these were mixed individually with the standard particle-size of both oxidants (see the footnote to Table 5.8). The smaller particle-size range of Mn produced compositions in both systems (i.e. 50% Mn/BaO_2 and 20% Mn/SrO_2) which sustained combustion, but the larger particle-size range of Mn produced mixtures in both systems which did not sustain burning. The three particle-size ranges of Mo metal which were commercially available were also mixed individually with the standard particle-size oxidants. The two smaller ranges produced mixtures which sustained burning in both systems (i.e. 50% Mo/BaO_2 and 40% Mo/SrO_2), but both mixtures made using the larger particle-size range of Mo would not burn. The linear burning rates and the maximum excess temperatures, for the mixtures which sustained combustion, were affected by the particle-size of the fuel as shown in Table 5.11.

TABLE 5.9 EFFECT OF Mo PARTICLE-SIZE ON v_{obs} AND U_{max}

SYSTEM	v_{obs} / mm s^{-1}	U_{max} / °C
Mo(medium)/BaO_2	5.9 ± 0.2	1385 ± 65
Mo(small)/BaO_2	12.9 ± 1.2	1457 ± 66
Mo(medium)/SrO_2	2.3 ± 0.1	1502 ± 99
Mo(small)/SrO_2	5.8 ± 0.6	1480 ± 156

Oxidants. Two particle-size ranges for each oxidant were prepared (Table 5.8) by passing the oxidants through successively smaller sieves. These samples of oxidant were mixed with the standard particle-size (see the footnote to Table 8) of the fuels and burnt in the channel. Within the limits of the reproducibility, neither the burning rate nor the maximum excess temperature were significantly different for the mixture with the smaller particle-size range of oxidant in any of the four pyrotechnic systems.

Mixing. Differences in mixing procedures (see Section 3.1 D) produced no observable changes in the burning rates or maximum excess temperatures, of all four systems.

5.4.3 Temperature profiles:

A. Effect of composition. Temperature profiles for various compositions for all four binary systems were recorded using the thermocouple technique described in Section 5.1.2. A representative temperature profile (recorded during the combustion of the 25% composition of Mn/SrO_2) is reproduced in Figure 5.23 to illustrate the general features of profiles. Profiles are generally of sigmoidal appearance. Although all features of the profile are important, particular attention is focused on the rise zone, the maximum temperature and the cooling zone.

Fig 5.23 A typical temperature profile (e.g. 25% Mn/SrO_2)

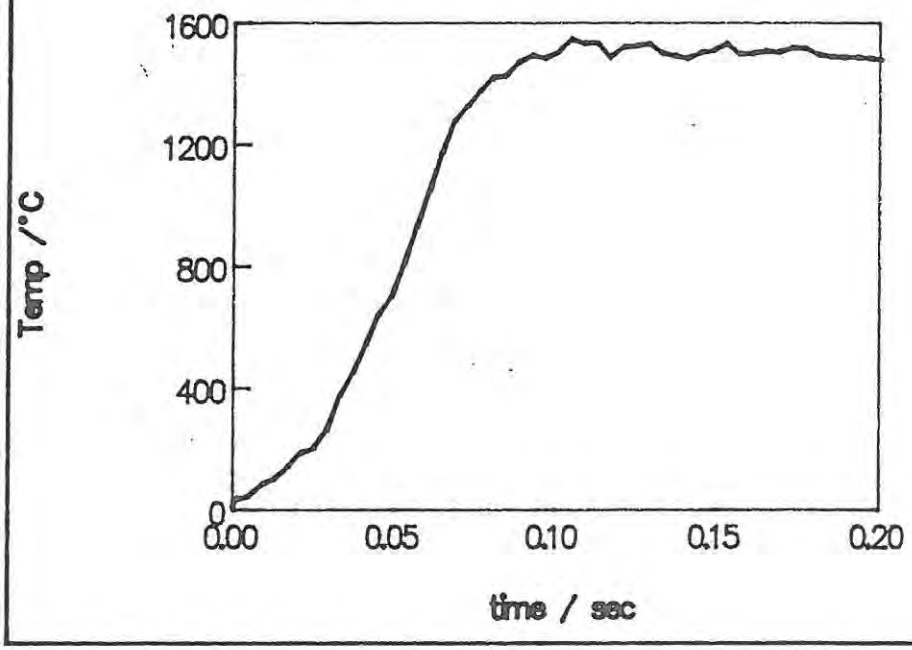

It was difficult to achieve a high degree of **reproducibility** of temperature profiles because measurements were affected by many factors including the size and shape of the thermocouple junction and variations in the local density of the powder. Despite attempts to standardize the measurement procedure, the reproducibility of the recorded temperature profiles of all four binary systems was not particularly good. Figures 5.24 to 5.27 show the variability within the temperature-time data for the 20% compositions of three of the binary systems and for 40% Mo/SrO_2. There is further discussion of reproducibility in Section 9.3.

The **composition** of the binary mixtures also affected the shape of the recorded temperature profiles without altering their overall sigmoidal form. These effects are shown in Figures 5.28 to 5.31 for the four binary systems. There was a composition in each of the four binary systems which gave a profile with the greatest slope in the rise zone and the largest amplitude for that system, while the profiles for the other compositions of that system had flatter rise zones and smaller maximum amplitudes. For the compositions illustrated in Figures 5.28 to 5.31 the maximum temperature decreased as the proportion of fuel was increased.

Some basis for comparing temperature profiles of compositions from different systems was required. Comparisons could be based on similar percentages by mass of fuel, or on similar mole ratios of fuel to oxidant. Figure 5.32 shows the comparison of temperature profiles for 20% compositions of the Mn/BaO_2, Mo/BaO_2 and Mn/SrO_2 systems (the 20% Mo/SrO_2 composition did not sustain combustion under the experimental conditions). Within the limited reproducibility these profiles have similar gradients in the rise zone and reach almost the same maximum temperatures.

Figure 5.33 shows the comparison of temperature profiles based on a fuel to oxidant mole ratio of ~4:1 which includes the following compositions: 55% Mn/BaO_2, 40% Mo/BaO_2 and 60% Mn/SrO_2. The 55% Mo/SrO_2 composition also has a 4:1 mole ratio, but did not sustain combustion under the experimental conditions. These temperature profiles have similar gradients at low temperature but differ in the recorded maximum temperature. Figure 5.34 shows the comparison of temperature profiles with a mole ratio of ~2:1 which includes the following compositions: 25% Mo/BaO_2, 45% Mn/SrO_2 and 40% Mo/SrO_2. A 35% Mn/BaO_2 composition, which also has a mole ratio of 2:1, burnt at temperatures above the melting point of the Pt thermocouple wire (~1760°C) and, therefore, no profiles could be recorded. Although the temperature profiles in Figure 5.34 have similar maximum temperatures for the respective pyrotechnic reactions, the gradients in the rise zone are noticeably different.

Fig 5.24 Reproducibility of temperature profiles (20% Mn/BaO_2)

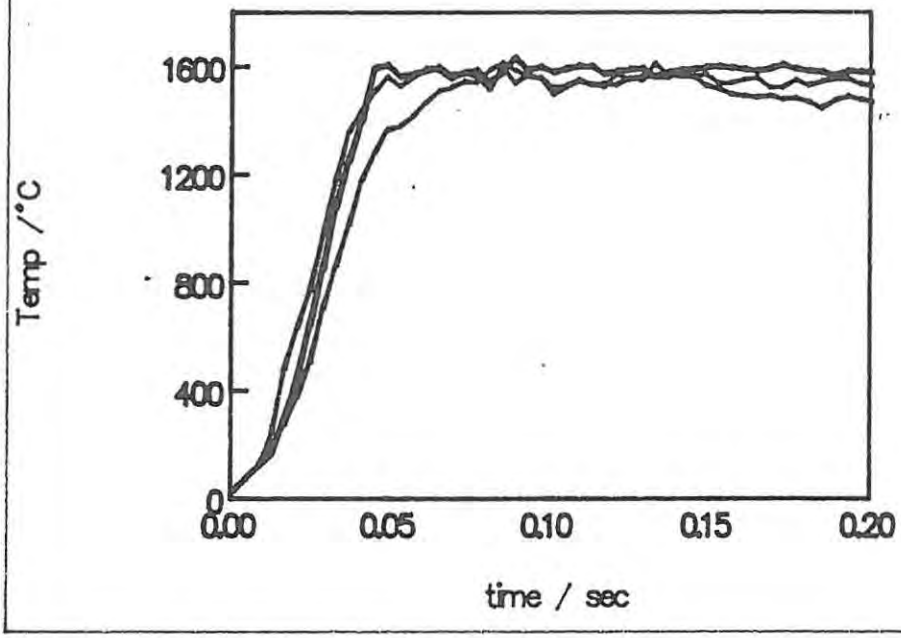

Fig 5.25 Reproducibility of temperature profiles (20% Mo/BaO_2)

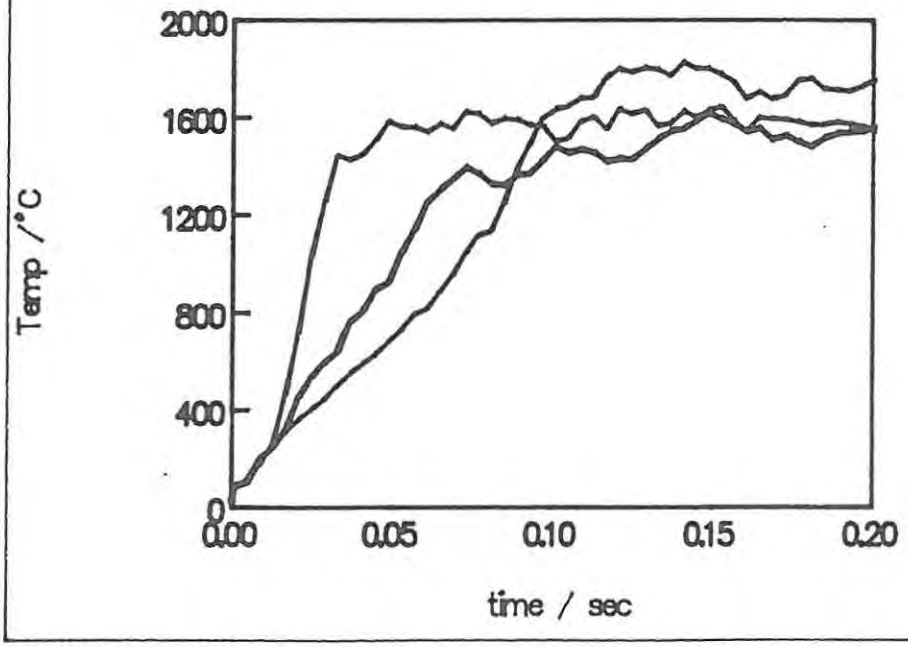

Fig 5.26 Reproducibility of temperature profiles (20% Mn/SrO_2)

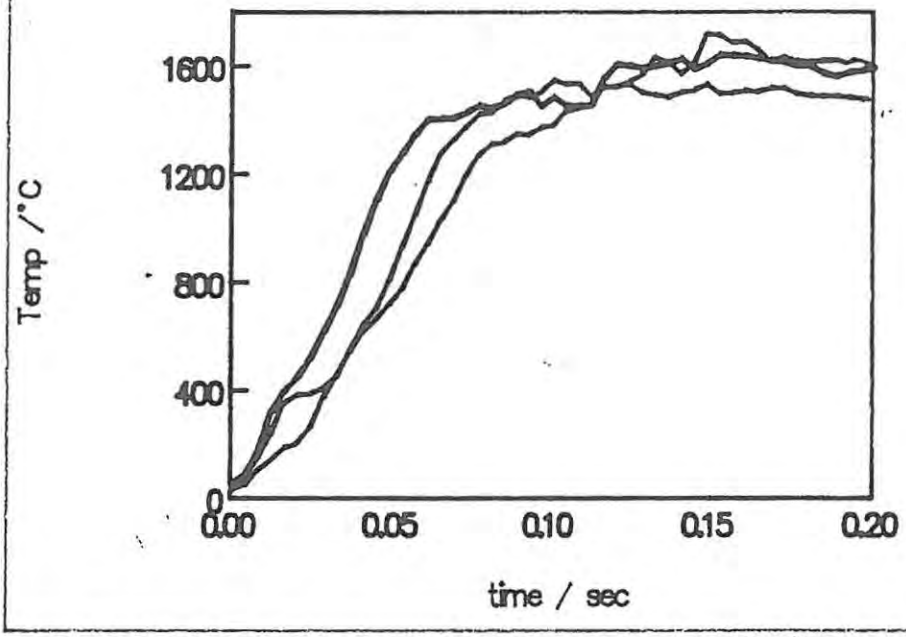

Fig 5.27 Reproducibility of temperature profiles (40% Mo/SrO_2)

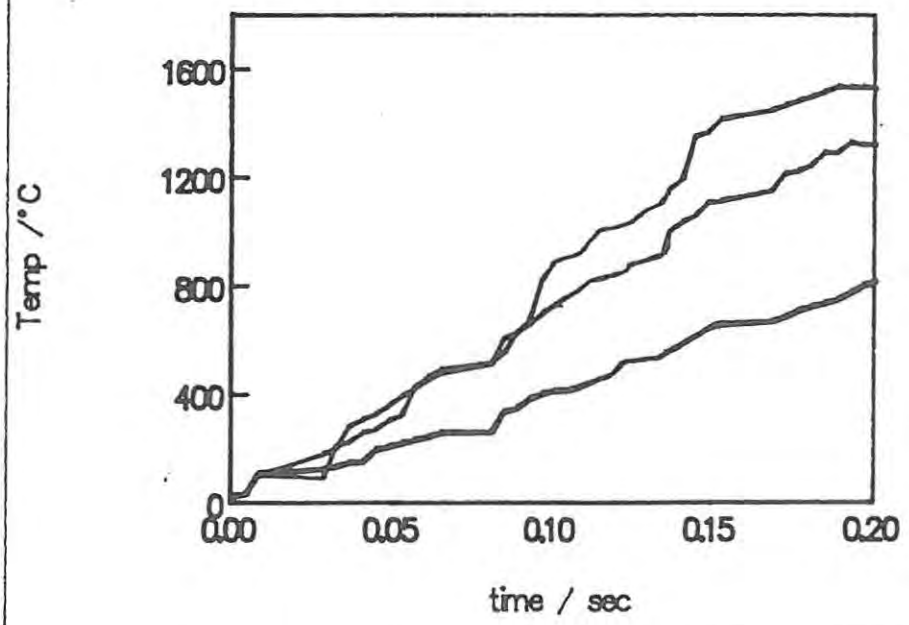

Fig 5.28 Temp profiles for different compositions of the Mn/BaO_2 system

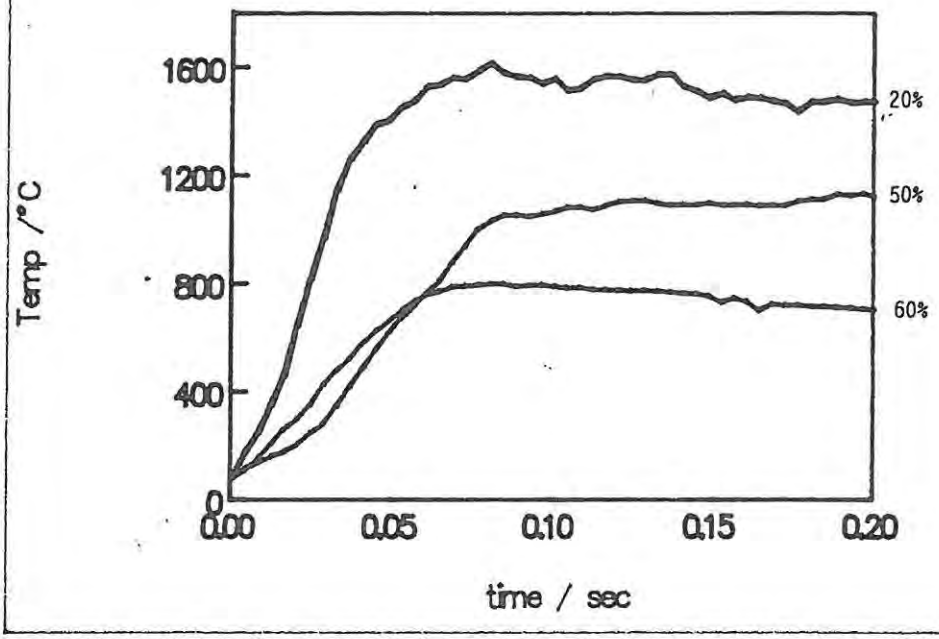

Fig 5.29 Temp profiles for different compositions of the Mo/BaO_2 system

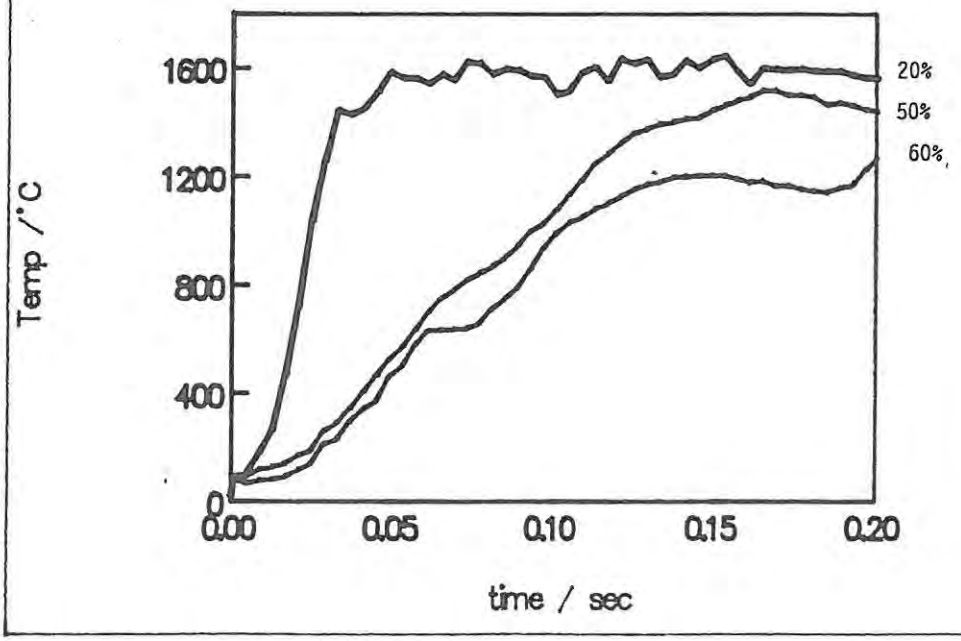

Fig 5.30 Temp profiles for different compositions of the Mn/SrO_2 system

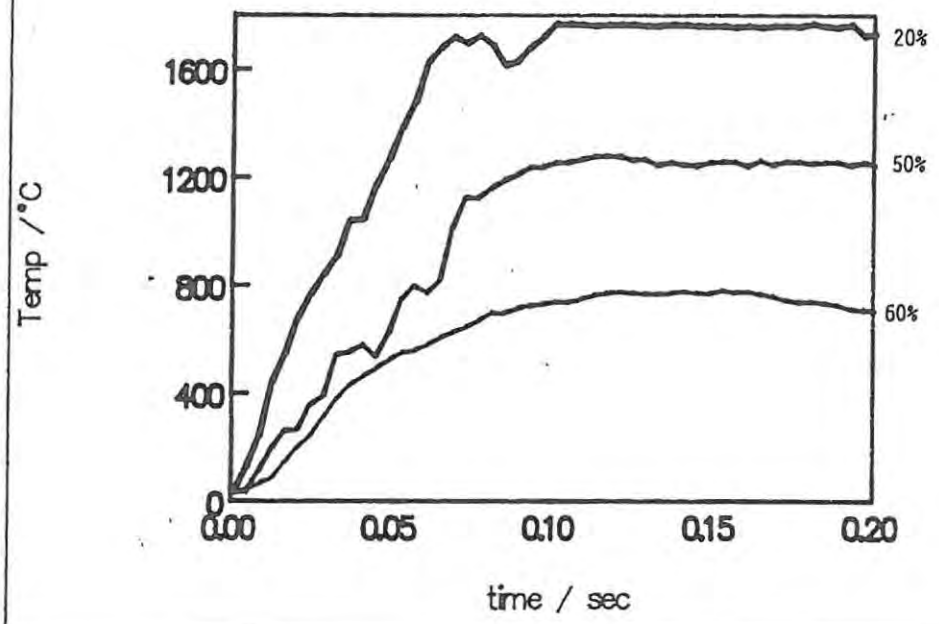

Fig 5.31 Temp profiles for different compositions of the Mo/SrO_2 system

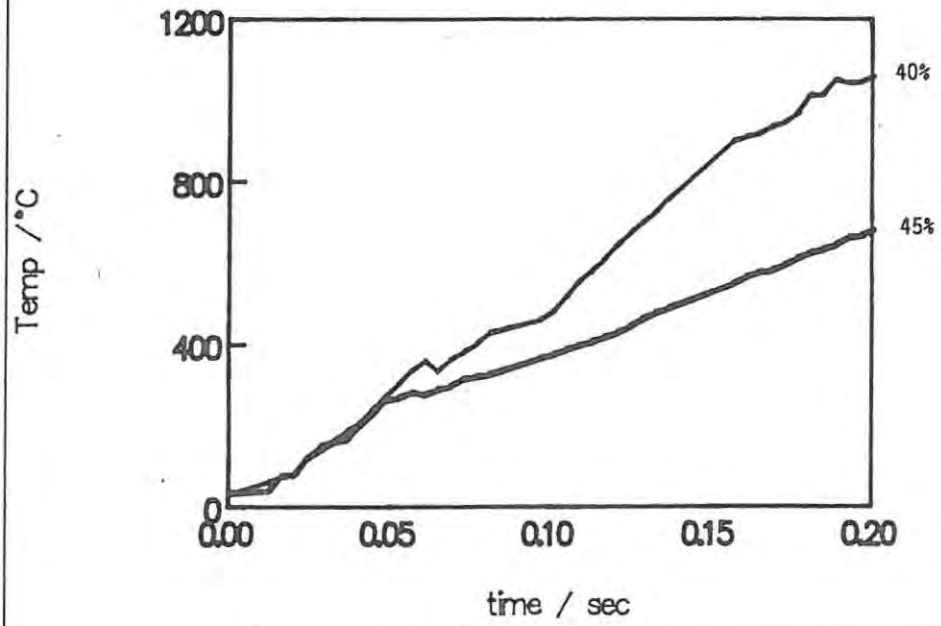

Fig 5.32 Comparison of temp profiles from different systems, 20% by mass

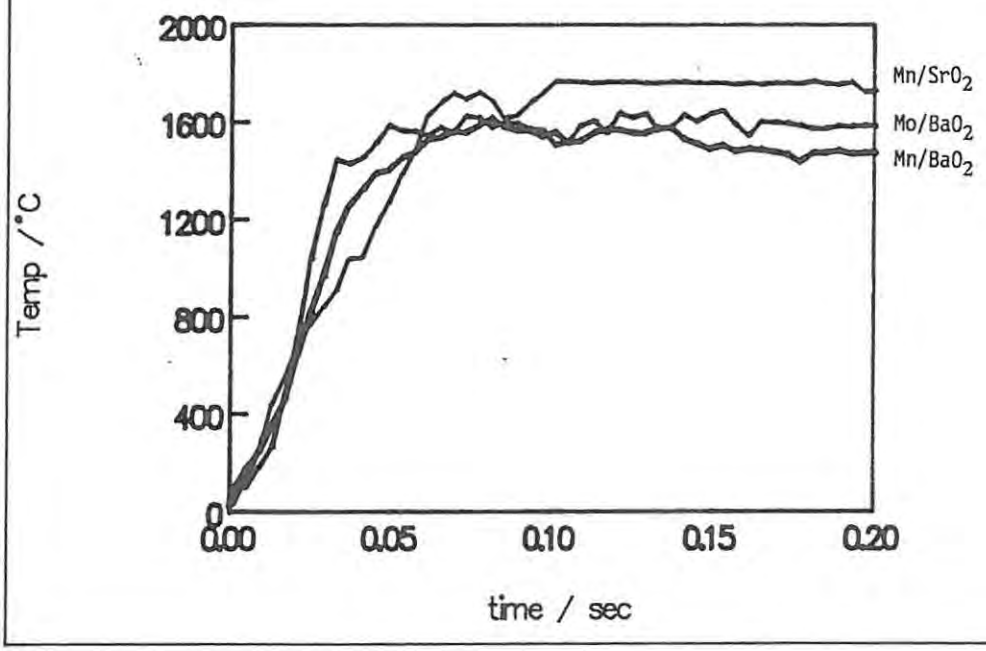

Fig 5.33 Comparison of temp profiles from different systems, mole ratio 4:1

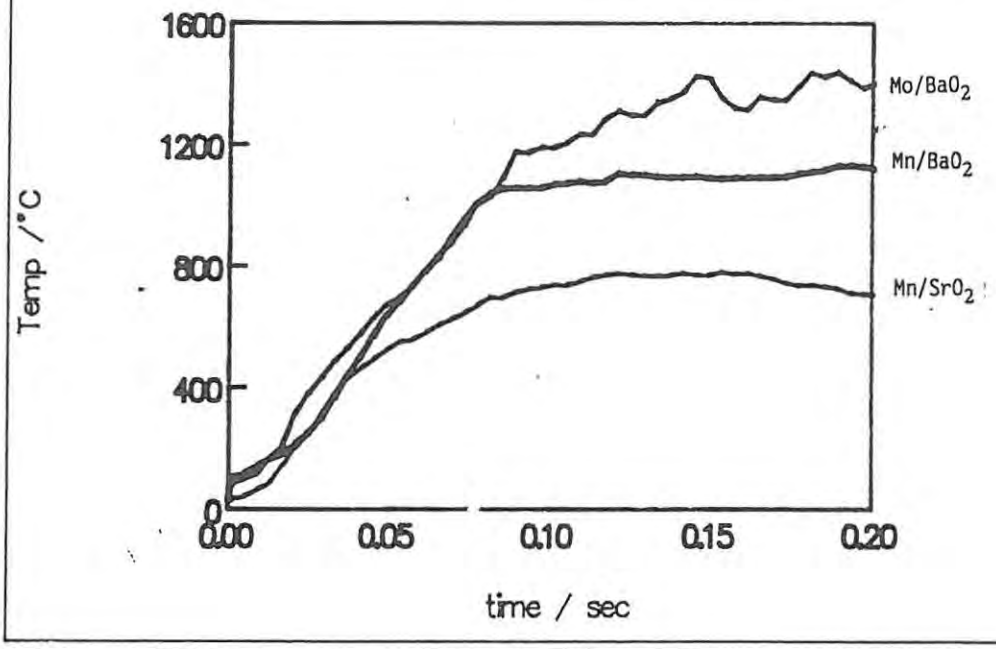

Fig 5.34 Comparison of temp profiles from different systems, mole ratio 2:1

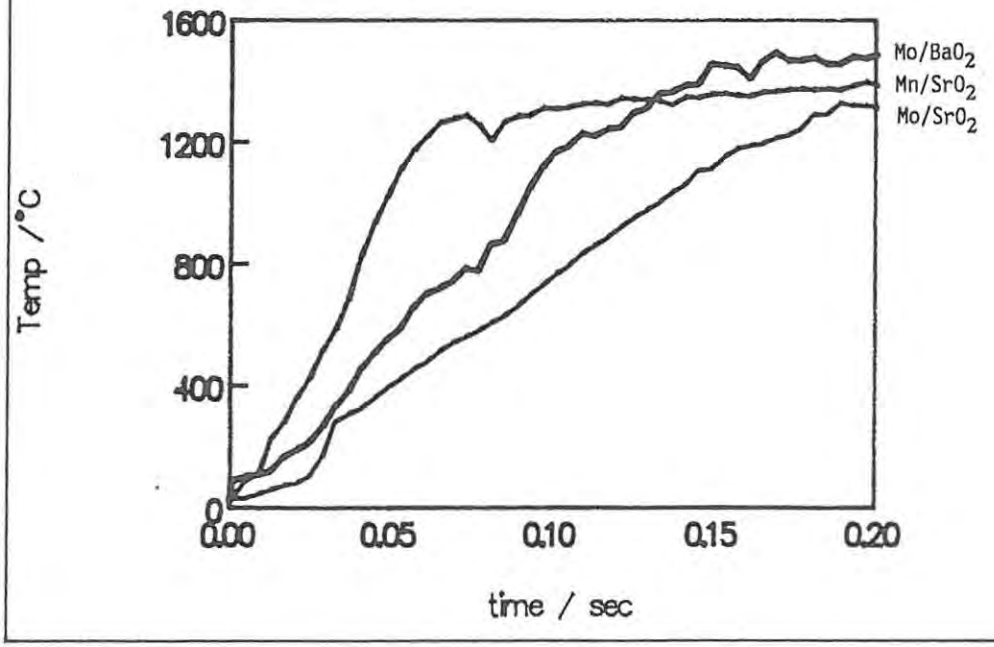

Exceptions to the regular sigmoidal temperature profiles were recorded in all four systems, especially in compositions near to the end of the range which supported combustion. In general, irregularities in a temperature profile may be related to phase changes such as melting of the fuel and/or oxidant in the rise zone or recrystallization of molten products in the cooling zone. For example, the temperature profile of 40% Mn/SrO_2 (Figure 5.35) showed a delayed exothermic process in the cooling zone. This could arise from further exothermic reaction, or from product recrystallization (ref 23). The temperature is about consistent with the recrystallization of MnO (melting point 1785°C, ref 59).

As might be expected, the irregular temperature profiles were less reproducible than those for the majority of compositions. Figure 5.36 shows the poor reproducibility of the irregular temperature profile of 70% Mo/BaO_2. Although the temperature profiles for all the compositions of Mo/BaO_2 do not show these irregularities (see Figure 5.29), the profiles for 60% compositions of Mo/BaO_2 show similar irregularities (Figure 5.37). These irregularities could be explained by the occurrence of endothermic processes which, in the approximately adiabatic conditions, delays the temperature rise or even causes a temporary decrease in temperature. The temperature range in which these endothermic deviations take place was from ~400° to ~800°C which includes the decomposition temperature of BaO_2 (~600°C, see Section 4.2.1).

The maximum excess temperatures, U_{max}, obtained from the temperature profiles of each system, are plotted against composition in Figure 5.38 for the two Mn systems and Figure 5.39 for the Mo systems. The combustion of the 25 to 45% compositions of Mn/BaO_2 caused the thermocouple to melt indicating that T_{max} for these compositions was greater than the melting point of Pt (~1760°C).

B. Corrections for the finite size of the thermocouple. The diameter, d, of the thermocouple wire used has a pronounced effect (ref 23) on the response of the thermocouple to the rapid passage of the burning front and hence the amplitude and shape of the temperature profiles recorded. The use of the thinnest thermocouple wire available (0.05 mm diameter) produced temperature profiles with considerable noise due to mechanical movement of the thermocouple during combustion. As the diameter of the thermocouple wire was increased, the amount of noise in the temperature profile decreased as did the response, as shown in Figure 5.40 (recorded for 20% Mn/SrO_2). Corrections thus have to be made to values of the parameters derived from temperature profiles to convert them to the values expected for a thermocouple wire of negligible diameter. The parameters include the remote rise time, t_r, where $t_r = \{d\ln U/dt\}^{-1}$, the remote decay time, t_d, where $t_d = -\{d\ln U/dt\}^{-1}$, the maximum excess temperature, U_{max}, and the kinetic parameters E_a and A.

Corrected values for the rise and decay times can be calculated by extrapolation of the approximately linear plots of t_r and t_d against either d or d^2. The parameters of the relationships, $t_r = md + C$ and $t_r = md^2 + C$ are shown in Table 5.10.

Fig 5.35 Temp profile for 40% Mn/SrO_2 showing irregularity in cooling zone

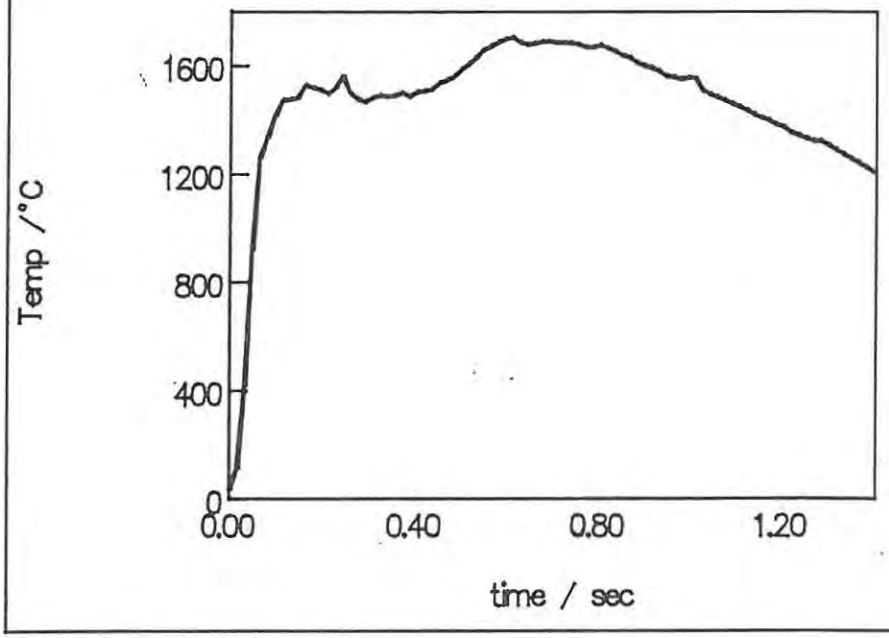

Fig 5.36 Temp profiles for 70% Mo/BaO_2 showing steps in the rise zone

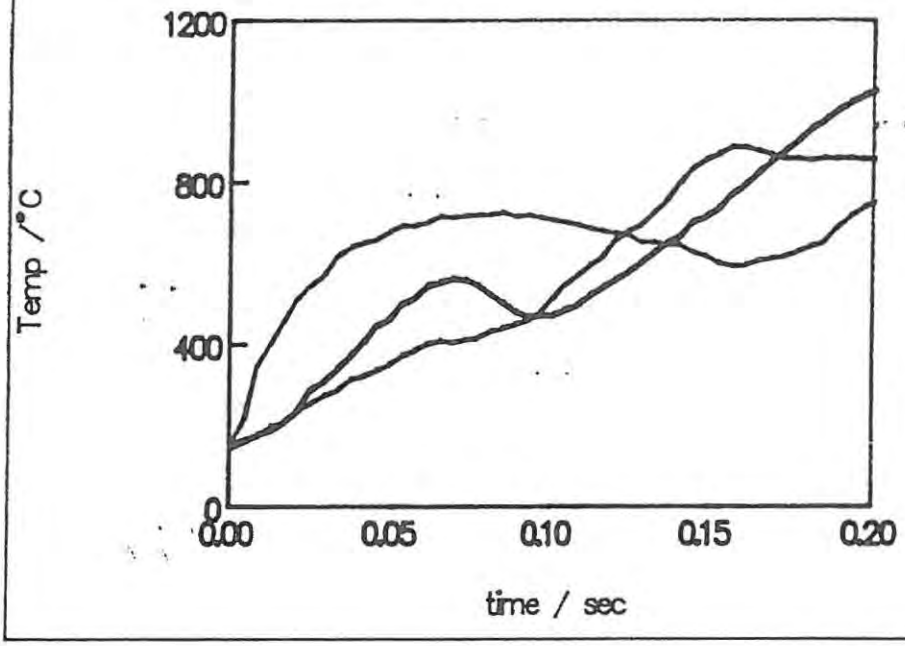

Fig 5.37 Temp profiles for 60% Mo/BaO_2 showing steps in the rise zone

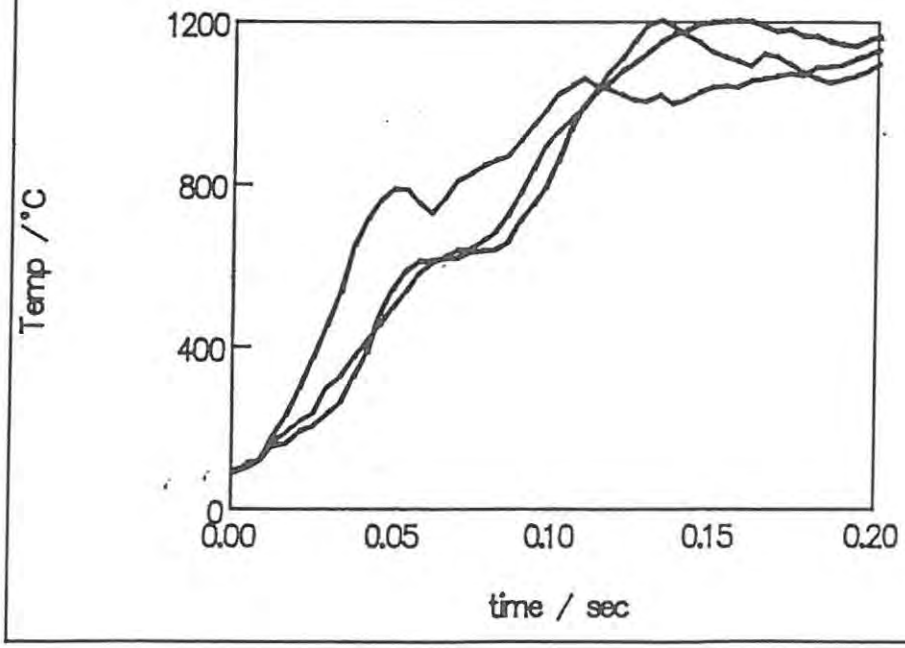

Fig 5.38 Max excess temp vs composition for the two systems containing Mn

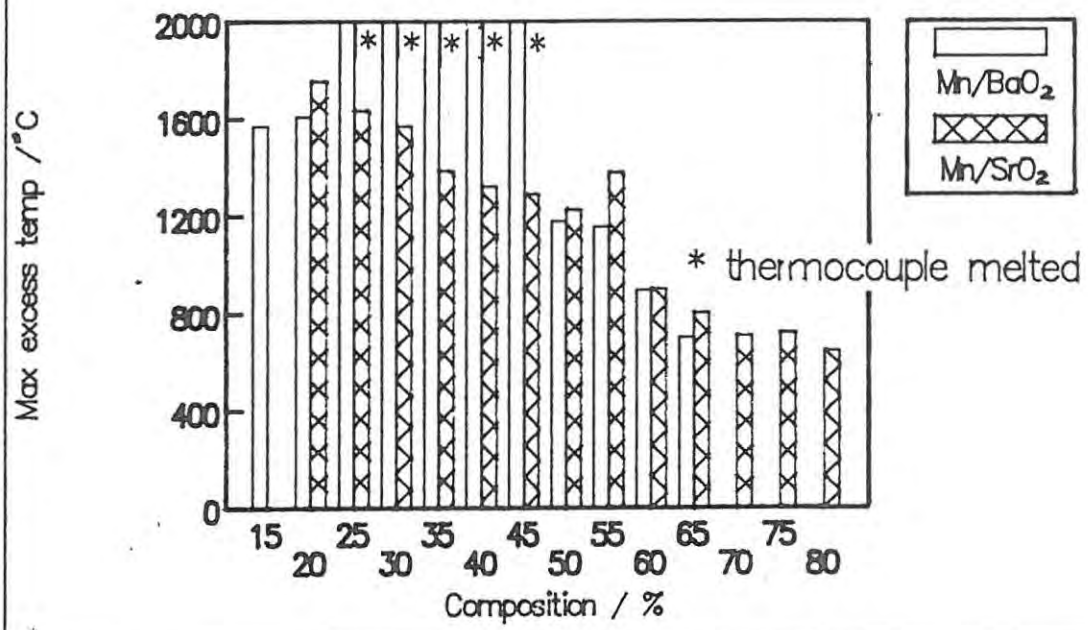

Fig 5.39 Max excess temp vs composition for the two systems containing Mo

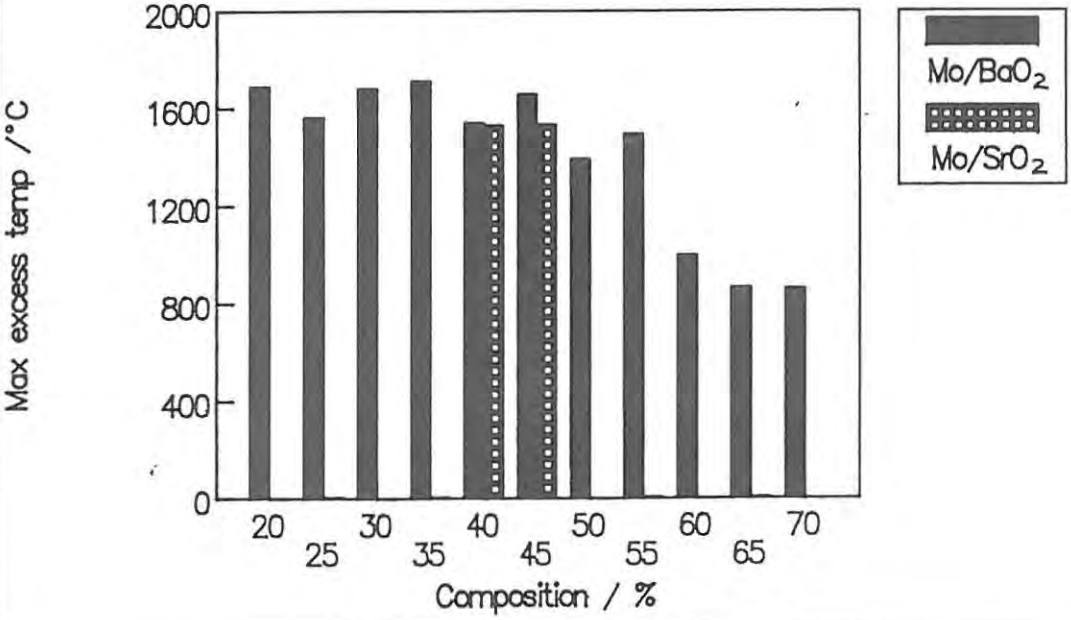

Fig 5.40 Temp profiles for 20% Mn/SrO_2 with different thermocouple diameters

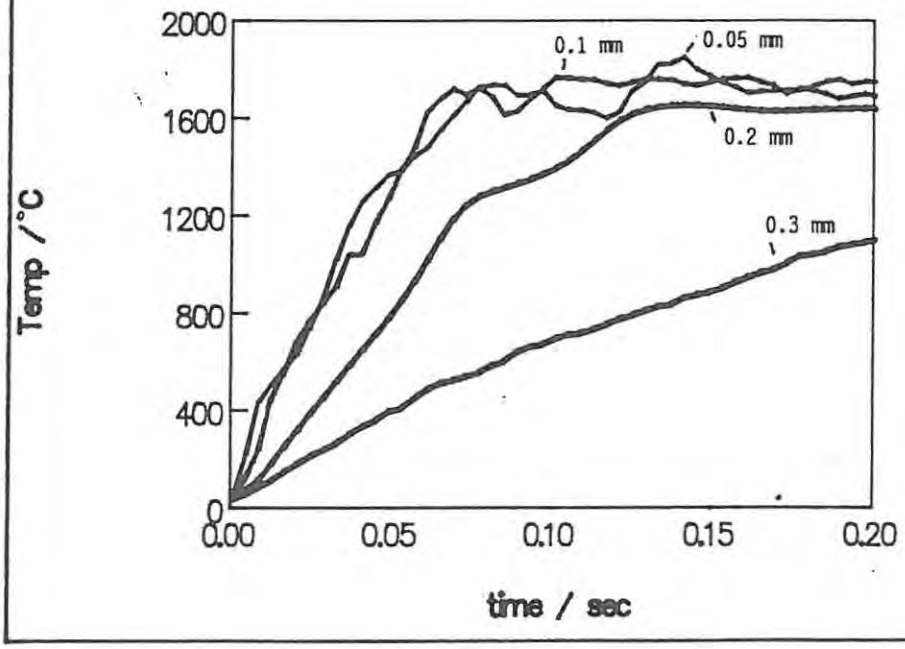

TABLE 5.10 PARAMETERS OF RELATIONSHIP BETWEEN t_r WITH d AND d^2			
SYSTEM	SLOPE / ms mm^{-1}	Y INTERCEPT / ms	CORRELATION COEFFICIENT
t_r vs d			
Mn/BaO_2	212 ± 52	15 ± 10	0.94
Mo/BaO_2	87 ± 13	18 ± 3	0.98
Mn/SrO_2	180 ± 17	-8 ± 3	0.99
Mo/SrO_2	44 ± 13	16 ± 2	0.93
t_r vs d^2			
Mn/BaO_2	587 ±157	29 ± 11	0.94
Mo/BaO_2	232 ± 64	24 ± 4	0.93
Mn/SrO_2	501 ± 54	4 ± 4	0.99
Mo/SrO_2	122 ± 39	19 ± 3	0.91

These corrections are described in Section 9.4, where they are used, together with thermal conductivity values, to calculate burning rates.

Plots of U_{max} against d and d^2 were also examined for linearity (ref 23). The parameters of the relationship, $U_{max} = md + C$, are given in Table 5.11 where C represents the corrected values of U_{max} on extrapolation to d equal to 0.

TABLE 5.11 PARAMETERS OF RELATION BETWEEN U_{max} AND d			
SYSTEM	SLOPE / °C mm^{-1}	Y INTERCEPT / °C	CORRELATION COEFFICIENT
60% Mn/BaO_2	-717 ± 248	1041 ± 48	0.90
50% Mo/BaO_2	-585 ± 410	1555 ± 79	0.83
20% Mn/SrO_2	-1826 ± 349	1871 ± 67	0.97
40% Mo/SrO_2	-466 ± 148	1580 ± 28	0.91

The difference between the corrected values of U_{max} and the measured values using a 0.1 mm thermocouple wire were on average: 14% higher for the Mn/BaO_2 system, 11% higher for the Mo/BaO_2 system, 6% higher for the Mn/SrO_2 system and 3% higher for the Mo/SrO_2 system.

C. Effect of compaction. Compaction (see Section 5.4.2 B) also affected the temperature profiles recorded during combustion of all four binary systems. The temperature profiles for these systems loaded under different pressures (Figures 5.41 to 5.44) show that the slope of the rise zone increases with compaction for three of the systems (i.e. Mn/BaO_2, Mo/BaO_2 and Mn/SrO_2), while the opposite occurred for the Mo/SrO_2 system. This behaviour was expected since the faster the burning rate the shorter the rise time.

Fig 5.41 Temp profiles of 25% Mn/BaO_2 compacted under different pressures

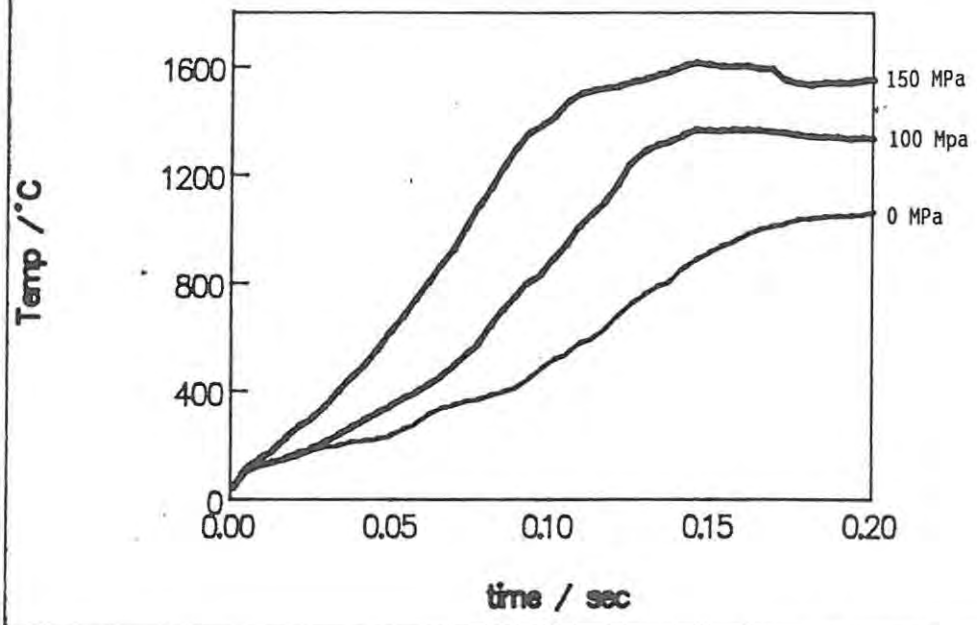

Fig 5.42 Temp profiles of 30% Mo/BaO_2 compacted under different pressures

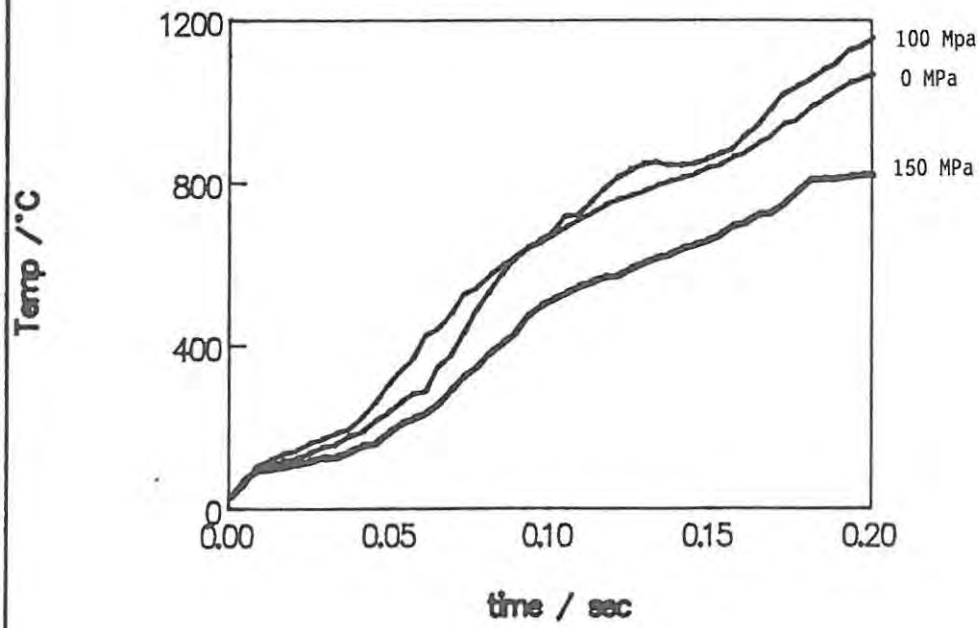

Fig 5.43 Temp profiles of 20% Mn/SrO_2 compacted under different pressures

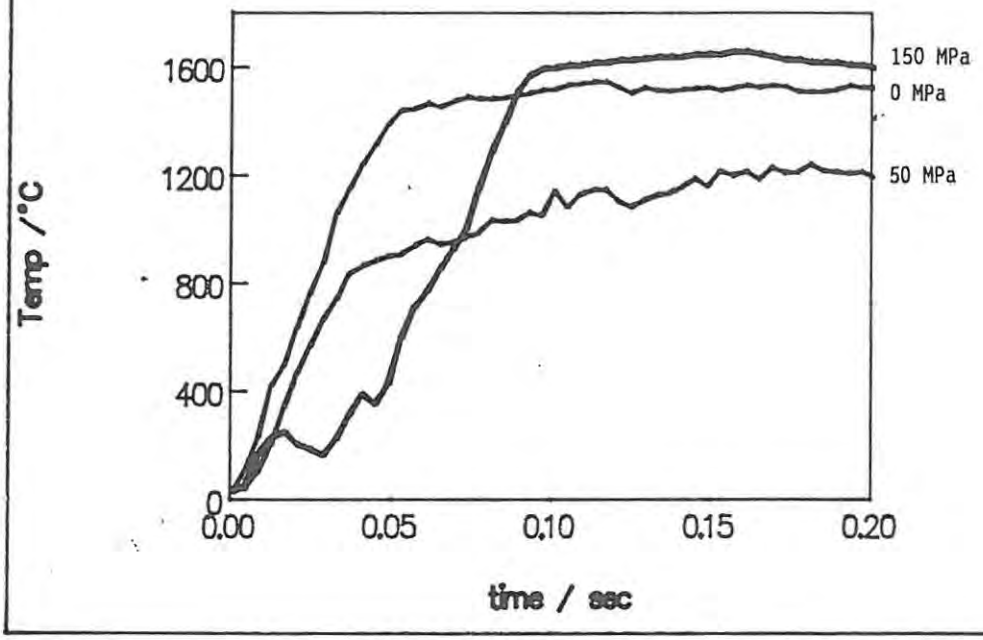

Fig 5.44 Temp profiles of 40% Mo/SrO_2 compacted under different pressures

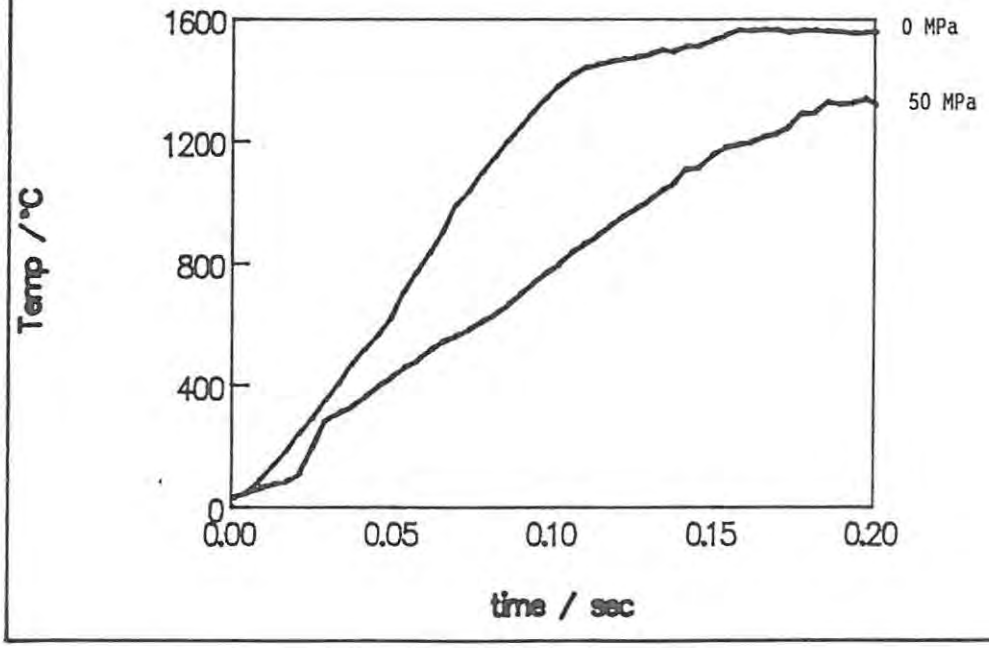

The profile for 20% Mn/SrO_2 compacted under 150 MPa (Figure 5.43) had an irregular shape similar to the profiles for high fuel compositions. Other irregular profiles were recorded during the combustion of the 30% Mo/BaO_2 compacted under 100 MPa (Figure 5.45). This profile had a slight endothermic depression at a temperature of about 845°C in the rise zone. Since this type of irregularity only appeared in the compositions under increased compaction, it is possible that this behaviour is related to the problems of the escape of gases from the compressed mixture.

Generally under increased compaction, 25% Mn/BaO_2 mixtures ignited easily and burnt reliably, producing smooth temperature profiles even at high loading compressions, while 30% Mo/BaO_2 mixtures were difficult to ignite and often failed to burn the complete length of the channel. The 20% Mn/SrO_2 mixtures burnt over the complete range of compressions tested, but 40% Mo/SrO_2 mixtures failed to burn when compaction was increased beyond 50 MPa.

D. Effect of particle-size. The effect of the fuel particle-size (see Section 5.4.2 C) on the temperature profiles is shown in Figure 5.46 for the Mo/BaO_2 system and Figure 5.47 for the Mo/SrO_2 system. The smaller particles gave shorter rise times, i.e. an increase in the burning rate, and higher maximum excess temperatures. The particle-size ranges of both metals had little effect on the density of the compressed pyrotechnic mixtures.

The particle-size of the oxidant (see Section 5.4.2 C) did not affect the temperature profiles within the limits of the reproducibility.

5.4.4 Effect of additives on burning:

The burning rate of a pyrotechnic mixture may be altered by changing its composition (Section 5.4.2 A), or by changing the pressure under which the mixture was compacted (Section 5.4.2 B), or by changing the particle-size of the fuel (Section 5.4.2 C). A further way of altering the burning characteristics of a pyrotechnic mixture is to introduce a suitable additive. Excluding additional fuels or oxidants, additives fall into three main categories:

(i) inert diluents, e.g. Al_2O_3

(ii) possible impurities in the oxidants, e.g. carbonates and hydroxides

(iii) possible reaction intermediates or products, e.g. MnO_2, MoO_3, etc.

A. The two BaO_2 systems. The additives tested for their effect on the burning characteristics of 20% compositions of the Mn/BaO_2 and Mo/BaO_2 systems were (i) Al_2O_3, (ii) $BaCO_3$ and $Ba(OH)_2$, and (iii) BaO and MoO_3 for the Mo/BaO_2 system and MnO_2 for the Mn/BaO_2 system. As the quantity of the additive was increased in steps, (1%, 5% and 10% of the total mass of the binary mixture) burning rates and temperature profiles were recorded for those mixtures which ignited. These results are listed in Table 5.12 for the Mn/BaO_2 system. Included in this table are the calculated heat capacities for the ternary mixture additive:fuel:oxidant.

Fig 5.45 Temp profile irregularity

30% Mo/BaO_2 loaded under 100 MPa

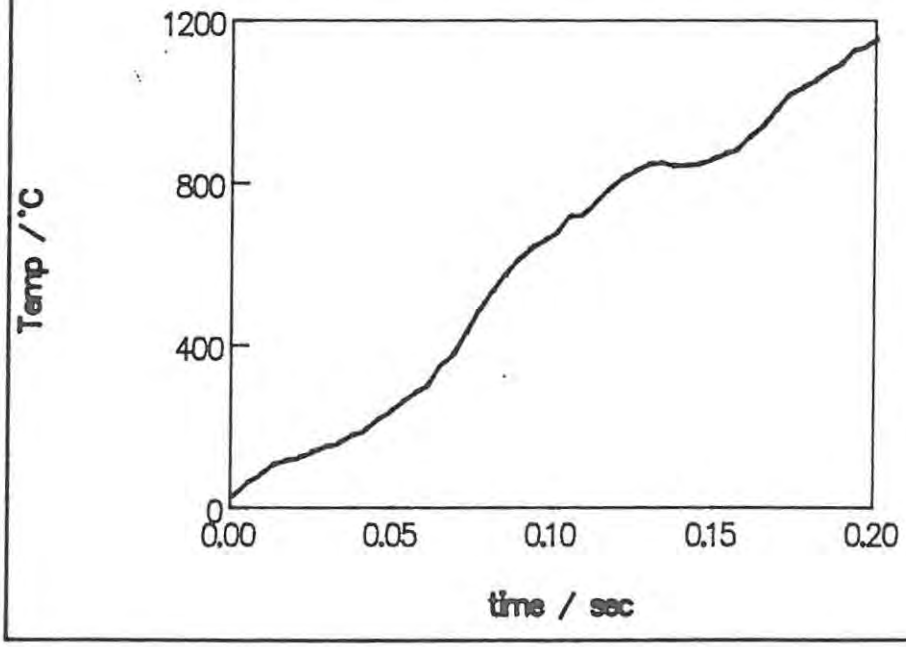

Fig 5.46 Temp profiles for different fuel particle sizes (50% Mo/BaO_2)

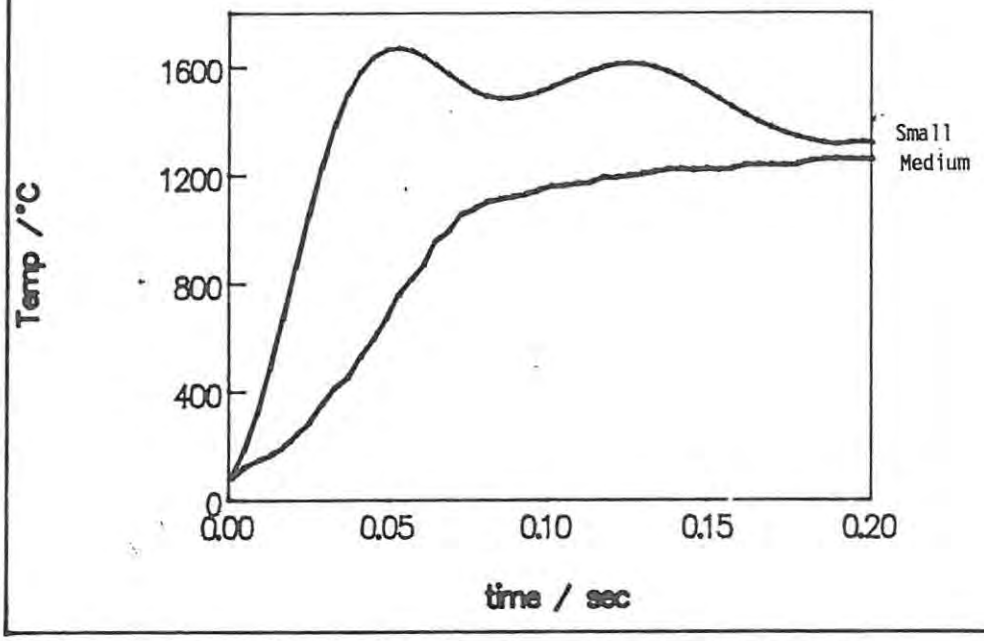

Fig 5.47 Temp profiles for different fuel particle sizes (40% Mo/SrO_2)

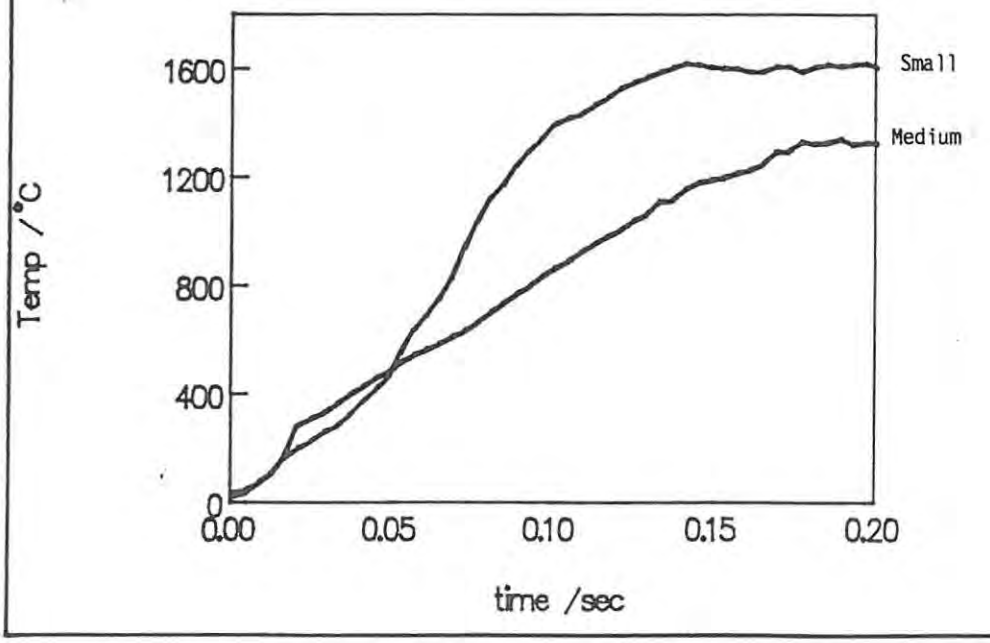

TABLE 5.12 EFFECTS ON BURNING OF THE 20% Mn/BaO_2 SYSTEM OF THE PRESENCE OF VARIOUS ADDITIVES

ADDITIVE	QUANTITY / %	v_{obs} / mm s^{-1}	U_{max} / °C	HEAT CAPACITY / J K^{-1} g^{-1}
Al_2O_3	0	11.7 ± 0.2	1609 ± 36	0.373
	1	7.8 ± 0.9	1487 ± 97	0.381
	5	6.0 ± 1.0	1509 ±108	0.396
	10	3.8 ± 0.6	1352 ± 11	0.414
$BaCO_3$	0	11.7 ± 0.2	1609 ± 36	0.373
	1	6.1 ± 0.4	1316 ± 10	0.381
	5	4.3 ± 0.4	1270 ± 30	0.398
	10	WOULD NOT BURN		0.417
$Ba(OH)_2$	0	11.7 ± 0.2	1609 ± 36	0.373
	1	6.2 ± 0.7	1476 ± 40	0.385 *
	5	6.2 ± 1.5	1557 ± 22	0.416 *
	10	WOULD NOT BURN		0.452 *
BaO	0	11.7 ± 0.2	1609 ± 36	0.373
	1	8.2 ± 1.0	1537 ± 98	0.376
	5	6.6 ± 0.6	1351 ±134	0.372
	10	WOULD NOT BURN		0.369
MnO_2	0	11.7 ± 0.2	1609 ± 36	0.373
	1	6.7 ± 0.5	1404 ± 88	0.379
	5	4.7 ± 1.4	1317 ± 68	0.388
	10	WOULD NOT BURN		0.399

* In the absence of heat capacity data for $Ba(OH)_2$, values for $Ca(OH)_2$ were used.

As the quantity of additive was increased, the maximum excess temperature was lowered, the burning rate decreased and the rise time increased. The decrease in burning rate, v_{obs}, of the Mn/BaO_2 system due to the increased quantity, X, of Al_2O_3 (Table 5.12) was linear and is defined by the equation; $v = mX + C$ where $m = -0.42 \pm 0.02$ mm s^{-1} and $C = 8.05 \pm 0.17$ mm s^{-1} with a correlation coefficient of 1.00. All the other additives had similar effects, to those of the inert diluent Al_2O_3, on the linear burning rate and maximum excess temperature of the Mn/BaO_2 system.

The temperature profiles recorded during the combustion of the Mn/BaO_2 system with increasing quantities of Al_2O_3 are shown in Figure 5.48. Some deviations from this typical shape were observed for other additives, e.g. the profile for Mn/BaO_2 with 5% $BaCO_3$ showed endothermic deviations in the rise zone at ~400°C and exothermic deviations in the decay zone at ~1200°C (Figure 5.49). The deviation in the rise zone was probably due to the decomposition of BaO_2 while the exothermic deviation at high temperature (~1200°C) was probably due to the recrystallization of the combustion products. The reported (ref 52) melting point for Mn_3O_4 is 1564°C. Similar irregularities were observed in the temperature profile of 20% Mn/BaO_2 with 1% $Ba(OH)_2$ at ~850°C in the rise zone and at about 1400°C in the decay zone (Figure 5.50).

The Mo/BaO_2 system failed to ignite in the presence of any of the additives except BaO and then only 5% BaO was sufficient to prevent combustion. The results for the mixture of 20% Mo/BaO_2 with BaO are listed in Table 5.13 with the calculated heat capacities.

Fig 5.48 Temp profiles for 20% Mn/BaO_2 containing different quantities of Al_2O_3

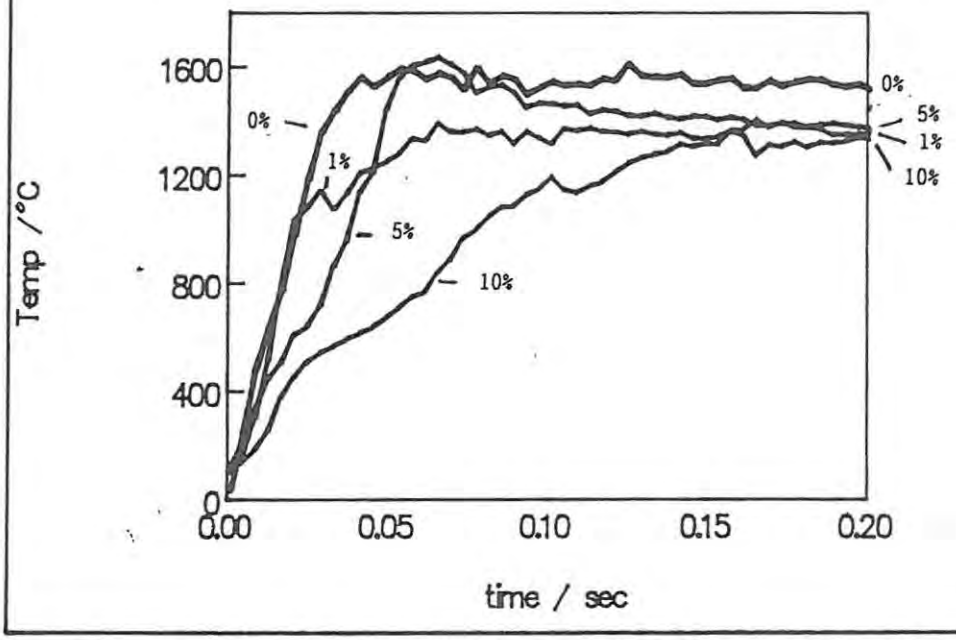

Fig 5.49 Temp profile for 20% Mn/BaO_2 containing 5% $BaCO_3$

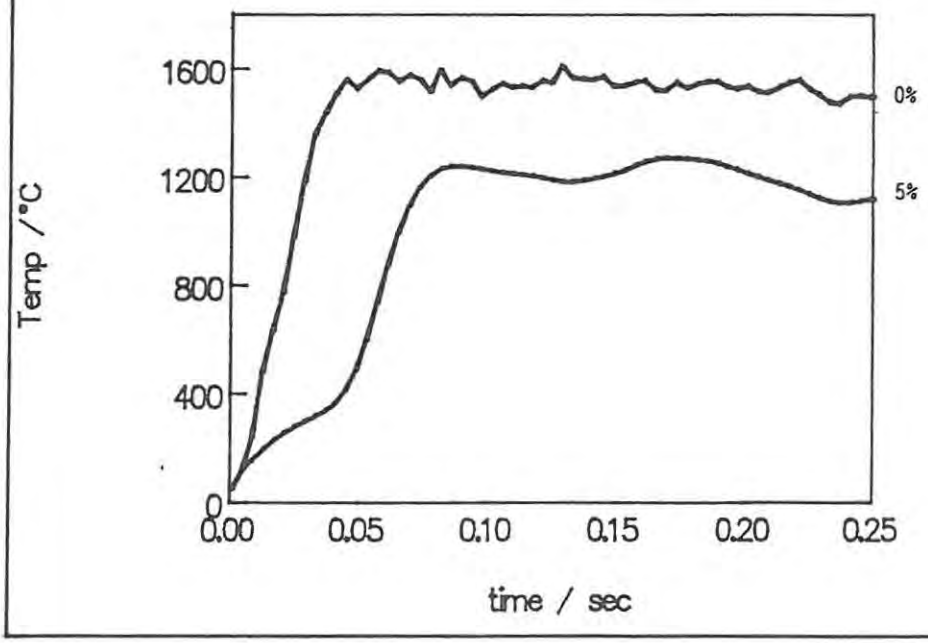

TABLE 5.13 EFFECTS ON BURNING OF THE 20% Mo/BaO_2 SYSTEM OF THE PRESENCE OF VARIOUS ADDITIVES

ADDITIVE	QUANTITY / %	v_{obs} / mm s^{-1}	U_{max} / °C	HEAT CAPACITY / J K^{-1} g^{-1}
BaO	0	2.7 ± 0.2	1687 ± 87	0.334
	1	3.5 ± 0.3	1554 ± 54	0.331
	5	WOULD NOT BURN		0.330
	10	WOULD NOT BURN		0.328

B. The two SrO_2 systems. The additives used were the Sr equivalents of those added to the BaO_2 systems, i.e. $SrCO_3$, SrO and $Sr(OH)_2$, as well as Al_2O_3 and MnO_2 and MoO_3 in their respective systems. Similar amounts (i.e. 1%, 5% and 10% of the total mass of the binary mixture) were added to 20% Mn/SrO_2 and to 40% Mo/SrO_2 (the 20% Mo/SrO_2 composition did not sustain combustion under the experimental conditions). The results for the Mn/SrO_2 system are listed in Table 5.14.

TABLE 5.14 EFFECTS ON BURNING OF THE 20% Mn/SrO_2 SYSTEM OF THE PRESENCE OF VARIOUS ADDITIVES

ADDITIVE	QUANTITY / %	v_{obs} / mm s^{-1}	U_{max} / °C	HEAT CAPACITY / J K^{-1} g^{-1}
Al_2O_3	0	4.5 ± 1.0	1756 ± 6	0.490
	1	3.9 ± 0.2	1689 ± 53	0.493
	5	2.3 ± 0.3	1667 ± 53	0.504
	10	WOULD NOT BURN		0.517
$SrCO_3$	0	4.5 ± 1.0	1756 ± 6	0.490
	1	3.7 ± 0.6	1441 ±213	0.495
	5	2.3 ± 0.4	1279 ±219	0.513
	10	WOULD NOT BURN		0.533
$Sr(OH)_2$	0	4.5 ± 1.0	1756 ± 6	0.490
	1	3.7 ± 0.2	1661 ± 61	0.497 *
	5	2.7 ± 0.4	1646 ± 57	0.524 *
	10	2.1 ± 0.1	1472 ± 7	0.555 *
SrO	0	4.5 ± 1.0	1756 ± 6	0.490
	1	3.7 ± 0.5	1498 ± 69	0.489
	5	2.5 ± 0.3	1331 ± 87	0.487
	10	WOULD NOT BURN		0.484
MnO_2	0	4.5 ± 1.0	1756 ± 6	0.490
	1	3.6 ± 0.3	1497 ± 22	0.491
	5	2.8 ± 0.3	1549 ±132	0.496
	10	1.4 ± 0.0	1478 ± 4	0.502

* In the absence of heat capacity data for $Ba(OH)_2$, values for $Ca(OH)_2$ were used.

The addition of increasing quantities of additive slowed the burning rate and lowered the maximum excess temperature. The addition of Al_2O_3 to the 20% Mn/SrO_2 system also decreased the burning rate, v_{obs}, in a linear fashion, according to $v = mX + C$ where $m = -0.43 \pm 0.01$ mm s^{-1} and $C = 4.33 \pm 0.08$ mm s^{-1} with a correlation coefficient of 1.00. All the other additives had similar effects to those of the inert diluent Al_2O_3, on the burning rate and maximum excess temperature of the Mn/SrO_2 system.

The temperature profiles recorded during the combustion of the Mn/SrO_2 system with increased quantities of Al_2O_3 are shown in Figure 5.51. The addition of 1% $Sr(OH)_2$ to 20% Mn/SrO_2 caused two irregularities in the rise zone of the temperature profiles (Figure 5.52) at ~250° and ~950°C. As these deviations from the expected sigmoidal temperature profile take place in the rise zone they are probably due to the decomposition of either SrO_2 (~390° and ~540°C , Section 4.2.3) or $Sr(OH)_2$, reported (ref 52) dehydration temperature is 710°C.

The 40% Mo/SrO_2 system failed to ignite in the presence of as little as 5% of most of the additives. The results are listed in Table 5.15. The addition of MoO_3 had no observable effect on the burning of the 40% Mo/SrO_2 system. Neither the burning rate nor the maximum excess temperature was altered, even at the 10% level. The temperature profiles recorded with 1, 5 and 10% MoO_3 in 40% Mo/SrO_2 were all similar (Figure 5.53).

TABLE 5.15 EFFECTS ON BURNING OF THE 40% Mo/SrO_2 SYSTEM OF THE PRESENCE OF VARIOUS ADDITIVES

ADDITIVE	QUANTITY / %	v_{obs} / mm s^{-1}	U_{max} / °C	HEAT CAPACITY / J K^{-1} g^{-1}
Al_2O_3	0	2.3 ± 0.1	1526 ± 19	0.407
	1	WOULD NOT BURN		0.410
	5	WOULD NOT BURN		0.417
	10	WOULD NOT BURN		0.433
$SrCO_3$	0	2.3 ± 0.1	1526 ± 19	0.407
	1	2.2 ± 0.1	1539 ±109	0.411
	5	WOULD NOT BURN		0.425
	10	WOULD NOT BURN		0.449
$Sr(OH)_2$	0	2.3 ± 0.1	1526 ± 19	0.407
	1	2.3 ± 0.0	1663 ± 10	0.409 *
	5	WOULD NOT BURN		0.436 *
	10	WOULD NOT BURN		0.471 *
SrO	0	2.3 ± 0.1	1526 ± 19	0.407
	1	2.4 ± 0.1	1511 ± 30	0.408
	5	WOULD NOT BURN		0.409
	10	WOULD NOT BURN		0.501
MoO_3	0	2.3 ± 0.1	1526 ± 19	0.407
	1	2.1 ± 0.4	1486 ± 41	0.501
	5	2.2 ± 0.1	1629 ± 22	0.505
	10	2.1 ± 0.2	1427 ±135	0.508

* In the absence of heat capacity data for $Ba(OH)_2$, values for $Ca(OH)_2$ were used.

Fig 5.50 Temp profile for 20% Mn/BaO_2 containing 1% $Ba(OH)_2$

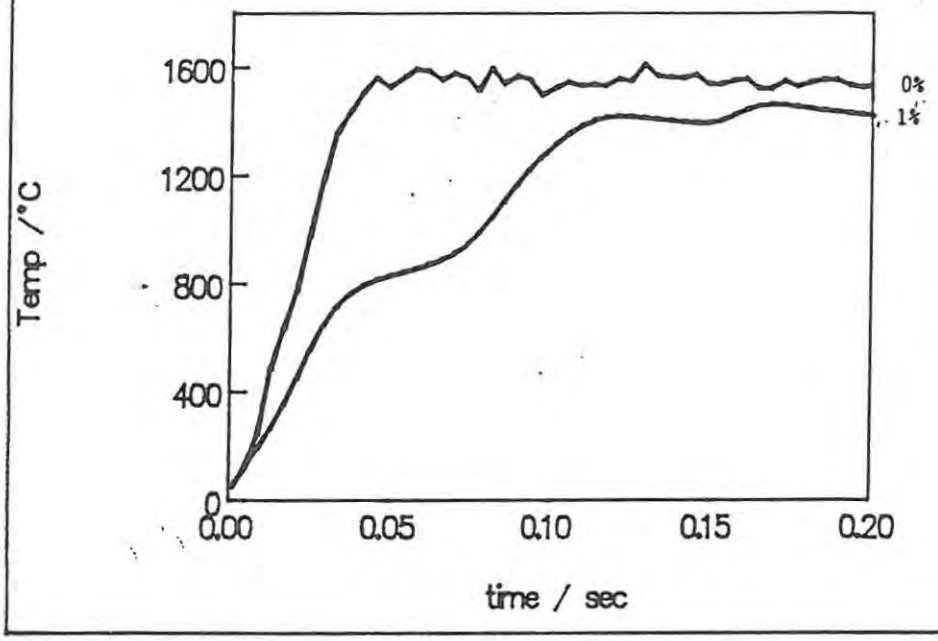

Fig 5.51 Temp profiles for 20% Mn/SrO_2 containing different quantities of Al_2O_3

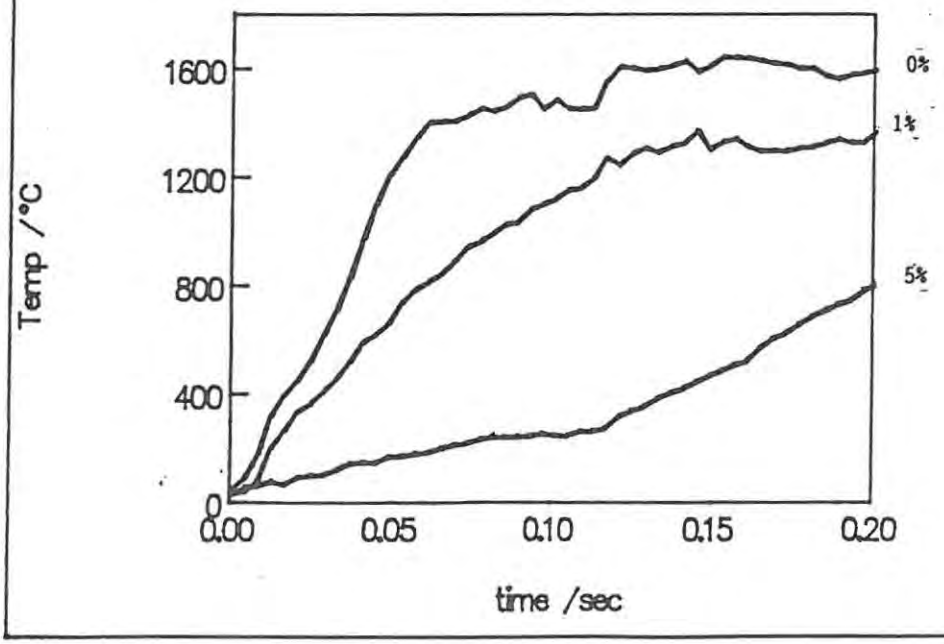

Fig 5.52 Temp profile for 20% Mn/SrO_2 containing 1% $Sr(OH)_2$

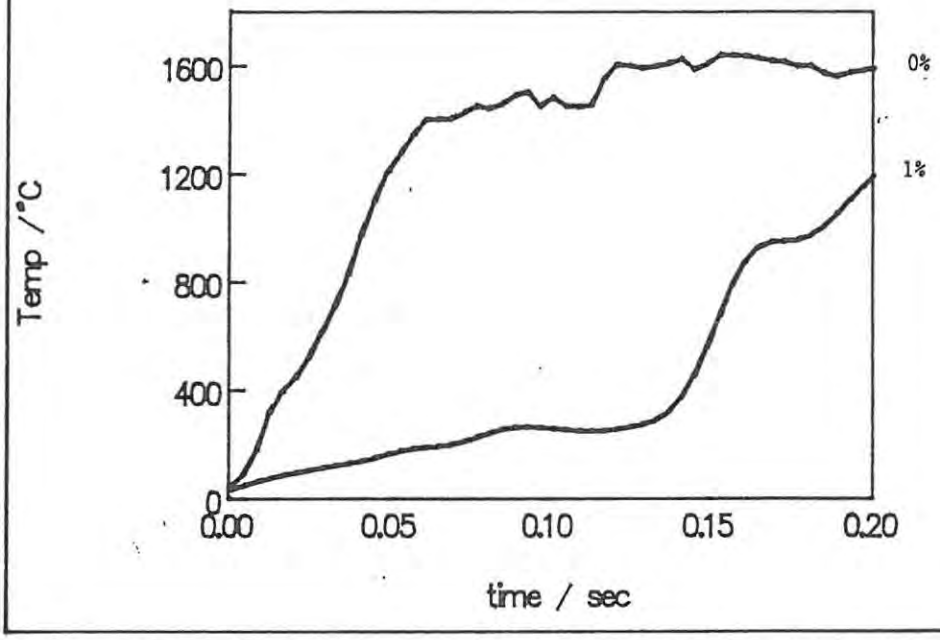

Fig 5.53 Temp profiles for 40% Mo/SrO_2 containing different quantities of MoO_3

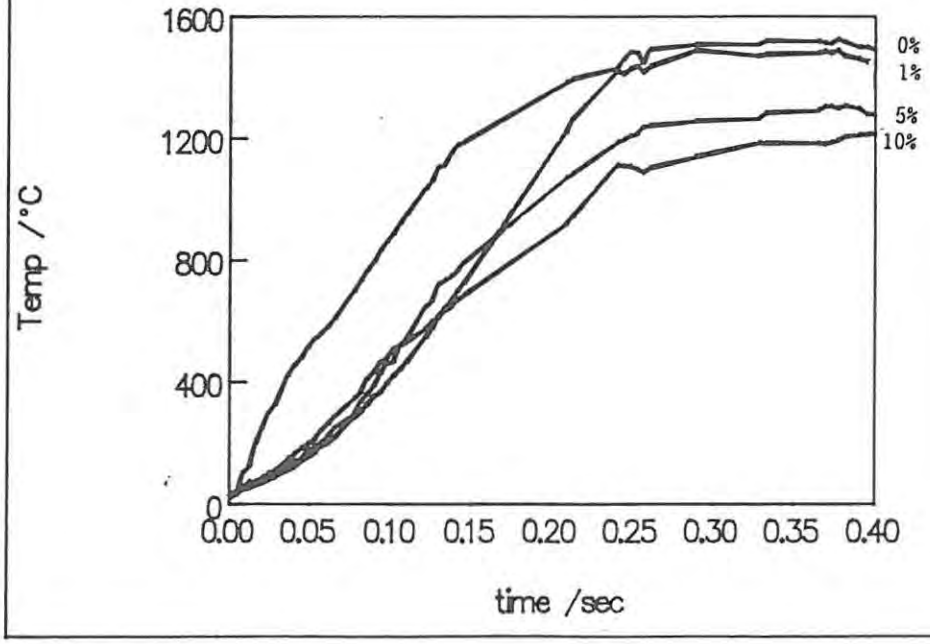

5.4.5 Effect of pre-heating on burning:

A. Oxidants. Thermal analyses of BaO_2 (see Section 4.2.1) indicated two endothermic events besides the loss of loosely bound water in the temperature range of 50° to 725°C. At ~360°C there was a structural rearrangement of a $Ba(OH)_2$ impurity preceding its decomposition, while at higher temperatures (~600°C) the BaO_2 itself underwent thermal decomposition. Under the conditions of thermal analysis, the rearrangement in the $Ba(OH)_2$ impurity was involved in a reaction (possibly a pre-ignition reaction) in the Mn/BaO_2 system. To investigate the influence of these processes on combustion, samples of BaO_2 were heated in a convection oven to 425 ± 20°C in air for one hour and then cooled, prepared and mixed in either dry air or dry nitrogen to give 40% binary compositions with Mn and Mo. All four of these mixtures burnt in the open channel; the burning rates are listed in Table 5.16.

TABLE 5.16 EFFECTS ON BURNING RATE OF 40% Mn/BaO_2 AND 40% Mo/BaO_2, WITH BaO_2 PREPARED IN AIR AND IN NITROGEN

SYSTEM	BURNING RATE / mm s^{-1}		
	UNTREATED	PREPARED IN DRY AIR	PREPARED IN DRY NITROGEN
Mn/BaO_2	6.6 ± 0.4	5.9 ± 0.4	4.6 ± 0.5
Mo/BaO_2	4.6 ± 1.0	5.3 ± 0.4	4.0 ± 0.8

XRD analysis (Chapter 8) of both the BaO_2 samples (i.e. cooled in dry air and in dry N_2) showed that little or no change had occurred to the peroxide content, but there was no evidence for $Ba(OH)_2$ in either sample. So the presence of $Ba(OH)_2$ in BaO_2 is not essential for combustion, but it may aid the combustion.

Thermal analyses of SrO_2 samples (see Section 4.2.3) confirmed the reported (refs 30, 37) two-step decomposition mechanism with stages at ~390° and ~540°C, respectively. To investigate the significance of the initial decomposition step in the pyrotechnic reactions, samples of SrO_2 were heated in air in a convection oven at ~520°C for one hour. The samples were then cooled (~1 hour) to room temperature and mixed with Mn and Mo, in either dry air or dry nitrogen. All the 40% compositions produced in this manner would not burn in the open channel. XRD analysis of samples of SrO_2 cooled in dry N_2 showed that most of the SrO_2 had been replaced by SrO. Some evidence for $SrCO_3$ was also noted, which presumably was present as an impurity before heating took place.

B. Pyrotechnic mixtures. Pre-ignition reactions have been reported (ref 7) for the Fe/BaO_2 pyrotechnic system. 40% compositions of all four pyrotechnic systems were heated for 10 minutes in a pre-heated convection oven (see Section 5.1.3) and after cooling to room temperature, the mixtures were burnt in the normal manner. At an oven temperature of ~360°C, combustion took place only in the Mn/BaO_2 system within the 10 minute period. At ~420°C, complete combustion occurred in the Mo/BaO_2 and the Mn/SrO_2 systems, but no obvious change besides darkening was observed in the Mo/SrO_2 system within the 10 minutes. These darkened residues of the Mo/SrO_2 system would not burn in the open

channel and thus had probably undergone some reaction in the oven.

Pre-heating was expected to drive off adsorbed water from the pyrotechnic mixtures. The extent of this drying is shown in Table 5.17, where the average mass losses of the pyrotechnic mixtures during pre-heating at ~140°C and the subsequent mass losses during combustion are compared to the mass losses of untreated mixtures.

TABLE 5.17 COMPARISON OF MASS LOSSES DURING DIFFERENT TREATMENTS

SYSTEM 40%	MASS LOSS / %			
	PRE-HEATED AT 140 ± 10°C	COMBUSTION OF PRE-HEATED MIXTURE	TOTAL	COMBUSTION OF UNTREATED MIX.
Mn/BaO_2	2.6 ± 0.8	8.7 ± 2.2	11.3	10.4 ± 3.7
Mo/BaO_2	2.8 ± 0.4	4.7 ± 2.1	7.5	6.1 ± 1.7
Mn/SrO_2	1.7 ± 0.9	13.2 ± 1.7	14.9	16.0 ± 0.1
Mo/SrO_2	1.1 ± 0.6	1.5 ± 0.7	3.6	1.8 ± 0.9

Table 5.18 shows the effects of the different pre-heating treatments on the linear burning rates and maximum excess temperatures of all four systems.

TABLE 5.18 LINEAR BURNING RATES AND MAXIMUM EXCESS TEMPERATURES FOR PYROTECHNIC SYSTEMS SUBJECTED TO PRE-HEATING TREATMENT

SYSTEM & RESULTS	TEMPERATURE OF PRE-HEAT TREATMENT / °C					
	UNTREATED	140 ± 10	220 ± 10	300 ± 10	360 ± 10	420 ± 10
40% Mn/BaO_2						
$v/mm\ s^{-1}$	6.6 ± 0.4	6.6 ± 0.1	7.6 ± 0.7	5.7 ± 0.3	IGNITION	IGNITION
$U_{max}/°C$	> 1760	1482 ± 135	1324 ± 85	1165 ± 92		
40% Mo/BaO_2						
$v/mm\ s^{-1}$	4.6 ± 1.0	2.4 ± 0.3	2.5 ± 0.3	2.3 ± 0.2	2.31 ± 0.3	IGNITION
$U_{max}/°C$	1536 ± 82	1167 ± 45	1236 ± 74	1197 ± 53	1089 ± 98	
40% Mn/SrO_2						
$v/mm\ s^{-1}$	7.5 ± 1.0	15 ± 2.4	9.7 ± 1.6	7.7 ± 1.9	4.6 ± 0.2	IGNITION
$U_{max}/°C$	1299 ±107	1612 ± 102	1604 ± 85	1274 ± 45	1580 ± 96	
40% Mo/SrO_2						
$v/mm\ s^{-1}$	2.3 ± 0.1	2.2 ± 0.1	1.9 ± 0.3	1.8 ± 0.2	1.6 ± 0.3	IGNITION
$U_{max}/°C$	1502 ± 99	1640 ± 110	1686 ± 97	1726 ± 125	1627 ± 68	

For temperatures below ~360°C, the pre-heating treatment did not affect the physical appearance of the Mn/BaO_2 system. Figure 5.54 shows the temperature profiles recorded during combustion of 40% Mn/BaO_2 compositions pre-heated at different temperatures (no profile was recorded for the untreated mixture since it burnt at temperatures above the melting point of the Pt thermocouple wire). The combustion products produced by this mixture at a pre-heating temperature of ~360°C had a metallic appearance and XRD analysis (Chapter 8) confirmed the presence of various manganese oxides such as MnO_2 and Mn_3O_4. Unreacted Mn and BaO_2 as well as BaO were also present.

The Mo/BaO_2 system was difficult to ignite after the pre-heating treatment, but once combustion was underway it burnt reliably. Figure 5.55 shows the temperature profiles recorded during combustion of

Fig 5.54 Temp profiles for 40% Mn/BaO_2 pre–heated to different temperatures

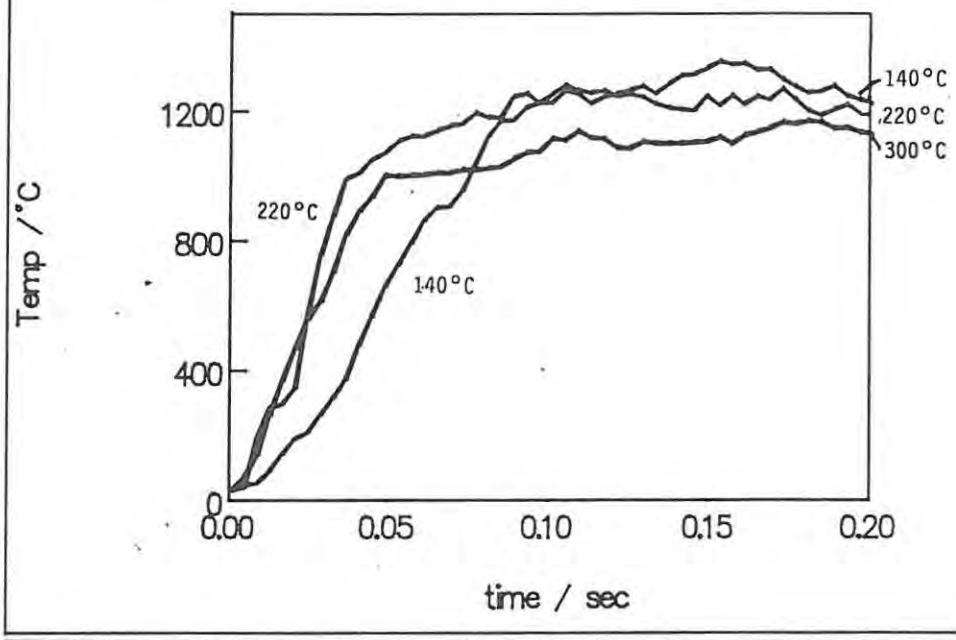

Fig 5.55 Temp profiles for 40% Mo/BaO_2 pre–heated to different temperatures

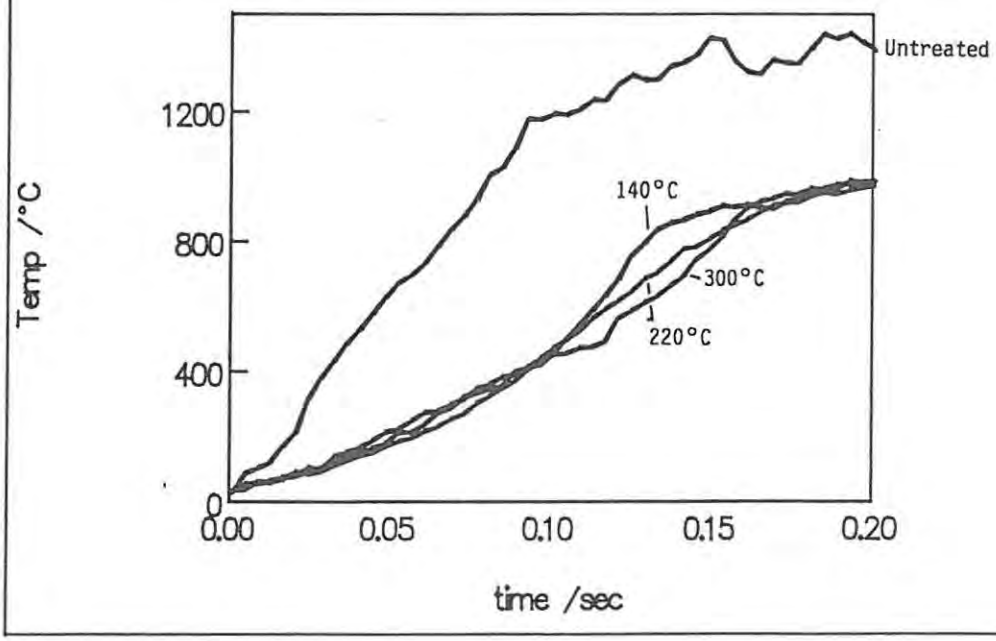

40% Mn/BaO_2 compositions pre-heated at different temperatures. The Mo/BaO_2 mixtures which had been heated to ~360°C had darkened. The products of combustion of the Mo/BaO_2 mixtures in the oven at ~420°C were green and had a non-metallic appearance. XRD analysis indicated the presence of unreacted Mo and BaO_2 and some BaO, MoO_3 and MoO_2 were also present. The Mn/SrO_2 mixtures burnt very vigorously after the pre-heating treatment. Figure 5.56 shows the temperature profiles recorded during combustion of 40% Mn/SrO_2 compositions pre-heated at different temperatures. The Mn/SrO_2 mixture after heating at ~360°C was darkened. After heating at ~420°C, the Mn/SrO_2 mixture appeared dark-grey and non-metallic and the XRD analysis showed that it contained mainly unreacted SrO_2 and Mn.

The burning rate of the 40% Mo/SrO_2 compositions was decreased (Table 5.18) by the pre-heating treatment. Figure 5.57 shows the temperature profiles recorded during combustion of 40% Mn/BaO_2 compositions pre-heated at different temperatures. Mixtures of Mo/SrO_2 heated to ~420°C showed no obvious signs of combustion, but would not burn under the normal experimental conditions in the open channel. The XRD pattern for this material was dominated by the presence of unreacted Mo and SrO_2, indicating that very little reaction had taken place.

5.5 BURNING OF BINARY SYSTEMS WITH OTHER FUELS:

During the selection of pyrotechnic systems for study, burning experiments with other transition metals and the two oxidants were attempted. These metal fuels (listed in Table 3.1) were mixed with BaO_2 or SrO_2 in the normal way (see Section 3.1 D) to give 20 and 40% binary compositions which (where possible) were ignited in the channel so that burning rates and temperature profiles could be recorded. The observed burning rates, maximum excess temperatures and mole ratios for these systems are shown in Table 5.19. The mass losses during combustion were also recorded (cooling in air over silica gel) and the results are included in Table 5.19.

TABLE 5.19 RESULTS OF BURNING EXPERIMENTS WITH SOME TRANSITION METAL FUELS, UNDER THE NORMAL EXPERIMENTAL CONDITIONS

SYSTEM	v_{obs} / mm s^{-1}	U_{max} / °C	MOLE RATIO FUEL:OXIDANT	% MASS LOSS ON BURNING
20% Cr/BaO_2	WOULD NOT BURN		0.81 : 1.00	-
40% Cr/BaO_2	3.8 ± 0.4	1427 ± 14	2.17 : 1.00	7.2 ± 2.5
20% Cr/SrO_2	3.0 ± 0.4	>1760	0.58 : 1.00	1.4 ± 0.9
40% Cr/SrO_2	4.3 ± 0.6	1651 ± 82	1.53 : 1.00	1.1 ± 0.2
20% Nb/BaO_2	WOULD NOT BURN		0.46 : 1.00	-
40% Nb/BaO_2	8.3 ± 0.9	>1760	1.22 : 1.00	6.7 ± 0.8
20% Nb/SrO_2	3.0 ± 0.4	>1760	0.32 : 1.00	4.4 ± 1.4
40% Nb/SrO_2	8.5 ± 0.8	>1760	0.86 : 1.00	5.1 ± 0.4
20% W/BaO_2	WOULD NOT BURN		0.23 : 1.00	-
40% W/BaO_2	1.2 ± 0.2	>1760	0.61 : 1.00	9.1 ± 0.3
20% W/SrO_2	WOULD NOT BURN		0.16 : 1.00	-
40% W/SrO_2	2.6 ± 0.4	>1760	0.43 : 1.00	0.4 ± 0.2

Fig 5.56 Temp profiles for 40% Mn/SrO_2 pre-heated to different temperatures

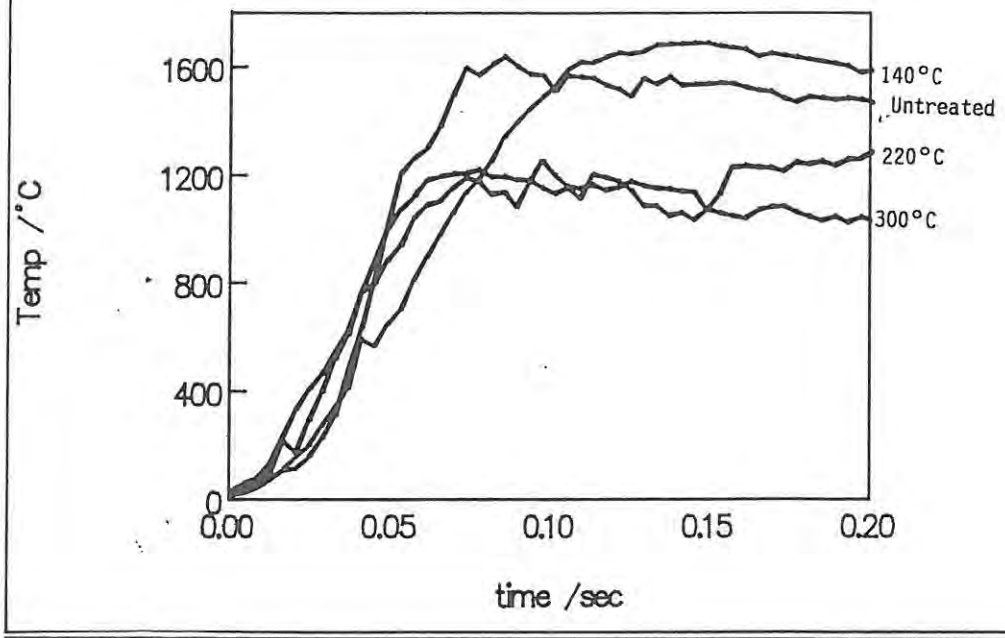

Fig 5.57 Temp profiles for 40% Mo/SrO_2 pre-heated to different temperatures

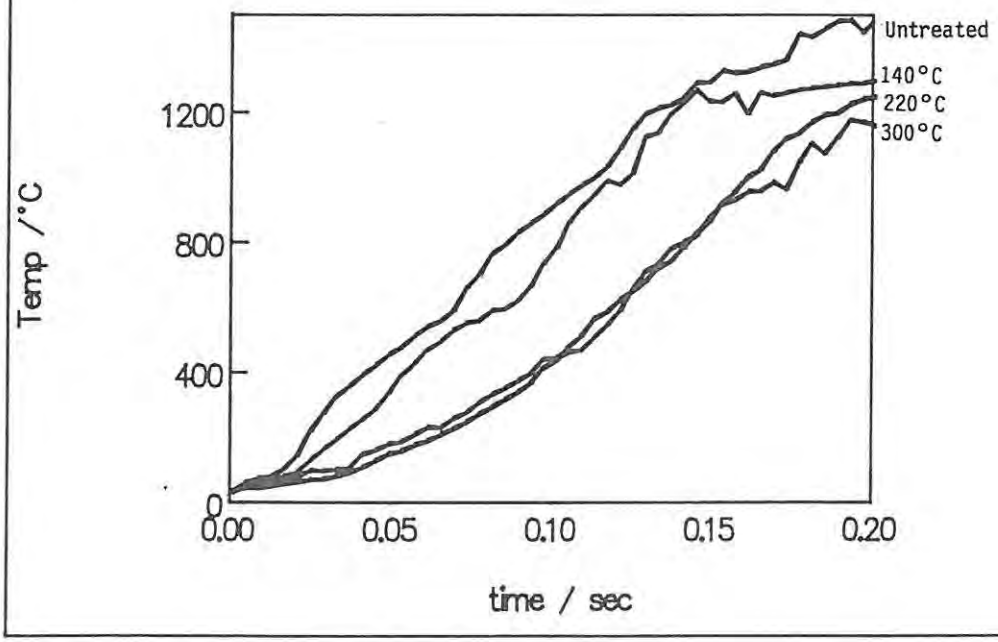

Nearly all of the above systems which burnt had maximum temperatures above the limit of the 1760°C for the thermocouples available and hence temperature profiles could not be recorded. Some points of interest which arise out of these few experiments are:

(i) there is generally a greater variation in burning rate with change in proportion of a given oxidant than by changing the oxidant at a fixed proportion by mass.

(ii) changing the fuel at a fixed proportion by mass and with a fixed oxidant has a more marked effect on the burning rate. This change may be complicated by the change in the molar proportions, but the order of atomic mass Cr, Nb, W, each with 60% BaO_2, does not give a regular sequence of burning rates (3.8, 8.3 and 1.2 mm s^{-1}). With 60% SrO_2 the sequence is similar: 4.3, 8.5 and 2.6 mm s^{-1}.

5.6 RESULTS FOR TERNARY SYSTEMS

Ternary pyrotechnic systems with various compositions were prepared in the normal way (see Section 3.1 D) and burnt in the open channel. Burning rates and temperature profiles were recorded for all the ternary systems and the results are presented in two categories: the mixed oxidant systems and the mixed fuel systems. Further discussion of these results is given in Chapter 10.

5.6.1 Mixed oxidant systems:

A. The Mn/BaO_2/SrO_2 system. The composition of this system was varied so that the quantity of SrO_2 was increased at the expense of the quantity of BaO_2. All the compositions from 50:50:0 (i.e. 50% Mn, 50% BaO_2 and 0% SrO_2) through to 50:0:50 (with 12.5% steps) burnt under the normal experimental conditions. The composition affected the burning rate and maximum excess temperature of the Mn/BaO_2/SrO_2 system as shown in Table 5.20. The mole ratio of the three constituents is also presented for comparison.

TABLE 5.20 EFFECTS OF COMPOSITION OF THE Mn/BaO_2/SrO_2 SYSTEM ON THE DENSITY, BURNING RATE AND MAXIMUM EXCESS TEMPERATURE

COMPOSITION / %	v_{obs} / mm s^{-1}	U_{max} / °C	MOLE RATIO
Mn / BaO_2 / SrO_2			
50 : 50 : 0	9.1 ± 0.41	1182 ± 57	1.00:0.32:0.00
50 : 37.5 : 12.5	3.5 ± 0.69	1173 ± 3	1.00:0.24:0.11
50 : 25 : 25	4.1 ± 0.46	1228 ± 5	1.00:0.16:0.23
50 : 12.5 : 37.5	4.8 ± 0.18	1340 ± 20	1.00:0.08:0.34
50 : 0 : 50	6.8 ± 1.23	1198 ± 27	1.00:0.00:0.46

The temperature profiles for the different compositions of this ternary system are shown in Figure 5.58. Although these profiles are all very similar, the profiles of the ternary mixtures are more like the profiles of the Mn/BaO_2 system than of the Mn/SrO_2 system.

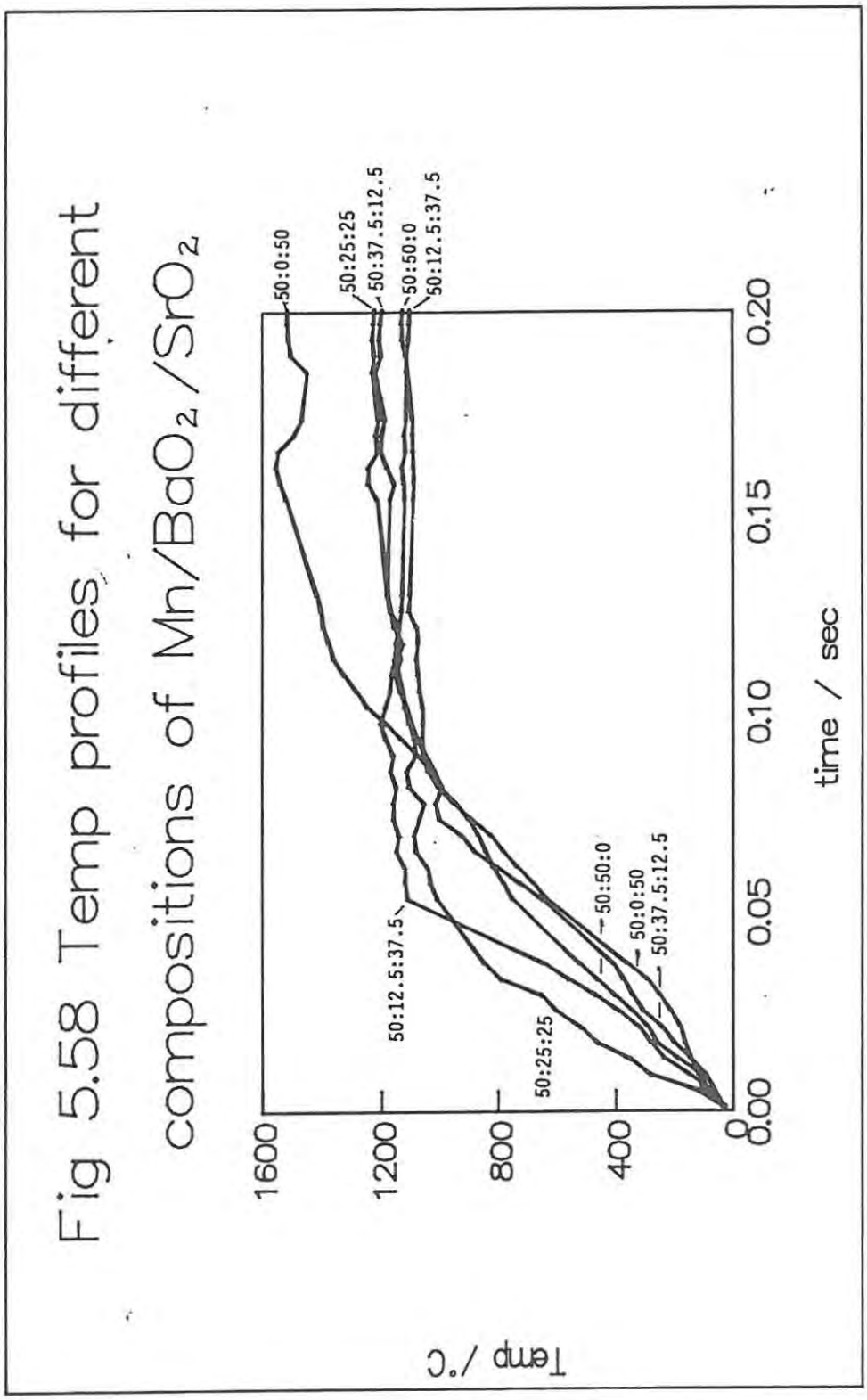
Fig 5.58 Temp profiles for different compositions of Mn/BaO2 /SrO2
Temp /°C
time / sec
1600
1200
800
400
0.00
0.05
0.10
0.15
0.20
50:0:50
50:25:25
50:37.5:12.5
50:50:0
50:12.5:37.5
50:12.5:37.5
50:25:25
50:50:0
50:0:50
50:37.5:12.5

B. The $Mo/BaO_2/SrO_2$ system. In this system, the ratio of the masses of the two oxidants was changed in steps of 10% from 30:70:0 (i.e. 30% Mo, 70% BaO_2 and 0% SrO_2) to 30:0:70. These compositions were all difficult to ignite and only one ternary mixture (30:20:50) and one binary mixture (30% Mo/BaO_2) sustained combustion over the complete length of the channel. The results are shown in Table 5.21. Extra amounts of starting increment (i.e. a 2 mm thick layer of 50% $Mn/KMnO_4$, see Section 5.1.2 A) were used without success to promote ignition.

TABLE 5.21 EFFECTS OF COMPOSITION OF THE $Mo/BaO_2/SrO_2$ SYSTEM ON THE BURNING RATE AND MAXIMUM EXCESS TEMPERATURE

COMPOSITION / %	v_{obs} / mm s^{-1}	U_{max} / °C	MOLE RATIO
Mo / BaO_2 / SrO_2			
30 : 70 : 0	4.4 ± 0.8	1678 ± 14	1.00:1.32:0.00
30 : 60 : 10	WOULD NOT BURN		1.00:1.13:0.27
30 : 50 : 20	WOULD NOT BURN		1.00:0.94:0.53
30 : 40 : 30	WOULD NOT BURN		1.00:0.76:0.80
30 : 30 : 40	WOULD NOT BURN		1.00:0.57:1.07
30 : 20 : 50	1.8 ± 0.1	1593 ± 127	1.00:0.38:1.34
30 : 10 : 60	WOULD NOT BURN		1.00:0.19:1.60
30 : 0 : 70	WOULD NOT BURN		1.00:0.00:1.87

5.6.2 Mixed fuel systems:

A. The $Mo/Mn/BaO_2$ system. The composition of this ternary mixture was varied by increasing the quantity of Mn, at the expense of the quantity of Mo metal, in steps of 10% from 30:0:70 (i.e. 30% Mo, 0% Mn and 70% BaO_2) to 0:30:70. Both ternary compositions were difficult to ignite and only one (10:20:70) sustained combustion throughout the length of the channel. The results are shown in Table 5.22.

TABLE 5.22 EFFECTS OF COMPOSITION OF THE $Mo/Mn/BaO_2$ SYSTEM ON THE BURNING RATE AND MAXIMUM EXCESS TEMPERATURE

COMPOSITION / %	v_{obs} / mm s^{-1}	U_{max} / °C	MOLE RATIO
Mo / Mn / BaO_2			
30 : 0 : 70	4.4 ± 0.8	1678 ± 14	0.76:0.00:1.00
20 : 10 : 70	WOULD NOT BURN		0.50:0.44:1.00
10 : 20 : 70	2.0 ± 0.1	1481 ± 78	0.25:0.88:1.00
0 : 30 : 70	9.4 ± 0.4	>1760	0.00:1.32:1.00

B. The Mo/Mn/SrO_2 system. Ternary compositions of this system were made up in a similar way to the system above, but two extra compositions (25:5:70 and 22.5:7.5:70) were included. The effects of composition on the burning rate and maximum excess temperature are shown in Table 5.23.

TABLE 5.23 EFFECTS OF COMPOSITION OF THE Mo/Mn/SrO_2 SYSTEM ON THE BURNING RATE AND MAXIMUM EXCESS TEMPERATURE

COMPOSITION / %	v_{obs} / mm s^{-1}	U_{max} / °C	MOLE RATIO
Mo / Mn / SrO_2			
30 : 0 : 70	WOULD NOT BURN		0.53:0.00:1.00
25 : 5 : 70	WOULD NOT BURN		0.45:0.16:1.00
22.5: 7.5 : 70	2.3 ± 0.3	1489 ± 85	0.40:0.23:1.00
20 : 10 : 70	2.2 ± 0.4	1508 ± 206	0.36:0.31:1.00
10 : 20 : 70	5.2 ± 0.3	1557 ± 9	0.18:0.62:1.00
0 : 30 : 70	6.6 ± 1.0	1547 ± 129	0.00:0.93:1.00

The two extra compositions were included to identify more precisely the quantity of Mn that had to be added to the 30% composition of the Mo/SrO_2 binary system, which was known (see Section 5.4.2) not to burn under the experimental conditions, to make it sustain combustion. Table 5.23 shows that if 7.5% of the total mass was replaced by Mn then the ternary composition would sustain combustion in the channel.

The temperature profiles for the compositions of this ternary system which burnt are shown in Figure 5.59. As the proportion of Mo was increased the amplitude of the profiles increased. However, when the proportion of Mo was greater than the proportion of Mn (20:10:70) the slope of the rise zone decreased markedly and the binary mixture of Mo and SrO_2 (30:0:70) would not burn.

5.7 THERMOCHEMICAL INFORMATION FROM TEMPERATURE PROFILES

The total heat evolved by the combustion wave in a pyrotechnic mixture (ref 23) is given by:

$$Q = cU_{ad}$$

where U_{ad} is calculated by integration of the excess temperature function between arbitrary times t_1 and t_2 in the remote rise and decay zones respectively. The specific heat capacities of the powdered pyrotechnic mixtures can be estimated from the composition, masses and the specific heat capacities of the pure bulk solids. Plots of Q against composition are given in Figures 5.60 a and 5.60 b for the two BaO_2 systems and the two SrO_2 systems, respectively, and in Figures 5.61 a and 5.61 b for the two Mn systems and the two Mo systems, respectively.

The thermocouple diameter will affect these values of Q since they are calculated from temperature profiles and so they will need to be converted to values expected for a thermocouple wire of negligible diameter. As before, correction was done by extrapolation of the approximately linear plots of Q against the thermocouple wire diameter d. The parameters of the relationship, $Q = md + C$ are shown in Table 5.24.

Fig 5.59 Temp profiles for different compositions of Mo/Mn/SrO_2

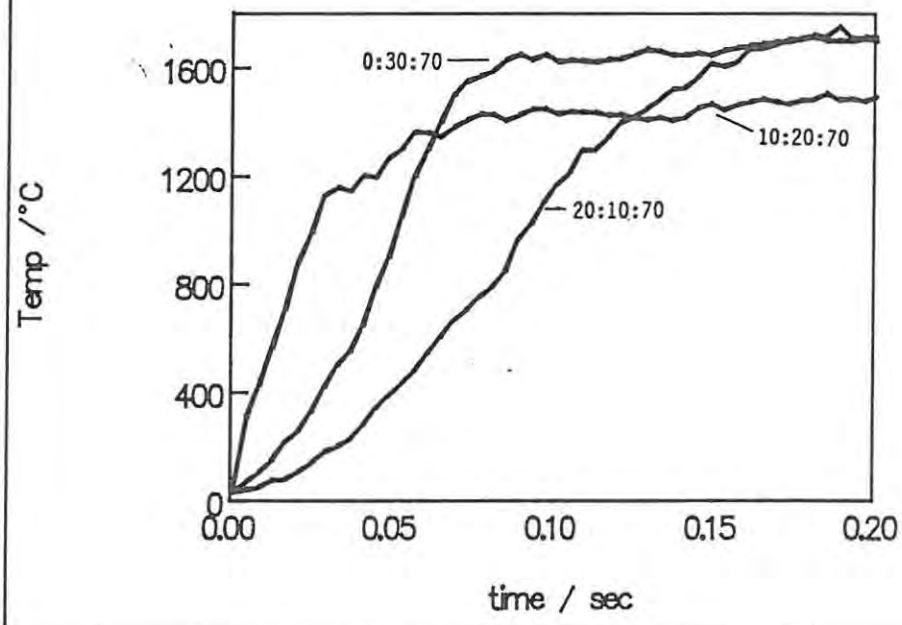

Fig 5.60a Qvs composition for the two BaO_2 systems

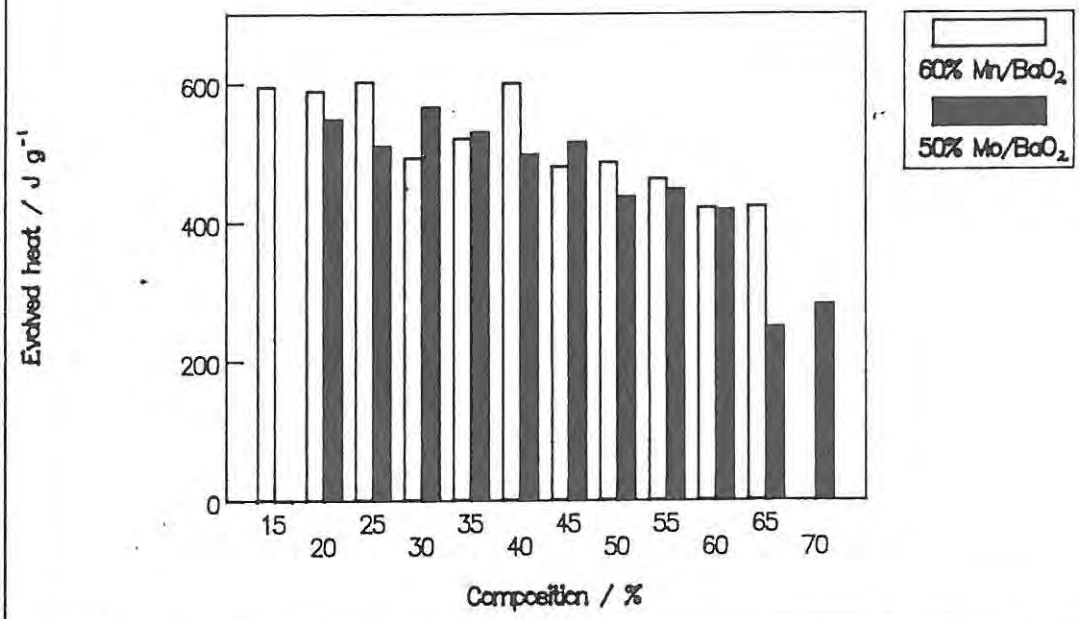

Fig 5.60b Q vs composition for the two SrO_2 systems

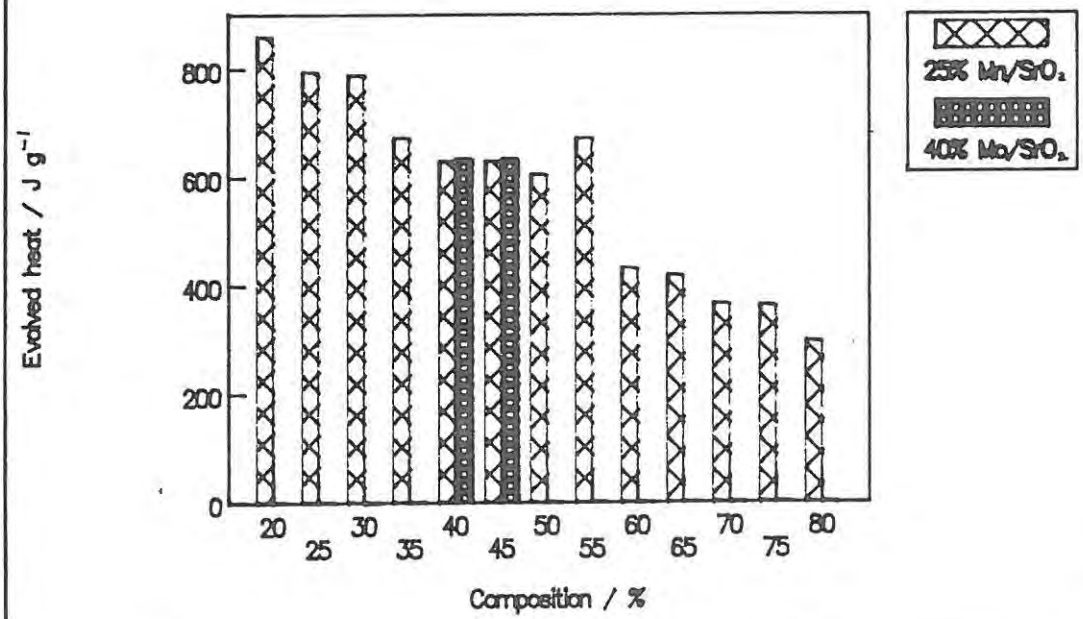

Fig 5.61aQ vs composition for the two Mn systems

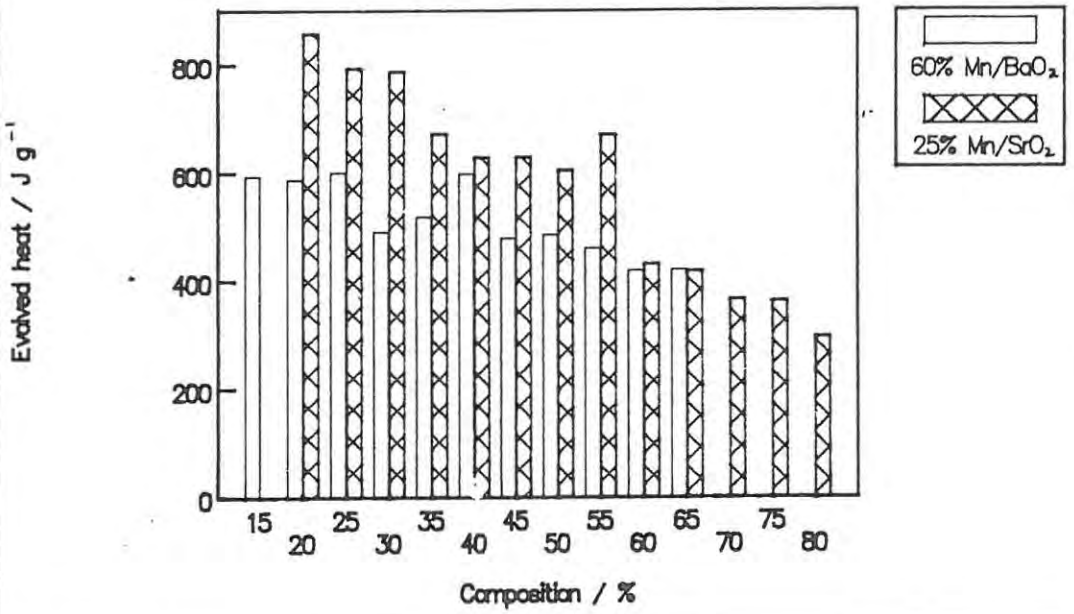

Fig 5.61bQ vs composition for the two Mo systems

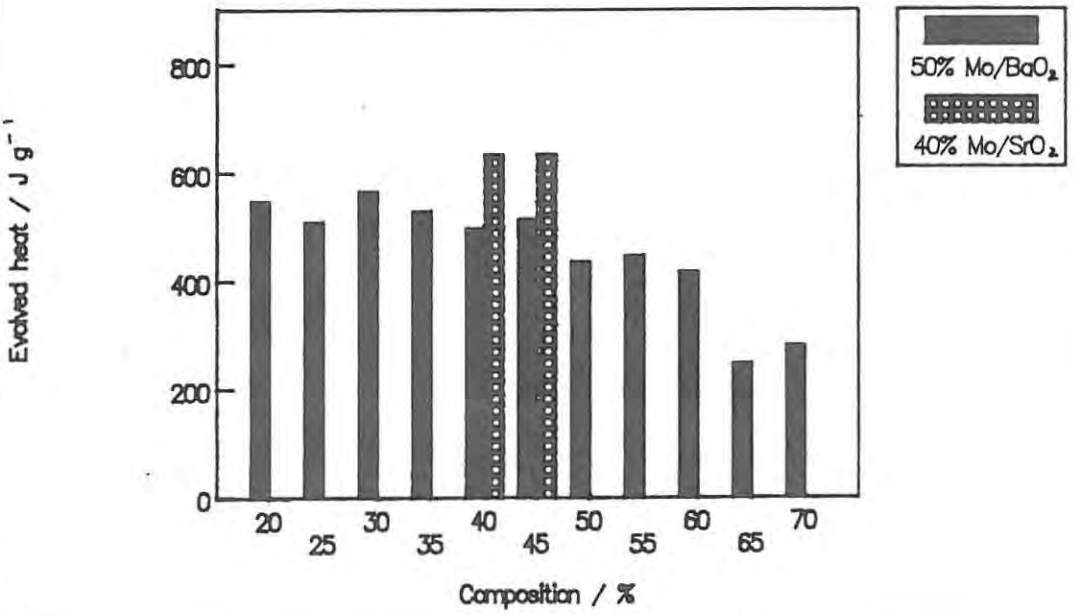

TABLE 5.24 PARAMETERS OF RELATIONSHIP BETWEEN Q AND d			
SYSTEM	SLOPE / J g^{-1} mm^{-1}	Y INTERCEPT / J g^{-1}	CORRELATION COEFFICIENT
Mn/BaO_2	-322 ± 103	455 ± 20	0.91
Mo/BaO_2	-405 ± 155	520 ± 30	0.88
Mn/SrO_2	-1116 ± 116	1019 ± 22	0.99
Mo/SrO_2	-409 ± 131	714 ± 25	0.91

Values calculated from $Q = cU_{ad}$ are compared with values determined by thermal analysis and bomb calorimetry (see Section 6.2) in the discussion of the binary systems (Chapter 9).

5.8 KINETIC INFORMATION FROM TEMPERATURE PROFILES

The temperature profiles for all compositions of the four binary systems were analysed (see Section 5.2) using the Hill approach (Section 1.3 A) by inspecting plots of $\{\ln(d\alpha/dt) - n \ln(1 - \alpha)\}$ against 1/T for linearity, using various values for the "order-of-reaction", n. The effect of the value of n on the derived kinetic parameters for 20% compositions of three systems and 40% for the Mo/SrO_2 is shown in Table 5.25.

TABLE 5.25 KINETIC PARAMETERS FOR BINARY COMPOSITIONS (HILL APPROACH)						
SYSTEM	VALUES FOR n					
	0.5		1		2	
	E_a/kJ mol^{-1}	A	E_a/kJ mol^{-1}	A	E_a/kJ mol^{-1}	A
20% Mn/BaO_2	5.9 ± 0.9	73 ± 5	11.1 ± 1.3	170 ± 10	21.4 ± 2.3	1000 ± 50
20% Mo/BaO_2	3.0 ± 1.2	32 ± 1	5.5 ± 1.3	54 ± 8	10.4 ± 1.7	148 ± 15
20% Mn/SrO_2	4.8 ± 1.5	26 ± 3	11.7 ± 2.1	114 ± 50	31.6 ± 0.3	4390 ± 100
40% Mo/SrO_2	8.4 ± 3.7	74 ± 30	10.8 ± 3.1	125 ± 50	17.6 ± 2.4	456 ± 130

The relationship between the activation energy, calculated using n equal to 1, and composition is shown in Figures 5.62 a and 5.62 b for the two BaO_2 systems and the two SrO_2 systems, respectively, and in Figures 5.63 a and 5.63 b for the two Mn and the two Mo systems, respectively. As might be expected the curves for the Mn/BaO_2 and Mn/SrO_2 systems are more similar to each other than either is to the curve for the Mo/BaO_2 system. Reaction is more likely to be controlled by the properties of the metal and its oxidation product than by the properties of the oxidant.

Since the values for the activation energy were also calculated from temperature profiles they will be affected by diameter of the thermocouple wire and therefore need correction to values expected for a thermocouple wire of negligible diameter (Section 5.4.3 B). Corrected values for the activation energy, E_a, can be calculated by extrapolation of the approximately linear plots of E_a (calculated using n = 1) against the thermocouple wire diameter d. The parameters of the relationship, $E_a = md + C$ are shown in Table 5.26.

Fig 5.62a Ea vs composition for the two BaO_2 systems (n = 1)

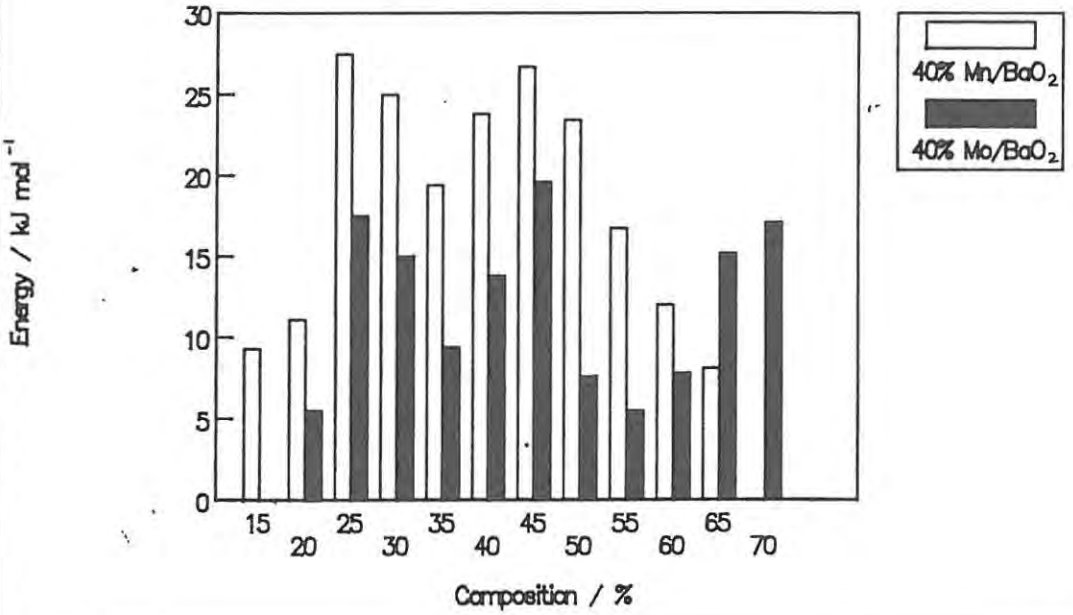

Fig 5.62b Ea vs composition for the two SrO_2 systems (n = 1)

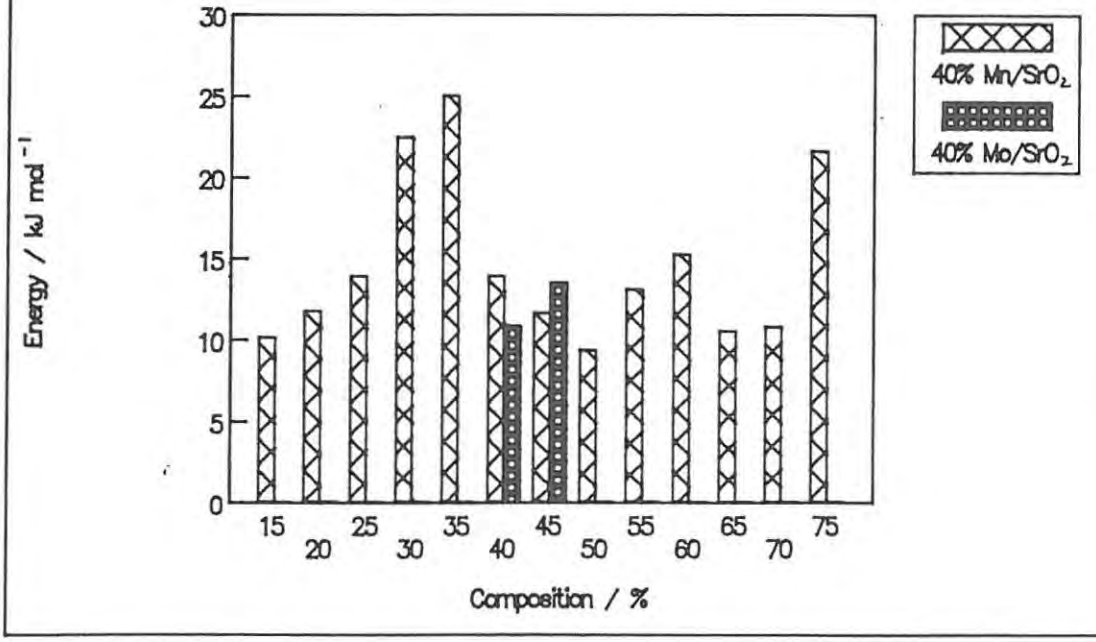

Fig 5.63a Ea vs composition for the two Mn systems (n = 1)

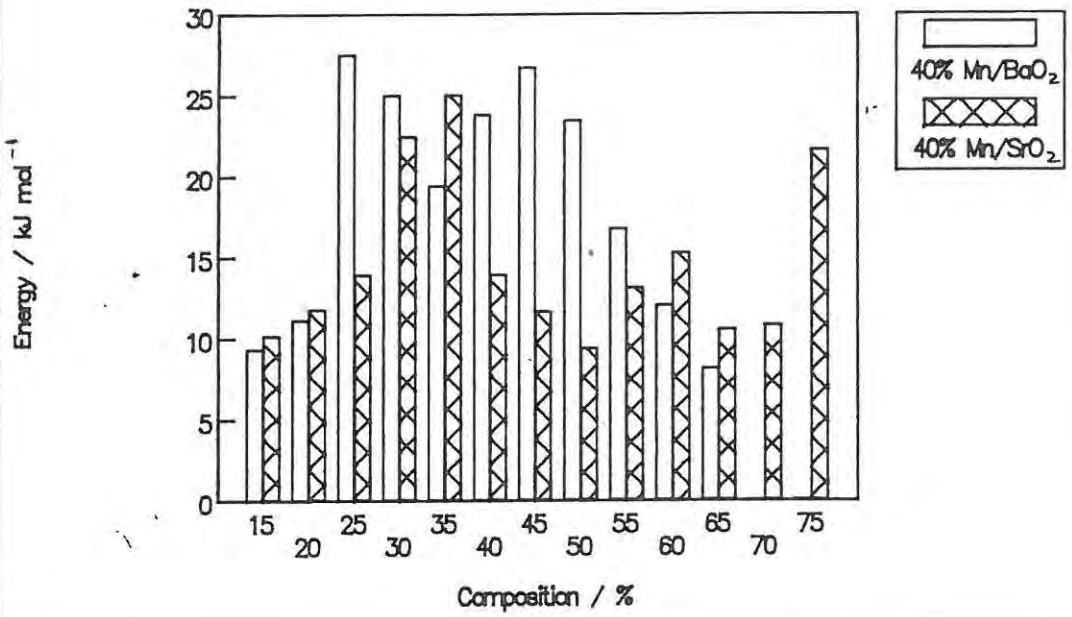

Fig 5.63b Ea vs composition for the two Mo systems (n = 1)

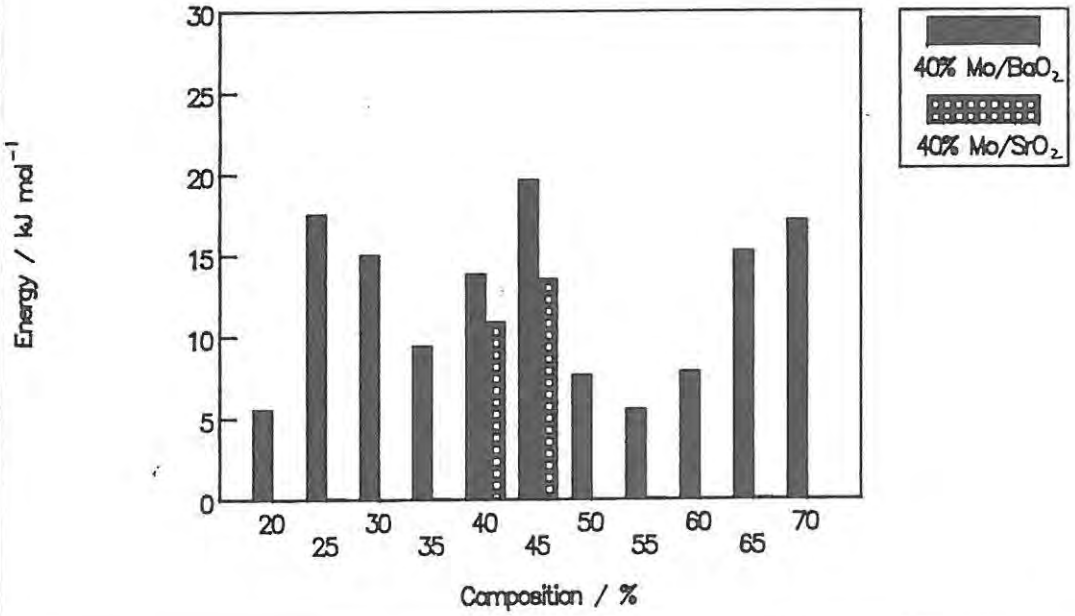

TABLE 5.26 PARAMETERS OF RELATIONSHIP BETWEEN E_a & d			
SYSTEM	SLOPE /kJ mol^{-1} mm^{-1}	Y INTERCEPT / kJ mol^{-1}	CORRELATION COEFFICIENT
60% Mn/BaO_2	-24.0 ± 6.2	14.2 ± 1.2	0.94
50% Mo/BaO_2	-33.5 ± 1.6	10.9 ± 0.3	1.00
20% Mn/SrO_2	-19.0 ± 4.7	14.5 ± 0.9	0.95
40% Mo/SrO_2	-22.9 ± 6.2	14.1 ± 1.2	0.93

Leeds approach. This approach to temperature profile analysis (see Section 5.2) was applied to the 20% compositions for three of the systems and to 40% Mo/SrO_2. An algorithm was used to minimize the sum of the residuals $(G_{exp} - G_{calc})^2$, and thus values for E_a, A and n were calculated (see Sections 1.3 B and 5.2). The results of this approach are shown in Table 5.27. The correlation between G_{exp} and G_{calc}, using both linear and non-linear regression routines, is shown in Figures 5.64 to 5.67 for the four systems.

TABLE 5.27 KINETIC PARAMETERS USING THE LEEDS TREATMENT						
SYSTEM	BMDP	a x 10^3	b	n	E_a / kJ mol^{-1}	A
20% Mn/BaO_2	L	169.8	1501 ± 143	0.38 ± 0.02	12.5 ± 1.2	107.6
	NL	344.9 ± 32.0	1864 ± 86	0.65 ± 0.03	15.5 ± 0.7	218.6 ± 20.2
20% Mo/BaO_2	L	122.5	2245 ± 83	0.18 ± 0.01	18.7 ± 0.7	74.6
	NL	139.5 ± 8.6	2595 ± 79	0.20 ± 0.01	21.6 ± 0.6	85.0 ± 5.2
20% Mn/SrO_2	L	2214.0	2823 ± 252	0.57 ± 0.05	23.5 ± 2.1	1264.4
	NL	1585.0 ±407.0	2445 ± 186	0.65 ± 0.05	20.3 ± 1.6	905.2 ± 232.4
40% Mo/SrO_2	L	183.6	4000 ± 111	0.13 ± 0.01	33.2 ± 1.0	118.0
	NL	282.1 ± 61.7	4530 ± 271	0.15 ± 0.02	37.7 ± 2.2	181.3 ± 39.7

In the two BaO_2 systems and in the two SrO_2 systems, the two Mo containing systems have higher E_a values than the two Mn containing systems. This supports the possibility that the reaction mechanism is dependent on the fuel rather than the oxidant.

Comparison of results obtained by the Hill and Leeds approaches. The α-time curves obtained from the two different approaches are similar (Figure 5.13) and are dependent upon the value of the rise time, t_r. The definitions of α are:

$$\text{Hill: } \alpha = \theta - t_r(d\theta/dt)$$

$$\text{where } \theta = U/U_{max} \text{ and } U = T - T_a$$

$$\text{Leeds: } \alpha = \int_0^t G\,dt \Big/ \int_0^{t_f} G\,dt$$

$$\text{where } G = (U/t_d) + (du/dt) - t_r(d^2U/dt^2)$$

The Hill approach requires selection of a value for the apparent order of reaction, n, before the Arrhenius parameters, E_a and A, are derived. The Leeds approach optimizes all three parameters.

Fig 5.64 Correlation between G_{Exp} & G_{Calc}

20% Mn/BaO_2

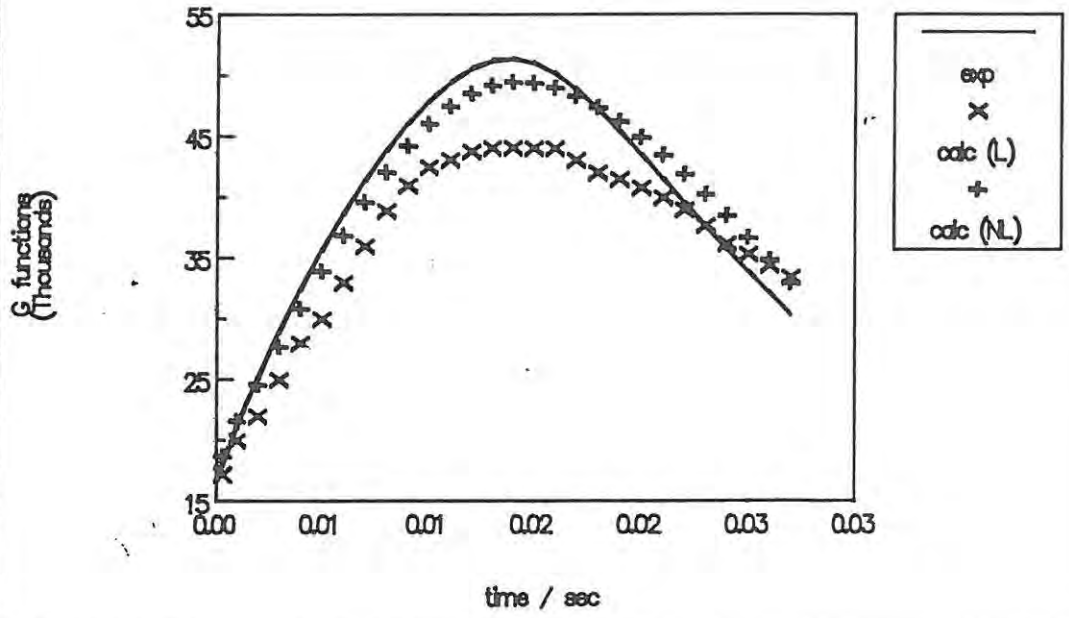

Fig 5.65 Correlation between G_{Exp} & G_{Calc}

20% Mo/BaO_2

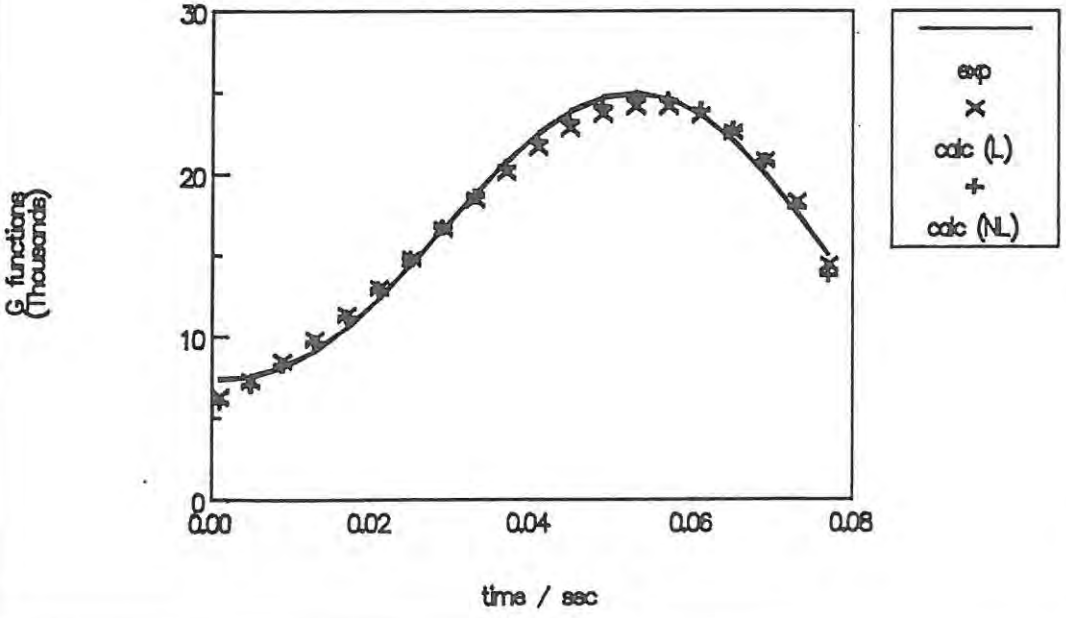

Fig 5.66 Correlation between G_{Exp} & G_{Calc}

20% Mn/SrO_2

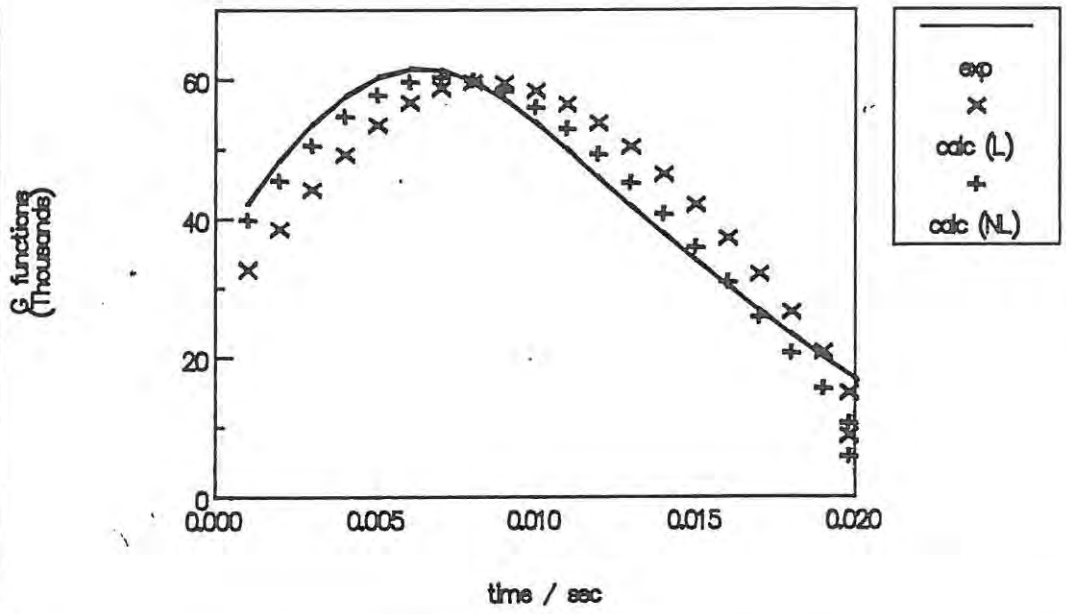

Fig 5.67 Correlation between G_{Exp} & G_{Calc}

40% Mo/SrO_2

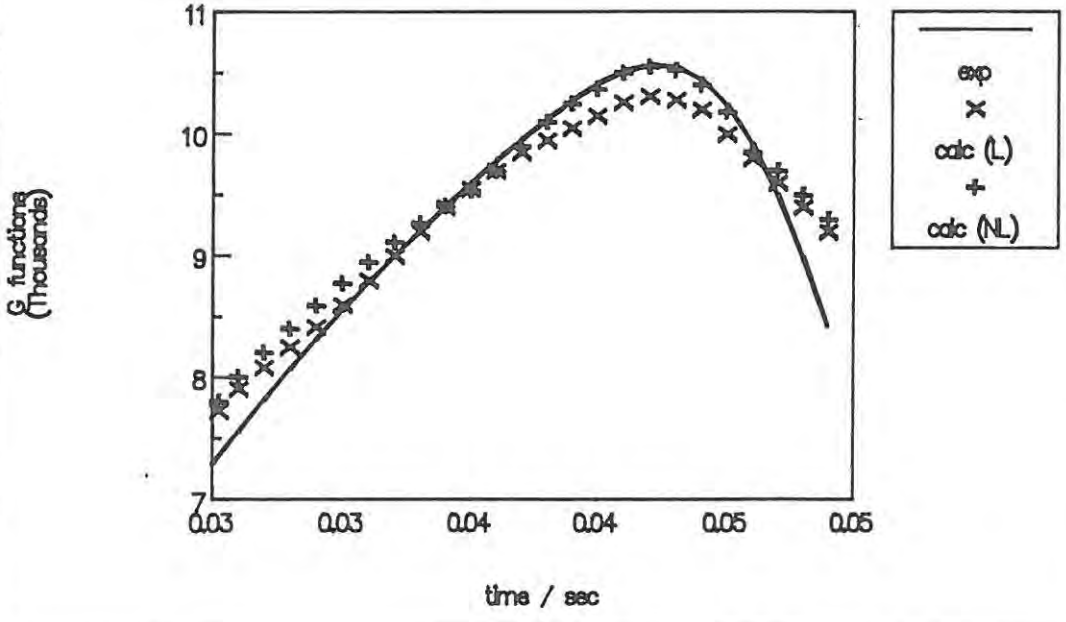

The values of n obtained from the Leeds analysis (Table 5.27) are generally low (0.1 to 0.7) with the linear optimization giving slightly lower values than the non-linear method.

Considering only the 20% Mn/SrO_2 system as an example, the value of n was 0.65 and E_a was 20.3 ± 1.6 kJ mol^{-1} (Table 5.27). The Hill treatment (Table 5.25) for the same composition gave values of E_a from 5 to 32 kJ mol^{-1} as n was increased from 0.5 to 2.0. Using n = 0.65, the value of E_a (Table 5.28) was 13.9 ± 1.4 kJ mol^{-1}. This is fair agreement considering the sensitivity of the value of E_a to the values of n and t_r, the considerable data processing involved and, in the Hill approach, the choice of temperature range to be regarded as linear in the Arrhenius plot.

TABLE 5.28 COMPARISON OF KINETIC DATA FOR THE 20% Mn/SrO_2 COMPOSITION

n = 0.65		t_r = 0.02 s	
LEEDS		HILL	
E_a/kJ mol^{-1}	A	E_a/kJ mol^{-1}	A
20.3 ± 1.6	905.2 ± 232.4	13.9 ± 1.4	220.3 ± 2.7

CHAPTER 6: THERMAL CONDUCTIVITY

Theoretical background. Since the theoretical model for the propagation of a combustion wave in a pyrotechnic mixture is based on the conduction of heat, it is important to know something of the thermal conductivity of these mixtures. A relatively simple technique, adapted specially to determine the thermal conductivity of pyrotechnic powders by Beck *et al* (ref 68), was used in this study. In this technique, a thermal probe made of copper metal, containing a heater resistance and a thermocouple junction, is surrounded by the sample material. A known potential is applied to the heater circuit and the EMF generated by the thermocouple junction is used to monitor the temperature of the probe as a function of time. Within the first short time period the temperature of the probe is determined by the applied potential and the heat capacity of the copper metal. Later the temperature rise is determined by the thermal properties of the surrounding material.

If the copper probe is assumed to be spherical with effective radius, a, and to have infinite thermal conductivity, then equation 6.1 can be used (ref 69) to estimate its temperature, when it is embedded with negligible contact resistance in a uniform material of infinite extent.

$$T = Q\{1 - (2/\pi)I\}/\{4\pi a \lambda\} \qquad \text{——— 6.1}$$

Q is the rate of supply of heat and λ is the thermal conductivity of the surrounding medium. If u is taken as the radial distance in the medium from the probe (relative to the effective radius of the probe, a), then I is the integral between u = zero and u = infinity of a two dimensional function, f, of u and the time, t, such that:

$$f(u,t) = \frac{\exp(-\lambda t u^2/a^2 \rho c)}{\{(u^2/k)-1\}^2 + u^2} \qquad \text{——— 6.2}$$

where the probe is in contact with a medium of density, ρ, and specific heat capacity, c. The quantity k is characteristic of the specific probe (of effective radius a, mass M_p, and specific heat capacity c_p) and is given by:

$$k = 4\pi a^3 \rho c/M_p c_p \qquad \text{——— 6.3}$$

The trapezoidal rule was used to determine the area under the curve of function f against u using steps of 0.1 and terminating the integration at a function value of 1×10^{-10}. These values of I were substituted into equation 6.1 and so the theoretical probe temperature could be calculated at any time. These theoretical temperature-time curves were made to fit the measured data by adjusting the values of the effective probe radius and the thermal conductivity of the reference material, Al_2O_3. Once a suitable effective radius was determined, only the thermal conductivity was varied on subsequent runs on other powdered samples.

6.1 EXPERIMENTAL

The dimensions of the probe are shown in Figure 6.1. The mass was 4.63 g and the specific heat capacity of copper was taken as 0.385 J K^{-1} g^{-1} (ref 59). A chromel-alumel thermocouple with a wire diameter of 0.25 mm was used and the 10 Ω heating resistor was connected to a regulated low-voltage *DC* source. The input power, Q, was determined from measurements of current and voltage. A value of approximately 0.2 W was required to produce a steady-state temperature of about 20°C above ambient. The output of the thermocouple was referenced to ice. The signal was then amplified (255x) and read at 1 s intervals, via a 12 bit ADC, by an IBM-compatible microcomputer.

The thermal conductivities of powders are very sensitive to interparticle contact, so samples were loaded with gentle tamping into a cylinder surrounding the probe (Figure 6.2) and then compacted by pressing the piston with a dead load of 13 MPa (unless otherwise stated) for 1 minute. The probe and sample are thermally insulated from the base by a "Perspex" platform. The dimensions of the cylinder used by Beck *et al* (ref 68) were reduced in order to decrease the amount of sample required. The decrease in the dimensions was shown to have no effect on the temperature-time curves. The equation used to estimate the temperature of the probe (equation 6.1) assumes infinite extent of sample.

Sample densities were determined from the measured masses and the dimensions of the cylinder. Specific heat capacities were estimated from the composition, masses and the specific heat capacities of the pure bulk solids. The heat capacity of the residual air was neglected.

The materials used are listed in Table 6.1, together with estimates of their particle-size ranges (see Section 3.1 A). The void fractions were calculated from the published (ref 53) bulk densities and the measured densities of the powdered materials compressed under a load of 13 MPa for 1 minute. The thermal conductivities of various compositions of the four binary pyrotechnic systems (mixed in the normal way, see Section 3.1 D) were also measured.

TABLE 6.1 MATERIALS USED

SAMPLE	PARTICLE SIZE μm	BULK DENSITY g cm^{-3}	SAMPLE DENSITY* g cm^{-3}	VOID* FRACTION
BaO_2	36.6 (median size)	5.67	2.43 ± 0.12	0.57
SrO_2	3.5 (median size)	4.71	1.49 ± 0.09	0.68
Mn	16.6 (median size)	7.44	2.87 ± 0.05	0.61
Mo	34.4 (median size)	10.28	5.40 ± 0.94	0.47
Al_2O_3	< 120 (sieve size)	3.97	1.82 ± 0.14	0.54

*Compressed under a load of 13 MPa for 1 minute

Fig 6.1 Thermal conductivity probe

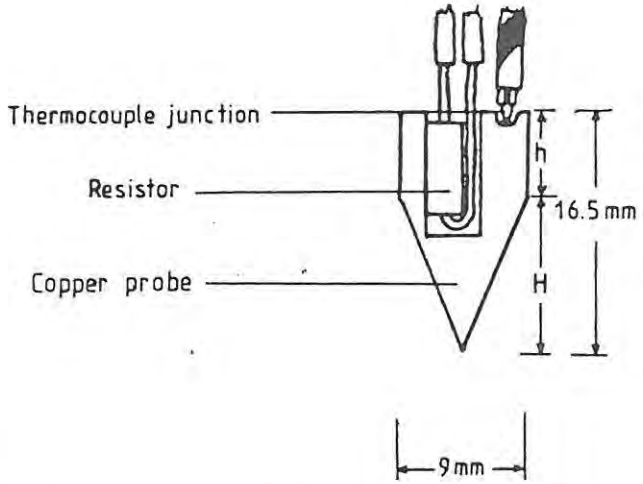

Fig 6.2 Apparatus for measuring thermal conductivity

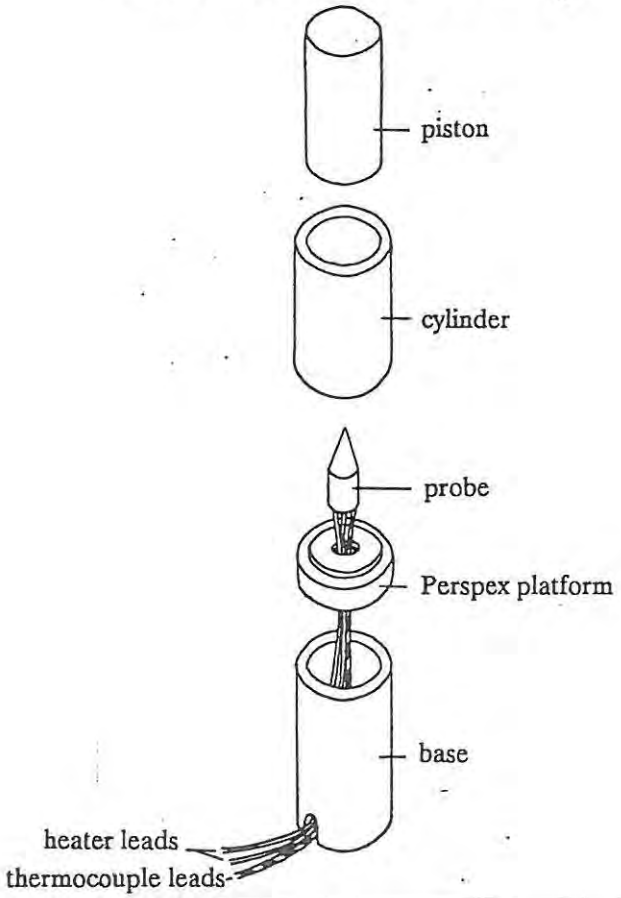

6.2 RESULTS

The temperature-time curves consisted of a relatively rapid rise over about 100 s to a maximum steady-state temperature. Typical results for the various materials are shown in Figure 6.3. The reproducibility of the temperature-time curves is illustrated by the three unsmoothed examples shown in Figure 6.4 for BaO_2 compressed under a load of 13 MPa for 1 minute. The thermal conductivities calculated from these curves are 0.61, 0.56 and 0.49 W m^{-1} K^{-1}. Three main factors influence the reproducibility: the uncertainty in λ arising from fitting the calculated curve to a single experimental curve; the reproducibility of the current and voltage settings; and the effect on λ of irreproducibility of compaction. The three runs give $\lambda = 0.55 \pm 0.06$ W m^{-1} K^{-1}.

The radius, r, of the probe is 4.5×10^{-3} m giving an actual surface area of 4.7×10^{-4} m^2 ($2\pi r\{h + H\}$, where h and H are as in Figure 6.1). The initial value for the effective radius was taken to be 6.1×10^{-3} m since this gives a spherical surface area equal to the actual surface area. A range of values (from 5.5×10^{-3} to 6.6×10^{-3} m) for the effective radius was used to fit the theoretical temperature-time curve to the measured profile for Al_2O_3. The shape of the theoretical profile was not very sensitive to this range of values, so the initial value was used. With this value of a, the thermal conductivity for Al_2O_3 was estimated to be 0.23 W m^{-1} K^{-1}. This is in excellent agreement with the 0.22 W m^{-1} K^{-1} measured by Beck *et al* (ref 68) using this technique. The results for the other materials are listed in Table 6.2, along with the calculated values of the thermal diffusivity ($D = \lambda / \rho c$) and the void fractions.

TABLE 6.2 RESULTS FOR INDIVIDUAL POWDERS (COMPRESSED UNDER 13 MPa FOR 1 MINUTE)

SAMPLE	λ W m^{-1} K^{-1}	c J K^{-1} g^{-1}	ρ g cm^{-3}	$D_2 \times 10^{-7}$ m^2 s^{-1}	VOID FRACTION
BaO_2	0.55 ± 0.05	0.387	2.43 ± 0.12	5.93 ± 0.77	0.49
SrO_2	0.31 ± 0.03	0.568	1.49 ± 0.09	3.69 ± 0.58	0.33
Mn	0.39 ± 0.02	0.495	2.87 ± 0.05	2.74 ± 0.19	0.40
Mo	0.46 ± 0.02	0.256	5.40 ± 0.14	3.33 ± 0.31	0.53
Al_2O_3	0.23 ± 0.02	1.098	1.82 ± 0.14	1.15 ± 0.10	0.51

Interparticle contact and void fractions affect the thermal conductivities of powdered samples. The values of λ for uncompacted samples of BaO_2, SrO_2 and Mn are compared in Table 6.3 with values for the same samples compressed under loads of 13 and 50 MPa. The particle-size of the sample also affects the thermal conductivity. Results of measurements on two different particle-size ranges of the Mn sample are shown in Table 6.3.

Fig 6.3 Temperature–time curves

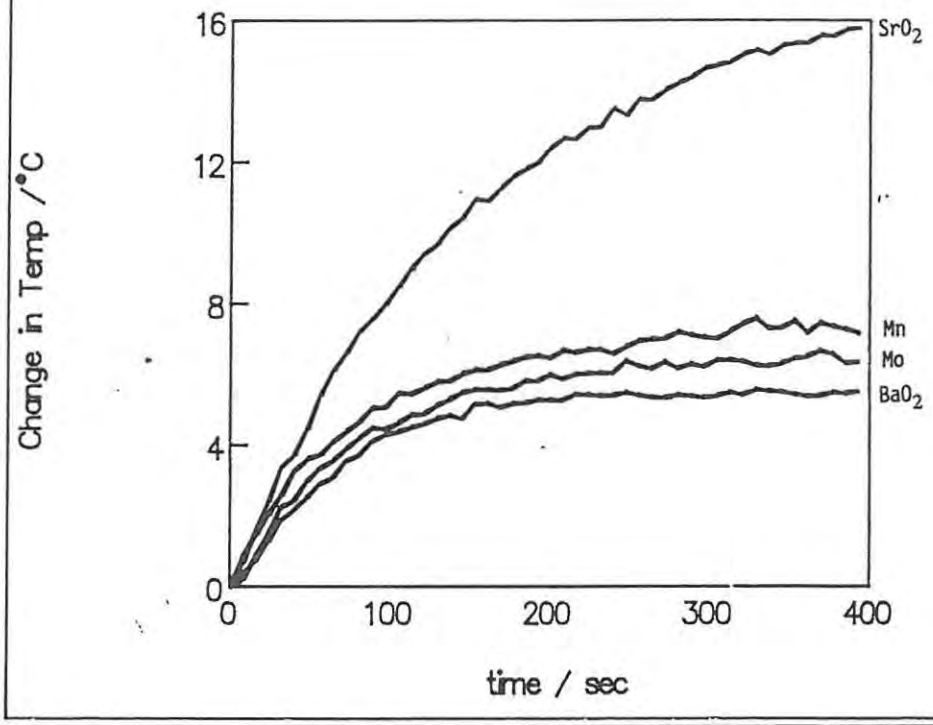

Fig 6.4 Reproducibility of temperature–time curves (BaO_2)

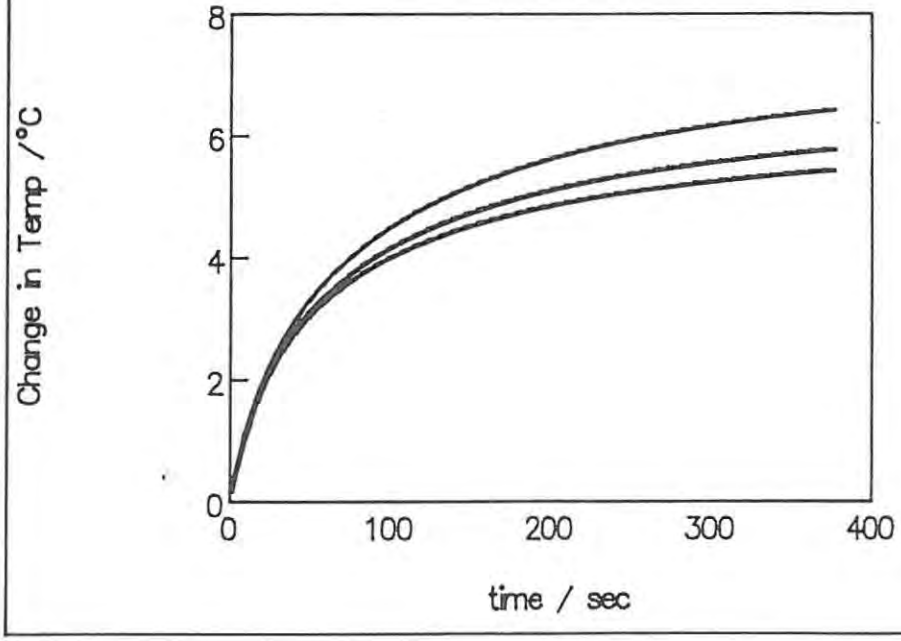

TABLE 6.3 INTERPARTICLE CONTACT AND THERMAL CONDUCTIVITY					
SAMPLE	COMPRESSION M Pa	MEDIAN PARTICLE-SIZE / μm	λ W m^{-1} K^{-1}	SAMPLE ρ g cm^{-1}	VOID FRACTION
BaO_2	0	36.6	0.33 ± 0.02	1.77 ± 0.01	0.69
BaO_2	13	36.6	0.55 ± 0.05	2.43 ± 0.12	0.57
BaO_2	50	36.6	0.59 ± 0.05	2.96 ± 0.16	0.48
SrO_2	0	3.5	0.21 ± 0.02	0.68 ± 0.03	0.86
SrO_2	13	3.5	0.31 ± 0.03	1.49 ± 0.09	0.68
SrO_2	50	3.5	0.27 ± 0.02	2.57 ± 0.09	0.45
Mn	0	16.6	0.27 ± 0.05	2.19 ± 0.03	0.71
Mn	13	16.6	0.39 ± 0.03	2.85 ± 0.04	0.62
Mn	13	112.6	0.40 ± 0.03	3.39 ± 0.01	0.54

The technique was applied to binary pyrotechnic mixtures of various compositions. The results are listed in Table 6.4.

TABLE 6.4 RESULTS FOR PYROTECHNIC MIXTURES (COMPRESSED UNDER 13 MPa FOR 1 MINUTE)					
SAMPLE	λ W m^{-1} K^{-1}	c J K^{-1} g^{-1}	ρ g cm^{-3}	$D_2 \times 10^{-7}$ m^2 s^{-1}	VOID FRACTION
10% Mn/BaO_2	0.55 ± 0.021	0.362	2.44 ± 0.12	6.23 ± 0.91	0.58
20% Mn/BaO_2	0.52 ± 0.030	0.373	2.61 ± 0.08	5.35 ± 0.33	0.56
40% Mn/BaO_2	0.48 ± 0.034	0.397	2.76 ± 0.19	4.38 ± 0.36	0.56
10% Mo/BaO_2	0.63 ± 0.024	0.343	2.69 ± 0.14	6.82 ± 0.25	0.55
20% Mo/BaO_2	0.70 ± 0.042	0.334	2.82 ± 0.11	7.44 ± 0.52	0.55
40% Mo/BaO_2	0.67 ± 0.072	0.316	3.42 ± 0.29	6.21 ± 0.61	0.50
10% Mn/SrO_2	0.27 ± 0.030	0.492	1.61 ± 0.09	3.41 ± 0.22	0.67
20% Mn/SrO_2	0.28 ± 0.021	0.490	1.86 ± 0.10	3.08 ± 0.19	0.63
40% Mn/SrO_2	0.31 ± 0.017	0.488	2.21 ± 0.12	2.88 ± 0.12	0.60
10% Mo/SrO_2	0.26 ± 0.021	0.472	1.74 ± 0.18	3.16 ± 0.23	0.65
20% Mo/SrO_2	0.31 ± 0.023	0.451	1.94 ± 0.09	3.54 ± 0.20	0.63
40% Mo/SrO_2	0.30 ± 0.016	0.407	2.29 ± 0.11	3.21 ± 0.19	0.62

Contrary to expectations, the thermal conductivities of pyrotechnic mixtures (except for the Mn/SrO_2 system) did not increase with an increase in metal over the range of compositions investigated.

CHAPTER 7: CALORIMETRY

Introduction. The theoretical model for the propagation of a combustion wave through a pyrotechnic mixture allows the total heat evolved by the wave, Q, to be obtained from the product of the adiabatic excess temperature, U_{ad} (where $U = T_{exp} - T_a$), and the heat capacity of the mixture (see Section 1.3 B). Values for U_{ad} can be calculated by numerical integration of the excess temperature function, U, between arbitrary times t_1 and t_2 in the remote rise and decay zones, respectively, of the temperature profile recorded during combustion. The specific heat capacities of the powdered pyrotechnic mixtures can be estimated from the composition, masses and the specific heat capacities of the pure bulk solids. Values of Q, calculated in this way, (Section 5.4) can be compared with values determined from DSC traces and from bomb calorimetry.

The DSC investigation of the four binary pyrotechnic systems was discussed in Chapter 4. The bomb calorimetry investigation of 40% compositions of the four binary pyrotechnic systems is presented here.

7.1 EXPERIMENTAL

In bomb calorimetry, changes in internal energy, ΔU, due to the combustion of a sample in a constant volume reaction vessel (bomb), can be monitored by observing the temperature changes in a plain jacket calorimeter. If only pV work is involved, the change of internal energy is related to the enthalpy of reaction by the expression:

$$\Delta H = \Delta U + [pV](\text{products}) - [pV](\text{reactants})$$

This expression can be simplified, for reactions of the type A(s) + B(s)→ C(s), to:

$$\Delta H \approx \Delta U$$

since the volumes of the products and reactants are nearly the same. Thus results of bomb calorimetry can be compared with ΔH values determined from DSC traces and from temperature profiles.

A PAAR 1341 plain jacket bomb calorimeter was used with a known mass of water as the calorimetric fluid. Uniform temperature of the calorimetric water was insured by continuous mechanical stirring and temperature changes were measured with a digital thermometer which had a reported precision of ±0.01°C. The heat capacity of the calorimeter was determined by burning a known mass of chemically pure benzoic acid (Holpro, S.A.) in an atmosphere of pure oxygen at a pressure of 20 atm and monitoring the resulting temperature rise. This procedure was repeated four times. The benzoic acid sample was contained in a gelatin capsule (calorific value 18500 J g^{-1}) inside the bomb. The sample was ignited with a known length of electrically heated fuse wire (calorific value 9.6 J cm^{-1}).

Known masses of 40% compositions of the four binary pyrotechnic systems (Mn/BaO_2, Mo/BaO_2, Mn/SrO_2 and Mo/SrO_2), mixed in the normal way, were loaded with gentle tamping into gelatin capsules and burnt in an atmosphere of pure nitrogen at a pressure of about 1 atm. Each experiment was repeated three times. The heated fuse wire alone was not sufficient to cause ignition in all of the pyrotechnic compositions, so a slurry of the starter increment used in the burning experiments (i.e. 50% $Mn/KMnO_4$) was used to coat the fuse wire in order to aid the ignition stimulus. Corrections were made for the quantity of heat produced by the starter increment.

Attempts were made to use the open stainless-steel channel, used in the temperature profile experiments, as a receptacle for the pyrotechnic mixtures in the calorimetric bomb. The fuse wire was inserted length-wise in the channel and the composition was gently tamped around the wire. The lid and spacer (see Figure 4.1 a) were then placed on the assembly and pressed with a dead load of 50 MPa for a period of 1 minute. The fuse wire within the compressed sample in the channel did not reach sufficiently high temperatures to ignite the composition before the uncovered extremities of the wire melted thus breaking the electrical circuit. The experimental conditions of bomb calorimetry thus refer to the use of gelatin capsules.

7.2 RESULTS

The heat capacity of the bomb and calorimeter, calculated from the calibration experiments, was 10.43 ± 0.82 kJ K^{-1}.

The results of the bomb calorimetry for 40% compositions for the four binary pyrotechnic mixtures are given in Table 7.1.

TABLE 7.1 RESULTS OF BOMB CALORIMETRY

SAMPLE	Q / kJ g^{-1}
40% Mn/BaO_2	1.42 ± 0.32
40% Mo/BaO_2	1.07 ± 0.03
40% Mn/SrO_2	1.54 ± 0.24
40% Mo/SrO_2	-

Under the conditions of bomb calorimetry, the 40% Mo/SrO_2 composition would not ignite, even with the aid of the $Mn/KMnO_4$ starting increment. This is compatible with the DSC traces which showed no exothermic event when the composition was heated at rates between 10 and 160°C min^{-1} in N_2 and with sample masses of up to ~30 mg (see Section 4.4.2). Only two compositions (40 and 45%) of the Mo/SrO_2 system (with sample masses of 2 to 3 g compacted under loads of about 50 MPa) would ignite and burn in the open channel (see Section 5.4).

CHAPTER 8: CHARACTERIZATION OF REACTANTS AND PRODUCTS

Characterization of the starting materials and the reaction products was attempted using X-ray powder diffraction (XRD) and infrared (IR) spectroscopy. The physical shapes and sizes of powdered materials were observed using scanning electron microscopy (SEM).

8.1 EXPERIMENTAL

8.1.1 Materials:

The materials used are listed in Tables 3.1 and 3.2. Unless otherwise stated, pyrotechnic mixtures containing BaO_2 were made from the Merck sample of this oxidant.

8.1.2 Apparatus:

XRD. The XRD patterns were recorded, at room temperature, on a Phillips diffractometer with Cu Kα radiation monochromatized with graphite. The resulting wavelength was 1.54050 Å. The XRD patterns were measured from $2\theta = 4°$ to 72° and the intensities of the diffractions were calculated relative to the largest response. The corresponding d-spacings were calculated using the Bragg law.

IR. IR spectra, in KBr pellets, were recorded in the range 4000-200 cm^{-1} with a Perkin-Elmer 180 spectrophotometer.

SEM. Micrographs of finely powdered samples were taken using a Joel scanning electron microscope at a filament voltage of 10 kV. The samples were sputter coated with gold prior to examination.

8.2 RESULTS

Neither IR or XRD analysis gave totally conclusive results on their own. Thus the assignments of the observed absorption bands in the IR spectra and diffractions in the XRD patterns were made in conjunction with each other.

The reactants. The IR spectra for the Merck sample of BaO_2 and SrO_2 are reproduced in Figures 8.1 and 8.2. The bands at ~840 cm^{-1} as well as the broad bands starting at ~1530 cm^{-1} were assigned (refs 70, 71, 72, 73) to ν_2 intra-ionic vibrations in carbonate ions. The peroxides were advertised as only 85% pure, and carbonate is an expected impurity. Exposure of BaO_2 and SrO_2 to moist atmospheres is reported (refs 8, 10, 29, 74, 53) to promote the reaction:

$$2MO_2(s) + 2CO_2(g) \rightarrow 2MCO_3(s) + O_2(g)$$

where M = Ba or Sr. Thus varying quantities of carbonate surface layer were expected, depending on the length and quality of storage. A further band which was also assigned (ref 70) to the carbonate ion

Fig 8.1 IR spectrum for BaO_2 (Merck)

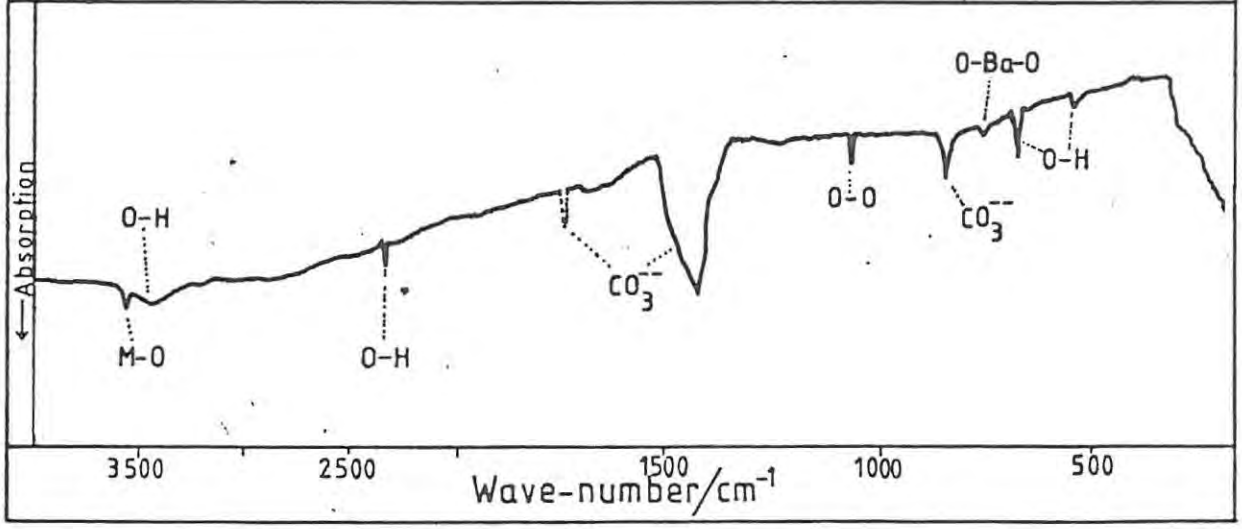

Fig 8.2 IR spectrum for SrO_2

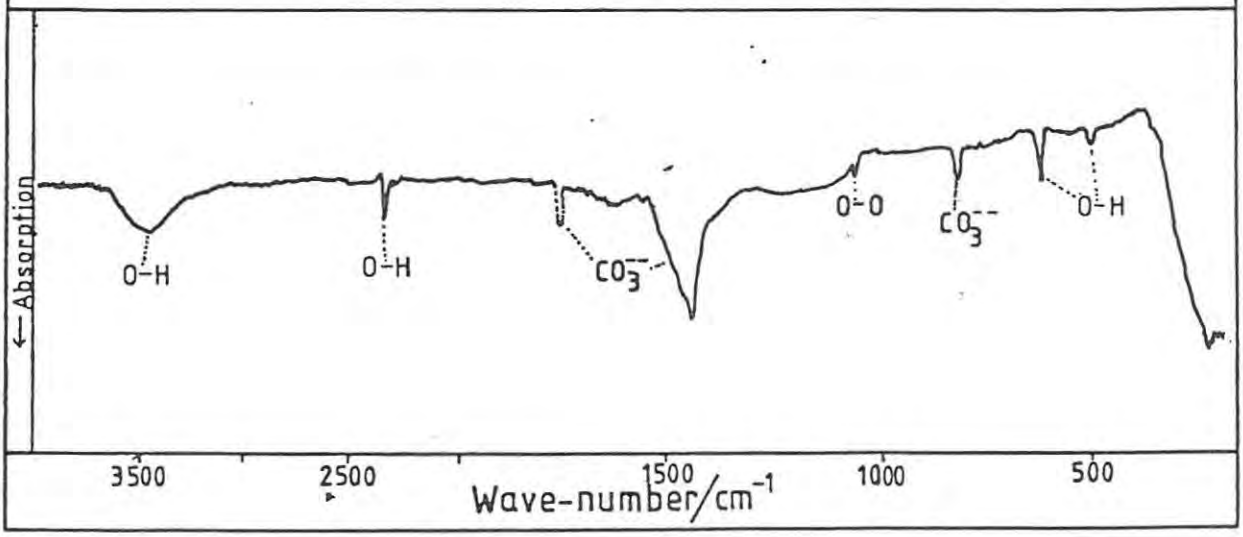

(see dotted line in Figure 8.1 at 1750 cm^{-1}), was noted in the IR spectrum for the BDH sample of BaO_2 and probably indicated an increased presence of $BaCO_3$ in this sample. Chemical analysis of the BDH sample of BaO_2 (Section 3.1 A) showed that it contained less peroxide than the Merck sample of BaO_2, presumably because more carbonate had formed.

Another expected (refs 8, 29, 53) impurity of alkali earth peroxides is hydroxide, which forms during the exposure of the peroxide to water vapour. The bands at 685 and 700 cm^{-1} in Figures 8.1 and 8.2, respectively, were assigned (ref 70) to vibrations within the hydroxide ion.

SEM showed that the shape and texture of the particles of the Merck BaO_2 (Plate 1) were significantly different from the particles of the BDH BaO_2 (Plate 2). The texture of the BDH particles was very rough giving a "furry" and striated appearance. This rough texture was probably due to the formation of a surface layer of $BaCO_3$ (ref 10). The particles of artificially aged Merck BaO_2 (Plate 3) also had a rough texture. By comparison of Plates 3 and 4 (BDH BaO_2) it can be seen that the artificially aged sample was very similar in appearance to the naturally aged BDH sample.

SEM of the SrO_2 samples showed that the artificially aged sample of SrO_2 had no observable differences from the untreated sample of SrO_2 (Plate 5). This plate also shows that the SrO_2 samples are large compacts of small particles seen in more detail at higher magnifications (Plate 6).

The absorption band at 1055 cm^{-1} (Figure 8.1) in the IR spectrum for Merck BaO_2 was assigned (ref 75) to the ν_1 intra-ionic O-O stretching mode in $Ba^+O_2^-$ species. The corresponding absorption in the IR spectrum for SrO_2 (Figure 8.2) was observed at 1070 cm^{-1}. Since the Sr^{2+} ion is smaller than the Ba^{2+} ion, the stabilizing effect due to the polarizing of the Sr^{2+} ion will not be as great as for Ba^{2+} and, therefore, this absorption takes place at a slightly higher wave-number for SrO_2 than for BaO_2.

Ault and Andrews (ref 75) argue two different assignments for the 780 cm^{-1} absorption band which is seen in the spectrum of Merck BaO_2. One assignment is the ν_3 vibration of a O-Ba-O species, resulting in an estimated O-Ba-O bond angle of 40°, which is consistent with predicted $Ba^+O_2^-$ species. Alternatively, this band could be due to the peroxide $(O\text{-}O)^{2-}$ stretching mode in a $Ba_2^{2+}O_2^{2-}$ species. Similar absorptions are predicted but not observed for SrO_2.

The XRD pattern for the Merck sample of BaO_2 (Figure 8.3 a) was consistent with the pattern reported (ref 76) for pure BaO_2 (Figure 8.3 b). However, the XRD patterns for the BDH sample of BaO_2 and the two artificially aged samples (moist BaO_2 Merck and dried BaO_2 BDH) all had diffractions at smaller 2θ angles than exhibited by Merck BaO_2 and their maximum intensity diffractions were at larger d-spacings than the maximum intensity diffraction for pure BaO_2 (3.33 Å). The presence of $BaCO_3$ and $Ba(OH)_2$ whose maximum intensity diffractions are at 3.72 Å and at 6.00 Å, respectively, is probably responsible for these additional lines in the XRD patterns.

Fig 8.3a Reference XRD pattern for BaO_2

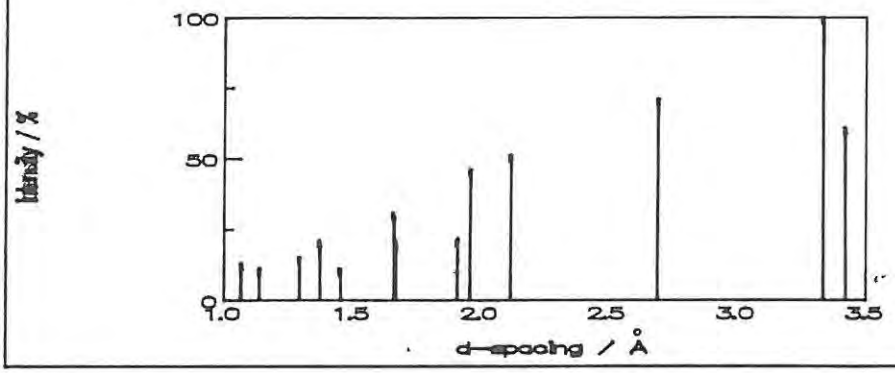

Fig 8.3b XRD pattern for BaO_2 (Merck)

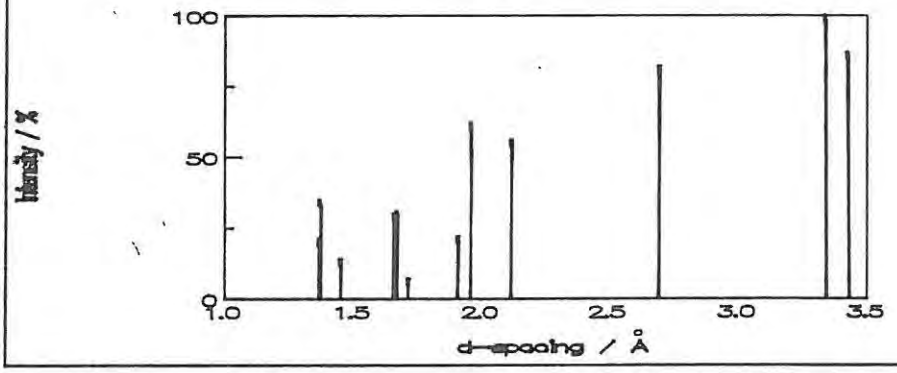

Fig 8.4a Reference XRD pattern for SrO_2

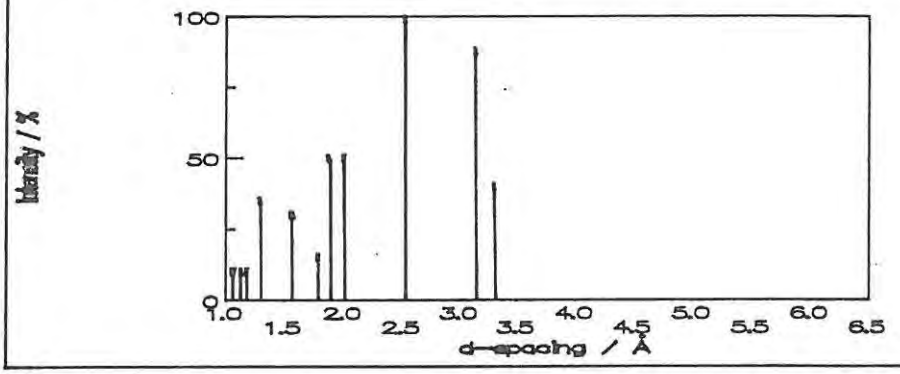

Fig 8.4b XRD pattern for SrO_2

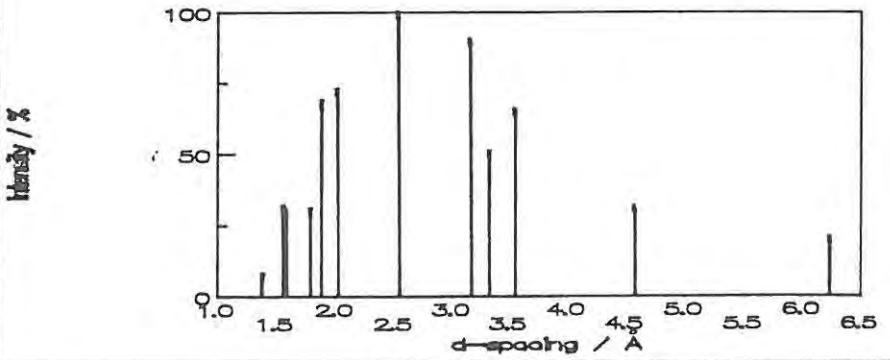

Fig 8.5a XRD pattern for Mn

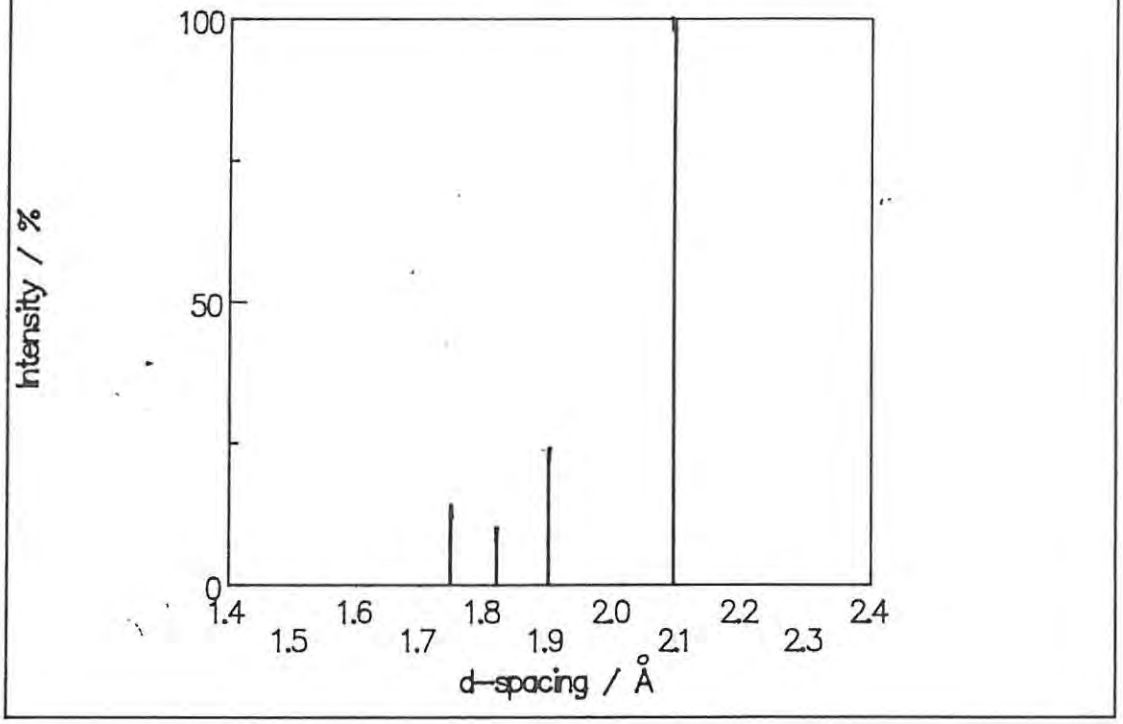

Fig 8.5b XRD pattern for Mo

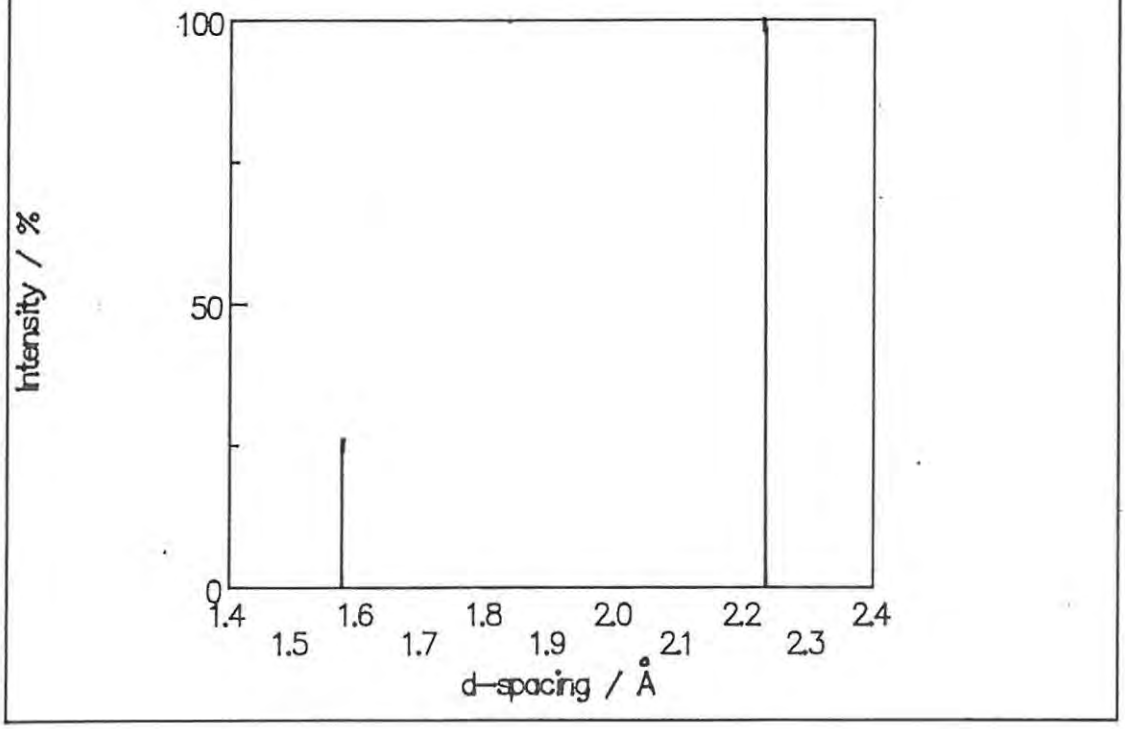

Fig 8.6a XRD pattern for combustion products of 40% Mn/BaO_2

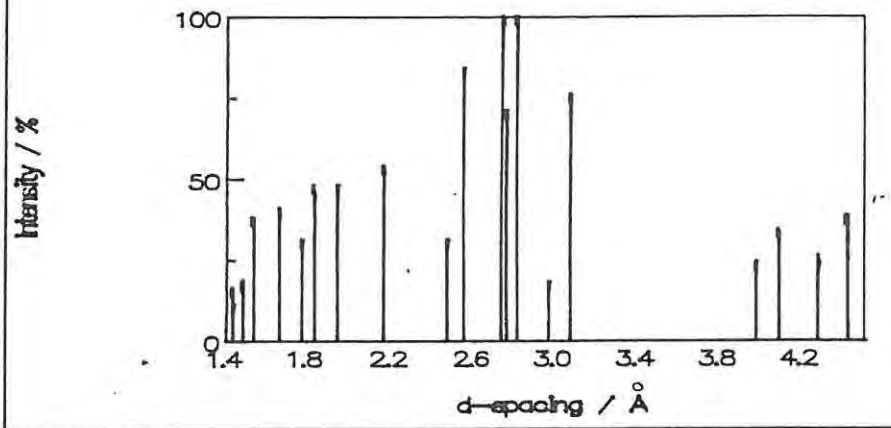

Fig 8.6b XRD pattern for sample of 40% Mn/BaO_2 heated to 360°C in oven

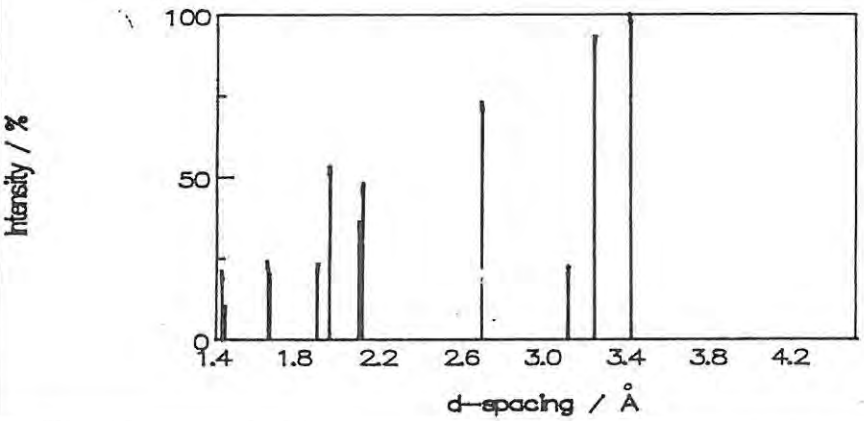

Fig 8.6c XRD pattern for sample of 40% Mn/BaO_2 heated to 950°C in TG

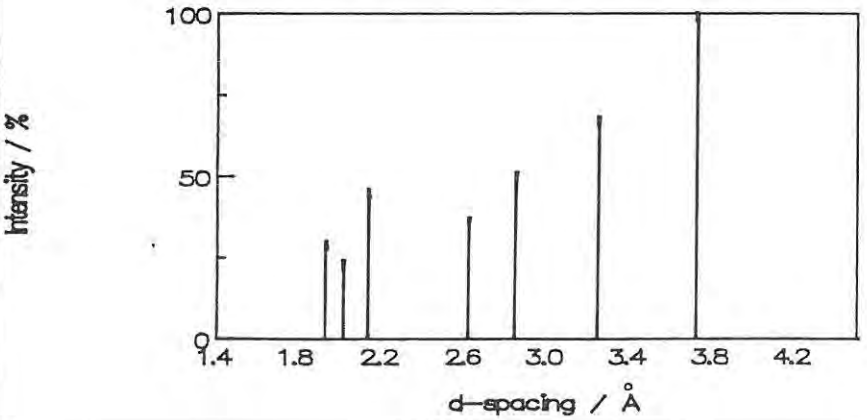

The dried sample of SrO_2 produced an XRD pattern (Figure 8.4 a) which was most like the reported (ref 76) pattern for strontium peroxide (Figure 8.4 b). Diffractions at large d-spacings (6.232 and 6.366 Å) indicated that SrO_2 and, especially the moist sample of SrO_2, either contain sufficient quantities of adsorbed water to produce XRD patterns similar to that of $SrO_2.8H_2O$, or they retain the crystal structure of the hydrate. The samples of SrO_2 and moist SrO_2 showed signs of contamination with small amounts of $SrCO_3$ and $Sr(OH)_2$.

As expected, the very pure samples of Mn and Mo (Table 3.1) produced simple XRD patterns (Figure 8.5 a and b) corresponding closely to the reported data (ref 76) for these metals. SEM showed that the range of particle-sizes of Mn (Plate 7) was large and that the particles were generally sharp chips, typical of mechanical grinding. Many of the Mo particles (Plate 8) had a twisted appearance suggesting that this sample was prepared from metal turnings.

Reactants after various heat treatments. Thermal analysis (Section 4.2) showed that both the oxidants, BaO_2 and SrO_2, underwent two thermal events at temperatures greater than ~300°C that were important in the initiation of reaction with either Mn or Mo. To investigate the role of these thermal events in the combustion reaction, the oxidants were subjected to heat treatment before being mixed with the fuels (see Section 5.4.5). XRD and IR analysis of the oxidants after this heat treatment showed that little thermal decomposition had taken place in the BaO_2 sample after it had been heated to about 420°C but that considerable quantities of the SrO_2 had been replaced by SrO and $SrCO_3$ after it had been heated to about 520°C. The XRD patterns of both samples showed no signs of diffractions due to the crystalline hydroxides. Similar results were obtained for samples of BaO_2 and SrO_2, which had been heated (to 420°C for BaO_2 and 520°C for SrO_2) and cooled for 30 minutes in dry N_2 in the DSC.

Reaction products. The products of the reactions which took place in either the open channel (Chapter 5), the thermal analysis equipment (Chapter 4), or in the convection oven (Section 5.4.5) were characterized using XRD and IR analysis. Generally these products were similar and consisted of complex mixture of unreacted starting materials, metal oxides of varying metal to oxygen ratios and complex oxides consisting of two metals and oxygen (e.g. $BaMoO_4$). However, the proportion of unreacted materials to metal oxides in the products from non-ignition studies (i.e. thermal analysis and pre-combustion heat treatments) was higher than in the products from the combustion in the open channel. Although precise identification of all the products from the reactions in all these situations was not possible, comparison of results from the different situations is of interest.

Inspection of the IR spectra of the combustion products of all four binary systems showed that they were dominated by the bands previously assigned to vibrations in carbonate ions and water molecules adsorbed by the newly formed products. These processes probably occurred during the cooling of the products and, despite precautions, during storage.

Fig 8.7a XRD pattern for combustion products of 40% Mo/BaO_2

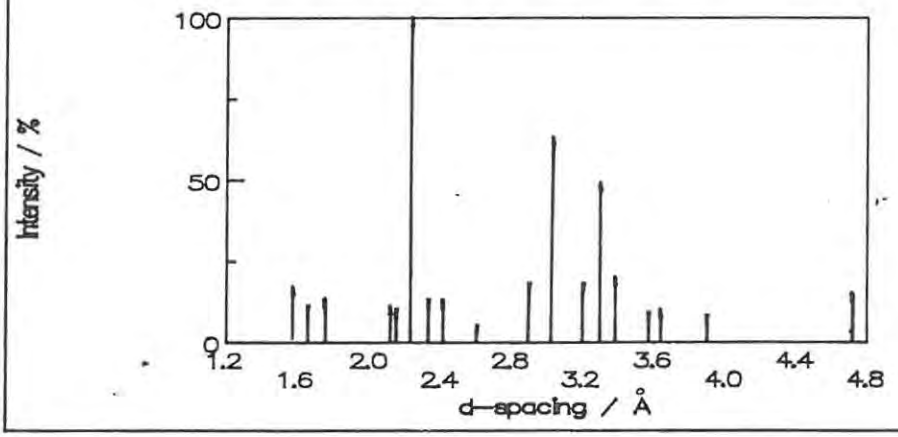

Fig 8.7b XRD pattern for sample of 40% Mo/BaO_2 heated to 360°C in oven

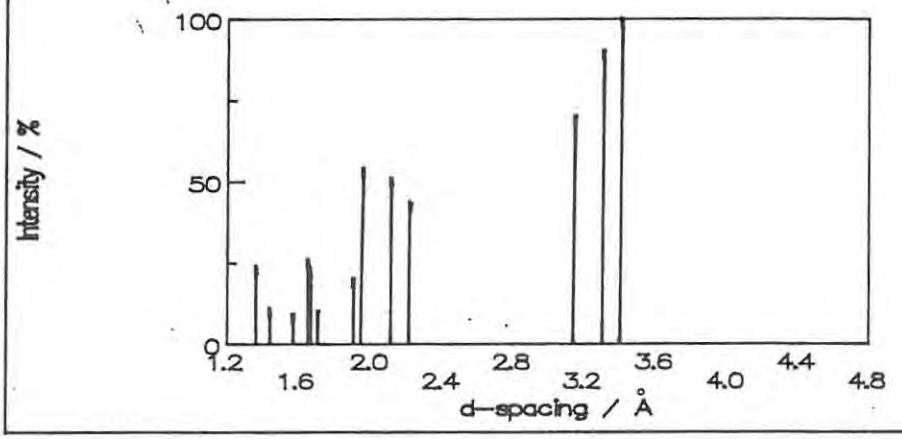

Fig 8.7c XRD pattern for sample of 40% Mo/BaO_2 heated to 950°C in TG

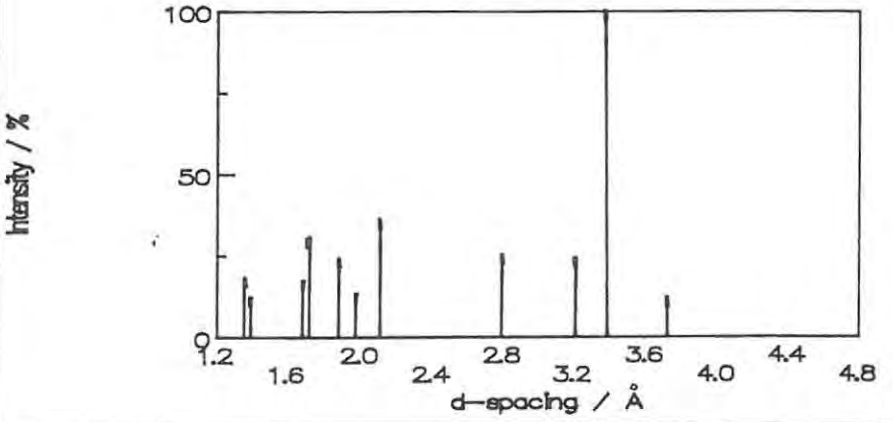

8.2.1 The Mn/BaO_2 system:

The products of the combustion in the open channel of the 25 and 50% compositions of Mn/BaO_2 gave XRD patterns with the same d-spacings for the three maximum relative intensities (2.86 Å, 100; 2.74 Å, 92; 2.55 Å, 100 for 25% products and 2.81 Å, 100; 2.75 Å, 100; 2.55 Å, 83 for 50% products). By use of the KWIC (ref 77) guide to the powder diffraction file (ref 76) the presence of Mn, BaO and Mn_3O_4 in the products of 50% Mn/BaO_2 was confirmed. Mn_3O_4 was apparently in a form similar to hausmannite which is a spinel of manganese and can be written as $MnO.Mn_2O_3$. The manganese/oxygen (Mn:O) ratio for hausmannite is 1:1.3. Two other manganese oxides, with a higher oxygen proportions, were also identified: Mn_2O_3 in the γ form, with Mn:O = 1:1.5, and MnO_2 with a pattern similar to the mineral ramsdellite (Mn:O = 1:2).

The products of 25% Mn/BaO_2 contain the same three oxides of manganese, however, the oxide with the higher oxygen content, MnO_2, dominates the mixture. Therefore, it appears that the metal:oxygen ratio of the products was controlled by the composition of the pyrotechnic mixture.

Figure 8.6 shows the XRD patterns for the products of the Mn/BaO_2 system from reactions in the open channel, in the thermal analysis equipment and in the convection oven. Comparison of these diffractions shows that the combustion products contain the least amounts of unreacted starting materials.

The IR spectra of the combustion products of the two compositions (20 and 50%) of Mn/BaO_2 showed two broad bands at 600 cm^{-1} and at 320 cm^{-1}. These were assigned (ref 70) to the presence of MnO. The band at 440 cm^{-1}, in the spectrum of the products of 50% Mn/BaO_2, was probably due to an asymmetric MO stretch in MnO_2.

8.2.2 The Mo/BaO_2 system:

The products from combustion in the open channel of the 30 and 50% compositions of Mo/BaO_2 produced similar XRD patterns. The expected products for this system are BaO, unreacted Mo metal and some oxides of Mo. Comparison of XRD patterns with reference data (ref 76) confirmed the presence of Mo metal. The existence of BaO in the products was not conclusively confirmed, but the presence of barium molybdate ($BaMoO_4$) was strongly indicated by the d-spacings 3.36, 2.10, 2.79 Å. Rajendran *et al* (ref 64), in their study of the $Mo/BaCrO_3/K_2ClO_4$ delay system, suggested a secondary reaction between BaO and MoO_3 producing the complex salt $BaMoO_4$.

As there was a large excess of Mo, it would be expected that the molybdenum:oxygen ratio (Mo:O) in the Mo oxide would be high. In gaseous oxygen, MoO_3 is formed at 688°C (ref 75), (IR data also confirmed that MoO_3 was formed at 607°C in DSC experiments with oxygen as carrier gas).

Fig 8.8a XRD pattern for combustion products of 40% Mn/SrO_2

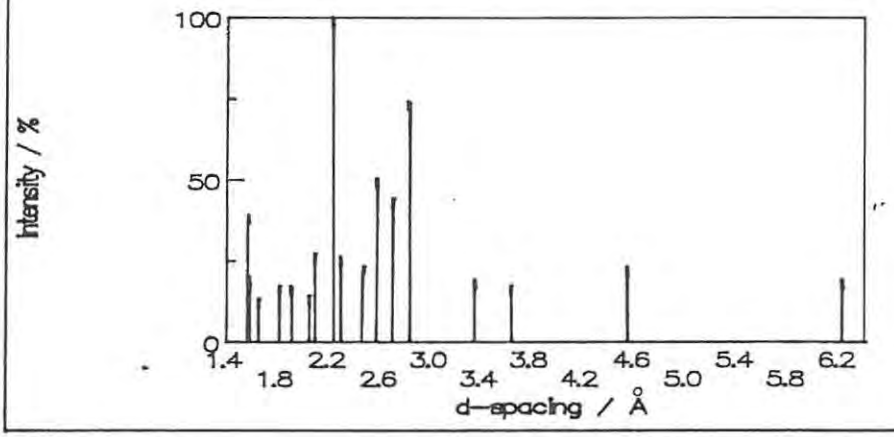

Fig 8.8b XRD pattern for sample of 40% Mn/SrO_2 heated to 360°C in oven

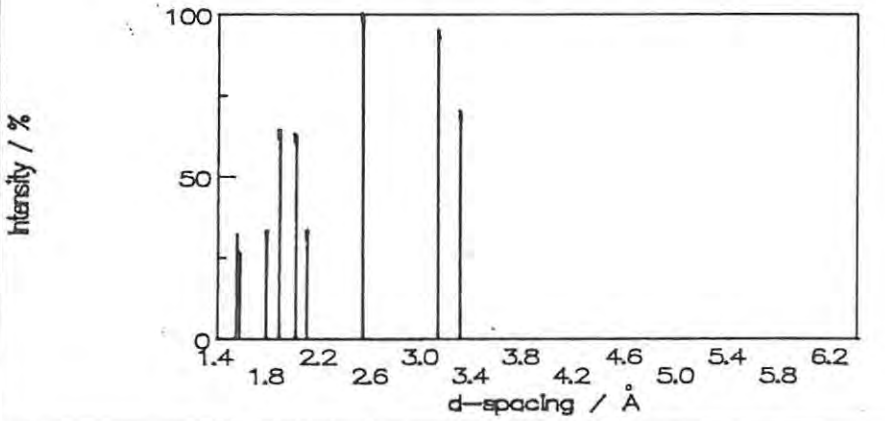

Fig 8.8c XRD pattern for sample of 40% Mn/SrO_2 heated to 950°C in TG

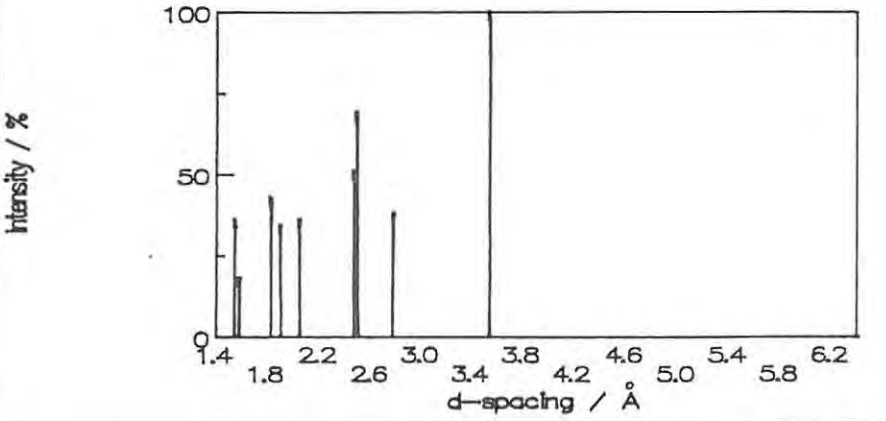

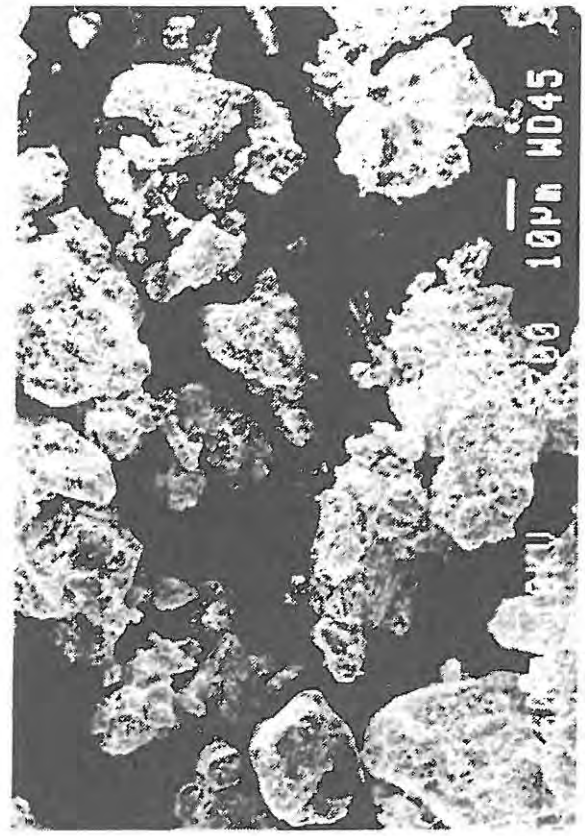

Plate 2 BaO_2 (BDH)

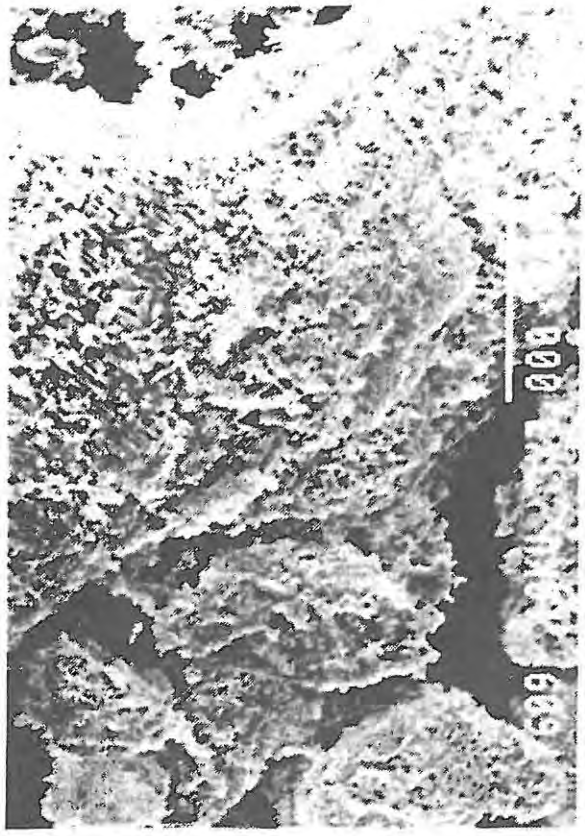

Plate 4 BaO_2 (BDH)

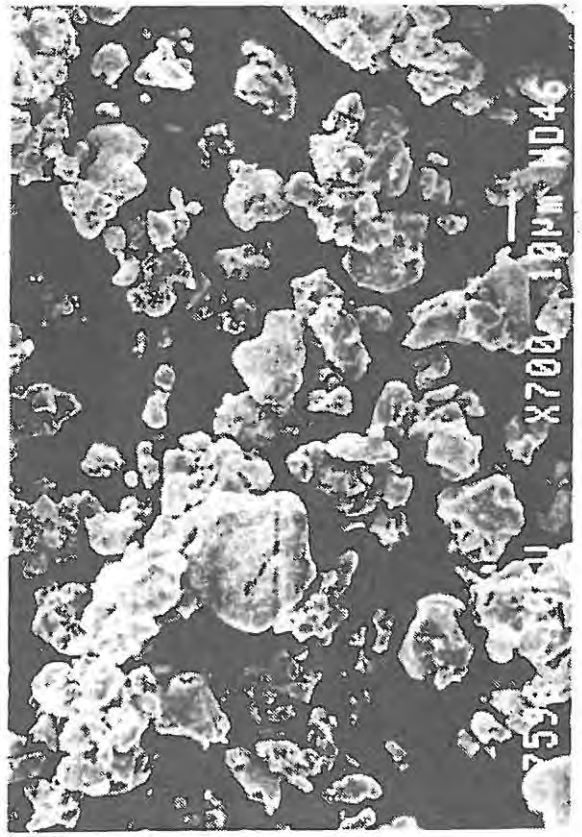

Plate 1 BaO_2 (Merck)

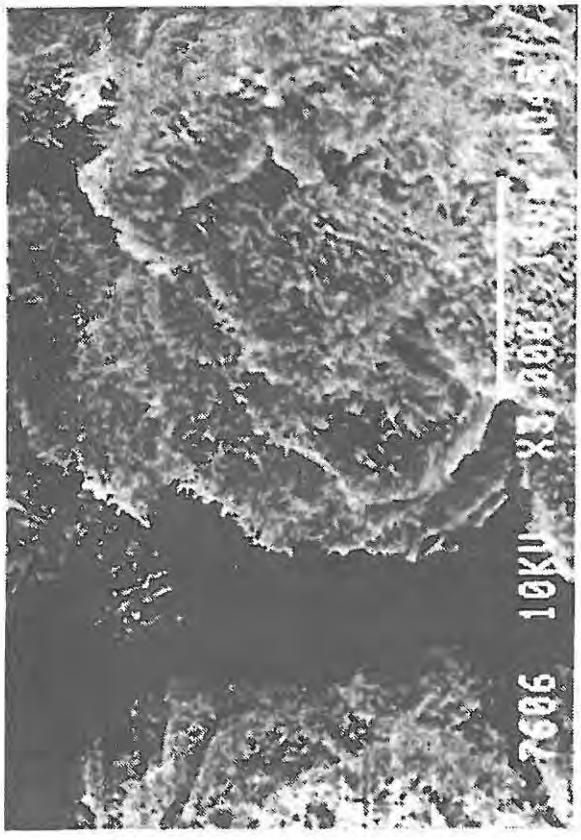

Plate 3 Moist BaO_2 (Merck)

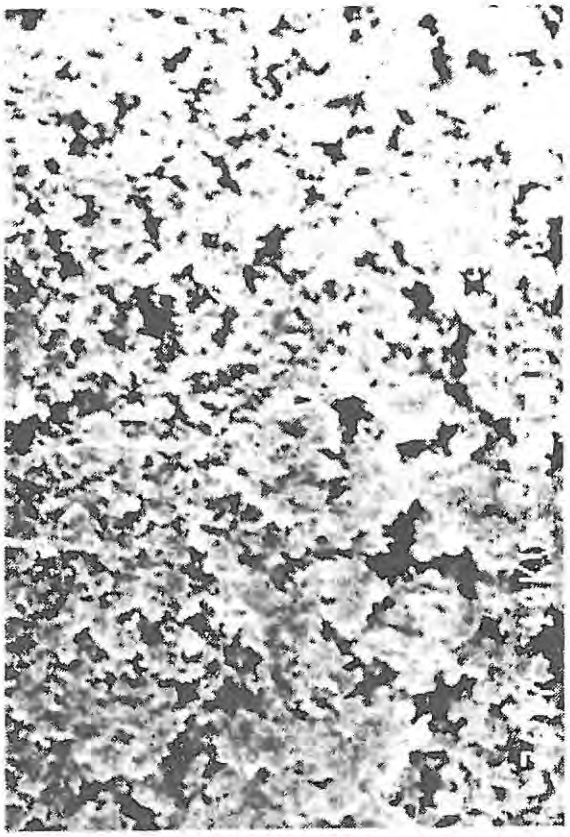

Plate 6 SrO_2

Plate 8 Mo

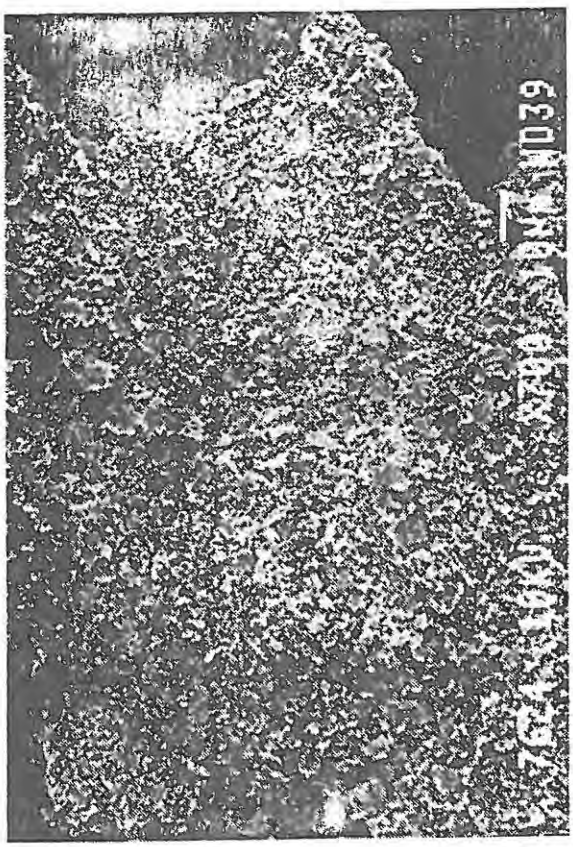

Plate 5 SrO_2

Plate 7 Mn

The XRD pattern also indicated the presence of molybdenum(IV) oxide (MoO_2 Mo:O = 0.50) and molybdenum(VI) oxide (MoO_3 Mo:O = 0.33) in the products of combustion of the Mo/SrO_2 system. Another possible product was $Mo_5O_7(OH)_8$ formed during cooling of the reaction products by the adsorption of moisture, despite the precautions taken to prevent this. Mo_9O_{26} (Mo:O = 2.89) was also a possible product. It is only formed at temperatures above about 700°C (ref 76).

The comparison of XRD patterns for the products of reaction of the Mo/BaO_2 system in the three situations (open channel, thermal analysis and convection oven) is shown in Figure 8.7. As expected the combustion products contain the least amounts of unreacted starting materials.

The IR spectra of the two compositions of Mo/BaO_2 showed a strong band at 800 cm^{-1} which was assigned (refs 70, 71) to the molybdate ion (MoO_4^{2-}). Furthermore, the bands at 580 and 680 cm^{-1} were assigned (ref 70) to MoO_2, while bands at 370 and 320 cm^{-1} were assigned to MoO_3.

8.2.3 The Mn/SrO_2 system:

The XRD patterns of the products of the 30 and 50% compositions of Mn/SrO_2 showed the presence of SrO, unreacted Mn and various oxides of Mn, including two forms of MnO, i.e. manganosite and hausmannite, and MnO_2 (pyrolusite). The Mn:O ratio for these products ranges between 1:1 and 1:2.

Figure 8.8 compares the XRD patterns for the products of reactions of the Mn/SrO_2 system in the open channel, in the thermal analysis equipment and in the convection oven. As expected the combustion products contain the least amounts of unreacted starting materials.

The IR spectra of the products have absorption bands at 600, 610 and 320 cm^{-1} which can be assigned to MnO. The band at 350 cm^{-1} was assigned (ref 70) to Sr-O vibrations.

8.2.4 The Mo/SrO_2 system:

The products of combustion of the 40% composition of Mo/SrO_2 system gave XRD patterns showing the presence of unreacted Mo metal, SrO and the molybdate, $SrMoO_4$ (d-spacings 3.36, 2.10, 2.79 Å). Evidence for the presence of MoO_2 (Mo:O = 0.50) and MoO_3 (Mo:O = 0.33) was also found. The d-spacings at 3.23, 3.16, 2.82 and 2.05 Å indicated that Mo_9O_{26} (Mo:O = 2.89) was part of the product mix. This compound is reported (ref 76) to form only at temperatures above about 700°C.

The comparison of reaction products produced in the three situations for the Mo/SrO_2 system is shown in Figure 8.9. As expected the combustion products contain the least amounts of unreacted starting materials.

The IR spectra for the products showed absorption bands at 610 and 600 cm^{-1} which were assigned (ref 70) to MnO_2. The bands at 315 and 210 cm^{-1} can be assigned to MoO_3.

Fig 8.9a XRD pattern for combustion products of 40% Mo/SrO_2

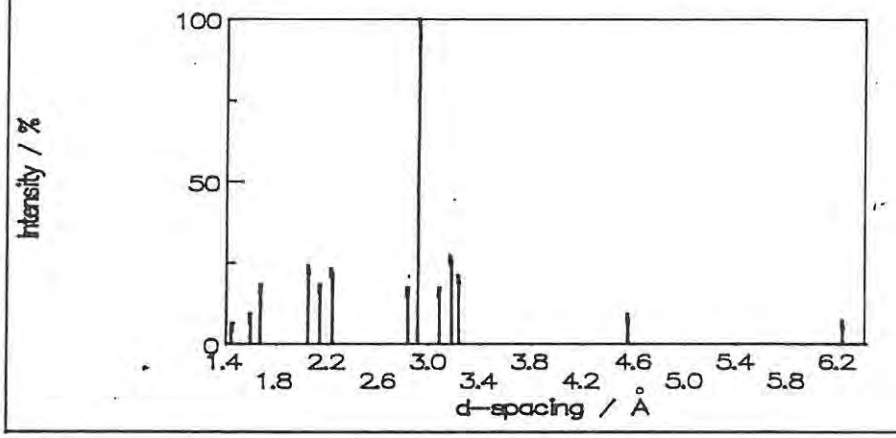

Fig 8.9b XRD pattern for sample of 40% Mo/SrO_2 heated to 360°C in oven

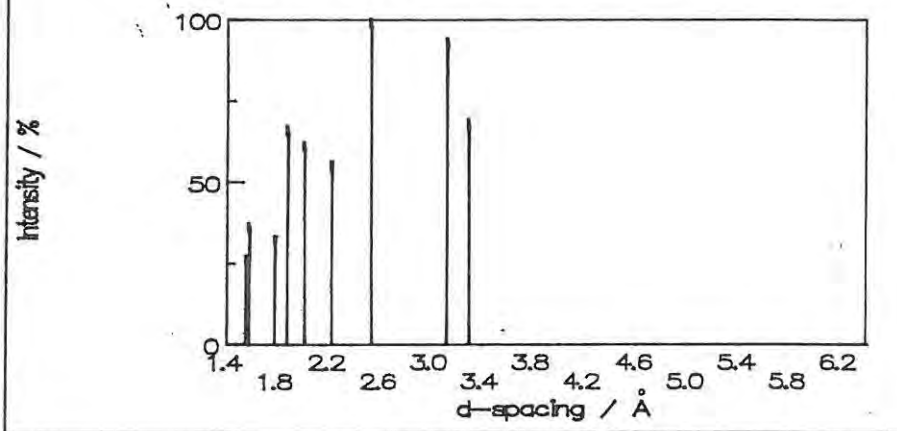

Fig 8.9c XRD pattern for sample of 40% Mo/SrO_2 heated to 950°C in TG

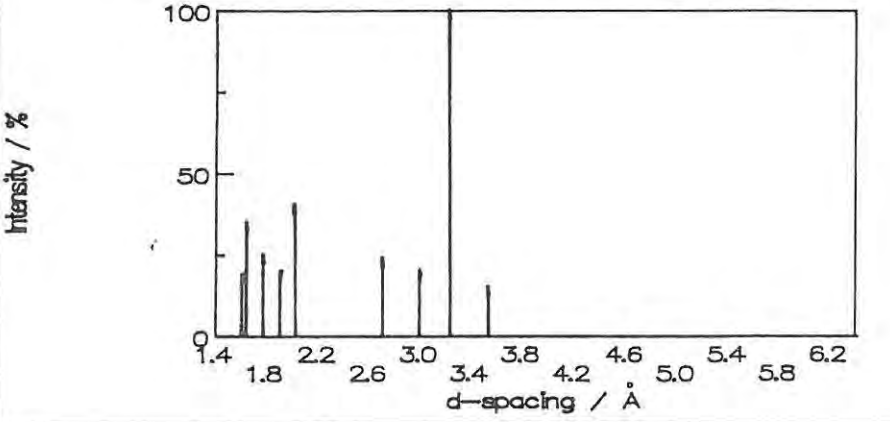

8.3 SUMMARY

The presence of impurities such as carbonates and hydroxides formed during either natural or accelerated aging was identified in both oxidants. The reported (ref 10) surface formation of $BaCO_3$ on BaO_2 was tentatively observed in micrographs of various BaO_2 samples, but no observable changes were found for the SrO_2 samples.

The combustion products of all four binary systems consisted of mixtures of unreacted metal fuel, the solid product of oxidant decomposition and oxides of the metal. The Mo containing systems appeared to form molybdates of Ba and Sr either by direct reaction between fuel and oxidant or by secondary reactions between decomposed oxidant (i.e. BaO or SrO) and newly formed metal oxide.

Depending on the experimental conditions and the proportion of fuel present in the original composition, the products consisted of different amounts of unreacted metal and the metal:oxygen ratio of the oxides also changed. The Mn oxides, especially in Mn/BaO_2 system, tended to be in the form of a manganese spinel, $MnO.Mn_2O_3$.

CHAPTER 9: DISCUSSION OF BINARY SYSTEMS

9.1 THERMAL ANALYSIS

9.1.1 The individual reactants:

Barium peroxide may contain absorbed water and also traces of hydroxide and carbonate as impurities. No evidence of melting was observed and endothermic decomposition to BaO(s) and O_2(g) occurs above 600°C and is fairly reversible on cooling in air.

Strontium peroxide may also contain absorbed water and possibly hydroxide and carbonate impurities. Decomposition occurs in two endothermic stages, the first above about 400°C and the second at above about 530°C. No intermediate other than SrO(s) was identified.

The powdered metals, Mn and Mo, react readily on heating in O_2(g) in the DSC above 500°C (Mn) and above 600°C (Mo). In the more open sample configuration of the TG these onset temperatures were lowered to 350°C (Mn) and 450°C (Mo). The greater reactivity of the Mn powder was seen in the results for TG runs in N_2 where great difficulty was experienced in flushing all traces of oxidizing gases from the thermobalance housing. MoO_3 sublimes above ~750°C, in O_2, in the TG.

9.1.2 The two binary pyrotechnic systems containing BaO_2:

The Mn/BaO_2 system. The proposed endothermic rearrangement in $Ba(OH)_2$ at about 360°C appeared to initiate an exothermic reaction between Mn and BaO_2. The large and incomplete exotherm at about 660°C appears to be initiated by the onset of peroxide decomposition. A solid-solid reaction between Mn and BaO_2 cannot be ruled out since the TG trace (Figure 4.13) showed no mass loss. Following previous suggested mechanisms (refs 7, 18), the first process (~360°C) could be a pre-ignition reaction (PIR) followed by bulk oxidation at 660°C. The DSC trace for 40% $Mn/Ba(OH)_2$ (Figure 4.18) did not show an exotherm so the presence of peroxide is probably also required.

The Mo/BaO_2 system. Only one exotherm was observed in the DSC trace (Figure 4.14) for this system. The endothermic rearrangement in the $Ba(OH)_2$ impurity, which was suggested to initiate the PIR in the Mn/BaO_2 system, was not associated with an exotherm in the Mo/BaO_2 system. The main exothermic reaction between Mo and BaO_2 at about 490°C is well below the temperature required for the onset of decomposition of the peroxide. The unreacted BaO_2 undergoes decomposition at higher temperatures which affects the shape of the oxidation exotherm. The exothermic reaction was not accompanied by a mass loss and therefore it is suggested that at least under the conditions of thermal analysis the reaction could be between reactants in the condensed phase, assuming that any gases involved had sufficient time to escape the solid material and thus change the sample mass. The metal fuel may also catalyse the decomposition of the oxidant.

An increase in the proportion of fuel up to a composition of 50% Mo/BaO_2 caused the main reaction to start at lower temperatures (Figure 4.15). Increasing the heating rate also lowered the onset temperatures of the main reaction exotherms (Figure 4.16).

9.1.3 The two binary pyrotechnic systems containing SrO_2:

The Mn/SrO_2 system: Only one exothermic reaction (onset ~380°C) was observed in the DSC traces of Mn/SrO_2 in both N_2 and in O_2. This exotherm is overlapped by the first of the two endothermic stages of decomposition of unreacted SrO_2 (Figures 4.19 and 4.20). The onset temperature of this proposed reaction between Mn and SrO_2 was altered by changes in the composition of the Mn/SrO_2 system (Figure 4.20). It is not possible from thermal analysis to distinguish between reaction of Mn with SrO_2(s) or with O_2(g) formed in the early stage of decomposition of SrO_2.

In O_2 (Figure 4.22), the large exotherm at about 550°C due to the oxidation of unreacted Mn by the atmosphere showed that some fuel remained unreacted in the 40% composition and that it was available (i.e. not protected by a layer of product) for reaction by the O_2(g) under the conditions of thermal analysis.

The Mo/SrO_2 system: The Mo/SrO_2 mixture differed from the other three binary systems in that no composition of Mo/SrO_2 would reproducibly produce an exotherm due to the reaction between Mo and SrO_2, under the conditions of the DSC. The one illustrated example (Figure 4.25) of exothermic activity in a DSC trace of Mo/SrO_2 was at temperatures above the decomposition of SrO_2 (~580°C), compared to (~380°C) for the Mn/SrO_2 system.

Evidence from the DSC and TG traces thus showed that except for the oxidation of the Mo by the O_2 carrier gas at about 660°C, there was no exothermic reaction between the fuel and oxidant under the conditions of thermal analysis.

9.2 BURNING RATES

Three of the four binary pyrotechnic systems have a wide range of compositions (Table 5.5) which sustained combustion. The Mo/SrO_2 system was the exception. Only two compositions (40 and 45%) of this system sustained combustion and they were the most susceptible to any changes in the experimental procedure. The reason for this restricted range of combustible compositions, is not obvious since the fuel, Mo, in the Mo/BaO_2 system supports combustion over a wide range of compositions and, similarly, the oxidant, SrO_2, burns well in the Mn/SrO_2 system.

Table 5.5 shows that the linear burning rates of all four binary systems are in the 2 to 12 mm s^{-1} range and that the maximum recorded combustion temperatures (with the exception of some Mn/BaO_2 compositions) lie in the 1600° to 1750°C range.

Ba and Sr carbonates and hydroxides retarded the burning of the corresponding pyrotechnic mixtures as has been previously reported (ref 29). Prolonged exposure of peroxides to a moist atmosphere promotes (refs 8, 10, 45, 53) the production of carbonates and hydroxides, so adequate storage of both peroxides is vital for the effective and reproducible functioning of pyrotechnic systems containing these oxidants.

9.2.1 The Mn/BaO_2 system:

The plot of linear burning rate of the Mn/BaO_2 system against composition was concave up (Figure 5.20a), with a maximum burning rate for the 20% composition. This composition would correspond approximately to the stoichiometric composition for complete reaction with products BaO(s) and Mn_3O_4(s) (see Section 9.5). The 50% Mn/BaO_2 composition gave a local maximum burning rate on this plot. Spice and Staveley proposed (ref 6) that the increased thermal conductivity due to the presence of a higher proportion of metal promotes faster burning rates beyond the stoichiometric composition. The measured thermal conductivities (Chapter 6) did not, however, increase significantly over the range of compositions investigated (see Section 9.4). The observed burning rates were similar to those reported by Spice and Staveley (ref 6) (Figure 5.20).

McLain (ref 5) has suggested that if the mass burning rate (g s^{-1}) increases as the compaction increases this may indicate the occurrence of a genuine solid-solid reaction, since the compaction will increase the inter-particle contact and hence increase the rate of propagation. It can also be argued that, within limits, the increased compaction would prevent the escape of the gaseous products of decomposition of the oxidant and hence promote the oxidation of the fuel. Figure 5.41 shows that the mass burning rate for the Mn/BaO_2 system more than doubled when the compaction was increased from 0 to 150 MPa. This increase was proportionally the largest of all the four binary systems.

The particle-size ranges available for Mn were too different in size to test the effects of particle size of the fuel on the burning of the Mn/BaO_2 system.

The burning characteristics of a pyrotechnic mixture can be altered (refs 1, 5) by the addition of certain materials. Small amounts (< 10%) of the additives chosen all slowed the burning rate of the 20% Mn/BaO_2 composition (Table 5.12). Additives may inhibit the reaction by decreasing the contact area between the fuel and oxidant particles, or by changing the heat capacity and/or the thermal conductivity of the mixture sufficiently to alter the burning rate of the mixture. As can be seen from Table 5.12 the changes in heat capacity and thermal conductivity at ambient temperature for the Mn/BaO_2 system are small enough to be negligible. Alternatively, the additive may take part in the reaction and compete for the unreacted materials. Depending on the heat of this competitive reaction, the total heat evolved and hence the rate of burning may be either increased, or decreased, or be unchanged.

Thermal analysis (Sections 4.4.1) of the Mn/BaO_2 system suggested that the combustion reaction could be influenced by the decomposition of $Ba(OH)_2$ at a temperature of about 360°C. Thus it might be expected that small quantities of $Ba(OH)_2$ mixed in with the pyrotechnic mixture would enhance the combustion to some extent, but this was not the case in the Mn/BaO_2 system.

The 40% Mn/BaO_2 composition, made with BaO_2 heated to ~425°C and cooled in air (Section 5.3), burned with burning rates comparable with the burning rates of the composition made with untreated BaO_2, but the same composition containing BaO_2 cooled under N_2 burnt significantly more slowly. This is probably due to partial decomposition of the peroxide.

9.2.2 The Mo/BaO_2 system:

A wide range of compositions of the Mo/BaO_2 system sustained combustion and gave burning rates which were consistently lower than the values published by Spice and Staveley (ref 6), and by Nakahara and Hikita (ref 28) for the same system (Figure 5.20).

The plot of burning rate against composition for the Mo/BaO_2 system (Figure 5.20) had a reproducible and yet unusual maximum at a composition of 45%. Due to the violence of the reaction of this particular composition, expulsion of the last portion of the unreacted composition by small amounts of expanding gas may contribute to this exceptionally high burning rate. The average standard deviation for the observed burning rates for the Mo/BaO_2 system (13%) was higher than for the Mn/BaO_2 system (9%). A local maximum in the burning rate was recorded at a composition of 60%. Both these compositions are well above the stoichiometric compositions of 16 and 22% (see Section 9.5) corresponding to complete reactions to produce BaO(s) and MoO_3(s) or MoO_2(s), respectively.

These effects of composition on burning rate are unlikely to be accounted for solely on the Spice and Staveley (ref 6) proposal of the increased thermal conductivity, although the thermal conductivity did increase slightly (Chapter 6 and Section 9.4) as the proportion of Mo in the Mo/BaO_2 composition was increased. Incomplete reaction of the fuel particles will shift the fuel proportion to higher values for the same overall stoichiometry. For metals such as Mn and Mo which can readily exist in several oxidation states, the occurrence of different reactions in fuel-rich or oxidant-rich compositions, or even fuel-rich or oxidant-rich regions of a nominally fixed composition, is possible.

The mass burning rate of the Mo/BaO_2 system also increased as the compaction was increased from 0 to 100 MPa (Figure 5.42). Further compaction caused no further increase in the burning rate.

In solid-solid pyrotechnic reactions, the particle size and shape will affect the contact area between fuel and oxidant and hence (refs 1, 5, 10) the burning rate of the mixture. (See Section 8.2 for the shape of reactant particles). The burning rate of the Mo/BaO_2 system was approximately doubled when, in the same composition, a smaller particle-size range of Mo was substituted for the standard size (Table 5.9).

Despite the relatively large difference in the median values (~17 μm) of the two particle-size ranges of BaO_2 available, compared with the difference between the two Mo samples (~10 μm), there was no observed change in the burning rates of the mixtures containing these two oxidant samples.

The particle-sizes of the fuel and oxidant may affect the thermal conductivity of the mixture (see Section 6.1), which in turn may affect the propagation rate of the combustion wave. Since the thermal conductivities of the bulk metals are greater than those of the bulk oxidants, the particle-size of the fuel might be expected to have more of an effect on the burning rate than the particle-size of the oxidant. A more likely explanation of the effect of the particle-size of the fuel is that more surface of the fuel is exposed for oxidation. If a protective layer of product is formed on the fuel particles and limits further reaction, more fuel will react when the particle-size is small and the specific surface area is large (Table 5.8), hence more energy will be released and faster burning will occur.

The Mo/BaO_2 system was much more sensitive to the presence of additives than the Mn/BaO_2 system. All the additives, except BaO, prevented combustion from taking place when even as little as 1% was added.

The 40% Mo/BaO_2 compositions, made with the samples of BaO_2 heated to ~425°C and cooled in air, burnt with rates comparable with those of compositions made with untreated BaO_2, but compositions containing BaO_2 cooled in N_2 burnt significantly more slowly. This follows the pattern of the results for the Mn/BaO_2 system.

9.2.3 The Mn/SrO_2 system:

The plot of burning rate against composition for the Mn/SrO_2 system was concave up with a maximum at ~75% Mn. This is well above the highest stoichiometric composition (31% for the production of MnO(s)) for all the suggested reactions in Section 9.5. The measured thermal conductivities (Chapter 6) for various compositions of Mn/SrO_2 did increase slightly with the increase in the quantity of Mn.

The burning rates of the Mn/SrO_2 systems had the highest standard deviations (18%) of all the four binary systems. No published values for the burning rates of the Mn/SrO_2 system were found.

The mass burning rate (g s^{-1}) increased with compaction (Figure 5.43). Although the Mn/SrO_2 system has the fastest linear burning rate (i.e. moving combustion front) (Figure 5.21) it does not consume the most reactant mixture in a given time.

The particle-size ranges available for Mn were too different in size, and, the particle-size ranges prepared for SrO_2 were too similar in size (Table 5.8), to test the affects of fuel/oxidant particle size on the burning of the Mn/SrO_2 system.

The burning characteristics of the Mn/SrO_2 pyrotechnic system were altered by the additives chosen for the SrO_2 systems. Table 5.14 shows that all the additives tested progressively decreased the burning rate until finally combustion failed. The maximum excess temperatures were not significantly affected by these additives.

Drying the SrO_2 at temperatures up to 140 ± 10°C increased the observed burning rate (Table 5.18). At higher temperatures the burning rates decreased, probably due to the loss of oxygen from partially decomposed peroxide. The 40% Mn/SrO_2 composition would not burn when the SrO_2 had been heated to ~520°C regardless of the atmosphere used during cooling. This indicates that enough decomposition had taken place to prevent initiation of the pyrotechnic reaction and that the dissociation of SrO_2 is not as readily reversible as that of BaO_2.

9.2.4 The Mo/SrO_2 system:

Of all the four binary systems, the Mo/SrO_2 system only supported combustion over the smallest range of compositions (Table 5.5). The two compositions which did burn, burnt with slightly different burning rates (Figure 5.21), but too few data were available to identify any trends in the observed burning rates as a function of composition. No published values for the burning rates of this system were found.

Compositions of the Mo/SrO_2 system which burnt under the normal experimental conditions, failed to ignite when they had been compacted under loads greater than 50 MPa. Despite this sensitivity of the Mo/SrO_2 system to the degree of compaction, the mass burning rate (g s^{-1}) did increase slightly when the compaction was increased from 0 to 50 MPa (Figure 5.41).

The burning rate was approximately doubled when, in the same composition, a smaller particle-size range of Mo was substituted for the standard size (Table 5.9). (See Section 8.2 for the shape of reactant particles). This behaviour was also observed for the Mo/BaO_2 system (above).

The Mo/SrO_2 system also behaved similarly to the Mo/BaO_2 system in that all the additives tested, except MoO_3, progressively decreased the linear burning rates until finally combustion failed (Table 5.15). Addition of up to 10% MoO_3 in 40% Mo/SrO_2 did not decrease the linear burning rate (or maximum excess temperature of the composition). The MoO_3 may play some part as an alternative oxidant (refs 66, 67) without altering the burning rates and maximum excess temperatures. It is also volatile at high temperatures (> 750°C, Figure 4.9) and hence may not hamper reaction.

As with the Mn/SrO_2 system, the 40% Mo/SrO_2 composition would not burn when the SrO_2 had been heated to ~520°C regardless of the atmosphere used during cooling.

The already slow burning composition of the Mo/SrO_2 system was made to burn even slower when mixtures of this system were subjected to pre-combustion heat treatments to various temperatures

(Table 5.18). This slowing of the burning rate, despite the loss of adsorbed water, was common to the two Mo containing systems.

9.2.5 Binary systems with other fuels:

The burning of binary pyrotechnic mixtures of BaO_2 with various non-metals, such as S (ref 6) and Se (ref 11), and with certain group II metals such as Mg (refs 5, 27) has been studied before. These fuels are all either reasonably reactive towards $O_2(g)$ at moderate temperatures or have low melting points relative to the decomposition temperature of the BaO_2. The use of transition metals, which are less reactive and have much higher melting points, as fuels in binary mixtures with BaO_2 has also been studied to a limited extent. Spice and Staveley (ref 6) investigated Fe, Mn, and Mo with BaO_2; Nakahara and Hikita (ref 28) and Yoshinaga *et al* (ref 29) have all studied the Mo/BaO_2 system. The results of burning experiments of Cr, Nb and W with BaO_2 and SrO_2 (Section 5.4) provide some additional information.

At least one composition of each of the 10 different binary systems sustained combustion in the open channel. Table 9.1 lists the compositions which burned and compares their mole ratios.

TABLE 9.1 BINARY SYSTEMS WHICH BURNT IN THE CHANNEL

SYSTEM	COMPOSITION / %	MOLE RATIO (FUEL:OXIDANT)	SYSTEM	COMPOSITION / %	MOLE RATIO (FUEL:OXIDANT)
--	--	--	Cr/SrO_2	20	0.58:1.00
Cr/BaO_2	40	2.17:1.00	Cr/SrO_2	40	1.53:1.00
Mn/BaO_2	20	0.77:1.00	Mn/SrO_2	20	0.54:1.00
Mn/BaO_2	40	2.05:1.00	Mn/SrO_2	40	1.45:1.00
Mo/BaO_2	20	0.44:1.00	Mo/SrO_2	20	0.31:1.00
Mo/BaO_2	40	1.18:1.00	Mo/SrO_2	40	0.83:1.00
--	--	--	Nb/SrO_2	20	0.32:1.00
Nb/BaO_2	40	1.22:1.00	Nb/SrO_2	40	0.89:1.00
W/BaO_2	40	0.61:1.00	W/SrO_2	40	0.43:1.00

The 20% compositions, which did not burn, all had mole ratios of less than one to one. These compositions probably had less than the stoichiometric quantity of fuel. The burning rates of the 40% compositions of all 10 systems including the results of Spice and Staveley (ref 6) for the Fe/BaO_2 system, are compared in Table 9.2.

TABLE 9.2 COMPARISON OF LINEAR BURNING RATES* OF 40% COMPOSITIONS OF BINARY PYROTECHNIC COMPOSITIONS

PERIOD	LINEAR BURNING RATE / mm s^{-1}			
	GROUP 5	GROUP 6	GROUP 7	GROUP 8
3 4 5	Nb/BaO_2 8.3 ± 0.9	Cr/BaO_2 3.8 ± 0.4 Mo/BaO_2 4.6 ± 1.0 W/BaO_2 1.2 ± 0.2	Mn/BaO_2 6.6 ± 0.4	Fe/BaO_2 4.7#
3 4 5	Nb/SrO_2 8.5 ± 0.8	Cr/SrO_2 4.3 ± 0.6 Mo/SrO_2 2.3 ± 0.1 W/SrO_2 2.6 ± 0.4	Mn/SrO_2 7.5 ± 1.0	Fe/SrO_2 -

*Measured under the same experimental conditions
#Measured by Spice and Staveley (ref 6)

No obvious trends could be discerned. Comparison could also be made at a constant mole ratio, but other factors, such as the thickness of a product layer formed, may determine the burning rate.

9.3 TEMPERATURE PROFILES

The range of compositions which sustained combustion for the four binary systems all produced similar shaped temperature profiles (sigmoidal). The various experimental techniques (e.g. compaction, quantities of additive, particle size, etc.) used to alter the burning of the four binary systems produced three kinds of changes to the shape of the temperature profile. These include changes to:

- the slope of the rise zone (i.e. t_r) of the temperature profile, which is related to the burning rate (Section 1.3)
- the amplitude (i.e. T_{max}) of the temperature profile and
- the overall S shape of the temperature profile.

The reproducibility of the temperature profiles for all four binary systems was limited as shown by Figures 5.24 to 5.27, despite efforts to control the factors which affected the reproducibility.

The thickness of the thermocouple wire was shown to affect the shape and the amplitude of the temperature profiles of all four binary systems, and the rise times, the maximum excess temperature values, the U_{ad} values and the derived activation energies were corrected to negligible thermocouple wire diameter.

9.3.1 The Mn/BaO_2 system:

The temperature profiles for the Mn/BaO_2 system were the most reproducible of all the binary systems (Figures 5.24 to 5.27). The composition of the Mn/BaO_2 system had a marked affect on the slope of the rise zone and on the amplitude (T_{max}) of the temperature profile (Figure 5.28). As the proportion of fuel was increased, both the slope and the amplitude decreased in magnitude. The plot of maximum excess temperature against composition for the Mn/BaO_2 system (Figure 5.38) shows that the compositions between 30 and 45% Mn burned with higher temperatures ($>$ 1760°C) than any of the other binary systems. These compositions of Mn/BaO_2 all contain a greater proportion of fuel than the largest stoichiometric composition of all the suggested reactions (see Section 9.5), which is 24% for the solid-solid reaction whose products are BaO(s) and MnO(s).

Irregularities in temperature profiles may arise (refs 23, 24) as a result of phase transitions accompanying chemical reactions (Section 1.3). Fewer irregularities were observed in the temperature profiles of the Mn/BaO_2 system than in the other systems (see below).

Compaction of Mn/BaO_2 pyrotechnic mixtures increased the slope of the rise zone and the amplitude of the temperature profile (Figure 5.41).

Temperature profiles (Figure 5.48) show how the slope of the rise zone decreased as the quantity of additive (Al_2O_3) was increased. The presence of additives may increase the complexity of the temperature profiles as demonstrated by the profile recorded during the combustion of the 5% $BaCO_3$ in 20% Mn/BaO_2 (Figure 5.49) and the combustion of 1% $Ba(OH)_2$ in 20% Mn/BaO_2 (Figure 5.50).

9.3.2 The Mo/BaO_2 system:

Many of the fuel rich compositions of the Mo/BaO_2 system gave irregularly shaped profiles (Figure 5.29). The reproducibility of the temperature profiles for this system was amongst the worst for the four binary systems. Despite the many irregularities, some sigmoidal profiles were noted (Figure 5.29). The fairly reproducible endothermic deviations in the rise zones of the profiles for the 60 and 70% compositions of Mo/BaO_2 (Figures 5.36 and 5.37) occur in the temperature range of from ~410° to ~730°C and may result from the decomposition of BaO_2 (decomposition occurs at about 600°C under the conditions of thermal analysis, Section 4.2.1) or the vaporization of MoO_3 which occurs above ~750°C. The removal of the oxide product by vaporization would expose more metal to oxidation.

The stoichiometric composition corresponding to the reaction with BaO(s) and MoO_3(s) as products is 16% Mo or 22% Mo for the reaction with BaO(s) and MoO_2(s) as products (see Section 9.5). Figure 5.29 shows that compositions with a low proportion of fuel have a particularly small rise time but with more fuel present the rise zone flattens out.

Figure 5.39 shows that the largest maximum excess temperature for the Mo/BaO_2 system was produced by the 35% composition which contained more fuel than both the above stoichiometric compositions. If it assumed that the Mo which does react all forms MoO_3, then the extent of reaction of the fuel in this composition is ~35%. If an average particle of Mo has a diameter of 35 μm (Table 5.8), 35% reaction would correspond approximately to a product layer of 2.5 μm around the unreacted core (ignoring density changes).

Two types of deviation from the typical sigmoidal temperature profile were observed for the combustion of mixtures which were loaded under increasingly greater compressions. Figure 5.42 shows how for the 30% Mo/BaO_2 composition, loaded under 100 MPa, there was endothermic deviation in the rise zone of the profile due probably to the decomposition of BaO_2 and or vaporization of MoO_3, as discussed above. The other type of deviation was shown in the temperature profile of the Mn/SrO_2 system (see below).

As the particle-size range of the fuel was decreased the slope of the rise zone of the profile increased corresponding to the increased burning rate (Figure 5.46). The amplitude of the profile was not much affected by the particle size changes.

9.3.3 The Mn/SrO_2 system:

Composition has a marked affect on the shape of the typically sigmoidal temperature profiles recorded during the combustion of the Mn/SrO_2 system (Figure 5.30). Both the slope of the rise zone and the amplitude of the profiles decreased as the proportion of fuel increased. The reproducibility of these temperature profiles was good compared to the two Mo containing systems. Irregularities in the typical sigmoidal temperature profile were fairly common for this system and occurred in the cooling zone. These irregularities may arise as a result of recrystallization of various reaction products. In the 40% Mn/SrO_2 composition (Figure 5.35) the temperature at which the exothermic deviation took place was about 1500°C shortly ($\sim$0.1 s) after T_{max} had been reached. The melting point of Mn_3O_4, one of the possible products of this reaction, is quoted (ref 59) as 1560°C and so the recrystallization of this compound could account for the brief temperature plateau.

The effect on the heat output of the pyrotechnic reactions in the Mn/SrO_2 system in the presence of the inert diluent, Al_2O_3, is shown in Figure 5.51. The amplitude and the slope of the rise zone are decreased by the addition of the diluent. The presence of some of the additives increased the complexity of the temperature profiles as demonstrated by the profile recorded during the combustion of 1% $Sr(OH)_2$ in 20% Mn/SrO_2 (Figure 5.52).

As the proportion of fuel is increased in compositions of Mn/SrO_2 the recorded maximum excess temperature consistently decreased. The largest maximum excess temperature recorded was for the 20% composition which is close to the stoichiometric composition (19%) for the reaction whose products include SrO(s) and MnO_2(s).

9.3.4 The Mo/SrO_2 system:

The two compositions of the Mo/SrO_2 system which sustained combustion under the experimental conditions also gave sigmoidal temperature profiles (Figure 5.31), over a longer time scale ($\sim$0.3 s) than for the other binary systems ($\sim$0.1 s). The reproducibility of the temperature profiles was poor (Figure 5.27). No irregularities were observed in the few temperature profiles recorded.

The burning of the Mo/SrO_2 system was particularly sensitive to increased compaction (Figure 5.44). Compositions loaded under pressures greater than 50 MPa caused combustion failure in this system. Compositions of Mo/SrO_2 with the smaller particle-size range of Mo produced temperature profiles with a steeper slope in the rise zone (Figure 5.47).

The Mo/SrO_2 system behaved similarly to the Mo/BaO_2 system in the presence of additives in that all the additives tested, except MoO_3, progressively slowed the reaction until finally combustion failed. Mixtures of MoO_3 in Mo/SrO_2 behaved differently in that the profiles recorded with increasing quantities of this additive were all similar to each other (Figure 5.53) in terms of slope and amplitude but were all different from the profile recorded without the additive.

9.3.5 Comparison of temperature profiles from different systems:

Comparison of temperature profiles from different systems may be done on the basis of similar percentages by mass of fuel, or on the mole ratios of fuel to oxidant. The choice of which composition (% fuel) or which mole ratio to compare was made difficult by the fact that only two compositions of Mo/SrO_2 burnt and that the 25 to 45% compositions of the Mn/BaO_2 system burnt at temperatures above the melting point of Pt and therefore no profiles were recorded for these compositions.

The 20% compositions of the two BaO_2 systems and the Mn/SrO_2 system (Figure 5.32) were remarkably similar in both slope and amplitude. In the comparison based on a mole ratio of 4:1 (Mn/BaO_2, Mo/BaO_2 and Mn/SrO_2) (Figure 5.33) the temperature profiles have a similar slope soon after ignition but have greatly different amplitudes, while in the 2:1 mole ratio comparison (Figure 5.34) the profiles have similar amplitudes but different slopes.

Comparison of temperature profiles for different systems based on mole ratios or common composition by mass of fuel is difficult, since the reactions do not go to completion. The rate of the reaction may be determined by the thickness of the product layer formed around the metal particles. The extent of the reaction is then dependent on the particle-size of the fuel. Although there is little data available, the fact that no influence on the reaction of the particle size of the oxidants was observed, may indicate reaction of the fuel with gaseous oxygen produced by partial decomposition of the oxidant.

9.3.6 Temperature profile analysis:

Only a few published values of activation energies of reactions in the BaO_2 or SrO_2 pyrotechnic systems were found. Hogan and Gordon (ref 5) measured an activation energy of 155 kJ mol^{-1} for the ignition of the Mg/BaO_2 system and Yoshinaga *et al* (ref 29) reported an ignition energy of between 44 and 49 kJ mol^{-1} for various compositions of the Mo/BaO_2 system. Hill *et al* (ref 18), calculated an activation energy of 24 kJ mol^{-1} for the Fe/BaO_2 system, while Spice and Staveley reported (ref 7) a value of about 200 kJ mol^{-1} for the pre-ignition reaction in the same system. Values reported for activation energies derived from temperature profiles are generally low e.g. Boddington *et al* (ref 24) reported E_a values of from 8 to 15 kJ mol^{-1} for different compositions of the $W/K_2Cr_2O_7$ system.

The activation energies derived from the temperature profiles of the 20% compositions of three of the binary systems, and the 40% Mo/SrO_2 system, using both the Hill and Leeds approaches (Tables 5.25 and 5.27) are similarly low values. The Hill approach gives smaller values for these compositions than the Leeds approach, using either regression routine. These low E_a values have been attributed to (ref 24) rate control by diffusion processes.

For all four binary systems the value chosen (using the Hill approach) for the order of reaction, n, affects the values of both the activation energy and the pre-exponential factor, A. As n was increased from 0.5 through 1.0 to 2.0 both E_a and A increased (Table 5.25) and their average standard deviation

decreased. In reactions involving solids an order of two is most unlikely and the standard deviations for E_a calculated using n = 0.5 are high, so all the E_a values were thereafter calculated using a first order kinetic model.

The Leeds optimization procedures gave lower values of n (0.1 to 0.7) and slightly higher activation energies for the same profile, than the Hill approach. The substitution of the n value, calculated from the Leeds analysis of a single profile, into the Hill analysis of the same profile (with the same t_r value) gave fair agreement (Table 5.28), especially in view of these small values for activation energies.

The values for the activation energy corrected to negligible thermocouple wire diameter (Table 5.26) relative to the values for the "standard" 0.10 mm diameter thermocouple were: 5% higher for the Mn/BaO_2 system; 17% for the Mo/BaO_2 system and 1% higher for both the Mn/SrO_2 and Mo/SrO_2 systems.

The Mn/BaO_2 system. In the plot of activation energy against composition for the Mn/BaO_2 system (Figure 5.63a) the lowest values were recorded for the 15 and 65% Mn compositions at the extremes of the range which supported combustion and which have reasonably slow burning rates and low maximum temperatures. A comparison of values of activation energy, burning rate and maximum excess temperature with the composition of the Mn/BaO_2 system (Figure 9.1) shows that the three quantities follow the same pattern of behaviour i.e. compositions with high burning rates burn at higher temperatures and have higher activation energies (temperature coefficient of reaction rate). There is also a pattern of double maxima in the plot - one maximum at low percentage fuel and the other at high percentage fuel.

The Mo/BaO_2 system. A similar comparison of the relationships between activation energy, burning rate and maximum temperature with composition for the Mo/BaO_2 system (Figure 9.2) does not show a clear relationship between the activation energy, the maximum temperature and the burning rate. The variations in these quantities with composition were smaller than for the Mn/BaO_2 system.

The Mn/SrO_2 system. The same comparison was made for the Mn/SrO_2 system (Figure 9.3) and the activation energy and the burning rate for this system follow approximately the same pattern as the Mn/BaO_2 system.

The Mo/SrO_2 system. Since only two compositions of this system actually burnt it was not possible to confirm these trends for the Mo/SrO_2 system.

Fig 9.1 Comparison of the relationships of U_{max}, v_{obs} & E_a with composition (Mn/BaO_2)

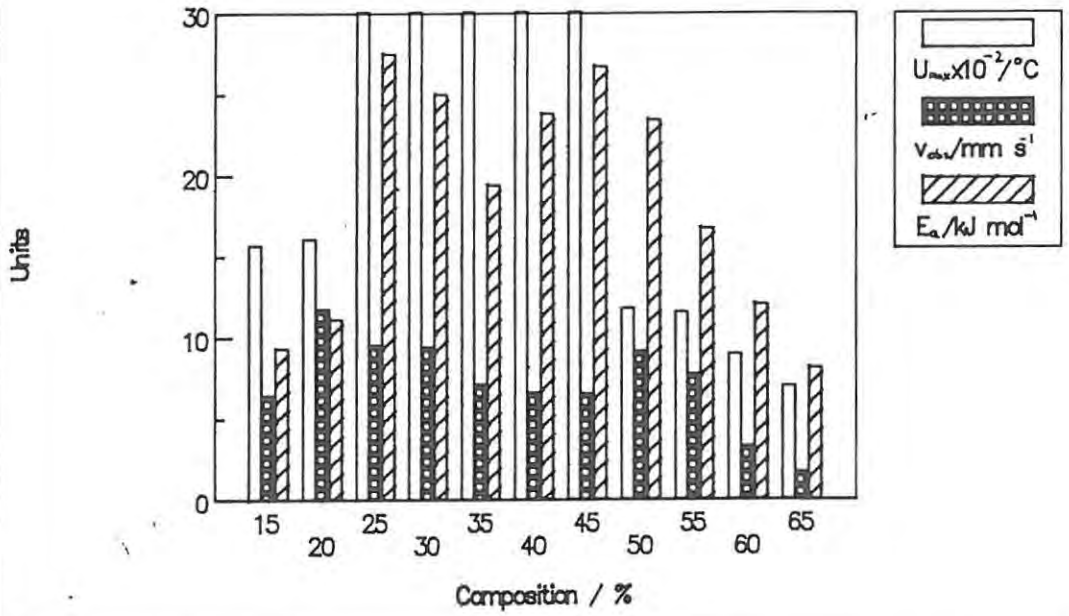

Fig 9.2 Comparison of the relationships of U_{max}, v_{obs} & E_a with composition (Mo/BaO_2)

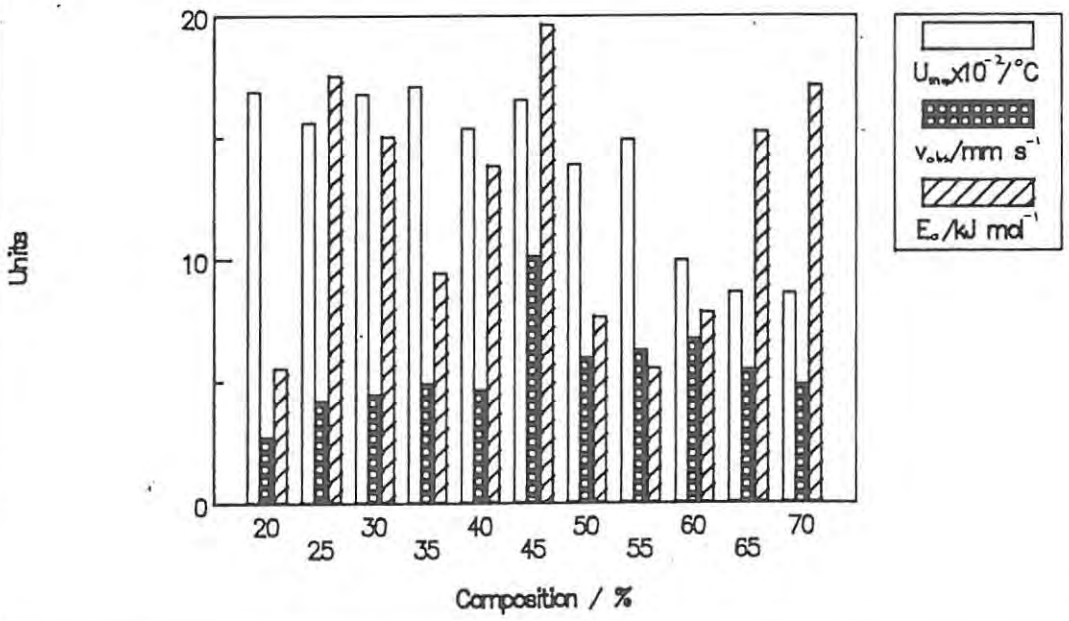

Fig 9.3 Comparison of the relationships of U_{max}, V_{obs} & E_a with composition (Mn/SrO_2)

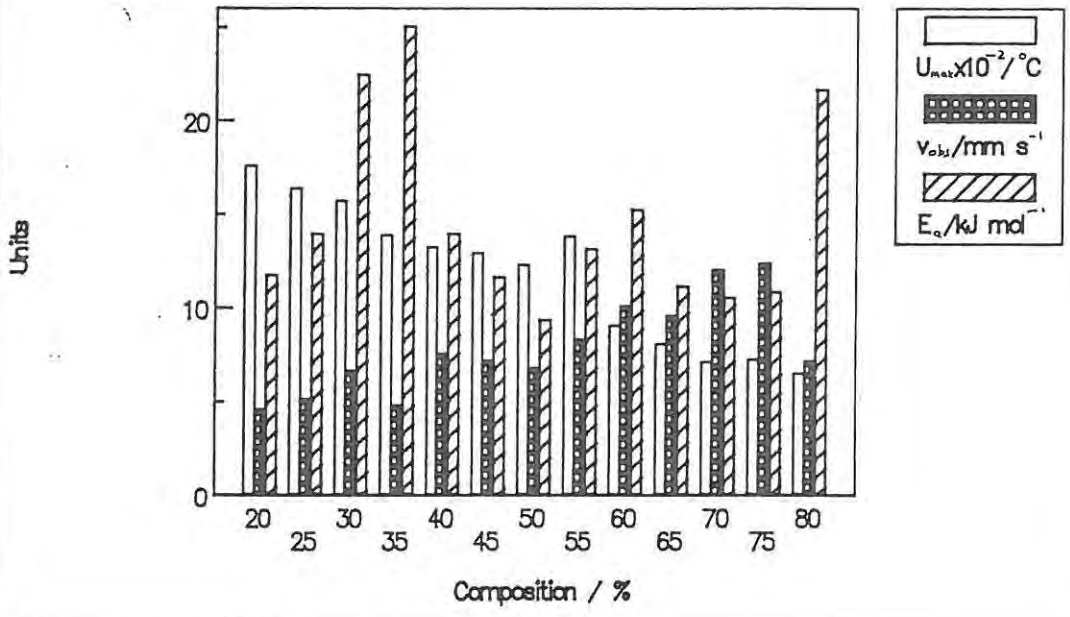

The applicability of the Arrhenius equation, and hence the significance of the parameters E_a and A, in reactions involving solid reactants has been debated in the literature without a generally agreed conclusion being reached. Arrhenius parameters are routinely derived from the thermal analysis, but the significance of these parameters is sometimes questionable. The Arrhenius parameters derived from analysis of temperature profiles generally imply higher reaction rates at low temperatures than are actually observed. Boddington *et al* (ref 48) proposed the use of a modified Arrhenius equation in describing the behaviour of pyrotechnic systems, which takes the form:

$$k^{-1} = k_{AR}^{-1} + (BT^m)^{-1}$$

where B is the diffusion coefficient and

$$k_{AR} = A_{AR} \exp(-E_{AR}/RT)$$

and A_{AR} and E_{AR} should, in principle, be determinable from thermal analysis experiments. At high temperatures, k_{AR} is very large, so that $k_{TPA} \approx BT^m$.

Table 9.3 compares the Arrhenius parameters for the 40% composition of the Mn/SrO_2 system, derived from the temperature profile recorded during the combustion of this mixture, with those derived from the thermal analysis of the same mixture (Section 4.6). As expected (ref 24), the E_a value from thermal analysis is considerably greater than from temperature profile analysis. Figure 9.4 compares the rate coefficients derived using the classical Arrhenius equation with kinetic data from the temperature profile and thermal analysis of 40% Mn/SrO_2 with the rate coefficient determined using this modified equation.

TABLE 9.3 COMPARISON OF KINETIC PARAMETERS FOR 40% Mn/SrO_2

n = 1			
THERMAL ANALYSIS		TEMPERATURE PROFILE ANALYSIS	
E_a / kJ mol^{-1}	A / s^{-1}	E_a / kJ mol^{-1}	A / s^{-1}
434 ± 9	$(2.0\pm0.3)\times10^{42}$	13.9 ± 1.5	1379 ± 100

From the results shown, in the range 600 to 1500 K, m = 1.75 ± 0.02, B = 1.35 ± 0.08 x 10^{-3} s^{-1} $K^{-1.75}$ and r = 0.99. For the 50% $W/K_2Cr_2O_7$ system, Boddington *et al* (ref 48) found m = 1.35 and B = 12.2 x 10^{-3} s^{-1} $K^{-1.35}$.

Fig 9.4 Comparison of rate coefficients for 40% Mn/SrO_2

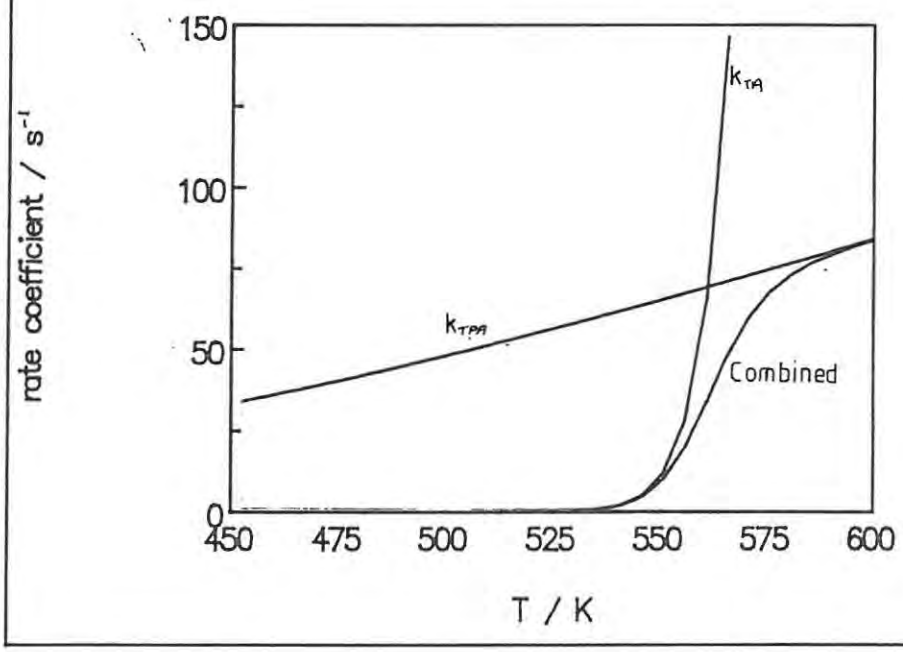

9.4 THERMAL CONDUCTIVITY

The bulk thermal conductivities, λ, of the metals Mn (7.81 W m^{-1} K^{-1}) and Mo (13.8 W m^{-1} K^{-1}) are decreased in the powdered samples to values of 0.39 and 0.46 W m^{-1} K^{-1}, respectively. These latter values are characteristic of powders (Table 6.2) where the main contribution to the thermal insulation is the void fraction in the powder. Hill *et al* (ref 18) reported a value of 0.76 W m^{-1} K^{-1} for Fe powder compared to 67 W m^{-1} K^{-1} for bulk Fe. Their value for pellets of BaO_2 powder was 0.67 W m^{-1} K^{-1} compared to the values in Table 6.4 of from 0.33 to 0.59 W m^{-1} K^{-1} as the compaction was increased. Beck *et al* (ref 27) reported values of λ from 0.22 to 0.40 W m^{-1} K^{-1} for the Sb/$KMnO_4$ system and Boddington *et al* (ref 24) 0.13 to 0.17 W m^{-1} K^{-1} for the W/$K_2Cr_2O_7$ system. Comparison of the individual powders (Table 6.2) shows that, over the relatively small range, BaO_2 has the highest thermal conductivity and SrO_2 the lowest, but SrO_2 has the smallest median particle size and largest void fraction (Table 6.1).

Substitution of up to 40% of the BaO_2 by Mn in a binary pyrotechnic composition (Table 6.4) has little effect on the thermal conductivity (or the void fraction). In general (Table 6.3), a decrease in the particle-size increases the void fraction (under the same compaction pressure). The median particle sizes of the Mn and BaO_2 differ only by a factor of $\sim$2 (Table 6.1). The minimum amount of compaction of BaO_2 (Table 6.3) thus has a greater effect on λ than does the addition of Mn. The compaction of Mn (Table 6.3) had a greater effect on λ than the effect of compacting separately two different particle-size ranges of Mn under the same load. A further increase of the compaction load used on any of the powders (Table 6.3) from 13 to 50 MPa did not significantly affect λ.

Although the Mo powder had a slightly lower thermal conductivity than BaO_2 (Table 6.2), substitution of up to 40% of BaO_2 by Mo slightly increased the value of λ. Median particle sizes were similar, as were void fractions. Similar substitution of SrO_2 by Mo did not have the same effect. The SrO_2 particles are $\sim$0.1x the diameter of the Mo particles.

Effect of thermal conductivity on the linear burning rate. The influence of the thermal conductivity, λ, on the burning rates, v, of pyrotechnic compositions is shown by the relationship:

$$v = (\lambda S / \rho c)^{\frac{1}{2}} = (\lambda / \rho c t_r)^{\frac{1}{2}}$$

where S (used in the Hill approach) is $1/t_r$ (used in the Leeds approach) (see Section 1.3).

Comparison of measured thermal conductivities of various compositions of the four binary systems with both measured and calculated burning rates for the same systems in Table 9.4, show that relatively small variations in the thermal conductivity of the system do not account for the changes in the measured and calculated burning rates.

TABLE 9.4 COMPARISON OF THERMAL CONDUCTIVITY & BURNING RATE			
SAMPLE	THERMAL CONDUCTIVITY / W m^{-1} K^{-1}	BURNING RATES / mm s^{-1}	
		MEASURED	CALCULATED
20% Mn/BaO_2	0.52 ± 0.02	11.7 ± 0.2	6.3 ± 0.4
40% Mn/BaO_2	0.48 ± 0.03	6.6 ± 0.4	4.3 ± 1.1
20% Mo/BaO_2	0.70 ± 0.04	2.7 ± 0.2	6.8 ± 1.8
40% Mo/BaO_2	0.67 ± 0.07	4.6 ± 1.0	3.9 ± 1.1
20% Mn/SrO_2	0.28 ± 0.02	4.5 ± 1.0	3.2 ± 0.4
40% Mn/SrO_2	0.31 ± 0.02	7.5 ± 1.0	7.5 ± 0.6
40% Mo/SrO_2	0.30 ± 0.02	2.3 ± 0.1	4.6 ± 0.5

In the calculation of burning rates, it is necessary to correct the rise time (derived from the slope of the temperature profile in the region of the remote rise zone, see Sections 1.3 B and 5.2.3) for the finite size of the thermocouple diameter, d, (ref 23). Plots of t_r against d and d^2 were examined for linearity and extrapolated to d equal to zero. The parameters of the relationships, $t_r = md + C$ and $t_r = md^2 + C$ are shown in Table 9.5.

TABLE 9.5 PARAMETERS OF RELATION BETWEEN t_r WITH d AND d^2			
SYSTEM	SLOPE / ms mm^{-1}	Y INTERCEPT / ms	CORRELATION COEFF
t_r vs d			
Mn/BaO_2	212 ± 52	15.2 ± 10.0	0.94
Mo/BaO_2	87 ± 13	18.1 ± 2.5	0.98
Mn/SrO_2	180 ± 17	-7.7 ± 3.2	0.99
Mo/SrO_2	44 ± 13	16.2 ± 2.4	0.93
t_r vs d^2	SLOPE / ms mm^{-2}		
Mn/BaO_2	587 ± 157	28.8 ± 10.8	0.94
Mo/BaO_2	232 ± 64	24.0 ± 4.4	0.93
Mn/SrO_2	501 ± 54	3.7 ± 3.7	0.99
Mo/SrO_2	122 ± 39	19.1 ± 2.7	0.91

The agreement between the measured and calculated linear burning rates improves when corrected rise times are used in the calculation (Table 9.6). The relationship, $t_r = md^2 + C$ (see Section 5.4), was used to calculate the corrected values for the rise time since this avoided the undefined negative rise time which was calculated for the Mn/SrO_2 system using the t_r/d relationship (Table 6.6).

TABLE 9.6 CALCULATED LINEAR BURNING RATES USING CORRECTED RISE TIMES		
SYSTEM	BURNING RATES / mm s^{-1}	
	MEASURED	CALCULATED
60% Mn/BaO_2	3.29 ± 0.80	2.84 ± 0.46
50% Mo/BaO_2	5.93 ± 0.20	4.26 ± 0.32
20% Mn/SrO_2	4.52 ± 0.98	5.53 ± 1.14
40% Mo/SrO_2	2.32 ± 0.06	3.42 ± 0.20

9.5 THERMOCHEMISTRY

Combustion reactions: BaO_2 and SrO_2 are known to decompose to the corresponding solid oxides and gaseous oxygen (refs 8, 9, 33) when heated (> 400°C), and manganese and molybdenum metals are reported (ref 53) to burn in oxygen to give Mn_3O_4(s) and MoO_3(s), respectively, at temperatures above 1000°C. The melting points of Mn and Mo are 1244 ± 3°C and 2620 ± 10°C (refs 52, 59), respectively. The vaporization temperature of MoO_3(s) is reported to be 1155°C (ref 52).

If it is assumed, in the first instance, that reactions in these four binary systems are solid-solid reactions:

fuel(s) + oxidant(s) → products(s)

then entropies of reaction will be small and the reactions will be driven by their exothermicity. The standard enthalpies of reaction for the various possible reactions were calculated from standard enthalpies of formation (ref 59) and are given below, together with the corresponding stoichiometric compositions (corrected where necessary for the impurity of the oxidant). The formation of complex oxides such as manganates or molybdates, XMO_n where X = Ba or Sr and M = Mn and Mo, by direct reaction or by secondary reaction between initially-formed simple oxides is also possible.

Alternatives to solid-solid reactions would include one or more of the following:

- melting of the fuel
- melting of the oxidant
- decomposition of the oxidant
- solid-gas reaction between the fuel and gaseous decomposition product or the surrounding atmosphere.

Mass losses were measured during combustion (Table 5.3), but ejection of solid and/or molten material was possible in addition to evolution of gas so that, except for the Mo/SrO_2 system, support for a mainly condensed phase reaction is inconclusive.

There is doubt whether barium or strontium peroxides melt. No evidence was observed in the thermal analyses of these two oxidants (Section 4.2) and no values for the enthalpy of melting were found. The enthalpies of melting of the metals were:

$Mn(s) \rightarrow Mn(l) \quad \Delta H = +13.8 \text{ kJ mol}^{-1}$

$Mo(s) \rightarrow Mo(l) \quad \Delta H = +27.6 \text{ kJ mol}^{-1}$

The decomposition of the oxidants:

$BaO_2(s) \rightarrow BaO(s) + \frac{1}{2}O_2(g) \quad \Delta H = +56.5 \text{ kJ mol}^{-1}$ (ref 59)

$SrO_2(s) \rightarrow SrO(s) + \frac{1}{2}O_2(g) \quad \Delta H = +51.1 \text{ kJ mol}^{-1}$ (ref 59)

TABLE 9.7 REACTIONS OF THE Mn/BaO_2 SYSTEM

REACTION	ΔH	STOICHIOMETRY / %	
	kJ mol^{-1}	PURE	85% PURE
$Mn(s) + BaO_2(s) \rightarrow BaO(s) + MnO(s)$	-328.5	24	21
$3Mn(s) + 4BaO_2(s) \rightarrow 4BaO(s) + Mn_3O_4(s)$	-386.9	20	17
$2Mn(s) + 3BaO_2(s) \rightarrow 3BaO(s) + Mn_2O_3(s)$	-393.8	18	15
$Mn(s) + 2BaO_2(s) \rightarrow 2BaO(s) + MnO_2(s)$	-407.1	14	12
$Mn(s) + 3BaO_2(s) \rightarrow 2BaO(s) + BaMnO_4(s)$	-428.9	10	8

TABLE 9.8 REACTIONS OF THE Mo/BaO_2 SYSTEM

REACTION	ΔH	STOICHIOMETRY / %	
	kJ mol^{-1}	PURE	85% PURE
$Mo(s) + 2BaO_2(s) \rightarrow 2BaO(s) + MoO_2(s)$	-472.8	22	19
$Mo(s) + 3BaO_2(s) \rightarrow 3BaO(s) + MoO_3(s)$	-576.2	16	14
$Mo(s) + 3BaO_2(s) \rightarrow 2BaO(s) + BaMoO_4(s)$	-797.1	16	14

A possible secondary reaction for this system:

$MoO_3(s) + BaO(s) \rightarrow BaMoO_4(s)$ $\Delta H = -220.9$ kJ mol^{-1} of BaO.

TABLE 9.9 REACTIONS OF THE Mn/SrO_2 SYSTEM

REACTION	ΔH	STOICHIOMETRY / %	
	kJ mol^{-1}	PURE	85% PURE
$Mn(s) + SrO_2(s) \rightarrow SrO(s) + MnO(s)$	-333.9	31	27
$3Mn(s) + 4SrO_2(s) \rightarrow 4SrO(s) + Mn_3O_4(s)$	-394.1	26	22
$2Mn(s) + 3SrO_2(s) \rightarrow 3SrO(s) + Mn_2O_3(s)$	-401.9	23	20
$Mn(s) + 2SrO_2(s) \rightarrow 2SrO(s) + MnO_2(s)$	-418.0	19	16

TABLE 9.10 REACTIONS OF THE Mo/SrO_2 SYSTEM

REACTION	ΔH	STOICHIOMETRY / %	
	kJ mol^{-1}	PURE	85% PURE
$Mo(s) + 2SrO_2(s) \rightarrow 2SrO(s) + MoO_2(s)$	-483.7	29	24
$Mo(s) + 3SrO_2(s) \rightarrow 3Sro(s) + MoO_3(s)$	-592.4	21	18

Bomb calorimetry. The results of bomb calorimetry for 40% compositions for the four binary pyrotechnic mixtures are compared in Table 9.11 with the changes of enthalpy measured using DSC, for samples heated at 40°C min^{-1} in N_2 (see Chapter 4). Values of ΔH calculated from temperature profiles for combustion in air of pyrotechnic mixtures, compressed under loads of 50 MPa for 1 minute, using the relationship, $\Delta H = Q = -cU_{ad}$, where c is the specific heat capacity of the mixture and U_{ad} is the adiabatic excess temperature. Since U_{ad} values are affected by the diameter of the thermocouple wire used to measure the profiles (see Section 1.3 B), the values in Table 9.11 are given for a thermocouple wire of diameter 0.1 mm and after correction to negligible diameter, determined by extrapolation of plots of Q against d to d equal to zero (see Section 5.7).

TABLE 9.11 COMPARISON OF HEATS OF REACTION				
SAMPLE	$-\Delta H = Q$ / kJ g^{-1}			
			PROFILES	
40%	BOMB CAL.	D S C	CALCULATED*	CORRECTED #
Mn/BaO_2	1.42 ± 0.32	0.44 ± 0.22	0.42 ± 0.06	0.46 ± 0.02
Mo/BaO_2	1.07 ± 0.03	1.04 ± 0.11	0.44 ± 0.03	0.52 ± 0.03
Mn/SrO_2	1.54 ± 0.24	0.27 ± 0.84	0.79 ± 0.04	1.02 ± 0.02
Mo/SrO_2	-	-	0.63 ± 0.03	0.71 ± 0.03

* Q values calculated from temperature profiles measured with a thermocouple wire of 0.1 mm diameter.
\# Q values corrected to negligible thermocouple wire diameter.

The bomb calorimetry values are generally higher than the Q values determined using DSC and those calculated from temperature profiles probably because the reactions in the bomb were reasonably complete and the measurements made were integral and any heat losses were accounted for. The slow heating of the sample in the DSC may have allowed formation of a protective oxide layer around the fuel which prevented complete combustion. Many of the temperature profiles had a long (~0.1 s) maximum temperature "plateau" which may indicate incomplete reaction as the burning front passes the thermocouple followed by further combustion which maintains the maximum temperature.

Previously published results for the heat evolved by pyrotechnic reactions of similar systems are shown in Table 9.12. Spice and Staveley (ref 6) used an adiabatic bomb calorimeter with a constant pressure reaction vessel to measure the heats of reaction of Mn/BaO_2 and Mo/BaO_2 in air. Yoshinaga *et al* (ref 29) used an inert atmosphere of Ar gas to determine their calorific values. Bomb calorimetry values from Table 9.11 have been repeated for ease of comparison.

TABLE 9.12 PREVIOUSLY PUBLISHED RESULTS FOR HEATS OF REACTION			
SAMPLE	Q / kJ g^{-1}		
	S&S (REF 6)	YOSHINAGA (REF 29)	BOMB CAL.*
40% Mn/BaO_2	1.2	-	1.42 ± 0.32
40% Mo/BaO_2	0.9	(FOR 50% COMPOSITION) 0.5	1.07 ± 0.03

* From Table 9.11.

The experimental values for heats of reaction of the pyrotechnic reactions are compared below with values calculated from the standard enthalpies of formation of reactants and possible products (Table 9.13). The standard enthalpy changes for the decompositions:

$$BaO_2(s) \rightarrow BaO(s) + \tfrac{1}{2}O_2(g) \quad \Delta H = 0.33 \text{ kJ } g^{-1}$$

$$SrO_2(s) \rightarrow SrO(s) + \tfrac{1}{2}O_2(g) \quad \Delta H = 0.43 \text{ kJ } g^{-1}$$

TABLE 9.13 ENTHALPIES OF FORMATION OF VARIOUS PRODUCTS (REF 59)

PRODUCT	ΔH / kJ g^{-1}	PRODUCT	ΔH / kJ g^{-1}
MnO	-5.43	MoO_2	-4.58
Mn_3O_4	-6.06	MoO_3	-5.18
Mn_2O_3	-6.06	BaO	-3.79
MnO_2	-5.98	SrO	-4.39

Possible reactions are reproduced here with standard enthalpies of reaction calculated for 40% compositions and reported as kJ per gram of pyrotechnic mixture.

$$Mn(s) + BaO_2(s) \rightarrow BaO(s) + MnO(s) \quad \Delta H = -1.2 \text{ kJ } g^{-1}$$

$$3Mn(s) + 4BaO_2(s) \rightarrow 4BaO(s) + Mn_3O_4(s) \quad \Delta H = -1.0 \text{ kJ } g^{-1}$$

$$2Mn(s) + 3BaO_2(s) \rightarrow 3BaO(s) + Mn_2O_3(s) \quad \Delta H = -0.9 \text{ kJ } g^{-1}$$

$$Mn(s) + 2BaO_2(s) \rightarrow 2BaO(s) + MnO_2(s) \quad \Delta H = -0.7 \text{ kJ } g^{-1}$$

$$Mo(s) + 2BaO_2(s) \rightarrow 2BaO(s) + MoO_2(s) \quad \Delta H = -0.8 \text{ kJ } g^{-1}$$

$$Mo(s) + 3BaO_2(s) \rightarrow 3BaO(s) + MoO_3(s) \quad \Delta H = -0.7 \text{ kJ } g^{-1}$$

The best agreement between ΔH values for suggested reactions and bomb calorimetric values (Table 9.12), assuming that bomb calorimetry gives complete reaction, occurs for the reactions which produce the following metal oxides: MnO(s) for the Mn/BaO_2 system and $MoO_2(s)$ for the Mo/BaO_2 system. The calculated heat evolved per gram of mixture by these two reactions for various compositions is compared with the experimental values determined from the temperature profiles (see Section 5.7) in Figure 9.5 for the Mn/BaO_2 system and in Figure 9.6 for the Mo/BaO_2 system.

The suggested pyrotechnic reactions using SrO_2 as oxidant, with their standard enthalpy changes during reaction, are given below.

$$Mn(s) + SrO_2(s) \rightarrow SrO(s) + MnO(s) \quad \Delta H = -1.7 \text{ kJ } g^{-1}$$

$$3Mn(s) + 4SrO_2(s) \rightarrow 4SrO(s) + Mn_3O_4(s) \quad \Delta H = -1.5 \text{ kJ } g^{-1}$$

$$2Mn(s) + 3SrO_2(s) \rightarrow 3SrO(s) + Mn_2O_3(s) \quad \Delta H = -1.3 \text{ kJ } g^{-1}$$

$$Mn(s) + 2SrO_2(s) \rightarrow 2SrO(s) + MnO_2(s) \quad \Delta H = -1.0 \text{ kJ } g^{-1}$$

$$Mo(s) + 2SrO_2(s) \rightarrow 2SrO(s) + MoO_2(s) \quad \Delta H = -1.2 \text{ kJ } g^{-1} \quad (1)$$

$$Mo(s) + 3SrO_2(s) \rightarrow 3SrO(s) + MoO_3(s) \quad \Delta H = -1.0 \text{ kJ } g^{-1} \quad (2)$$

In this series of reactions the best agreement with the experimental calorific values (Table 9.12) is with the reaction which produces $Mn_3O_4(s)$ for the Mn/SrO_2 system. In the absence of bomb calorimetry and DSC results for the Mo/SrO_2 system and with the small differences between reactions (1) and (2) above, no conclusions are possible for the Mo/SrO_2 reactions. The standard heat evolved per gram of mixture for various Mn/SrO_2 compositions is compared with the experimental values in Figure 9.7.

Fig 9.5 Comparison of Q values from different sources (Mn/BaO_2)

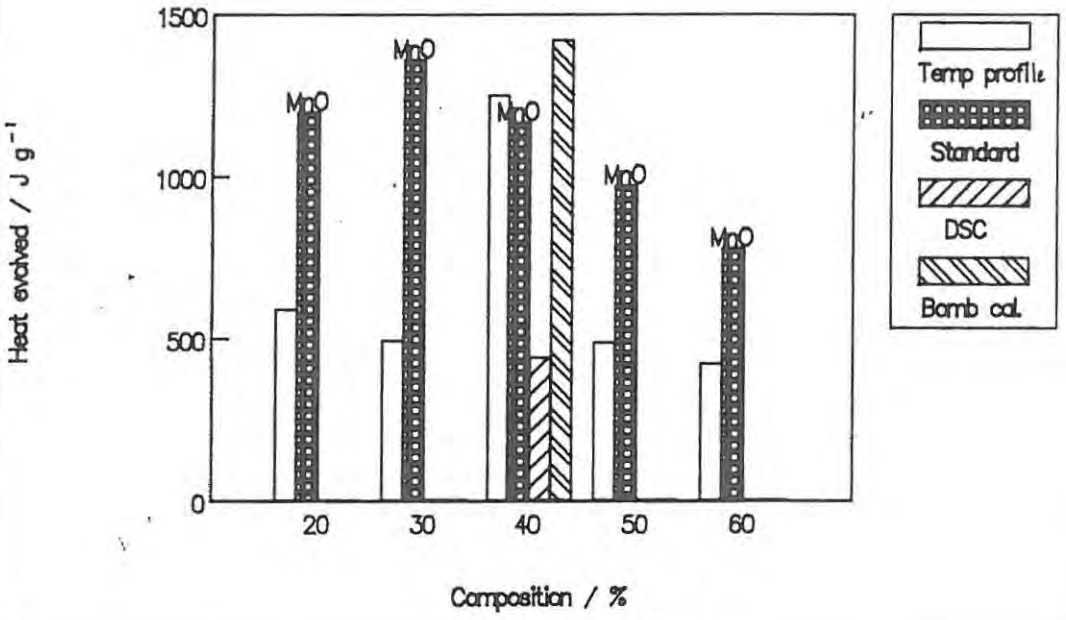

Fig 9.6 Comparison of Q values from different sources (Mo/BaO_2)

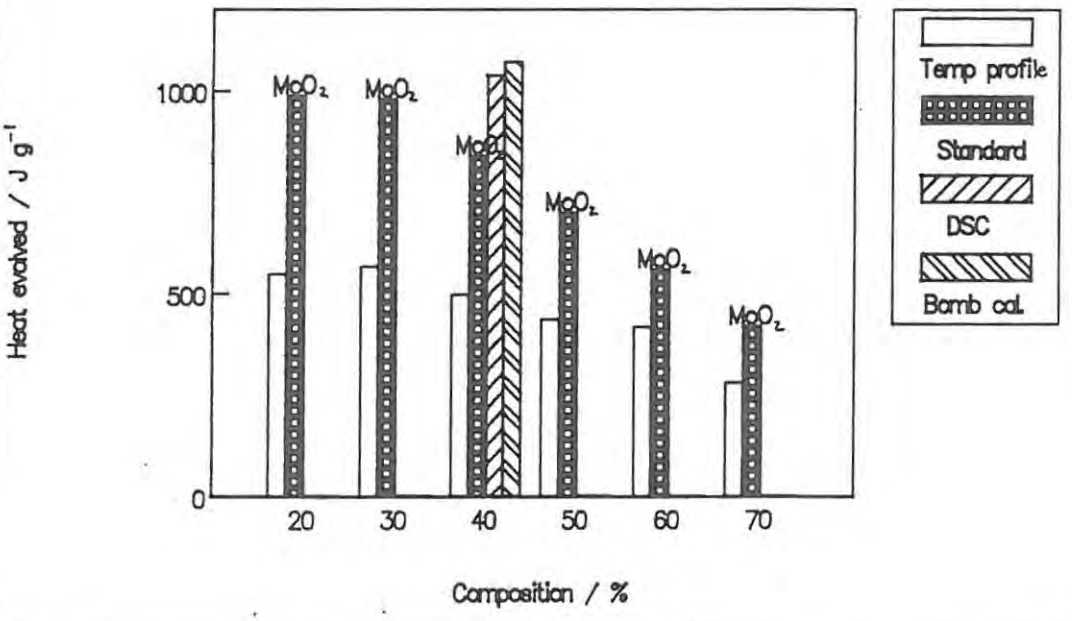

Fig 9.7 Comparison of Q values from different sources (Mn/SrO_2)

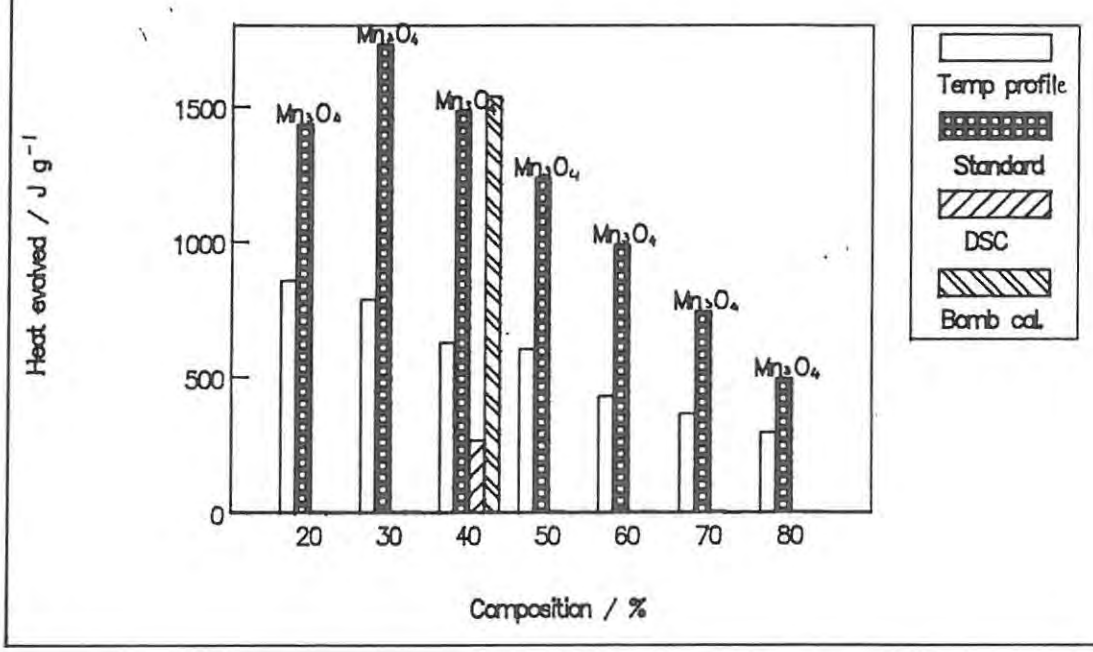

9.6 COMPARISONS BETWEEN BINARY SYSTEMS

Of all the binary systems the Mn/SrO_2 system burnt with the fastest rates ($\geq$ 12 mm s^{-1} for the 70 and 75% Mn compositions). The composition which burnt with the slowest rate but still with reliable combustion (i.e. combustion did not fail), was the 65% Mn/BaO_2 composition ($\sim$1.7 mm s^{-1}). Table 9.14 compares the burning rates for a common mass composition and common mole ratios for the four binary systems.

TABLE 9.14 COMPARISON OF BURNING RATES

BASIS OF COMPARISON	BURNING RATE / mm s^{-1}			
	Mn/BaO_2	Mo/BaO_2	Mn/SrO_2	Mo/SrO_2
40% FUEL	6.6 ± 0.4	4.6 ± 1.0	7.5 ± 1.0	2.3 ± 0.1
MOLE RATIO 4:1	7.7 ± 0.6	4.6 ± 1.0	10.1 ± 1.6	-
MOLE RATIO 2:1	7.1 ± 0.4	4.2 ± 0.3	7.1 ± 1.3	2.3 ± 0.1

Based on the mass percent of fuel or on the common mole ratio, the binary systems can be placed in order of decreasing burning rate as follows:

Mn/SrO_2 > Mn/BaO_2 > Mo/BaO_2 > Mo/SrO_2

Similar comparisons of maximum excess temperature values for the four systems are made in Table 9.15.

TABLE 9.15 COMPARISON OF MAXIMUM EXCESS TEMPERATURE

BASIS OF COMPARISON	MAXIMUM EXCESS TEMPERATURE / °C			
	Mn/BaO_2	Mo/BaO_2	Mn/SrO_2	Mo/SrO_2
40% FUEL	>1760	1536 ± 82	1323 ± 45	1526 ± 19
MOLE RATIO 4:1	1156 ± 28	1536 ± 82	901 ± 17	-
MOLE RATIO 2:1	1436 ± 92	1687 ± 87	1291 ± 63	1526 ± 19

Besides the compositions of the Mn/BaO_2 system which melted the thermocouple wire (25 to 45% Mn), the two Mo containing systems burned with higher temperatures than the two Mn containing systems.

Figures 5.63a and 5.63b show how the activation energy, E_a, values (based on a reaction order of n = 1) for the Mn/BaO_2 system are generally greater than those for the Mo/BaO_2 system. The E_a values are also higher for the mid-range compositions (25 to 55% fuel) than the values for the Mn/SrO_2 system. There is little difference between the E_a values for the Mn/SrO_2 and Mo/SrO_2 systems (Figure 5.64a) but the Mo/SrO_2 system has a limited range of compositions which sustain combustion. The E_a values for the 40 and 45% Mo/BaO_2 compositions are greater than the two E_a values for the 40 and 45% Mo/SrO_2 compositions (Figure 5.64b).

The comparison of E_a values for the binary systems in Table 9.16 shows that the Mn/BaO_2 system has the highest activation energy for similar mass proportions of fuel and for similar mole ratios.

TABLE 9.16 COMPARISON OF ACTIVATION ENERGIES (ASSUMING n = 1)				
BASIS OF COMPARISON	ACTIVATION ENERGY / kJ mol^{-1}			
	Mn/BaO_2	Mo/BaO_2	Mn/SrO_2	Mo/SrO_2
40% FUEL	23.8 ± 3.0	13.8 ± 3.0	13.9 ± 1.5	10.8 ± 3.1
MOLE RATIO 4:1	16.7 ± 1.0	13.8 ± 3.0	15.2 ± 4.6	-
MOLE RATIO 2:1	19.4 ± 5.3	17.5 ± 2.9	11.6 ± 1.2	10.8 ± 3.1

There is little difference between the heat outputs ($Q = cU_{ad}$) for the two BaO_2 systems (Figure 5.61a) and for the two SrO_2 systems (over the limited range of compositions of the Mo/SrO_2 system) (Figure 5.61b). However, the comparison of Q values for the systems with the same fuel (Figure 5.62a and 5.62b) shows that the two SrO_2 systems have greater heat outputs than the two BaO_2 systems, i.e. Mn/SrO_2 has generally greater Q values than the Mn/BaO_2 system, especially for low fuel compositions and Mo/SrO_2 has greater Q values for its two compositions which sustain combustion than the corresponding compositions of Mo/BaO_2.

The comparison of Q values in Table 9.17 confirms these comments, especially for the 2:1 mole ratio and the 40% fuel comparisons.

TABLE 9.17 COMPARISON OF HEAT OUTPUTS				
BASIS OF COMPARISON	Q / kJ mol^{-1} OF OXIDANT			
	Mn/BaO_2	Mo/BaO_2	Mn/SrO_2	Mo/SrO_2
40% FUEL	169 ± 4	140 ± 4	125 ± 14	126 ± 6
MOLE RATIO 4:1	174 ± 8	140 ± 4	129 ± 17	-
MOLE RATIO 2:1	136 ± 2	115 ± 5	137 ± 16	126 ± 6

Table 9.18 summarizes the trends in the four binary systems with respect to the parameters: burning rate (v_{obs}), maximum excess temperature (U_{max}). activation energy (E_a) and heat output (Q).

TABLE 9.18 SUMMARY OF TRENDS WITHIN THE FOUR BINARY SYSTEMS							
	DECREASE ——————>						
v_{obs}	Mn/SrO_2	>	Mn/BaO_2	>	Mo/BaO_2	>	Mo/SrO_2
U_{max}	Mo/BaO_2	>	Mo/SrO_2	>	Mn/BaO_2	>	Mn/SrO_2
E_a	Mn/BaO_2	>	Mn/SrO_2	≈	Mo/BaO_2	>	Mo/SrO_2
Q	Mn/BaO_2	>	Mo/BaO_2	>	Mn/SrO_2	≈	Mo/SrO_2

CHAPTER 10: DISCUSSION OF TERNARY SYSTEMS

10.1 THERMAL ANALYSIS

10.1.1 Mixed oxidant systems:

Thermal analysis of the BaO_2/SrO_2 mixture (Figure 4.28) indicated that there was no interaction between the two oxidants as they were heated to 950°C. All the thermal events observed could be interpreted solely in terms of the events observed for the individual oxidants. Similarly, the thermal behaviour of the ternary pyrotechnic systems could also be explained quantitatively in terms of their constituent binary systems.

Both of the mixed oxidant systems showed the low temperature loss of water from both oxidants. The $Mn/BaO_2/SrO_2$ system showed a low temperature ($\sim$365°C) exotherm, which, as for the Mn/BaO_2 system (see Section 9.2.1), was attributed to a pre-ignition reaction (PIR) between Mn and BaO_2. This reaction was initiated by the proposed endothermic rearrangement of the $Ba(OH)_2$ impurity, which has an onset temperature of $\sim$360°C in the DSC trace for BaO_2 (Figure 4.1). The $Mo/BaO_2/SrO_2$ system did not show a corresponding PIR and the endotherm due to the rearrangement of the $Ba(OH)_2$ in its DSC trace (Figure 4.32 a) was not obscured by an exotherm. This trace was similar to that for the Mo/BaO_2 system (Figure 4.14). Comparison of Figure 4.29 a ($Mn/BaO_2/SrO_2$) with Figure 4.11 a (Mn/BaO_2) and Figure 4.32 a ($Mo/BaO_2/SrO_2$) and Figure 4.14 a (Mo/SrO_2) shows that the DSC traces for the two mixed oxidant systems were dominated by the fuel/BaO_2 contributions.

10.1.2 Mixed fuel systems:

Thermal analysis of the Mn/Mo mixture indicated that there were no interactions between the two fuels as they were heated to 950°C. The only thermal event in the DSC trace of the mixture was assigned to the allotropic phase change which was observed in the DSC trace of Mn.

The existence of a PIR was again observed in the $Mn/Mo/BaO_2$ system, initiated by the proposed rearrangement of the $Ba(OH)_2$ impurity. Comparison of Figure 4.35 a ($Mn/Mo/BaO_2$) with Figure 4.11 a (Mn/BaO_2) shows that reaction in the ternary system was dominated by the reactions between Mn and BaO_2. Comparison of Figure 4.37 a ($Mn/Mo/SrO_2$) with Figures 4.19 (Mn/SrO_2) and 4.25 (Mo/SrO_2) shows that the DSC trace of this ternary system was qualitatively close to a combination of the DSC traces of the two binary systems.

10.2 BURNING RATES

The compositions used for the burning experiments of the ternary systems were chosen with knowledge of the burning characteristics of the four binary systems. Thus it was known, for example, that the 50% Mn/BaO_2 composition burnt faster than the 50% Mn/SrO_2 composition and that the 30% Mo/BaO_2 composition sustained combustion while the 30% Mo/SrO_2 did not burn in the open channel. The aim of these experiments, therefore, was to investigate how the addition of the second fuel or, second oxidant modified the burning of the binary systems.

10.2.1 Mixed oxidant systems:

All of the compositions mixed of the $Mn/BaO_2/SrO_2$ system, sustained combustion in the open channel. This might be expected since both the 50% Mn/BaO_2 and the 50% Mn/SrO_2 systems burnt, although with different burning rates (Table 5.20). The burning rates of these compositions are plotted against the percentage of both oxidants in Figure 10.1 and the resulting curve is concave-up. The burning rate of the 50% Mn/BaO_2 composition decreased initially on addition of SrO_2. The burning rate reached a minimum when a quarter of the BaO_2 has been replaced by SrO_2 and gradually increased as the quantity of SrO_2 was increased.

The maximum excess temperatures of the profiles for the various compositions of the $Mn/BaO_2/SrO_2$ system were not significantly altered by the composition.

The $Mo/BaO_2/SrO_2$ ternary system was of interest because 30% Mo/BaO_2 burns (Figure 5.20 a) while the 30% Mo/SrO_2 mixture does not burn (Figure 5.20 b). Combustion of the 30% Mo/BaO_2 composition failed when the proportion of the BaO_2 was decreased to 60% of the total mass (i.e. only 10% SrO_2). Only one further composition (30:10:60) of this system sustained combustion reproducibly, and the reason for this is not clear.

10.2.2 Mixed fuel systems:

The mixed fuels systems also burnt with significantly slower burning rates than expected from the relevant binary systems (Tables 5.22 and 5.23). Three dimensional plots of the burning rates against the composition of both fuels are shown in Figures 10.2 and 10.3.

All the compositions of the $Mo/Mn/BaO_2$ system were expected to burn since the two relevant binary compositions (30% Mo/BaO_2 and 30% Mn/BaO_2) both sustained combustion (Figure 5.20 a). With a mass ratio of 2:1 (Mo:Mn) the $Mo/Mn/BaO_2$ system failed to burn, but, as the proportion of Mn was increased the burning rate increased (Figure 10.2).

Fig 10.1 Burning rate against composition for the $Mn/BaO_2/SrO_2$ system

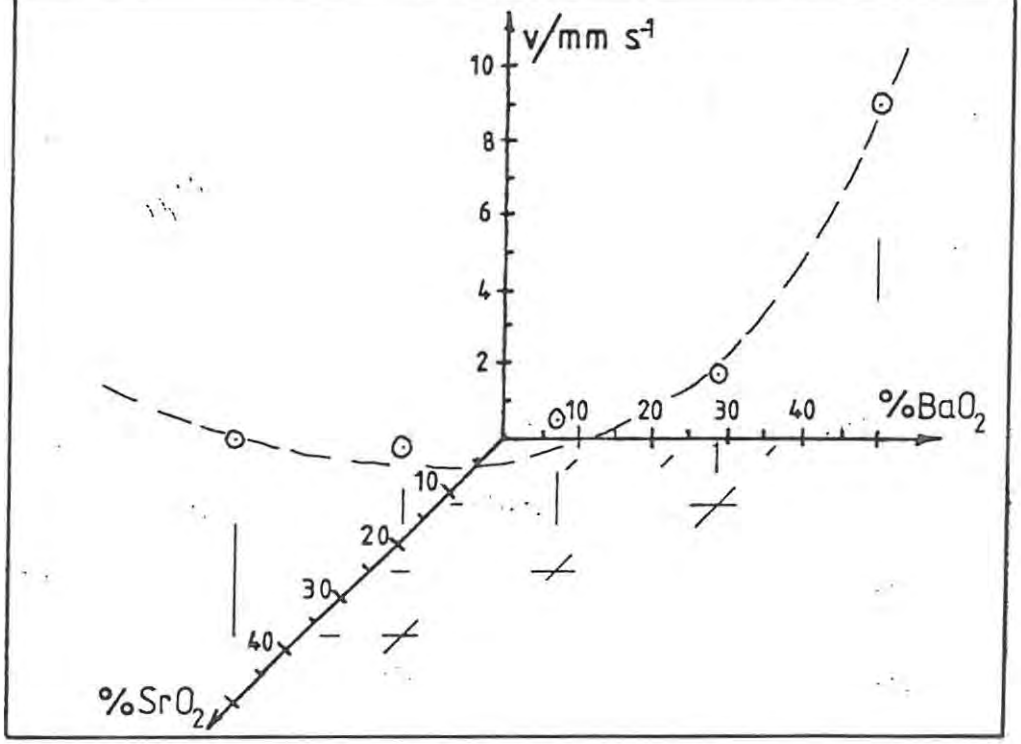

Fig 10.2 Burning rate against composition for the Mo/Mn/BaO_2 system

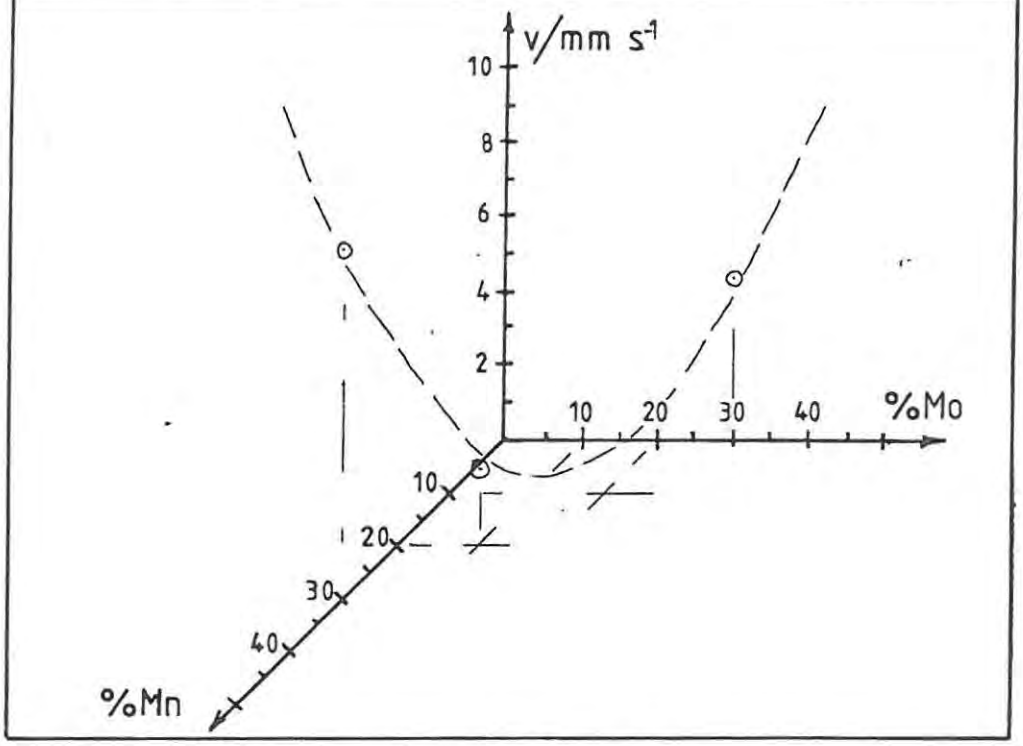

Fig 10.3 Burning rate against composition for the Mo/Mn/SrO_2 system

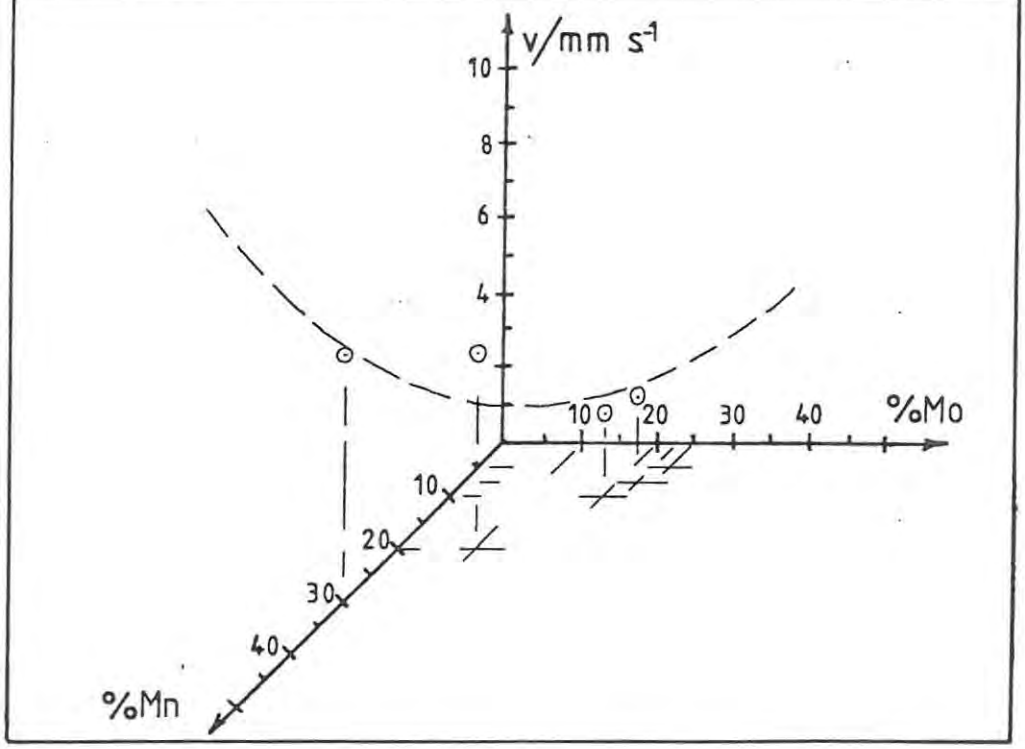

The Mo/Mn/SrO_2 system was of interest, because the 30% Mo/SrO_2 was known not to burn (Figure 5.20 b) while 30% Mn/SrO_2 burnt at a rate of ~7 mm s^{-1}. Only 7.5% Mn needed to be added before combustion was sustained with a burning rate of ~2 mm s^{-1} and as the percentage Mn was increased so did the burning rate.

One possible explanation for the slow burning rates of mixed fuel ternary systems is the possible interference between Mn and Mo due to the formation of an alloy which is reported (ref 53) to form at 1175°C containing between 62 and 73% Mn. The melting point of Mn (1244 ± 3°C) is close to the prevailing reaction temperatures (>1000 and <1700°C) and thus could also affect the burning of ternary mixtures.

10.3 TEMPERATURE PROFILES

The range of compositions which sustained combustion for the four ternary systems all produced temperature profiles of similar shape to the temperature profiles of a binary systems. The reproducibility of the temperature profiles for all four ternary systems was not good (see Section 5.6).

The composition of the Mn/BaO_2/SrO_2 ternary system had an affect on the slope of the rise zone and on the amplitude (T_{max}) of the temperature profile (Figure 5.58). The profiles of the ternary mixtures were more like the profile for the Mn/BaO_2 system than for the Mo/BaO_2 system. As the proportion of Mo was increased in the Mn/Mo/SrO_2 system, the amplitude of the profiles increased. However, when the proportion of Mo was greater than the proportion of Mn (20:10:70), the slope of the rise zone decreased markedly and the binary mixture (30% Mo/SrO_2) would not burn.

10.4 THERMOCHEMISTRY

In addition to the reactions between a single fuel and a single oxidant discussed in Section 9.5 for the binary systems, other possible reactions in the ternary systems include:

fuel(s or l) + fuel(s or l) → products(s or l)

oxidant(s) + oxidant(s) → products(s or l)

The binary alloy consisting of Mo and Mn, with a 1:1 composition, has been reported (ref 53) to form at temperatures of 1175°C, but no reports were found concerning a reaction between BaO_2 and SrO_2.

The reactions which take place in the ternary systems are likely to be similar to the reactions in the binary systems, complicated by competition between two fuels or two oxidants. The reaction in a mixed oxidant ternary system will depend on the relative stability of the two oxidants and the influence of the reverse reactions, i.e.:

$MO_2(s) \rightarrow MO(s) + \frac{1}{2}O_2(g)$

$M'O(s) + \frac{1}{2}O_2(g) \rightarrow M'O_2(s)$

Further complicating factors are the possibility of catalytic effects on the decomposition of the peroxides and the possible formation of either solid solutions or complex oxides during reaction. The thermally more stable of the two oxidants could act simply as an inert diluent at the start of combustion. At higher temperatures the role of this compound may then change to second oxidant. As the median particle size of the SrO_2 particles was approximately one tenth of the median size of the BaO_2 particles (Table 5.8), the SrO_2 particles may pack into the spaces formed by the metal/BaO_2 mixture and therefore change their contact area.

CHAPTER 11: CONCLUSIONS

Some compositions of all four of the binary pyrotechnic systems studied (Mn/BaO_2, Mo/BaO_2, Mn/SrO_2 and Mo/SrO_2) burnt in the open channel. Linear burning rates were all in the range from 2 to 12 mm s^{-1}, which is a relatively small segment of the overall range found in chemical delay systems. Maximum recorded combustion temperatures were mainly in the 1600° to 1750°C range. Heat outputs per gram of composition were in the range from 220 to 850 J.

Compaction and the use of smaller particle sizes of fuel increase the burning rates.

Although peroxides were chosen as oxidants on account of the apparent chemical simplicity of the decomposition reactions, they are also fairly susceptible to reaction with the surrounding atmosphere, to form hydroxides and carbonates, which were shown to influence their action as oxidants in pyrotechnic systems.

Examination of the residues after combustion of the binary systems showed that reaction was incomplete in all systems. The products consisted of mixtures of simple metal oxides of various stoichiometries and of complex oxides of the form XMO_4, where X = Ba or Sr and M = Mn or Mo. Onset of exothermic reaction appears to be associated with onset of decomposition of the respective oxidants, but is generally at temperatures below onset of oxidation of the metal powders by gaseous oxygen. Indications are that reactions are initially solid-solid reactions, in agreement with the proposals of Spice and Staveley (ref 7). This is supported by the slowing effect of inert additives.

Differences between the Mn and Mo systems may be related to some formation of MoO_3 which may volatilize at higher temperatures and thus not contribute to the formation of protective layers of product on the metal.

Values of the thermal conductivity of the various powders, measured at ambient temperature, did not show sufficient variation to account for the range of burning rates observed. Little information is available on the temperature dependences of the thermal conductivities of the materials used in pyrotechnic systems, and any such information would have to take into account the effects of phase transitions, decomposition and mass transport.

Values of activation energies derived from temperature profiles were all low (3 to 40 kJ mol^{-1} depending on the system and the assumptions made) and support the suggestion (ref 24) that reaction at high temperatures is controlled by diffusion processes. Activation energies derived from thermal analysis results were considerable higher (70 to 720 kJ mol^{-1}).

Some compositions of ternary systems with either mixed fuels or mixed oxidants could be ignited. No interactions between the fuels or between the oxidants were observed.

An ideal binary pyrotechnic system for detailed study would have a metal fuel which is oxidized predominantly to a single product. Mn and Mo are not ideal fuels in that they can readily exist in several oxidation states thus complicating attempts at determining reaction stoichiometry. Further complications arise from the formation of non-crystalline products and from rapid reactions of the products with water and CO_2 in the atmosphere.

As part of the research into the kinetics and mechanisms of pyrotechnic reactions, a parallel study (ref 78) of the reaction of a single fuel (silicon was chosen) with several individual oxidants, or combinations of oxidants, is in progress. The differences in the set of pyrotechnic systems chosen for comparison in this study (Figure 2.1) did not turn out to be as great as, for example, the differences between the fast-burning ($\sim$15 mm s^{-1}) $Si/K_2Cr_2O_7$ system and the slow-burning ($\sim$2 mm s^{-1}) $Si/BaCrO_4$ system.

There is a great need for extension of experimental techniques available to higher temperature ranges, which would remove some of the restrictions on the systems available for study.

REFERENCES

1. J. A. Conkling, "*Chemistry of pyrotechnics*", Marcel Dekker Inc., 1985.
2. S. Fordham, "*High explosives and propellants*" 2nd Edn., Pergamon Press, 1980.
3. R. Harris, Chem. Br., 13 (1977) 113.
4. P. Persson, 15th Int. Pyrotech. Sem., (1990) 757.
5. J. H. McLain, "*Pyrotechnics. From the view point of solid state chemistry*", Franklin Institute Press, 1980.
6. J. E. Spice & L. A. K. Staveley, J. Soc. Chem. Ind., 68 (1949) 348.
7. J. E. Spice & L. A. K. Staveley, J. Soc. Chem. Ind., 68 (1949) 313.
8. L. Till, J. Thermal Anal., 3 (1971) 177.
9. M. A. Fahim & J. D. Ford, Chem. Eng. J., 27 (1983) 21.
10. D. Beyens & E. Dubois, 10th Int. Pyrotech. Sem., (1985) 17-1.
11. L. B. Johnson, Jr, Ind. Eng. Chem., 52 (1960) 241.
12. O. Bowles, Mining and Met. 24 (1943) 85.
13. F. B. Clay & R. A. Sahlin, U.S. 2,709,129 (1955).
14. T. Stevenson & W. W. Cavell, U.S. 2,823,105 (1958).
15. J. Kristal & S. M. Kaye, A.D. 434664 (1965).
16. P. G. Laye, 14th Int. Pyrotech. Sem., (1989) 1.
17. R. Klein, M. Menster, G. von Elbe & B. Lewis, J. Phys. Chem., 54 (1950) 877.
18. R. A. W. Hill, L. E. Sutton, R. B. Temple & A. White, Research, 3 (1950) 569.
19. R. A. W. Hill & T. L. Cottrell, 4th Symp. Combustion, (1953) 349.
20. F. Booth, Trans. Faraday Soc., 49 (1953) 272.
21. S. F. Boys & J. R. Corner, Proc. R. Soc. London, Series A 197 (1949) 90.
22. S. Nakahara, J. Ind. Explos. Soc., 47 (1953) 277.
23. T. Boddington, P. G. Laye, J. R. G. Pude & J. Tipping, Comb. Flame, 47 (1982) 235.
24. T. Boddington, P. G. Laye, J. Tipping & D. Whalley, Comb. Flame, 63 (1986) 359.
25. R. A. W. Hill & A. A. Wallace, Nature, 178 (1956) 692.
26. V. D. Hogan & S. Gordon, J. Phys. Chem., 61 (1957) 1401.
27. T. J. Barton, N. Williams, E. L. Charsley, J. Rumsey & M. R. Ottaway, 8th Int. Pyrotech. Sem., (1982) 99.
28. S. Nakahara & T. Hikita, J. Ind. Expl. Soc., Japan, 20 (1959) 356.
29. S. Yoshinaga, K. Watanabe, M. Matsumoto & T. Nagaishi, Kyushu Sangyo Daigaku Kogakubu Kenkyu Hokoku, 21 (1984) 47.
30. J. D. Bernal, E. D'yatlova, I. Kasarnovskii, S. I. Raikhstein & A. G. Ward, Z. Krist., 92 (1935) 344.
31. I. A. Kazarnovskii, Khim. Referat. Zhur 4(1) (1941) 30.
32. L. I. Kazarnovskaya, J. Phys. Chem., 20 (1946) 1403.
33. H. G. Wiedemann & G. Bayer, Proc. 1st European Symp. Thermal Anal., (1976) 295.
34. M. Blumenthal, Roczniki Chem., 14 (1934) 598.

35. M. Blumenthal, J. Chim. Phy., 31 (1934) 489.
36. M. Tzentnershver & M. Blumenthal, Bull. Intern. Acad. Polonaise, Classe sci. math. nat. (1935)A 54.
37. M. Blumenthal, Roczniki Chem., 13 (1933) 5.
38. I. I. Vol'nov, Doklady Akad. Nauk SSSR, 94 (1954) 477.
39. Y. Azuma, M. Mizuide & K. Suehiro, Gyp. Lim., 162 (1979) 175.
40. J. M. Hildebrand, J. Am. Chem. Soc., 34 (1912) 256.
41. C. R. Le Chatelier, Acad. Sci., Paris, 115 (1892) 655.
42. J. A. Hedvall, Z. annorg. allg. Chem., 298 (1918) 164.
43. M. Centnerszwer & M. Blumenthal, Bull. int. Acad. Polon., Series A (1935) 540.
44. M. W. Beck, "*Intersolid combustion reactions in pyrotechnic systems*", Ph.D. Thesis, Rhodes University, 1984.
45. N. G. Vannerberg, Prog. Inorg. Chem., 4 (1962) 125.
46. E. Mallard & H. L. Le Chatelier, Ann. Mines, 4 (1895) 274.
47. T. Boddington & P. G. Laye, Thermochim. Acta, 120 (1987) 203.
48. T. Boddington, A. Cottrell & P. G. Laye, Comb. Flame, 79 (1990) 234.
49. P. G. Laye & E. L. Charsley, Thermochim. Acta, 120 (1987) 325.
50. M. E. Brown, Thermochim. Acta, 148 (1989) 521.
51. J. A. Conkling, Proc. Int. Symp. Anal. Detect. Explos., Fed. Bur. Invest., Washington, DC., 1983 129.
52. R. C. Weast (Ed), "*Handbook of Chemistry and Physics*", CRC Press, Florida, 67th Edn, 1986.
53. J. C. Bailar, H. J. Emeleus, R. Nyholm and A. F. Trotman-Dickenson (Eds)., "*Comprehensive inorganic chemistry*", Pergamon Press, New York, 1973.
54. J. Bassett, R. C. Denney, G. H. Jeffery & J. Mendham, "*Vogel's textbook of qualitative inorganic analysis*", Longman, 1981, 355.
55. L. V. de Yong & G. Wilson, 11th Int. Pyrotech. Sem., (1986) 81.
56. T. R. P. Gibb, "*Optical methods of chemical analysis*", McGraw-Hill, 1942, 128.
57. G. W. Ewing, "*Instrumental methods of chemical analysis*", McGraw-Hill, 1975, 136.
58. M. E. Brown, "*Introduction to thermal analysis*", Chapman and Hall, 1988.
59. O. Kubaschewski, E. Li. Evans & C. B. Alcock, "*Metallurgical thermochemistry*" 4th Edn, Pergamon Press, 1967.
60. R. J. M. Konings, E. H. P. Cordfunke, R. Shaviv & E. F. Westrum, Jr, Thermochim. Acta, 157 (1990) 307.
61. K. Ebert, H. Edeser & T. L. Isenhour, "*Computer applications in chemistry*", VCH Verlag, 1989, 337.
62. W. J. Dixon (Chief ed), "*BMDP statistical software manual*", University of California Press, 1985.
63. C. Das, Thermochim. Acta, 144 (1989) 363.
64. A. G. Rajendran, C. Ramachandran & V. V. Babu, Propellants, Explosives & Pyrotech., 14 (1989) 113.

65. M. E. Brown, D. Dollimore & A. K. Galwey, "*Reactions in the solid state*", Comprehensive Chemical Kinetics, Vol 22, Elsevier, 1980, 270.
66. A. D. Kirshenbaum & A. J. Beardell, Thermochim. Acta, 4 (1972) 239.
67. E. L. Charsley & M. R. Ottaway, "*Reactivity of solids*", Eds, J. Wood, O. Lindquist, C. Helgesson & N. G. Vannerberg, Plenum Press, 1977, 737.
68. M. W. Beck, M. E. Brown & N. J. H. Heideman, J. Phys. E: Sci. Instrum., 17 (1984) 793.
69. H. J. Goldsmith, K. E. Davies & V. Papazian, J. Phys. E: Sci. Instrum., 14 (1981) 1149.
70. R. A. Nyquist & R. O. Kagel, "*Infrared spectra of inorganic compounds*", Academic Press, 1971.
71. F. A. Miller & C. H. Wilkins, Anal. Chem., 24 (1952) 1253.
72. K. Nakanishi, "*Infrared absorption spectroscopy. Practical*", Holden-Day Inc., 1962.
73. J. R. Ferraro, J. Chem. Ed., 38 (1961) 201.
74. D. Barisin & I. Batinic-Haberle, Propellants, Explosives & Pyrotech., 14 (1989) 162.
75. B. S. Ault & L. Andrews, J. Chem. Phys., 62(6) (1975) 2312.
76. X-Ray Powder Data File, ASTM, 1960.
77. G. G. Johnson, Jr, & V. Vand, "*KWIC guide to the powder diffraction file 1966*", ASTM, 1966.
78. R. A. Rugunanan, Ph.D. Thesis, Rhodes University, in preparation.
79. H. J. Borchardt & F. Daniels, J. Am. Chem. Soc., 79 (1957) 41.

APPENDIX

1. Capture of raw data.

This was done with a PASCAL program called PROFILE.PAS. The main program is listed below, but the lengthy utility procedures have not been reproduced here. They are available on request from Professor M. E. Brown (°/o Chemistry Department, Rhodes University, Grahamstown, 6140, South Africa).

```
(* {$C-}                {Disable Ctrl-Break}  query - how in tp4*)

PROGRAM PROFILE;

uses dos,crt,general,inter,turbo3,graph, ghutils,
     globals,plot_graph,collect_,file_, init_sys;

{  ************************************************************** }
{  *                                                            * }
{  *   Temperature Profile software written in TURBO PASCAL V3.1  * }
{  *   for the PC-26 A/D card for the IBM-PC and Compatibles.     * }
{  *                                                            * }
{  *   The PC-26 card must be set to 0v to +10v mono-polar,       * }
{  *   with a base-address of $700 (Hex) !                      * }
{  *                                                            * }
{  *   Created by Barry Guthrie, RHODES UNIVERSITY, January 1988. * }
{  *   Some original code by Mattias H. Popp, April 1986.       * }
{  *                                                            * }
{  *   Modified by David Williams RHODES UNIVERSITY December 1989 * }
{  *        - proposed modifiation = accept the first 256       * }
{  *            points prior to the burn                        * }
{  *                                                            * }
{  *                                                            * }
{  *                                                            * }
{  ************************************************************** }

BEGIN
  for count := 0 to 30720 do
    values[count] := 0;

  GetDir(0,Help_drive);  (* drive containing program disk *)

  key := '0';
  Sample_No := 0;

  Text_Normal;
  Define_System;
  WHILE NOT (key = 'E') DO
  BEGIN
     MARK (heap_top);
     Process_Data;
     RELEASE (heap_top);
  END;
  CLRSCR;
  ChDir(Help_drive);  (* drive containing program disk *)
END.
```

2. Conversion of raw profile to a temperature profile.

The raw profile contains a time interval and set of counts. The conversions are:

(i) counts to milivolts - multiply by 2.44259/253.92

(ii) milivolts to temperature (°C) - substitute milivolts for V in the following polynomial:

$$T = 32.1108 + (120.180 \times V) - (2.45780 \times V^2) + (0.0410000 \times V^3) + (0.000636830 \times V^4)$$

3. Smoothing of profiles.

This was done with a BASIC program called MSPLINE.BAS (listed below).

```
0   REM "REGSPL1 "          EBERT/EDERER              881207
1 REM ************************************************
2 REM *** A regression - spline function is          ***
3 REM *** calculated. Equidistant grid points       ***
4 REM *** are needed.                               ***
5 REM *** The algorithm is taken from:              ***
6 REM *** Lawson/Hanson: Solving Least Squares      ***
7 REM *** Problems. Prentice Hall 1974.             ***
9 REM ************************************************
100   DIM X(300),Y(300),Z(300)
110   DIM A(352,5),D(352,7)
120   DIM B(300),C(300)
130 DIM YS(300)
200   DEF FNP(T)=.25*T*T*T
210   DEF FNQ(T)=1-.75*(1+T)*(1-T)*(1-T)
300   INPUT "How many grid points ";N
310   IF N<2 THEN N=2
320   GOSUB 10000 : REM Reading data in X() and Y()
330   GOSUB 11000 : REM Sorting data ascending in X()
360   IF N>=M-2 THEN N=M-2
400   B(1)=X(1) : B(N)=X(M)
410   H=(B(N)-B(1))/(N-1)
420   FOR I=2 TO N-1
430     B(I)=B(1)+H*(I-1)
440   NEXT I
460   GOSUB 12000 : REM Filling of matrix A
480   GOSUB 13000 : REM Filling of band matrices
481                 REM D=At*A und Z=At*Y
500   GOSUB 14000 : REM Solving equation D*C=Z
550   GOSUB 20000 : REM Calculating spline
560 GOSUB 24000
9900 PRINT:PRINT"run ended - data in file A:OUTPUT.DAT"
9999 END
10000 REM ****************************************
10001 REM *** Reading data in X() and Y()       ***
10002 REM ****************************************
10004 INPUT"Enter drive:filename ",FILE$
10006 OPEN"I",#1,FILE$
10008 FOR I=1 TO 300
10010 IF EOF(1) THEN 10026
10012 INPUT#1,X(I),Y(I)
10014 PRINT X(I),Y(I)
10020 NEXT I
10026 CLOSE#1
10028 M=I-2
10030 RETURN
11000 REM ****************************************
11001 REM ***  Data are sorted ascending in x.    ***
11002 REM ***  The minima and maxima in x and y   ***
11003 REM ***  are determined.                    ***
11005 REM ****************************************
```

```
11020 XO=X(1) : YO=Y(1) : XM=XO : YM=YO
11040 FOR I=2 TO M
11060   IF XO>X(I) THEN XO=X(I)
11080   IF XM<X(I) THEN XM=X(I)
11100   IF YO>Y(I) THEN YO=Y(I)
11120   IF YM<Y(I) THEN YM=Y(I)
11140 NEXT I
11200 D=INT(LOG(M)/LOG(2)):D=2^D-1
11220 FOR I=1 TO M-D
11240   FOR J=I TO 1 STEP -D
11260     IF X(J)<=X(J+D) THEN 11300
11270     HY=Y(J) : Y(J)=Y(J+D) : Y(J+D)=HY
11280     HX=X(J) : X(J)=X(J+D) : X(J+D)=HX
11290   NEXT J
11300 NEXT I
11300 NEXT I
11320 D=INT(D/2) :.IF D>0 THEN GOTO 11220
11900 RETURN
12000 REM ******************************************
12001 REM ***  Filling of the matrix A             ***
12002 REM ******************************************
12010 IB=1 : REM Index for grid points
12020 IX=1 : REM Index for data points
12050 IF X(IX)>B(IB+1) THEN GOTO 12150
12060 T=(X(IX)-B(IB))/H
12070 A(IX,1)=FNP(1-T)
12080 A(IX,2)=FNQ(1-T)
12090 A(IX,3)=FNQ(T)
12100 A(IX,4)=FNP(T)
12110 A(IX,5)=IB
12120 IF IX=M THEN GOTO 12200
12130 IX=IX+1 : GOTO 12050
12150 IB=IB+1 : GOTO 12050
12200 RETURN
13000 REM ******************************************
13001 REM *** Filling of the band matrices        ***
13002 REM *** D=At*A and Z=At*Y                   ***
13003 REM ******************************************
13060 FOR I=1 TO N+2
13080   FOR J=1 TO 7 : D(I,J)=0
13100   NEXT J : Z(I)=0 : NEXT I
13140 FOR K=1 TO M
13160   FOR I=1 TO 4 : FOR J=1 TO I
13200       I0=I+A(K,5)-1 : J0=J+A(K,5)-1
13220       D(I0,J0-I0+4)=D(I0,J0-I0+4)+A(K,I)*A(K,J)
13240       NEXT J : Z(I0)=Z(I0)+A(K,I)*Y(K)
13260   NEXT I : NEXT K
13300 FOR I=1 TO N+2 : FOR J=1 TO 3
13320     IF D(I,J)=0 THEN GOTO 13400
13340     D(J+I-4,8-J)=D(I,J)
13400 NEXT J : NEXT I
13900 RETURN
14000 REM ******************************************
14001 REM *** Solving equation system D*C=Z       ***
14002 REM ******************************************
14040 FOR I=1 TO N+2 : D4=D(I,4) : FOR J=1 TO 7
14060     D(I,J)=D(I,J)/D4 : NEXT J : Z(I)=Z(I)/D4
14080   J=I+3 : IF J>(N+2) THEN J=N+2
14100   IF I=N+2 THEN GOTO 14400
14140   FOR K=I+1 TO J
14150     L3=D(K,4 -(K-I))
14160     FOR L=1 TO 4
14180       L1=L+3 : L2=L+3-(K-I)
14200       D(K,L2)=D(K,L2)-L3*D(I,L1)
14220     NEXT L : Z(K)=Z(K)-L3*Z(I)
14240   NEXT K
14400 NEXT I
14500 FOR I=1 TO N+5 : C(I)= 0 : NEXT I
14520 FOR I=N+2 TO 1 STEP -1
14540 C(I)=Z(I)-D(I,5)*C(I+1)-D(I,6)*C(I+2)-D(I,7)*C(I+3)
14560 NEXT I
14900 RETURN
20000 REM ******************************************
20001 REM *** Calculating the spline function    ***
20002 REM ******************************************
20020 FOR I=1 TO M
20030   X=X(I)
20040   GOSUB 21000 : REM determining spline interval j
20060   T=(X-B(J))/H
20080   Y=C(J)*FNP(1-T)+C(J+1)*FNQ(1-T)+C(J+2)*FNQ(T)
20090   Y=Y+C(J+3)*FNP(T)
```

```
20100   PRINT I,X(I),Y(I),Y
20110 YS(I)=Y
20200 NEXT I
20990 RETURN
21000 REM ****************************************
21001 REM *** Determining spline interval j      ***
21002 REM ****************************************
21010 J=0
21020 IF X<=B(1) THEN : J=1 : RETURN
21040 IF X>=B(N) THEN : J=N-1 : RETURN
21060 J=J+1
21080 IF X>B(J) THEN GOTO 21060
21100 J=J-1
21200 RETURN
22000 REM ****************************************
22001 REM ***  Evaluating the spline function     ***
22002 REM ****************************************
22040 GOSUB 21000 : REM determining spline interval j
22060 T=(X-B(J))/H
22070 Y=C(J)*FNP(1-T)+C(J+1)*FNQ(1-T)+C(J+2)*FNQ(T)
22080 Y=Y+C(J+3)*FNP(T)
22900 RETURN
24000 REM ****************************************
24010 REM     OUTPUT TO FILE
24020 REM ****************************************
24025 PRINT:PRINT"smoothed data being written to file A:OUTPUT.DAT"
24030 OPEN"O",#2,"A:OUTPUT"
24040 FOR J=1 TO M
24050 WRITE#2,X(J),YS(J)
24060 NEXT J
24100 CLOSE#2
24200 RETURN
63999 END
```

4. Algorithms used for data processing on spreadsheets.

A. Differentiation.. 9-point Savitsky-Golay (ref P45), at point y_4:

$$(dy/dt) = (-4y_0-3y_1-2y_2-y_3+y_5+2y_6+3y_7+4y_8)/(60 \times \Delta t)$$

B. Integration.

Trapezoidal rule:

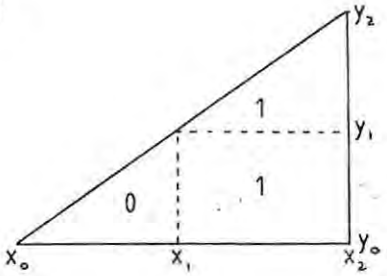

$$Area_0 = (x_1 - x_0) \times (y_1 - y_0)/2$$

$$Area_1 = (x_2 - x_1) \times \{(y_1 - y_0) + (y_2 - y_1)/2\}$$

$$Area_{cumulative} = Area_1 + Area_0$$

5. Preparation of a file for transfer and analysis.

The Leeds G function is calculated for given values of the rise and decay times, t_r and t_d. The G function is integrated and normalised to give α and $(1 - \alpha)$. From the original temperature profile, the time base is related to T values and hence 1/T values. Using FILE and XTRACT write out the section containing G, area, α, $1 - \alpha$, T and 1/T over the range $(1 - \alpha) = 0.99$ to 0.01 or closest. (NB! Use the option to convert formulae to values.)

Recall the extracted section and delete the area, α and T columns. Print the G, $1 - \alpha$ and 1/T values to a file using the required range.

Under DOS, use EDLIN A:filename to edit the file as necessary. (NB! Check that there are no strange lines or characters at the end of the file.) (Useful EDLIN commands are L to list, D to delete, E to end or Q to quit if a mistake has been made.)

6. Transfer of files to mainframe.

The file for transfer has to in the format y_i (= G), x_i (= 1 - α), z_i (= 1/T). Transfer is done by changing the directory to RMF and typing RMF. The serial output of the PC should be converted to a CYBER line. On receiving the RMF response, type T (for terminal mode). The CYBER responses should then be obtained and logging on is done as normal. CTRL \ is used to return to RMF for transfer of the file. Type S (for send) and enter as requested.

```
e.g.    PC FILENAME          CYBER FILENAME          TYPE
         A: data.dat              RUN23               T (for text)
```

RETURN

The data should then be transferred without error messages. SAVE, filename (e.g. RUN23) stores it permanently.

7. Use of BMDP routines.

Routines BROWN and BROWN3R, written by Mrs S. Radloff, are required and the data file to be processed should be renamed as CHMB1 (i.e. RENAME, CHMB1 = RUN23).

The files required must be made local, i.e. GET,RUNBMDP,BROWN,BROWN3R and set to start, i.e.

REWIND,*

RUNBMDP,BMDP1R,BROWN,OUTPUT1(name)

REWIND,*

RUNBMDP,BMDP3R,BROWN3,OUTPUT2(name)

PRINT,OUTPUT1,,,

PRINT,OUTPUT2,,,

It may be necessary to edit BROWN or BROWN3R to change the initial guesses (or input filename), e.g.

FSE,BROWN (edit using cursor and del key, etc.)

HOME QR to end.